

A Dynamic Duo

Fast ion conduction in
metal hydride/oxide nanocomposites



Laura de Kort

A Dynamic Duo

Fast ion conduction in
metal hydride/oxide nanocomposites

Laura Maria de Kort

Author: Laura Maria de Kort
Title: A Dynamic Duo
ISBN: 978-94-6458-892-7
Printing: Ridderprint | www.ridderprint.nl
Cover design: Eva Huang | www.happynutcreations.com

A Dynamic Duo

Fast ion conduction in metal hydride/oxide nanocomposites

Een Dynamisch Duo

Snelle ion geleiding in metaal hydride/oxide nanocomposieten

(met een samenvatting in het Nederlands)

Proefschrift

ter verkrijging van de graad van doctor aan de
Universiteit Utrecht
op gezag van de
rector magnificus, prof.dr. H.R.B.M. Kummeling,
ingevolge het besluit van het college voor promoties
in het openbaar te verdedigen op

woensdag 22 februari 2023 des middags te 4.15 uur

door

Laura Maria de Kort

geboren op 23 februari 1994
te Almere

Promotor:

Prof. dr. P. E. de Jongh

Copromotor:

Dr. P. Ngene

Beoordelingscommissie:

Prof. dr. M. Tromp

Prof. dr. A. Meijerink

Prof. dr. W. K. Kegel

Prof. dr. M. Dijkstra

Prof. dr. M. Gibescu

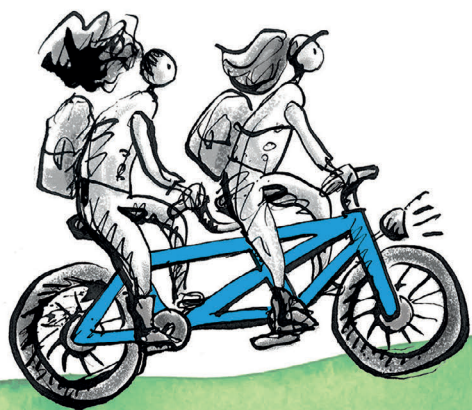
This PhD Thesis was financially supported by the Dutch Research Council (NWO) Materials for Sustainability program.

Table of contents

Chapter 1	Introduction	11
Chapter 2	The interplay between metal hydride and oxide in sodium-based metal hydride nanocomposites	37
Chapter 3	Preparation of ion-substituted metal hydride/oxide nanocomposites	63
Chapter 4	The effect of nanoscaffold porosity and surface chemistry on the Li-ion conductivity of $\text{LiBH}_4\text{-LiNH}_2$ /oxide nanocomposites	83
Chapter 5	X-ray Raman spectroscopy of conductive interfaces in LiBH_4 - and NaBH_4 /oxide nanocomposites	105
Chapter 6	Exploratory study on Li- and Na-ion conduction in nitrate- and nitrite/oxide nanocomposites	125
Chapter 7	Summary and Future perspectives	147
Chapter 8	Nederlandse samenvatting	157
	List of publications and presentations	169
	Acknowledgements Dankwoord	173
	About the author	177

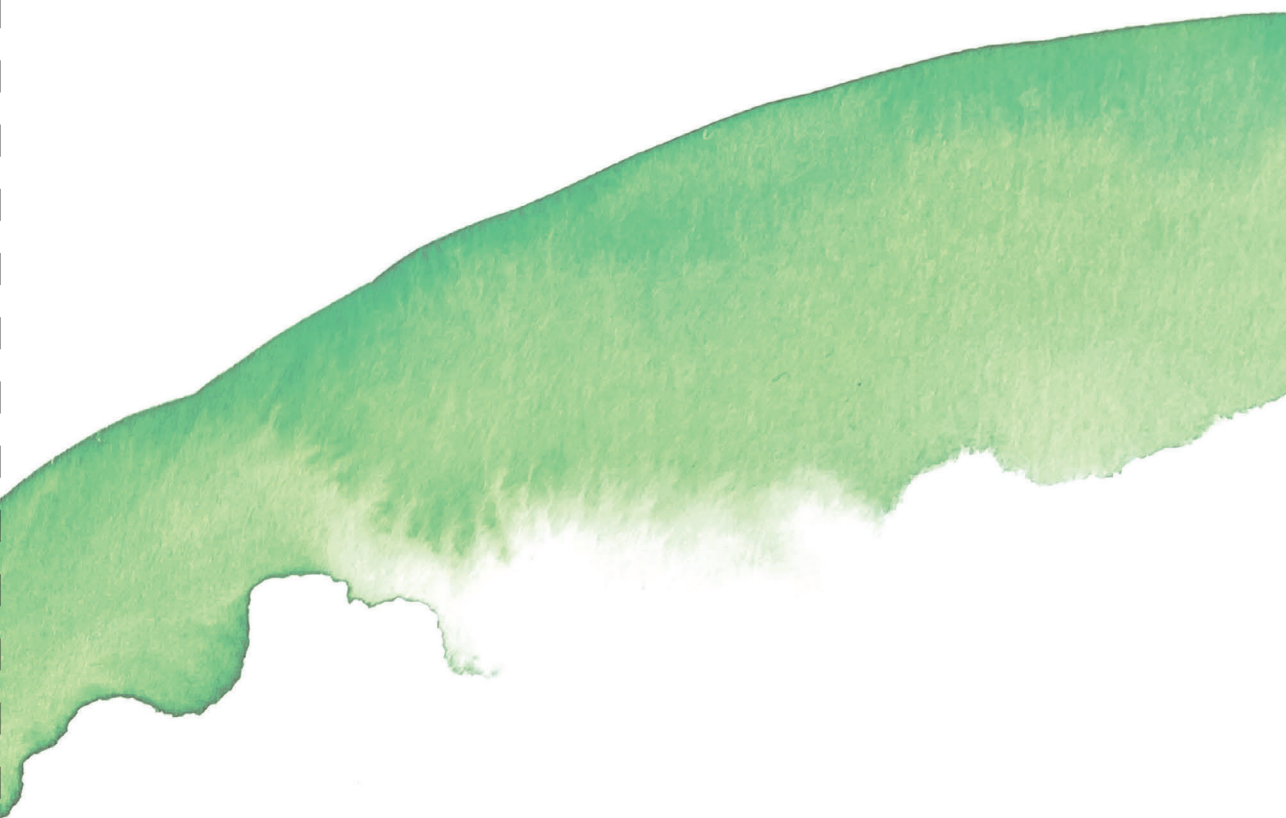
List of abbreviations

AC	Alternating current
a.u.	Arbitrary units
BET	Brunauer-Emmett-Teller
BJH	Barrett-Joyner-Halenda
C-rate	Rate at which a battery is charged or discharged relative to its capacity. At a C-rate of 1C, the discharge current will discharge the entire battery in 1 hour.
CPE	Constant phase element
DC	Direct current
DSC	Differential scanning calorimetry
DRIFTS	Diffuse reflectance infrared Fourier transform spectroscopy
EELS	Electron energy loss spectroscopy
EFG	Electrical field gradient
EIS	Electrochemical impedance spectroscopy
EM	Electron microscopy
FT-IR	Fourier transform infrared spectroscopy
LDHs	Layered double hydroxides
MAS	Magic angle spinning
MCM-41	Mobil Composition of Matter No. 41 (Mesoporous SiO ₂ scaffold)
NEXAFS	Near edge X-ray absorption fine structures
RIXS/NIXS	Resonant or Non-resonant inelastic X-ray scattering
RMS	Root mean square
SBA-15	Santa Barbara Amorphous-15 (Mesoporous SiO ₂ scaffold)
SEI	Solid electrolyte interphase
ssNMR	solid-state nuclear magnetic resonance
TCD	Thermal conductivity detector
TPD	Temperature programmed desorption
PF	Pore filling
PM	Physical mixture
XAS	X-ray adsorption spectroscopy
XRD	X-ray diffraction
XRS	X-ray Raman scattering
XPS	X-ray photoelectron spectroscopy



1

Introduction



This chapter is based on: de Kort, L. M., Gulino, V., de Jongh, P. E., & Ngene, P. (2021). Ionic conductivity in complex metal hydride-based nanocomposite materials: The impact of nanostructuring and nanocomposite formation. *Journal of Alloys and Compounds*, 163474.

1.1 Energy storage technologies

The world's increasing energy consumption combined with the need to minimize greenhouse gas emissions demands a transition to renewable energies. Unfortunately, most renewable energy sources, such as wind and solar power, lead to intermittent electricity output that can hugely differ over time, as illustrated in **Figure 1.1a**. During windy or sunny days, a large amount of renewable energy might be generated, resulting in an electricity surplus that cannot be used efficiently, while on other days the electricity generated from renewables is not as high as the required electricity demand. Effective energy storage would enable us to deal with the intermittent nature of renewable sources and, thereby, use their energy output effectively.¹⁻³ Among the various energy storage technologies, including mechanical-, thermal- and electrical storage, electrochemical energy storage in rechargeable batteries possesses a number of desirable features that make them a key candidate for future energy storage.¹

From the early twentieth century, batteries started to be widely used for energy storage. Their development started with primary (or non-rechargeable) batteries, such as Zn-MnO₂, and later Pb-acid and Ni-Cd batteries. The focus shifted to rechargeable Li-ion batteries, first commercialized by Sony in 1991.⁴ Similar to other rechargeable batteries, Li-ion batteries use reversible redox reactions to convert electrical energy to chemical energy, and vice versa.⁵ A schematic of a Li-ion battery is shown in **Figure 1.1b**. A commercial Li-ion battery consists of a layered transition metal oxide as the cathode, and a graphite-based anode. The two electrodes are separated by a porous membrane soaked with an ionically conductive electrolyte, typically a lithium salt (e.g., LiPF₆) dissolved in a mixture of organic liquids (e.g., ethylene carbonate or diethyl carbonate).⁵ Since the electrolyte is a poor electrical conductor, it allows Li-ions to shuttle between the electrodes, while electrons are forced through an external circuit. Nowadays, Li-ion batteries outperform competing battery technologies (Ni-metal hydride, Ni-Cd and Pb-acid batteries) due to their high-output voltages, high energy densities, long cycle life and high rate capability. These characteristics have enabled Li-ion batteries to dominate the portable electronics market and make them a serious contender to power the electric cars of the future.^{4,6}

While Li-ion batteries are highly optimized energy storage devices, their performance is continuously being improved. Specifically, several issues that hinder their

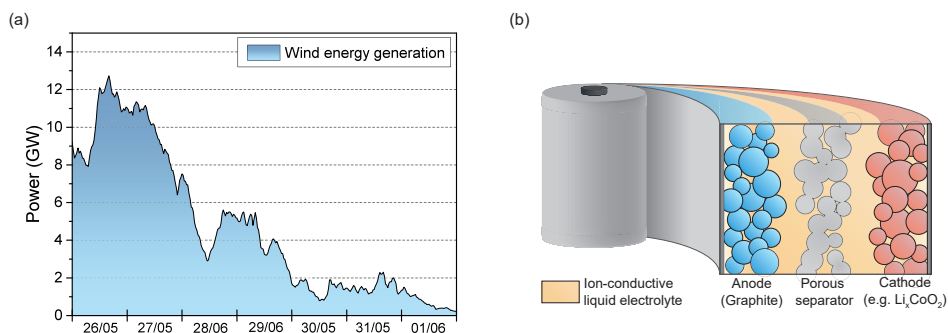


Figure 1.1 - (a) Renewable energy generated from wind power in the United Kingdom in the last week of May 2022. Data obtained from National Grid ESO Open Data. (b) Schematic representation of a conventional Li-ion battery based on electrodes separated by a membrane soaked with a liquid electrolyte

implementation for future applications need to be addressed. First of all, current battery systems often suffer from safety issues due to the flammable and volatile nature of the organic liquid electrolytes.^{7,8} Furthermore, the poor electrochemical stability of the liquid electrolytes with high capacity and high voltage electrodes also limits the storage capacity of the Li-ion battery.^{5,7} Finally, the application of Li-ion batteries for large scale electricity storage is impeded by the high cost of the battery components, in particular Li and Co.^{8,9} Consequently, the main goals of current battery research are to increase safety and energy density, while reducing cost. The first two goals could be reached by employing inorganic or polymeric solids as the ion-conducting electrolytes, resulting in the so-called all-solid-state battery.¹⁰

1.2 All-solid-state batteries

The development of next generation batteries with improved safety and energy density compared to the conventional Li-ion battery enables us to store and use renewable electricity more efficiently, minimizing the need for fossil fuels. One of the key candidates proposed is the all-solid-state battery, in which the conventional liquid electrolyte is replaced by a solid-state ion conductor.¹⁰ Solid-state electrolytes are intrinsically safer than the volatile and combustible liquid electrolytes and in many cases compatible with high energy density electrodes.^{10,11} Consequently, battery chemistries beyond the Li-ion technologies become available, such as Li-S, Li-air, Li-LiNi_{0.5}Mn_{1.5}O₄ and Na-, Mg- and Ca-ion batteries, which can lead to substantial gains in energy density.^{12,13} For example, the theoretical specific capacity of a metallic lithium anode (3862 mAh g⁻¹) is 10 times higher than that of the commonly used graphite anode (372 mAh g⁻¹).¹⁰ While the all-solid-state battery is a promising alternative to current battery technology, solid-state ion conductors that meet all requirements for battery application are still being developed. With this thesis we aim to contribute to the development of suitable solid electrolytes.

One of the main characteristics a solid must possess to be used as solid-state ion conductor is high ionic conductivity ($> 10^{-3} \text{ S cm}^{-1}$) at room temperature combined with negligible electronic conductivity ($10^{-7} \text{ S cm}^{-1}$).^{11,14,15} The mechanism of ion conduction in solids differs from that of a liquid. It can be described as a thermally activated process in which ions jump between point defect sites (either vacancies or interstitials) as first described by Frenkel, Schottky and Wagner.^{14,16} Therefore, ionic transport in a solid material generally relies on the concentration and distribution of defects. Fast ionic conduction in a solid can be achieved if it has a high density of mobile ions, sufficient vacant sites and a connected (continuous) diffusion pathway among the available sites, while the activation energy required for an ion to jump between adjacent available sites is low enough for an ion to easily hop from one site to another at a given temperature.^{11,14–16}

The ionic transport in a solid can be studied with solid-state nuclear magnetic resonance (ssNMR), transport measurements and electrochemical impedance spectroscopy (EIS), amongst others. The former probes local ion mobility, whereas the latter also provides insight in the long-range ionic transport. In this thesis, the ionic conductivity has often been determined with electrochemical impedance spectroscopy. While an electrical system that only contains pure resistances can be determined with Ohm's law, most real electrochemical systems, including solid-state ion conductors, also contain capacitive elements and hence exhibit more complex behaviour.^{17,18} In this case, impedance is needed

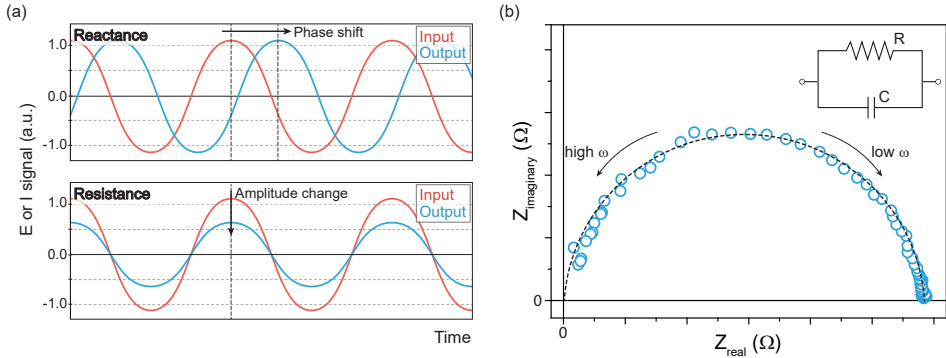


Figure 1.2 - (a) Representation of the response signal (output) that results from an oscillating input signal applied to an electrochemical system with reactance or resistance. (b) Typical Nyquist plot fitted with an equivalent circuit consisting of a resistor in parallel with a constant phase element (CPE).

to accurately describe the system. Simply put, impedance can be seen as a frequency-dependent resistance, and it has both a real and an imaginative (capacitive) component.

The impedance of a material is obtained by applying a small amplitude oscillating potential or current signal over a wide range of frequencies ($E(t) = |E| \sin(\omega t)$). The oscillating response signal ($I(t) = |I| \sin(\omega t + \theta)$) in current or voltage is measured. As shown in **Figure 1.2a**, this output signal differs from the input signal due to the reactance (e.g., capacitance or inductance) of the electrochemical system, which shifts the phase of the signal, and the resistance of the system, which changes the amplitude. Consequently, the impedance can be expressed by equation 1.1:

$$Z = \frac{E(t)}{I(t)} = \frac{|E| \sin(\omega t)}{|I| \sin(\omega t + \theta)} = |Z| \frac{\sin(\omega t)}{\sin(\omega t + \theta)} = |Z| e^{j\theta} = |Z|(\cos \theta + j \sin \theta) \quad (1.1)$$

In equation 1.1, Euler's relationship is used to express the impedance as a complex function, with $j = \sqrt{-1}$. The impedance can be visualized in a Nyquist plot, in which the imaginary impedance component ($|Z| \sin(\theta)$) is plotted against the real impedance component ($|Z| \cos(\theta)$) at each excitation frequency, as shown in **Figure 1.2b**. With this representation method, it is possible to directly read the ohmic and polarization resistance. More complex information can be obtained by fitting the data to an equivalent circuit, for example consisting of a resistor (R) and a capacitor (C). A detailed explanation on electrochemical impedance spectroscopy, as well as equivalent circuit fitting, can be found in the work of Orazem and Tribollet.¹⁷ In most cases, the conductivity of a solid ion conductor can be determined from the resistance (R) obtained from the equivalent circuit fit. The conductivity of the solid electrolyte (σ) can be calculated with $\sigma = t/(AR)$, using the thickness of the measured sample (t) and the geometric surface area (A) of the electrodes. The activation energy for ionic transport in the sample can be obtained from the Arrhenius expression ($\sigma = A/T e^{-E_a/KbT}$) after determining the conductivity over a range of temperatures.

For application of solid-state ion conductors in batteries, other properties besides high ionic conductivity are important. The most important requirements are a large electrochemical stability window, good chemical compatibility with electrode materials, excellent thermal stability, excellent mechanical properties, simple fabrication processes

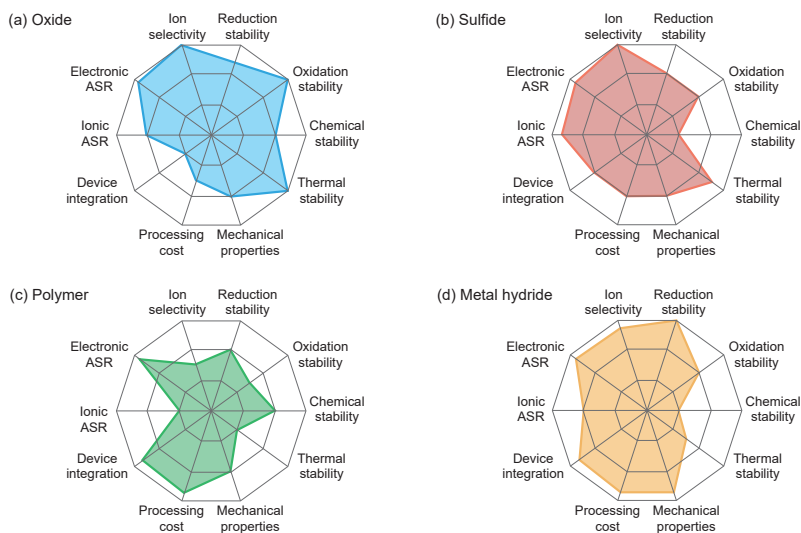


Figure 1.3 - Radar plots of the performance properties of (a) oxide-, (b) sulfide-, (c) polymer- and (d) metal hydride solid electrolytes.¹¹ ASR stands for area-specific resistance.

and low cost.¹¹ In recent years, different classes of solid-state ion conductors have been proposed, each with their own advantages and disadvantages. An indicative overview of the performance properties of several material classes is displayed in **Figure 1.3**, though the exact values can vary widely within a specific class. Generally, sulfide-type electrolytes display excellent ionic conductivity at ambient temperature, but their chemical stability is poor.^{19,20} Oxide-based ion conductors, on the other hand, have a higher (electro)chemical stability, though their manufacturing process is expensive and their poor interfacial contact with electrodes remains a concern.²¹ Finally, polymer-based solid electrolytes possess excellent processability and good interfacial contact with electrodes, but exhibit low ionic conductivity. While research has been largely focused on oxide-, sulfide-, and polymer-type solid-state electrolytes, complex metal hydrides have recently emerged as interesting alternative.

Compared to conventional solid ion conductors, complex metal hydrides display several unique properties that could be beneficial for all-solid-state batteries. Especially their low weight, combined with a generally high electrochemical stability (e.g., > 3 V versus Li/Li^+ for $\text{Li}_2\text{B}_{12}\text{H}_{12}$)^{22,23} and the ability to form a good interface with electrode materials (e.g., metallic lithium anode), distinguish them from most other solid-state ion conductors. Most complex metal hydrides possess high ionic mobility only after a reversible polymorphic phase change above room temperature. Consequently, their moderate room temperature ionic conductivity remains a challenge for successful implementation in an all-solid-state battery. Therefore, research in the metal hydride field focusses mainly on the ion mobility in metal hydrides and strategies that enhance room temperature conductivity. This is the focus of the work described in this thesis as well.

1.3 Complex metal hydrides as solid-state ion conductors

Complex metal hydrides are a subclass of metal hydrides. They are solids with an ionic lattice composed of metal cations, and complex anions in which the hydrogen is covalently

bonded to atoms of another element, such as in NiH_4^- , FeH_6^- , BH_4^- , AlH_6^{3-} and $\text{B}_{12}\text{H}_{12}^{2-}$. This class of materials, commonly known for their application as reducing agents in organic synthesis, has recently shown great potential in various energy-related applications, such as reversible hydrogen storage and electrochemical energy storage. Interest on metal hydrides as solid electrolytes was initiated by the discovery of unexpectedly high Li-ion mobility in lithium borohydride. Specifically, researchers from Orimo's group observed high lithium-ion mobility ($10^{-3} \text{ S cm}^{-1}$) after a reversible polymorphic transition from orthorhombic to hexagonal phase at 109°C .²⁴ Similar behaviour was later found in several other complex hydrides as well, such as $\text{Li}_2\text{B}_{12}\text{H}_{12}$ and $\text{NaCB}_9\text{H}_{10}$.^{25,26}

1.3.1 High ionic conductivity in LiBH_4

At room temperature, LiBH_4 has a low ionic conductivity ($10^{-8} \text{ S cm}^{-1}$ at 30°C), but a remarkable increase in conductivity is observed with increasing temperatures ($10^{-3} \text{ S cm}^{-1}$ at 120°C).^{24,27} This behaviour is caused by a reversible polymorphic transition from the orthorhombic phase to the hexagonal phase at 109°C , as schematically depicted in **Figure 1.4**.²⁴ The Nyquist plots obtained by electrochemical impedance spectroscopy show only a single arc in both the low temperature (LT) and high temperature (HT) polymorph, which indicates a single diffusion mechanism and limited grain boundary resistance.²⁸ Matsuo *et al.* were the first to confirm that the increased conductivity is related to fast Li-ion mobility in the hexagonal polymorph using ^7Li NMR measurements.²⁴ In the orthorhombic polymorph, NMR spectra show broad peaks, whereas in the high-temperature polymorph each spectrum displays sharp peaks. This decrease in linewidth shows that there is a high Li-ion mobility, which explains the high conductivity in hexagonal LiBH_4 .²⁴

To understand the origin of the fast-moving lithium ions, the conduction mechanism in LiBH_4 has been investigated. In the high-temperature hexagonal phase, the

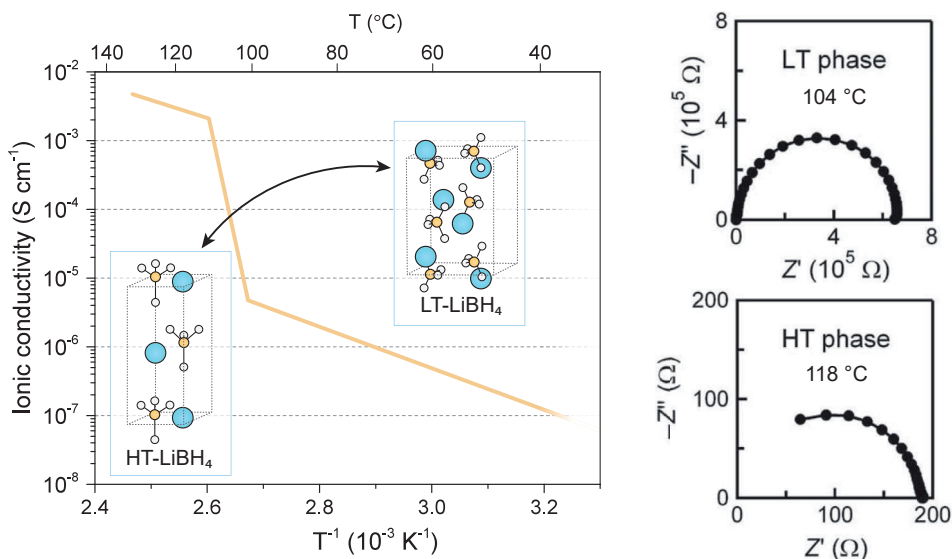


Figure 1.4 - Arrhenius plot of the conductivity of LiBH_4 , including a schematic representation of the phase transition from orthorhombic LiBH_4 (LT) to hexagonal LiBH_4 (HT) and the Nyquist plots obtained for the respective phases.²⁴

Li-ions are arranged in layers with nearly equivalent Li sites.²⁹ In this structure, the ionic conduction likely occurs via Frenkel-pair defects, i.e., Li^+ vacancies combined with interstitial Li^+ sites.^{28–30} It has been proposed that the movement of interstitial Li^+ ions in LiBH_4 is accommodated by the rotation of neighbouring BH_4^- -units, the so-called paddlewheel mechanism.^{28,31} In this way, the interstitial Li^+ -ions can easily jump from one interstitial site to the next. Interestingly, the diffusion energy barrier of Li^+ interstitials in *o*- LiBH_4 and *h*- LiBH_4 is similar, which means that the improvement in conductivity in *h*- LiBH_4 cannot be explained by changes in energy barrier for ion migration. On the other hand, the formation energy of defects in the hexagonal structure is substantially lower than in the orthorhombic phase.^{31,32} This results in a higher density of defect sites, hence, the higher ion mobility in *h*- LiBH_4 likely originates from the lower defect formation energy.³²

1.3.2 Ionic mobility in other metal hydrides

Besides LiBH_4 , other complex metal hydrides could be interesting candidates for application in all-solid-state batteries as well. Initially, research was focussed on metal hydrides similar to LiBH_4 , including LiAlH_4 , Li_3AlH_6 , LiNH_2 and Li_2NH , as well as their Na-based counterparts, NaBH_4 , NaAlH_4 and Na_3AlH_6 . The latter are relevant for sodium-based all-solid-state batteries, a cheaper alternative to lithium-based batteries. Unfortunately, most of these metal hydrides show low ionic conductivities at room temperature ($< 10^{-9} \text{ S cm}^{-1}$) and none of them undergoes a polymorphic transition that results in an increased Li^+ or Na^+ ion mobility.^{33–40} The highest conductivities are observed for Li_3AlH_6 , Na_3AlH_6 and Li_2NH , with conductivities of, respectively, $1.4 \cdot 10^{-7} \text{ S cm}^{-1}$, $6.4 \cdot 10^{-7} \text{ S cm}^{-1}$ and $2.5 \cdot 10^{-4} \text{ S cm}^{-1}$ at room temperature. Note that Li_2NH was one of the first complex hydrides investigated as possible ion conductor, already reported by Boukamp *et al.* in 1979.³⁶ However, due to the relatively small electrochemical stability window of 0.7 V, interest in Li_2NH quickly decreased. After the discovery of fast ionic conductivity in LiBH_4 combined with the increased interest in solid-state ion conductors, this compound has been investigated in more detail recently.^{38–40} Similar to LiBH_4 , it has been reported that anion dynamics and a low defect formation energy are key to achieving high ionic conductivity in the Li-N-H system.⁴⁰

In addition to solid electrolytes based on monovalent cations (e.g., Li^+ , Na^+), compounds with multivalent ion transport have also been gaining popularity for their application in Mg- and Ca-based batteries. Correspondingly, metal borohydride compounds based on Mg^{2+} and Ca^{2+} , such as $\text{Mg}(\text{BH}_4)_2$ and $\text{Ca}(\text{BH}_4)_2$, could be interesting solid electrolytes as well. Unfortunately, first principles studies on a variety of complex metal hydrides by Lu *et al.* indicated slow ion transport for divalent species.²² For example, pristine magnesium borohydride displays a low ionic conductivity of $10^{-12} \text{ S cm}^{-1}$ at room temperature. This is the case for most Mg-ion conductors, as divalent cations experience stronger ionic interaction to the lattice compared to monovalent ions. Consequently, the energy barrier for hopping is higher. Luckily, with specific modifications, which will be discussed in section 1.3.3, it is possible to increase the conductivity of $\text{Mg}(\text{BH}_4)_2$ by over 8 orders of magnitude⁴¹.

Recently, a novel series of metal hydride solid-state ion conductors has been proposed based on *closo*-borate and *closo*-carborate cluster anions, e.g., $[\text{B}_{12}\text{H}_{12}]^{2-}$ and $[\text{CB}_9\text{H}_{10}]^-$, depicted schematically in **Figure 1.5a**.^{25,26,42–48} This class of materials consists of a variety of geometrically similar (car)borate anions, which offers a toolkit of solid-state

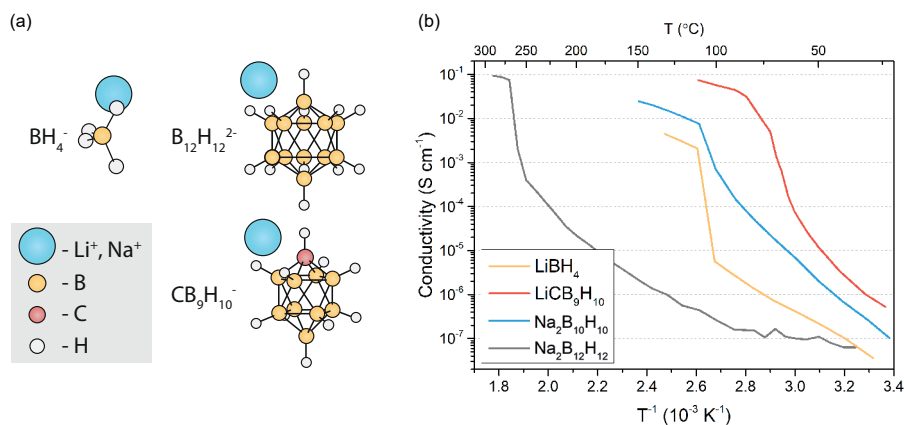


Figure 1.5 - (a) Schematic representation of Li^+ - and Na^+ -borohydride, *closo*-borate and *closo*-carborate compounds. (b) Arrhenius plot of the conductivity of different metal hydride compounds. Graphs are adapted with permission from ref. [26] Copyright 2016 Wiley, [43] Copyright 2014 Royal Society of Chemistry and [52] Copyright 2014 Wiley.

metal hydride-based compounds with great potential as solid electrolytes. Most *closo*-borates and *closo*-carborates undergo polymorphic transitions from ordered to disordered phases by heating to high temperatures (e.g., 315 °C for $\text{Li}_2\text{B}_{12}\text{H}_{12}$, 106 °C for $\text{NaCB}_{11}\text{H}_{12}$). Akin to LiBH_4 , these order-disorder polymorphic transitions are accompanied by a fast reorientational motion of the cage-like cluster anions (the paddle wheel mechanism) and a remarkable increase in ionic conductivity.

Ab initio molecular dynamics calculations strongly suggest that the fast cation mobility observed in *closo*-(car)borates is closely linked to the motion of the complex hydride anions.^{49–51} For example, in $\text{Na}_2\text{B}_{10}\text{H}_{10}$, the reorientation and disorder of the $\text{B}_{10}\text{H}_{10}^{2-}$ anion facilitates Na^+ hopping to octahedral sites, which link to the tetrahedral sites to form a connected network for fast ion diffusion.⁴⁹ The conductivities of LiBH_4 , $\text{Na}_2\text{B}_{10}\text{H}_{10}$, $\text{Na}_2\text{B}_{12}\text{H}_{12}$, and $\text{LiCB}_9\text{H}_{10}$ are presented in **Figure 1.5b**.^{26,43,52} Just above their polymorphic transition temperature (T_{trans}) both Li^+ and Na^+ -*closo*-borate-based ion conductors exhibit conductivities over 0.01 S cm^{-1} . In fact, at temperatures above T_{trans} , the ionic conductivities of some *closo*-(car)borate compounds are comparable to those of state-of-the-art solid-state ion conductors, such as $\text{Li}_x\text{La}_x\text{TiO}_2$ ($10^{-3} \text{ S cm}^{-1}$ at 30 °C) and sulfide glass-ceramics ($10^{-2} \text{ S cm}^{-1}$ at 30 °C).^{19,53,54}

Overall, it is clear that several metal hydrides demonstrate high ionic conductivities above their polymorphic transition temperature. Combined with their low density and good mechanical properties, this makes them promising candidates for next-generation batteries. However, for application in all-solid-state batteries, conductivities of at least $10^{-3} \text{ S cm}^{-1}$ at 30 °C are required. The room temperature ion conductivity of most metal hydrides is not yet sufficient and remains inferior to other solid ion conductors.⁵³ The room temperature Li-ion conductivities for sulfide-based electrolytes are, for example, in the order of $10^{-2} \text{ S cm}^{-1}$, which is orders of magnitude higher than the room temperature conductivity of most metal hydride-based solid electrolytes. Consequently, a main challenge for the development of metal hydride electrolytes is to improve their high ionic mobilities at room temperature.

1.3.3 Conductivity enhancement methods for metal hydrides

Over the past few years different strategies to improve room temperature conductivities in metal hydride-based ion conductors have been explored.⁵⁵ These strategies can be classified into three categories, i.e., partial ionic substitution, nanostructuring and nanocomposite formation (or interface engineering), which are schematically depicted in **Figure 1.6**. The most common method, partial ionic substitution, is based on replacing part of the metal hydride anions with other anions.^{28,56,57} As a result, either a homogenous solid solution is formed, in which the highly conductive polymorph is stabilized at lower temperatures, or a double-anion compound is formed with another crystallographic structure (and possibly enhanced conductivity).^{58,59} For example, ionic substitution of BH_4^- ($r_{\text{BH}_4^-} = 2.03 \text{ \AA}$) in pristine LiBH_4 with either I^- ($r_{\text{I}^-} = 2.20 \text{ \AA}$) or Br^- ($r_{\text{Br}^-} = 1.96 \text{ \AA}$) leads to stabilization of the high temperature hexagonal LiBH_4 phase at lower temperatures (**Figure 1.6a**). It has been observed that this method only works within the appropriate solubility limits ($h\text{-Li}(\text{BH}_4)_{1-x}(\text{I})_x$ is only stable in the range $0.18 \leq x \leq 0.50$ ⁶⁰), and with substituting anions of the appropriate size (Cl^- substitution ($r_{\text{Cl}^-} = 1.81 \text{ \AA}$) in LiBH_4 does not result in stabilization of $h\text{-Li}(\text{BH}_4)_{1-x}(\text{Cl})_x$ ⁶¹). Over the past years several notable solid solution or double-anion (and even triple-anion) compounds have been developed, including $\text{Li}(\text{BH}_4)_{1-x}(\text{Br})_x$ ⁶², $\text{Li}(\text{BH}_4)_{1-x-y}(\text{Br})_x(\text{Cl})_y$ ⁶³, $\text{Li}(\text{BH}_4)_{1-x}(\text{NH}_2)_x$ ⁵⁹, $(\text{LiCB}_9\text{H}_{10})_{0.7}(\text{LiCB}_{11}\text{H}_{12})_{0.3}$ ⁶⁴, $\text{Na}_4(\text{CB}_{11}\text{H}_{12})_2(\text{B}_{12}\text{H}_{12})$ ⁶⁵ and $\text{Na}_4(\text{B}_{12}\text{H}_{12})(\text{B}_{10}\text{H}_{10})$ ⁶⁶.

Nanostructuring and nanocomposite formation are less widely applied strategies. Nonetheless, it has been established that these methods can greatly improve ionic mobility in solid-state electrolytes. In the former method, nanostructuring, the metal hydride is mechanochemically activated by high-energy ball milling of the coarse-grained starting material for several minutes up to tens of hours. In general, this process reduces the grain size of the starting material to about 5 to 50 nm, while introducing defects and structural disorder (**Figure 1.6b**). These nanostructured grains typically consist of two regions, nanometer-sized crystallites separated by a large volume fraction of grain boundaries or interfacial regions.^{67,68} The impact of the milling process on the ion mobility is rather complex and not well understood. In fact, while the formation of defects and

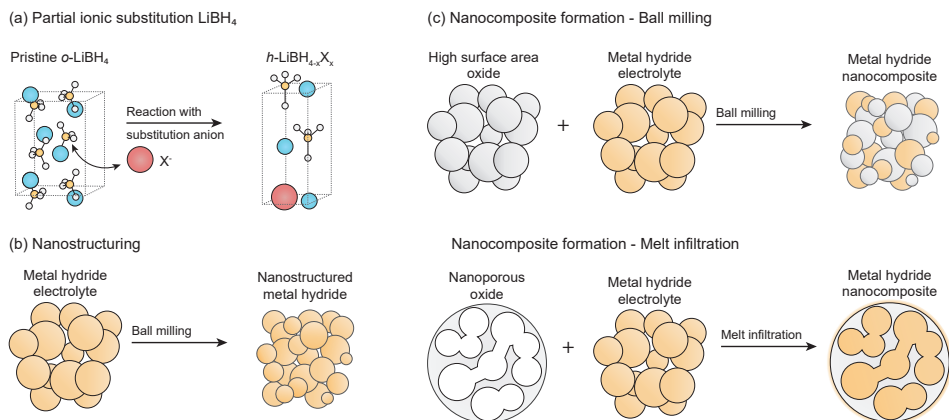


Figure 1.6 - Schematic illustrations of the different strategies that can be used to enhance ionic conductivity in metal hydrides: (a) partial ionic substitution, (b) nanostructuring and (c) nanocomposite formation.⁵⁵

grain boundaries can be detrimental for long range ionic transport in some fast ion conductors, ion conductors that largely depend on defect sites can benefit from defect rich grain boundaries that enhance their ionic conductivity. In both cases, nanostructuring clearly alters the ion dynamics in the ionic conductors. First reports on the application of this strategy focussed on the improvement of ionic conductivity in lithium oxides, such as LiNbO_3 and LiTaO_3 .^{67,69–71} Recently, the method has also been applied to several metal hydrides, e.g. LiBH_4 and LiAlH_4 , and *closo*-(car)borate compounds, including $\text{Li}_2\text{B}_{12}\text{H}_{12}$ and $\text{NaCB}_{11}\text{H}_{12}$.^{72–77} Often, milling indeed leads to an improved conductivity. However, since in most cases the conductivity improvement originates from the formation of non-stable defects, thermal (and likely long term) stability remains an issue.

In the research described in this thesis, we investigated how nanocomposite formation influences metal hydride conductivity. Nanocomposite formation also involves nanostructuring, but in this case the solid electrolyte compound is additionally mixed with a high surface area scaffold, often mesoporous oxides (SiO_2 , Al_2O_3) and in some cases carbon matrices^{78,79}, thereby forming a nanocomposite (**Figure 1.6c**). Close contact between the two components is achieved by high-energy ball milling of the metal hydride with the oxide scaffold or via nanoconfinement of the metal hydride in the nanopores of the oxide by melt infiltration. In this thesis, we will only make use of the latter approach, melt infiltration, to prepare our metal hydride/oxide nanocomposites. During the synthesis, the metal hydride and a porous metal oxide are mixed and heated to a temperature above the melting point of the metal hydride. Melt infiltration makes use of capillary forces to draw the molten metal hydride inside the pores of the metal oxide. Note that this phenomenon only occurs when the liquid easily spreads over, or 'wets', the surface of the solid, which depends on the surface energy of the solid, the surface tension of the liquid and the solid-liquid interface energy. In 1973 Liang *et al.* were the first to report on the ionic conductivity of composite solid electrolytes.⁸⁰ They showed that combining LiI with Al_2O_3 increased the ion conductivity from $10^{-7} \text{ S cm}^{-1}$ to $10^{-5} \text{ S cm}^{-1}$. Since then, this method has been applied to several different ion conductors, including AgI , LiNO_3 and, more recently, LiBH_4 and other complex metal hydrides.^{81–83}

The enhancement in ionic conductivity upon introduction of the scaffold can be attributed to several effects. A schematic representation of the effects is provided in **Figure 1.7**. Here, a short overview of the main phenomena will be discussed and for a more detailed description the reader is referred to a recent work by Zou *et al.*⁸⁴ In general,

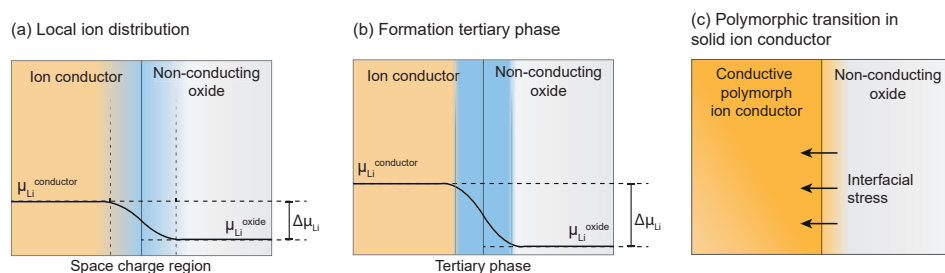


Figure 1.7 - Schematic illustration of the different interfacial interactions occurring in nanocomposite ion conductors. Fast ionic transport in composite solid electrolytes can be induced by (a) the formation of a space charge layer, (b) the formation of a tertiary phase at the conductor-insulator interface or (c) stabilization of a conductive polymorph of the ion conductor. Illustration adapted with permission from ref. [84] Copyright 2021 American Chemical Society.

the addition of dispersed oxide particles in the ion conductor introduces interfacial stress between the two components. In most cases, this interaction between the scaffold and the ion-conducting compound results in local ion redistribution, or a space-charge region, while the bulk components remain unaffected (**Figure 1.7a**). The modified defect thermodynamics close to the ion conductor-scaffold interface can be described by the space-charge model as proposed by Maier. In short, the discontinuity at the interface leads to deviations from local electroneutrality and consequently the formation of a space-charge zone where the concentration of the charge carrying defects is modified and the conductivity is influenced accordingly.^{85,86}

The space charge model is often used to explain an increase of ionic conductivity in composite solid electrolytes. However, if the local redistribution of ions is not sufficient to compensate for structural mismatches or large differences in chemical potential between the two components, chemical reactions may occur at the interface. In this case, a third compound is formed at the interface with a structure that is intrinsically different from the ion conductor and the insulating scaffold (**Figure 1.7b**). This new interphase compound is generally highly defected, and possibly more conductive compared to the starting compounds.⁸⁴ For example, LiBH_4 can become partially oxidized upon reaction with oxide surface groups, which creates Li^+ vacancies and improves ionic transport. Unfortunately, few studies have been reported on this topic, likely because the interphase compounds are difficult to characterize due to their amorphous nature and nanometric thickness.

Besides the formation of a tertiary phase at the interface between the two components, strong interfacial stresses may also lead to (polymorphic) transitions in the ion conducting host (**Figure 1.7c**).^{84,87} Some ion conductors can exist in different polymorphs with distinctly different transport properties. For these compounds, inclusion of dispersed oxides can alter the stability of the polymorphs and consequently the crystallographic structure. In this case, a conductive polymorph that is normally stable only at elevated temperatures can become stable at ambient temperature due to a depression of the polymorphic transition temperature. This phenomenon has been observed both in polymer-based nanocomposites (e.g., $\text{PEO}/\text{Al}_2\text{O}_3$ nanocomposites) and in inorganic-based nanocomposites (e.g., $\text{AgI}/\text{Ag}_3\text{BO}_3$, nanoconfined LiBH_4). Note that in the latter case a large interfacial stress is often induced by nanoconfinement of the ion conductor in the pores of a mesoporous scaffold. The phase transition temperature of the confined materials (T_m) depends on the size of the confining pore (r_{eff}) following the Gibbs-Thomson equation,

$$\Delta T = T_0 - T_m(r_{\text{eff}}) = \frac{(2T_0(\gamma_{\text{ws}} - \gamma_{\text{wl}})v_l)}{(\Delta H_m r_{\text{eff}})} \quad (1.2)$$

where T_0 is the bulk melting temperature, ΔH_m is the melting enthalpy, v_l is the molar volume of the liquid and γ_{ws} and γ_{wl} are the pore wall-solid and pore wall-liquid interface energies.⁸⁸

The interaction of the ion conductor with the insulating scaffold plays a key role in the conductivity enhancement of nanocomposite solid electrolyte, whether it is through the formation of a space-charge region or the stabilization of a conductive polymorph. This has also been observed for metal hydride nanocomposites. In the next section, this will be discussed for LiBH_4 , NaBH_4 , $\text{Li}_2\text{B}_{12}\text{H}_{12}$ and $\text{NaCB}_{11}\text{H}_{12}$.^{77,89,90}

1.4 Ionic conductivity in metal hydride-based nanocomposites

This section provides an overview of the current literature on metal hydride/oxide nanocomposite electrolytes, as well as their implementation in all-solid-state batteries.

1.4.1 Borohydride/oxide nanocomposites

In 2012, Verkuijlen and co-workers observed highly mobile Li^+ -ions upon melt infiltration of LiBH_4 in a mesoporous SiO_2 scaffold (MCM-41).⁹¹ Their static ^7Li and ^{11}B NMR measurements demonstrated that the mobility of both Li^+ and BH_4^- is strongly increased after nanoconfinement. In a subsequent study by Blanchard *et al.*, it was shown for the first time that confining LiBH_4 in the pores of ordered mesoporous silica scaffolds leads to high Li^+ conductivity of $0.1 \cdot 10^{-3} \text{ S cm}^{-1}$ at room temperature, as displayed in **Figure 1.8a**.⁸³ The Nyquist plots obtained with electrochemical impedance spectroscopy measurements at 30 °C, 50 °C and 80 °C consist of single, slightly depressed semi-circles, which suggests that the ionic conduction in the nanoconfined LiBH_4 , or $\text{LiBH}_4/\text{SiO}_2$ nanocomposite, is governed by only one diffusion process. Notably, upon nanocomposite formation the activation energy for lithium diffusion was reduced accordingly, from 0.7 eV (o- LiBH_4) to 0.43 eV. In contrast to nanostructured LiBH_4 , the conductivity of the $\text{LiBH}_4/\text{SiO}_2$ nanocomposite is very stable in time and against temperature changes. Furthermore, the authors proposed that the high ionic mobility originates from a fraction of the confined borohydride that is located close to the interface with the SiO_2 pore walls, a conductive interfacial layer of about 1.0 nm thickness (**Figure 1.8b**).⁸³ Subsequent studies confirmed that interface interactions between LiBH_4 and the mesoporous SiO_2 scaffold are essential to the conductivity in $\text{LiBH}_4/\text{SiO}_2$ nanocomposites obtained via melt infiltration.^{77,78,92,93} The thickness of the interfacial layer was 1.9 – 2.0 nm, in this case.^{77,78}

The conductivity of $\text{LiBH}_4/\text{SiO}_2$ nanocomposites obtained via ball milling has been investigated as well. Choi *et al.* prepared composites of LiBH_4 and two different types of high surface area SiO_2 (MCM-41 and fumed SiO_2) with high-energy ball milling. The ion conductivity of the composites ranged from $10^{-5} \text{ S cm}^{-1}$ (MCM-41) to $10^{-4} \text{ S cm}^{-1}$ (fumed SiO_2) at room temperature. By employing a continuum percolation model, the conductivity of the $\text{LiBH}_4/\text{SiO}_2$ interface layer was estimated to be 10^5 times higher than that of pure macrocrystalline LiBH_4 .⁹⁴ The conductive interface layer is likely the result of a reaction between the surface silanol groups and the confined LiBH_4 , as suggested by

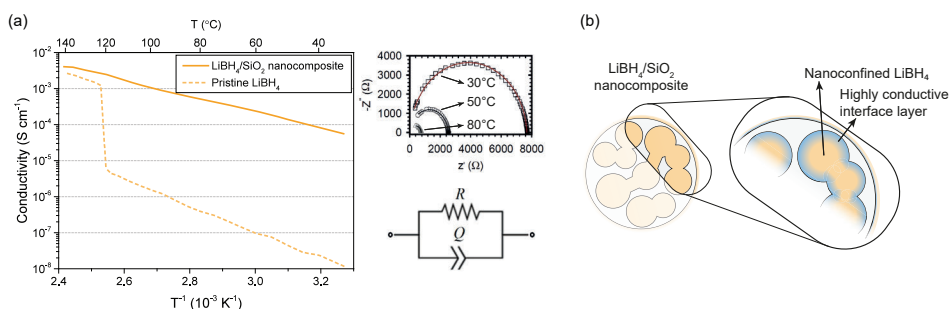


Figure 1.8 - (a) Arrhenius plot of the conductivity of pristine and nanoconfined LiBH_4 , including Nyquist plots of the $\text{LiBH}_4/\text{SiO}_2$ nanocomposite obtained at 30 °C, 50 °C and 80 °C. Data is reprinted with permission from ref. [83] Copyright 2015 Wiley. (b) Schematic visualization of the metal hydride-metal oxide interface layer.

Lefevr *et al.* for ball milled $\text{LiBH}_4/\text{SiO}_2$ aerogel.⁹⁵ Both studies highlight the importance of the interface and indicate that significant enhancement in ionic conductivity can be achieved via nanocomposite formation, both with melt infiltration and ball milling.

The Li-ion mobility in $\text{LiBH}_4/\text{oxide}$ nanocomposites can be improved by maximizing the contact area between LiBH_4 and the oxide, or by optimizing the interaction between the components, for example by changing the density or nature of the active surface groups. Since the nature and density of surface groups differs greatly between different oxide scaffolds, using a different oxide greatly affects the conductivity of LiBH_4 nanocomposite electrolytes. In fact, Choi *et al.* demonstrated that $\gamma\text{-Al}_2\text{O}_3$ is more effective in making a highly conducting interface layer in ball-milled $\text{LiBH}_4/\text{oxide}$ nanocomposites than the previously investigated SiO_2 .⁸⁹ The ionic conductivity of their $\text{LiBH}_4/\text{Al}_2\text{O}_3$ nanocomposite reached a value of $2 \cdot 10^{-4} \text{ S cm}^{-1}$, which is twice as high as that of the $\text{LiBH}_4/\text{SiO}_2$ nanocomposite.

Likewise, in a recent study by Dou *et al.* LiBH_4 nanocomposites were prepared based on layered double hydroxides (LDHs), high surface area materials with a high density of active surface hydroxyls.⁹⁶ By using LDHs as scaffold, the interface interaction with LiBH_4 was maximized, which resulted in a remarkable increase in ionic conductivity. For example, $\text{LiBH}_4/\text{MgAl-LDH}$ nanocomposites exhibited a five order of magnitude increase in room temperature conductivity, reaching $0.31 \cdot 10^{-3} \text{ S cm}^{-1}$. For both studies the enhancement in conductivity was ascribed to a higher density of surface hydroxyl groups in the scaffold compared to SiO_2 resulting in an interface layer with more B-O bonds and more mobile Li^+ ions. Note that the exact mechanism for B-O bond formation and the nature of the interface interaction is still under debate. It has been speculated that SiO-BH_3 species form upon reaction of LiBH_4 with the surface hydroxyl groups, but this was contradicted in a recent study by Lambregts *et al.* in which highly dynamic silicon-hydride-borohydride bonds have been observed.⁹⁷

The effect of the nature of the oxide scaffold on LiBH_4 nanocomposite conductivity was explored systematically.⁷⁷ In this study, $\text{LiBH}_4/\text{oxide}$ nanocomposites were prepared through ball milling with various nanosized oxides, including SiO_2 , $\gamma\text{-Al}_2\text{O}_3$, CaO , MgO and ZrO_2 . In all cases, 25 v/v% of oxide was present in the nanocomposites. The ionic conductivity of the nanocomposites was enhanced for all oxides (**Figure 1.9a**). Preparation with ZrO_2 and MgO resulted in the most conductive nanocomposite electrolytes, with conductivities of 0.26 and $0.18 \cdot 10^{-3} \text{ S cm}^{-1}$ at 40 °C, respectively. These values are more than four orders of magnitude higher than that of macrocrystalline LiBH_4 , and also clearly higher than those observed for the SiO_2 - and Al_2O_3 -based nanocomposites prepared in the same manner. The activation energies for ionic transport also depend on the oxide that is used. The lowest activation energies, 0.44 and 0.46 eV, were observed for ZrO_2 and MgO -containing nanocomposites, while the nanocomposites based on SiO_2 and Al_2O_3 show activation energies of 0.52 and 0.55 eV.

Based on their results the authors deduced a set of design rules to optimize the influence of the oxide on the overall conductivity.⁷⁷ This study demonstrates that nanocomposite formation is an effective strategy to improve LiBH_4 conductivity, especially by choosing the optimal oxide scaffold and optimizing overall composition. Additional studies are required to determine which scaffold property, e.g., surface chemistry, acidity,

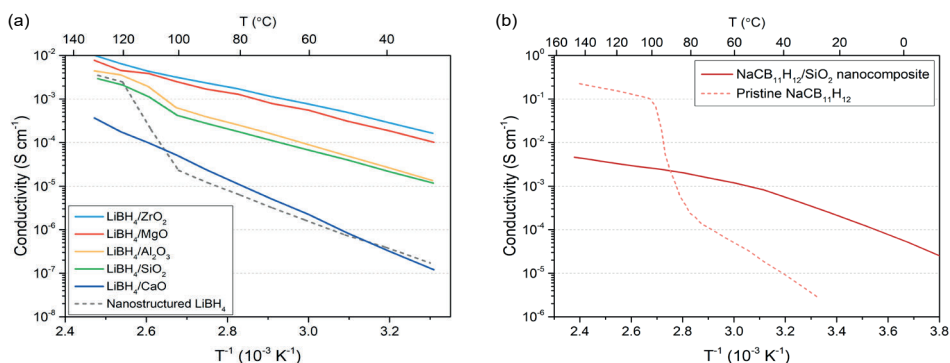


Figure 1.9 - (a) Li-ion conductivity of ball milled mixtures of LiBH₄ with 25 v/v% of different oxides. Data is adapted with permission from ref. [77] Copyright 2020 American Chemical Society. (b) Na-ion conductivity of pristine NaCB₁₁H₁₂ and NaCB₁₁H₁₂ nanoconfined in a SiO₂ scaffold. Data is adapted with permission from ref. [99] Copyright 2021 American Chemical Society.

or physical structure (morphology, particle size and porosity), is most important to the formation of a conductive interface. It is also important to note that only non-reducible scaffolds can be used in metal hydride-based nanocomposites, as the formation of oxygen vacancies in reducible oxides, such as TiO₂, due to reactions with the highly reducing hydrides can induce electrical conductivity.⁷⁷

While several studies have shown the benefits of nanocomposite formation on the ionic conductivity of LiBH₄, studies on other metal hydride ion conductors, such as alanates and amines, are scarce. It has only recently been demonstrated that nanocomposite formation can also be applied to tune the properties of sodium-based metal hydrides, though for these compounds the strategy seems less effective.³⁷ In fact, upon melt infiltration of NaBH₄ in mesoporous SiO₂ (MCM-41) a limited improvement in ionic conductivity of just one order of magnitude is observed. The small enhancement in conductivity is attributed to the formation of Na₂B₁₂H₁₂ in the pores of the scaffold upon nanoconfinement. Moreover, both IR and NMR analysis demonstrate the formation of B-O bonds, similar to LiBH₄/Al₂O₃.⁸⁹ This indicates that like interface engineered LiBH₄ an interface layer is formed at the metal hydride-metal oxide interface, though it is not highly conductive in the case of NaBH₄/SiO₂.³⁷ Therefore, nanoconfined NaBH₄ might benefit greatly from the application of other scaffolds that could introduce stronger interface interactions. Indeed, by using MgAl-layered double hydroxides (LDHs) for NaBH₄-based nanocomposites, Dou *et al.* were able to achieve a conductivity increase of three orders of magnitude.⁹⁶ The hydroxyl rich surface of the LDHs enhances the interface interaction between NaBH₄ and the scaffold, thereby promoting Na⁺ ion diffusion.

1.4.2 Closo-borate- and closo-carborate/oxide nanocomposites

Metal hydride compounds based on *closo*-borate and *closo*-carborate anions, e.g., B₁₂H₁₂²⁻, were introduced in section 1.3.2. Similar to borohydrides, nanocomposite formation might be used to enhance their room temperature conductivity. Recently, Yan *et al.* prepared nanocomposites with Li₂B₁₂H₁₂ using mesoporous SiO₂ as scaffold.⁹⁸ Since Li₂B₁₂H₁₂ has a high melting point (T_m > 500 °C), the nanocomposite cannot be formed via melt infiltration. Hence, a two-step synthesis method was applied in which first nanoconfined LiBH₄ was prepared, after which the nanoconfined LiBH₄ was treated with a H₂/B₂H₆ atmosphere at

150 °C to form nanoconfined $\text{Li}_2\text{B}_{12}\text{H}_{12}$. It was confirmed with ^{11}B MAS NMR that all LiBH_4 is successfully converted to 94 mol% $\text{Li}_2\text{B}_{12}\text{H}_{12}$ and 6 mol% $\text{Li}_2\text{B}_{10}\text{H}_{10}$.

Unfortunately, the as-synthesized nanocomposite exhibited a low ionic conductivity of $1.0 \cdot 10^{-7} \text{ S cm}^{-1}$ at 25 °C, similar to the value obtained for bulk $\text{Li}_2\text{B}_{12}\text{H}_{12}$.⁹⁸ It should be considered that the preparation method can influence the formation of a conductive interface layer between the metal hydride and the oxide. As a result, the $\text{Li}_2\text{B}_{12}\text{H}_{12}$ /oxide nanocomposite might display a limited Li-ion mobility, in contrast to interface engineered LiBH_4 . This study does not firmly resolve whether nanocomposite formation can help stabilize the high-temperature superionic polymorph of (car)borate metal hydrides or improve their room temperature conductivity. Therefore, it would be interesting to compare the conductivities of $\text{Li}_2\text{B}_{12}\text{H}_{12}$ nanocomposites prepared via this method, to a $\text{Li}_2\text{B}_{12}\text{H}_{12}/\text{SiO}_2$ nanocomposite synthesized through other methods, such as high-energy ball milling.

In a recent study by Andersson *et al.* a novel approach was proposed to prepare *closo*-carborate nanocomposites.⁹⁹ In their work, nanodispersion of $\text{NaCB}_{11}\text{H}_{12}$ in porous SiO_2 was achieved via salt-solution infiltration followed by vacuum desolvation, an approach similar to melt infiltration. Structural characterization with DSC and XRD indicated that the metal hydride was confined in the scaffold pores. This nanoconfined $\text{NaCB}_{11}\text{H}_{12}$ phase resembled the high-temperature superionic polymorph of bulk $\text{NaCB}_{11}\text{H}_{12}$, with dynamically disordered $\text{CB}_{11}\text{H}_{12}^-$ anions exhibiting fast re-orientational mobility. The high anion mobilities promote fast cation diffusion, which yields Na-ion conductivities of $0.3 \cdot 10^{-3} \text{ S cm}^{-1}$ at room temperature (**Figure 1.9b**). Notably, it is expected that the conductivity of the $\text{NaCB}_{11}\text{H}_{12}/\text{SiO}_2$ nanocomposite can be further improved by optimization of the preparation method, for example by applying ball milling or improving the solution impregnation method, as well as tuning of the nanocomposite composition, e.g., by scaffold chemistry and volume fraction. Nevertheless, this work demonstrates that the formation of a nanocomposite is a viable strategy to stabilize highly conductive phases not only in borohydride-based compounds, but also in *closo*-(car)borate-based solid electrolytes.

From the works described in previous sections, it is clear that the conductivity of complex metal hydrides can be greatly enhanced via nanocomposite formation. The conductivity of the nanocomposite ion conductors is closely linked to the properties of the scaffold materials. Both the chemical nature and the physical properties (e.g., morphology or porosity) of the non-conducting oxide can influence the overall conductivity and activation energy of ion hopping, though the exact extent depends on the metal hydride.

1.4.3 All-solid-state batteries based on metal hydride/oxide nanocomposites

So far, we focused on the ionic conductivity of the nanocomposite electrolytes. In this section, the incorporation of metal hydride/oxide nanocomposite electrolytes in all-solid-state batteries will be discussed. For a complete overview of all investigated metal hydride-based all-solid-state batteries, the reader is referred to two excellent reviews on this topic by Latroche *et al.* and Duchêne *et al.*^{56,100}

Pristine LiBH_4 has been used as a solid electrolyte in several batteries, typically using TiS_2 or sulfur as cathode materials.¹⁰⁰ Due to the necessity of a sufficiently high Li-

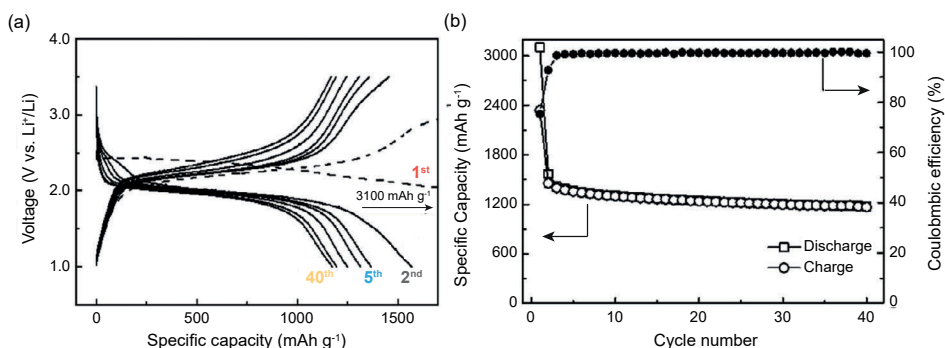


Figure 1.10 - (a) Discharge-charge profiles of a Li|LiBH₄/SiO₂|S-C cell operating at 55 °C with a C-rate of C/30. (b) Specific capacity and Coulombic efficiency as a function of cycle number for the same cell.¹⁰²

ion conductivity, these batteries operate at a temperature of about 120 °C to ensure the electrolyte remains in the conductive hexagonal polymorph.¹⁰¹ In 2016, Das *et al.* were the first to implement nanoconfined LiBH₄ in an all-solid-state lithium-sulfur battery that could operate at moderate temperature, i.e. 55 °C.¹⁰² The battery was based on LiBH₄ confined in mesoporous silica (MCM-41) as electrolyte. The electrolyte demonstrated promising properties for battery operation, including a room temperature conductivity of $0.1 \cdot 10^{-3}$ S cm⁻¹, a cationic transport number of 0.96, excellent stability against metallic lithium and good interfacial contact with the electrodes.

The studied Li|LiBH₄/SiO₂|S-C battery was cycled for 40 cycles, at 0.03 C-rate and a working upper and lower cut-off voltage of 3.5 and 1.0 V versus Li⁺/Li, respectively (**Figure 1.10a**). Though a cell voltage of 2.5 V is not ideal for most applications, this work shows that the cell exhibits a Coulombic efficiency around 99.6% after the third cycle (**Figure 1.10b**), demonstrating the good cycling stability of the battery. After 40 cycles, the battery delivered a high capacity versus sulfur mass of typically 1220 mAh g⁻¹, 73% of the theoretical sulfur capacity (1675 mAh g⁻¹). During the first discharge, the cell exhibits a much larger capacity than the theoretical capacity expected from the amount of sulfur in the cathode. This is most likely related to electrochemical reaction of LiBH₄ with the sulfur-based cathode materials, forming a solid electrolyte interphase (SEI) layer.

Similar battery performance was reported by Lefevr *et al.*, who successfully applied ball milled LiBH₄/SiO₂ composite electrolytes in Li-S batteries.¹⁰³ After 10 discharge-charge cycles at 55 °C with a 0.03 C-rate, the batteries showed a reasonable capacity retention of 794 mAh g⁻¹ sulfur with a Coulombic efficiency of 89% and an average capacity loss of 7.2% during the first 10 cycles. In accordance with the results of Das *et al.*, the initial discharge capacity was more than double the theoretical capacity indicating the formation of an SEI layer. While it seems that the formed SEI layer does not limit the following charge-discharge cycles, more work is needed to determine the exact origin of high initial discharge capacity as well as the capacity fading during cycling.

Recently, an all-solid-state battery using a LiBH₄-based electrolyte that could be operated at room temperature was demonstrated for the first time by Gulino *et al.*¹⁰⁴ In this work, a nanocomposite electrolyte was prepared by ball milling LiBH₄ with MgO nanoparticles, and subsequently incorporated in a Li-TiS₂ battery. Initial cycling of

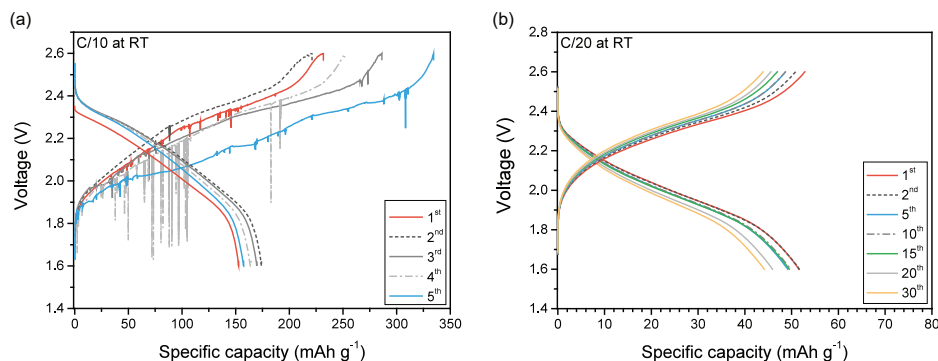


Figure 1.11 - Discharge-charge profiles of Li|LiBH₄/MgO|TiS₂ cells, (a) operating at room temperature with a C-rate of C/10 without any prior heat treatment or cycling experiments and (b) operating at room temperature with a C-rate of C/20 after charging and discharging for 65 cycles at 60 °C with a rate of C/20. Data has been adapted with permission from ref. [104] Copyright 2020 American Chemical Society.

a Li|LiBH₄/MgO|TiS₂ battery at room temperature resulted in cell failure after only five cycles (**Figure 1.11a**). In the charge profiles spikes can be observed, that are attributed to inhomogenous Li plating which is likely caused by a current density that exceeds the so-called critical current density. Additionally, the authors speculated that in this case only a small SEI layer is formed due to slow kinetics at room temperature.

By conditioning the battery at 60 °C prior to operation, it was possible to charge and discharge the battery in a stable manner for 30 cycles at room temperature. During the application of several charge/discharge cycles at 60 °C, a stable SEI layer forms. While the SEI formation caused an initial increase in contact resistance, it also limited further decomposition of the composite electrolyte. Surprisingly, thereafter it was possible to cycle the battery at room temperature for up to 30 cycles with a specific capacity of about 50 mAh g⁻¹ and a capacity retention of about 80% after the 30 cycles (**Figure 1.11b**). Note that the cycling profile is different and specific capacity is lower compared to the cell that was operated without prior conditioning, because this cell was already charged and discharged for 65 cycles at 60 °C, during which the capacity faded. This study emphasizes the importance of the electrode-electrolyte interface, as it often determines the life time of an all-solid-state battery. It will be interesting to study whether this remarkable strategy is also applicable to other batteries based on metal hydride electrolytes, thereby facilitate room temperature operation for other systems as well. In addition, the effect of stack pressure on the cycle life of these type of batteries should be investigated, because the application of pressure could further improve the mechanical (and thereby electrical) contact at the electrode-electrolyte interfaces.

Besides LiBH₄-based batteries, several reports on the implementation of lithium- and sodium *closo*-(car)borate electrolytes in all-solid-state batteries have been published in the past few years. Most of these batteries are based on partially ion-substituted *closo*-borate compounds, such as Na₂(B₁₂H₁₂)_{0.5}(B₁₀H₁₀)_{0.5}¹⁰⁵, and Li₂(CB₉H₁₀)(CB₁₁H₁₂)⁶⁴, while only few report on the implementation of nanostructured *closo*-borates. So far, no studies have been published on the application of *closo*-borate nanocomposites in all-solid-state batteries.

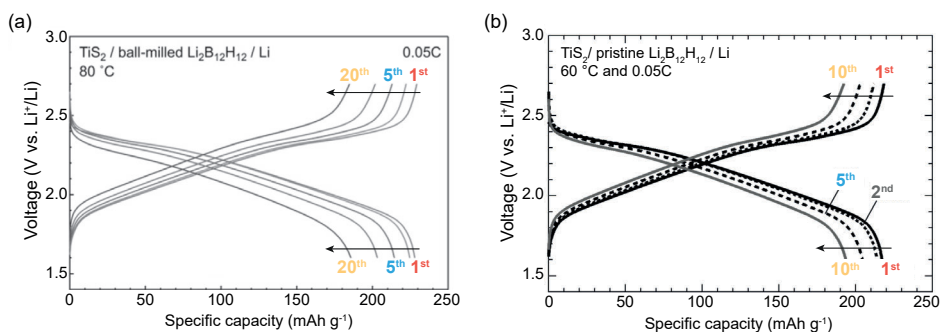


Figure 1.12 - Discharge-charge profiles of all-solid-state $\text{Li}|\text{Li}_2\text{B}_{12}\text{H}_{12}|\text{TiS}_2$ battery cells cycled with a C-rate of C/20, based on (a) ball milled $\text{Li}_2\text{B}_{12}\text{H}_{12}$ ⁷⁶ and (b) pristine $\text{Li}_2\text{B}_{12}\text{H}_{12}$.⁴⁷

Both Kim *et al.* and Teprovich *et al.* show that nanostructured $\text{Li}_2\text{B}_{12}\text{H}_{12}$ outperforms macrocrystalline $\text{Li}_2\text{B}_{12}\text{H}_{12}$ as solid electrolyte in an all-solid-state battery.^{76,106} In **Figure 1.12**, the discharge-charge curves of an all-solid-state $\text{Li}-\text{TiS}_2$ battery based on ball-milled $\text{Li}_2\text{B}_{12}\text{H}_{12}$ are depicted, during cycling in the voltage range of 1.6 – 2.7 V vs Li^+/Li at 80°C and 0.05 C. The battery exhibits an initial discharge capacity of 228 mAh g^{-1} and a good capacity retention over 20 cycles.⁷⁶ The battery performs better than a similar cell prepared with pristine $\text{Li}_2\text{B}_{12}\text{H}_{12}$ as the solid electrolyte, which delivered a smaller capacity that faded more rapidly during cycling.⁴⁷ In addition, the performance of nanostructured $\text{Li}_2\text{B}_{12}\text{H}_{12}$ in a $\text{Li}-\text{LiCoO}_2$ battery was examined.¹⁰⁶ Cycling of the $\text{Li}-\text{LiCoO}_2$ cell was performed at moderate temperature (50°C) between 3.0 V and 4.2 V at a rate of 0.2 C. The battery exhibited an initial discharge capacity of 63 mAh g^{-1} , which dropped to 37 mAh g^{-1} over 20 charge-discharge cycles (59% capacity retention). Although the capacity for this battery is far below the theoretical capacity (274 mAh g^{-1}), it does demonstrate that nanostructured $\text{Li}_2\text{B}_{12}\text{H}_{12}$ can be incorporated into full battery cells utilizing both sulfur and oxide-based cathode materials.

To the best of our knowledge no other studies on the implementation of nanostructured *closo*-(car)borates and *closo*-(car)borate/oxide nanocomposites in all-solid-state batteries have been published. On the other hand, work on pristine *closo*-(car)borates, including $\text{LiCB}_{11}\text{H}_{12}$ and $\text{NaCB}_{11}\text{H}_{12}$ ⁴⁸, does reveal that these materials can be cycled in batteries working at moderate temperatures even without modifications. Since their room temperature conductivities can be improved substantially upon nanocomposite formation (section 1.4.2), *closo*-(car)borate nanocomposites remain very promising candidates for metal hydride-based batteries operating at ambient temperature.

1.5 Scope of this thesis

The goal of the work described in this thesis was to study the effect of nanocomposite formation on the ionic conductivity of complex metal hydrides. The main research question we tried to answer was how and why the physical and chemical properties of the metal oxide scaffold affect the overall ion mobility in different complex metal hydrides. In other words, how do a metal hydride and a metal oxide form a dynamic duo. To this end, electrochemical impedance spectroscopy, differential scanning calorimetry, X-ray Raman scattering, and several other characterization techniques were employed to obtain in-depth understanding of the conductivity enhancement observed in the nanocomposites.

First of all, in **Chapter 2** the effect of nanocomposite formation on the Na-ion conductivity is discussed for NaBH_4 - and NaNH_2 /oxide nanocomposites. The observed conductivity enhancement originates from the formation of a conductive interface layer between the metal hydride and the metal oxide. This study demonstrates that the reactivity of the metal hydride, and correspondingly its interaction strength with the oxide scaffold, play a key role.

In **Chapter 3**, we report on the synthesis of LiI- and LiNH_2 -substituted LiBH_4 /oxide nanocomposites. This chapter shows that the combination of both partial ionic substitution and nanocomposite formation further improves the ionic conductivity of the solid electrolytes via the formation of interconnected Li^+ diffusion pathways. The conductivity depends on the properties of the mesoporous oxide, but the exact role could not be resolved. Therefore, the investigation of LiNH_2 -substituted LiBH_4 /oxide nanocomposites is continued in **Chapter 4**, to determine how the chemical and physical properties of the metal oxide influence the overall conductivity. By systematically tuning the scaffold properties we established structure-performance relationships and determined the origin of the conductivity enhancement.

For the metal hydride/oxide nanocomposites discussed in the first chapters, it is clear that the interaction between the metal hydride and the metal oxide plays an important role. However, due to the nanocrystalline nature and the light elements present in the nanocomposites, it is difficult to determine the composition and structure of the interface. To this end, X-ray Raman scattering was used to study the chemical and structural transformations that occur at the metal hydride-metal oxide interface of LiBH_4 - and NaBH_4 /oxide nanocomposites in **Chapter 5**. In this synchrotron-based technique, hard X-rays could be employed to obtain chemical information on light elements, like Li, Na and B, with bulk sensitivity.

To demonstrate that nanocomposite formation is widely applicable to various solid ion conductors, the effect of nanocomposite formation on LiNO_3 , NaNO_2 and NaNO_3 is explored in **Chapter 6**. The ionic conductivity was improved up to three orders of magnitude, though the exact enhancement depends on both the solid ion conductor and the mesoporous oxide. For the LiNO_3 /oxide nanocomposites, a correlation between their conductivity and the acidity of the oxide was found. Finally, a summary and future perspectives as well as a Dutch summary are provided in **Chapter 7** and **Chapter 8**, respectively.

1.6 References

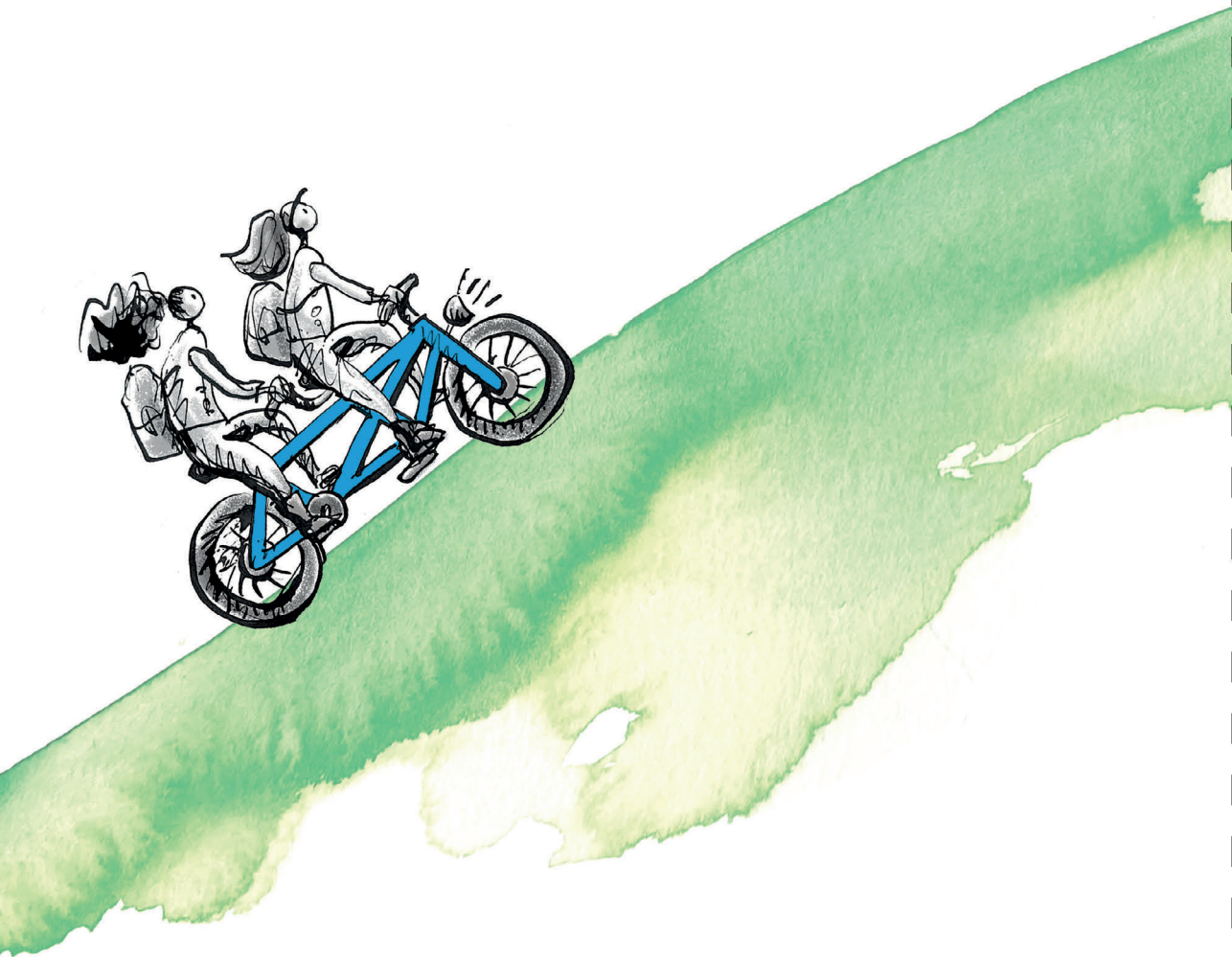
1. Davies, D. M. *et al.* Combined economic and technological evaluation of battery energy storage for grid applications. *Nat. Energy* **4**, 42–50 (2019).
2. Balali, M. H., Nouri, N., Omrani, E., Nasiri, A. & Otieno, W. An overview of the environmental, economic, and material developments of the solar and wind sources coupled with the energy storage systems. *Int. J. Energy Res.* **41**, 1948–1962 (2017).
3. Kittner, N., Lill, F. & Kammen, D. M. Energy storage deployment and innovation for the clean energy transition. *Nat. Energy* **2**, 1–6 (2017).
4. Armand, M. & Tarascon, J. M. Building better batteries. *Nature* **451**, 652–657 (2008).
5. Goodenough, J. B. & Park, K. S. The Li-ion rechargeable battery: A perspective. *J. Am. Chem. Soc.* **135**, 1167–1176 (2013).
6. Dunn, B., Kamath, H. & Tarascon, J. M. Electrical energy storage for the grid: A battery of choices. *Science* (80-.). **334**, 928–935 (2011).
7. Liu, K., Liu, Y., Lin, D., Pei, A. & Cui, Y. Materials for lithium-ion battery safety. *Sci. Adv.* **4**, (2018).
8. Mauger, A. & Julien, C. M. Critical review on lithium-ion batteries: are they safe? Sustainable? *Ionics (Kiel)*. **23**, 1933–1947 (2017).
9. Vaalma, C., Buchholz, D., Weil, M. & Passerini, S. A cost and resource analysis of sodium-ion batteries. *Nat. Rev. Mater.* **3**, (2018).
10. Janek, J. & Zeier, W. G. A solid future for battery development. *Nat. Energy* **1**, 1–4 (2016).
11. Manthiram, A., Yu, X. & Wang, S. Lithium battery chemistries enabled by solid-state electrolytes. *Nat. Rev. Mater.* **2**, 1–16 (2017).
12. Li, J., Ma, C., Chi, M., Liang, C. & Dudney, N. J. Solid electrolyte: The key for high-voltage lithium batteries. *Adv. Energy Mater.* **5**, 1–6 (2015).
13. Luntz, A. Beyond Lithium Ion Batteries. *J. Phys. Chem. Lett.* **6**, 300–301 (2015).
14. Padma Kumar, P. & Yashonath, S. Ionic Conduction in the Solid State. *ChemInform* **37**, 135–154 (2006).
15. Mehrer, H. Fast Ion Conductors. in *Diffusion in Solids* 475–490 (Springer Berlin Heidelberg, 2007). doi:10.1007/978-3-540-71488-0_27.
16. Mehrer, H. Diffusion Mechanisms. in 95–104 (Springer Berlin Heidelberg, 2007). doi:10.1007/978-3-540-71488-0_6.
17. Orazem, M. E. & Tribollet, B. *Electrochemical impedance spectroscopy*. vol. 1 (John Wiley & Sons, Inc., 2017).
18. Pyun, S.-I., Shin, H.-C., Lee, J.-W. & Go, J.-Y. Electrochemical Methods. in *Electrochemistry of Insertion Materials for Hydrogen and Lithium* 11–32 (Springer Berlin Heidelberg, 2012). doi:10.1007/978-3-642-29464-8_2.
19. Seino, Y., Ota, T., Takada, K., Hayashi, A. & Tatsumisago, M. A sulphide lithium super ion conductor is superior to liquid ion conductors for use in rechargeable batteries. *Energy Environ. Sci.* **7**, 627–631 (2014).
20. Rangasamy, E. *et al.* An iodide-based $\text{Li}_7\text{P}_2\text{S}_8\text{I}$ superionic conductor. *J. Am. Chem. Soc.* **137**, 1384–1387 (2015).
21. Thangadurai, V., Narayanan, S. & Pinzaru, D. Garnet-type solid-state fast Li ion conductors for Li batteries: Critical review. *Chem. Soc. Rev.* **43**, 4714–4727 (2014).
22. Lu, Z. & Ciucci, F. Metal Borohydrides as Electrolytes for Solid-State Li, Na, Mg, and Ca Batteries: A First-Principles Study. *Chem. Mater.* **29**, 9308–9319 (2017).
23. Asakura, R. *et al.* Electrochemical Oxidative Stability of Hydroborate-Based Solid-State Electrolytes. *ACS Appl. Energy Mater.* **2**, 6924–6930 (2019).
24. Matsuo, M., Nakamori, Y., Orimo, S. I., Maekawa, H. & Takamura, H. Lithium superionic

- conduction in lithium borohydride accompanied by structural transition. *Appl. Phys. Lett.* **91**, 2–5 (2007).
25. Verdal, N. *et al.* Anion reorientations in the superionic conducting phase of $\text{Na}_2\text{B}_{12}\text{H}_{12}$. *J. Phys. Chem. C* **118**, 17483–17489 (2014).
 26. Tang, W. S. *et al.* Liquid-Like Ionic Conduction in Solid Lithium and Sodium Monocarbido-closo-Decaborates Near or at Room Temperature. *Adv. Energy Mater.* **6**, 1–6 (2016).
 27. Gulino, V. *et al.* Combined DFT and geometrical-topological analysis of Li-ion conductivity in complex hydrides. *Inorg. Chem. Front.* **7**, 3115–3125 (2020).
 28. Matsuo, M. & Orimo, S. I. Lithium fast-ionic conduction in complex hydrides: Review and prospects. *Adv. Energy Mater.* **1**, 161–172 (2011).
 29. Ikeshoji, T. *et al.* Fast-ionic conductivity of Li^+ in LiBH_4 . *Phys. Rev. B - Condens. Matter Mater. Phys.* **83**, 1–5 (2011).
 30. Myrdal, J. S. G., Blanchard, D., Sveinbjörnsson, D. & Vegge, T. Li-ion conduction in the $\text{LiBH}_4\text{:LiI}$ system from density functional theory calculations and quasi-elastic neutron scattering. *J. Phys. Chem. C* **117**, 9084–9091 (2013).
 31. Verdal, N., Udovic, T. J. & Rush, J. J. The nature of BH_4^- reorientations in hexagonal LiBH_4 . *J. Phys. Chem. C* **116**, 1614–1618 (2012).
 32. Lee, Y. S. & Cho, Y. W. Fast Lithium Ion Migration in Room Temperature LiBH_4 . *J. Phys. Chem. C* **121**, 17773–17779 (2017).
 33. Oguchi, H. *et al.* Lithium-ion conduction in complex hydrides LiAlH_4 and Li_3AlH_6 . *J. Appl. Phys.* **107**, 105–108 (2010).
 34. Oguchi, H., Matsuo, M., Kuromoto, S., Kuwano, H. & Orimo, S. Sodium-ion conduction in complex hydrides NaAlH_4 and Na_3AlH_6 . *J. Appl. Phys.* **111**, 4–7 (2012).
 35. Matsuo, M. *et al.* Sodium and magnesium ionic conduction in complex hydrides. *J. Alloys Compd.* **580**, S98–S101 (2013).
 36. Boukamp, B. A. & Huggins, R. A. Ionic conductivity in lithium imide. *Phys. Lett. A* **72**, 464–466 (1979).
 37. Luo, X., Rawal, A. & Aguey-Zinsou, K. F. Investigating the factors affecting the ionic conduction in nanoconfined NaBH_4 . *Inorganics* **9**, 1–10 (2021).
 38. Paik, B. & Wolczyk, A. Lithium Imide (Li_2NH) as a Solid-State Electrolyte for Electrochemical Energy Storage Applications. *J. Phys. Chem. C* **123**, 1619–1625 (2019).
 39. Paik, B. *et al.* Effect of the structural evolution on the ionic conductivity of Li-N-H system during the dehydrogenation. *Appl. Phys. Lett.* **108**, 213903 (2016).
 40. Li, W., Wu, G., Xiong, Z., Feng, Y. P. & Chen, P. Li^+ ionic conductivities and diffusion mechanisms in Li-based imides and lithium amide. *Phys. Chem. Chem. Phys.* **14**, 1596–1606 (2012).
 41. Yan, Y. *et al.* Ammine Magnesium Borohydride Nanocomposites for All-Solid-State Magnesium Batteries. *ACS Appl. Energy Mater.* **3**, 9264–9270 (2020).
 42. Verdal, N. *et al.* Complex high-temperature phase transitions in $\text{Li}_2\text{B}_{12}\text{H}_{12}$ and $\text{Na}_2\text{B}_{12}\text{H}_{12}$. *J. Solid State Chem.* **212**, 81–91 (2014).
 43. Udovic, T. J. *et al.* Sodium superionic conduction in $\text{Na}_2\text{B}_{12}\text{H}_{12}$. *Chem. Commun.* **50**, 3750–3752 (2014).
 44. Skripov, A. V. *et al.* Nuclear magnetic resonance study of atomic motion in $\text{A}_2\text{B}_{12}\text{H}_{12}$ ($\text{A} = \text{Na}, \text{K}, \text{Rb}, \text{Cs}$): Anion reorientations and Na^+ mobility. *J. Phys. Chem. C* **117**, 25961–25968 (2013).
 45. Skripov, A. V., Solonin, A. V., Babanova, O. A. & Skoryunov, R. V. Nuclear magnetic resonance studies of atomic motion in borohydride-based materials: Fast anion reorientations and cation diffusion. *J. Alloys Compd.* **645**, S428–S433 (2015).
 46. He, L. *et al.* Synthesis of a Bimetallic Dodecaborate $\text{LiNaB}_{12}\text{H}_{12}$ with Outstanding Superionic Conductivity. *Chem. Mater.* **27**, 5483–5486 (2015).

47. Unemoto, A., Yoshida, K., Ikeshoji, T. & Orimo, S. I. Bulk-type all-solid-state lithium batteries using complex hydrides containing cluster-anions. *Mater. Trans.* **57**, 1639–1644 (2016).
48. Tang, W. S. *et al.* Unparalleled lithium and sodium superionic conduction in solid electrolytes with large monovalent cage-like anions. *Energy Environ. Sci.* **8**, 3637–3645 (2015).
49. Lu, Z. & Ciucci, F. Structural origin of the superionic Na conduction in $\text{Na}_2\text{B}_{10}\text{H}_{10}$ closo-borates and enhanced conductivity by Na deficiency for high performance solid electrolytes. *J. Mater. Chem. A* **4**, 17740–17748 (2016).
50. Kweon, K. E. *et al.* Structural, Chemical, and Dynamical Frustration: Origins of Superionic Conductivity in closo-Borate Solid Electrolytes. *Chem. Mater.* **29**, 9142–9153 (2017).
51. Varley, J. B. *et al.* Understanding Ionic Conductivity Trends in Polyborane Solid Electrolytes from Ab Initio Molecular Dynamics. *ACS Energy Lett.* **2**, 250–255 (2017).
52. Udovic, T. J. *et al.* Exceptional superionic conductivity in disordered sodium decahydro-closo-decaborate. *Adv. Mater.* **26**, 7622–7626 (2014).
53. Boaretto, N. *et al.* Lithium solid-state batteries: State-of-the-art and challenges for materials, interfaces and processing. *J. Power Sources* **502**, 229919 (2021).
54. Stramare, S., Thangadurai, V. & Weppner, W. Lithium Lanthanum Titanates: A Review. *Chem. Mater.* **15**, 3974–3990 (2003).
55. de Kort, L. M., Gulino, V., de Jongh, P. E. & Ngene, P. Ionic conductivity in complex metal hydride-based nanocomposite materials: The impact of nanostructuring and nanocomposite formation. *J. Alloys Compd.* **901**, 163474 (2021).
56. Duchêne, L., Remhof, A., Hagemann, H. & Battaglia, C. Status and prospects of hydroborate electrolytes for all-solid-state batteries. *Energy Storage Mater.* **25**, 782–794 (2020).
57. Paskevicius, M. *et al.* Metal borohydrides and derivatives-synthesis, structure and properties. *Chem. Soc. Rev.* **46**, 1565–1634 (2017).
58. Maekawa, H., Matsuo, M., Takamura, H., Ando, M. & Noda, Y. Halide-Stabilized LiBH_4 , a Room-Temperature Lithium Fast-Ion Conductor. *J. Am. Chem. Soc.* **131**, 894–895 (2009).
59. Yan, Y. *et al.* A Lithium Amide-Borohydride Solid-State Electrolyte with Lithium-Ion Conductivities Comparable to Liquid Electrolytes. *Adv. Energy Mater.* **7**, 1–7 (2017).
60. Miyazaki, R. *et al.* Room temperature lithium fast-ion conduction and phase relationship of LiI stabilized LiBH_4 . *Solid State Ionics* **192**, 143–147 (2011).
61. Matsuo, M., Takamura, H., Maekawa, H., Li, H. W. & Orimo, S. I. Stabilization of lithium superionic conduction phase and enhancement of conductivity of LiBH_4 by LiCl addition. *Appl. Phys. Lett.* **94**, 2–5 (2009).
62. Gulino, V., Dematteis, E. M., Corno, M., Palumbo, M. & Baricco, M. Theoretical and Experimental Studies of LiBH_4 -LiBr Phase Diagram. *ACS Appl. Energy Mater.* **4**, 7327–7337 (2021).
63. Gulino, V. *et al.* Phase Stability and Fast Ion Conductivity in the Hexagonal LiBH_4 -LiBr-LiCl Solid Solution. *Chem. Mater.* **31**, 5133–5144 (2019).
64. Kim, S., Kisu, K., Takagi, S., Oguchi, H. & Orimo, S. I. Complex Hydride Solid Electrolytes of the $\text{Li}(\text{CB}_9\text{H}_{10})$ - $\text{Li}(\text{CB}_{11}\text{H}_{12})$ Quasi-Binary System: Relationship between the Solid Solution and Phase Transition, and the Electrochemical Properties. *ACS Appl. Energy Mater.* **3**, 4831–4839 (2020).
65. Brighi, M. *et al.* A mixed anion hydroborate/carba-hydroborate as a room temperature Na-ion solid electrolyte. *J. Power Sources* **404**, 7–12 (2018).
66. Duchêne, L. *et al.* A highly stable sodium solid-state electrolyte based on a dodeca/deca-borate equimolar mixture. *Chem. Commun.* **53**, 4195–4198 (2017).
67. Bork, D. & Heitjans, P. NMR relaxation study of ion dynamics in nanocrystalline and polycrystalline LiNbO_3 . *J. Phys. Chem. B* **102**, 7303–7306 (1998).
68. Gleiter, H. Nanostructured materials: basic concepts and microstructure. *Acta Mater.* **48**, 1–29 (2000).
69. Heitjans, P., Masoud, M., Feldhoff, A. & Wilkening, M. NMR and impedance studies of

- nanocrystalline and amorphous ion conductors: Lithium niobate as a model system. *Faraday Discuss.* **134**, 67–82 (2007).
70. Heitjans, P., Tobschall, E. & Wilkening, M. Ion transport and diffusion in nanocrystalline and glassy ceramics. *Eur. Phys. J. Spec. Top.* **161**, 97–108 (2008).
 71. Wilkening, M., Epp, V., Feldhoff, A. & Heitjans, P. Tuning the Li diffusivity of poor ionic conductors by mechanical treatment: High Li conductivity of strongly defective LiTaO₃ nanoparticles. *J. Phys. Chem. C* **112**, 9291–9300 (2008).
 72. Epp, V. & Wilkening, M. Motion of Li⁺ in nanoengineered LiBH₄ and LiBH₄:Al₂O₃ comparison with the microcrystalline form. *ChemPhysChem* **14**, 3706–3713 (2013).
 73. Sveinbjörnsson, D. *et al.* Effect of heat treatment on the lithium ion conduction of the LiBH₄-LiI solid solution. *J. Phys. Chem. C* **117**, 3249–3257 (2013).
 74. Nakagawa, Y., Kimura, T., Ohki, T., Isobe, S. & Shibayama, T. Effect of mechanical milling on lithium-ion conductivity of LiAlH₄. *Solid State Ionics* **365**, 115656 (2021).
 75. Tang, W. S. *et al.* Stabilizing lithium and sodium fast-ion conduction in solid polyhedral-borate salts at device-relevant temperatures. *Energy Storage Mater.* **4**, 79–83 (2016).
 76. Kim, S. *et al.* Fast Lithium-Ion Conduction in Atom-Deficient closo-Type Complex Hydride Solid Electrolytes. *Chem. Mater.* **30**, 386–391 (2018).
 77. Gulino, V., Barberis, L., Ngene, P., Baricco, M. & De Jongh, P. E. Enhancing Li-Ion Conductivity in LiBH₄-Based Solid Electrolytes by Adding Various Nanosized Oxides. *ACS Appl. Energy Mater.* **3**, 4941–4948 (2020).
 78. Suwarno *et al.* Confinement Effects for Lithium Borohydride: Comparing Silica and Carbon Scaffolds. *J. Phys. Chem. C* **121**, 4197–4205 (2017).
 79. Liu, X. *et al.* Probing the unusual anion mobility of LiBH₄ confined in highly ordered nanoporous carbon frameworks via solid state NMR and quasielastic neutron scattering. *J. Mater. Chem. A* **1**, 9935–9941 (2013).
 80. Liang, C. C. Conduction Characteristics of the Lithium Iodide-Aluminum Oxide Solid Electrolytes. *J. Electrochem. Soc.* **120**, 1289 (1973).
 81. Agrawal, R. C. & Gupta, R. K. Superionic solids: composite electrolyte phase - an overview. *J. Mater. Sci.* **34**, 1131–1162 (1999).
 82. Skobelev, I., Uvarov, N. & Hairetdinov, E. Composite solid electrolytes MeNO₃-Al₂O₃ (Me = Li, Na, K). *Solid State Ionics* **88**, 86–89 (1996).
 83. Blanchard, D. *et al.* Nanoconfined LiBH₄ as a fast lithium ion conductor. *Adv. Funct. Mater.* **25**, 184–192 (2015).
 84. Zou, Z. *et al.* Mobile Ions in Composite Solids. *Chem. Rev.* **120**, 4169–4221 (2020).
 85. Maier, J. Ionic conduction in space charge regions. *Prog. Solid State Chem.* **23**, 171–263 (1995).
 86. Maier, J. Point-defect thermodynamics and size effects. *Solid State Ionics* **131**, 13–22 (2000).
 87. Remhof, A. *et al.* Hydrogen dynamics in nanoconfined lithiumborohydride. *J. Phys. Chem. C* **117**, 3789–3798 (2013).
 88. De Jongh, P. E. & Eggenhuisen, T. M. Nanoporous Materials and Confined Liquids. in *Nanoparticles: Workhorses of Nanoscience* (ed. de Mello Donegá, C.) 99–120 (Springer Berlin Heidelberg, 2014). doi:10.1007/978-3-662-44823-6_4.
 89. Choi, Y. S. *et al.* Enhanced Li Ion Conductivity in LiBH₄-Al₂O₃ Mixture via Interface Engineering. *J. Phys. Chem. C* **121**, 26209–26215 (2017).
 90. De Kort, L. M., Harmel, J., De Jongh, P. E. & Ngene, P. The effect of nanoscaffold porosity and surface chemistry on the Li-ion conductivity of LiBH₄-LiNH₂/metal oxide nanocomposites. *J. Mater. Chem. A* **8**, 20687–20697 (2020).
 91. Verkuijlen, M. H. W. *et al.* Nanoconfined LiBH₄ and enhanced mobility of Li⁺ and BH₄⁻ studied by solid-state NMR. *J. Phys. Chem. C* **116**, 22169–22178 (2012).

92. Ngene, P. *et al.* The influence of silica surface groups on the Li-ion conductivity of $\text{LiBH}_4/\text{SiO}_2$ nanocomposites. *Phys. Chem. Chem. Phys.* **21**, 22456–22466 (2019).
93. Lambregts, S. F. H. *et al.* Phase Behavior and Ion Dynamics of Nanoconfined LiBH_4 in Silica. *J. Phys. Chem. C* **123**, 25559–25569 (2019).
94. Choi, Y. S., Lee, Y. S., Oh, K. H. & Cho, Y. W. Interface-enhanced Li ion conduction in a $\text{LiBH}_4\text{-SiO}_2$ solid electrolyte. *Phys. Chem. Chem. Phys.* **18**, 22540–22547 (2016).
95. Lefevr, J., Cervini, L., Griffin, J. M. & Blanchard, D. Lithium Conductivity and Ions Dynamics in $\text{LiBH}_4/\text{SiO}_2$ Solid Electrolytes Studied by Solid-State NMR and Quasi-Elastic Neutron Scattering and Applied in Lithium-Sulfur Batteries. *J. Phys. Chem. C* **122**, 15264–15275 (2018).
96. Dou, Y., Hansen, H. A., Xu, S. M. & Blanchard, D. Layered double hydroxides as advanced tracks to promote ionic conductivity in metal borohydride. *Mater. Chem. Front.* **5**, 4989–4996 (2021).
97. Lambregts, S. F. H., van Eck, E. R. H., Ngene, P. & Kentgens, A. P. M. The Nature of Interface Interactions Leading to High Ionic Conductivity in $\text{LiBH}_4/\text{SiO}_2$ Nanocomposites. *ACS Appl. Energy Mater.* (2022) doi:10.1021/acsaem.2c00527.
98. Yan, Y., Rentsch, D., Battaglia, C. & Remhof, A. Synthesis, stability and Li-ion mobility of nanoconfined $\text{Li}_2\text{B}_{12}\text{H}_{12}$. *Dalt. Trans.* **46**, 12434–12437 (2017).
99. Andersson, M. S. *et al.* Promoting Persistent Superionic Conductivity in Sodium Monocarbocloso-dodecaborate $\text{NaCB}_{11}\text{H}_{12}$ via Confinement within Nanoporous Silica. *J. Phys. Chem. C* **125**, 16689–16699 (2021).
100. Latroche, M. *et al.* Full-cell hydride-based solid-state Li batteries for energy storage. *Int. J. Hydrogen Energy* **44**, 7875–7887 (2019).
101. Unemoto, A. *et al.* Stable Interface Formation between TiS_2 and LiBH_4 in Bulk-Type All-Solid-State Lithium Batteries. *Chem. Mater.* **27**, 5407–5416 (2015).
102. Das, S. *et al.* All-Solid-State Lithium-Sulfur Battery Based on a Nanoconfined LiBH_4 Electrolyte. *J. Electrochem. Soc.* **163**, A2029–A2034 (2016).
103. Lefevr, J., Cervini, L., Griffin, J. M. & Blanchard, D. Lithium Conductivity and Ions Dynamics in $\text{LiBH}_4/\text{SiO}_2$ Solid Electrolytes Studied by Solid-State NMR and Quasi-Elastic Neutron Scattering and Applied in Lithium-Sulfur Batteries. *J. Phys. Chem. C* **122**, 15264–15275 (2018).
104. Gulino, V. *et al.* Room-Temperature Solid-State Lithium-Ion Battery Using a $\text{LiBH}_4\text{-MgO}$ Composite Electrolyte. *ACS Appl. Energy Mater.* **4**, 1228–1236 (2021).
105. Duchêne, L. *et al.* A stable 3 V all-solid-state sodium-ion battery based on a closo-borate electrolyte. *Energy Environ. Sci.* **10**, 2609–2615 (2017).
106. Teprovich, J. A. *et al.* Bi-functional $\text{Li}_2\text{B}_{12}\text{H}_{12}$ for energy storage and conversion applications: Solid-state electrolyte and luminescent down-conversion dye. *J. Mater. Chem. A* **3**, 22853–22859 (2015).



A large, abstract green watercolor splash at the top of the page, with a large blue number '2' centered within it.

2

The interplay between metal hydride and oxide in sodium-based metal hydride nanocomposites

In Chapter 1, it was discussed that nanocomposite formation has been employed as strategy to increase the ionic conductivity in metal hydrides, in particular LiBH_4 . In this chapter, we show that the conductivity enhancement in sodium-based metal hydride/oxide nanocomposites results from interface reactions between the metal hydride and the metal oxide. Conductive NaBH_4 and NaNH_2 /oxide nanocomposites were obtained by optimizing the interface reaction, which strongly depends on the interplay between the surface chemistry of the oxides and reactivity of the metal hydrides. Notably, for NaBH_4 the best performance is obtained with $\gamma\text{-Al}_2\text{O}_3$, while $\text{NaNH}_2/\text{SiO}_2$ is the most conductive NaNH_2 /oxide nanocomposite with conductivities of, respectively, $4.7 \cdot 10^{-5}$ and $2.1 \cdot 10^{-5} \text{ S cm}^{-1}$ at 80°C . Detailed structural characterization revealed that this disparity originates from the formation of different tertiary interfacial compounds resulting from reactions between the metal hydride and oxide. These results demonstrate that the conductivity enhancement in these nanocomposites is caused by the formation of a tertiary phase at the metal hydride-oxide interface rather than a space charge layer, as is often proposed for other classes of composite electrolytes.

This chapter is based on: de Kort, L. M., Brandt Corstius, O. E., Gulino, V., Gurinov, A., Baldus, M. & Ngene, P. (2023). Designing conductive sodium-based metal hydride nanocomposites: Interplay between hydride and oxide properties. *Advanced Functional Materials*, accepted.

2.1 Introduction

Due to the high abundance, accessibility and hence low cost of sodium, sodium-ion batteries have been proposed as a promising energy storage devices for large scale applications.^{1–3} Analogous to Li-ion batteries, replacing the liquid electrolyte with a solid-state Na-ion conductor to form an all-solid-state sodium-ion battery could lead to safer and affordable energy storage devices.⁴ Presently, Na-batteries based on a β'' - Al_2O_3 solid electrolyte are commercially available, but these operate at elevated temperatures above 300 °C.⁵ For the development of all-solid-state Na-ion batteries that operate at room temperature, Na-ion conductors with high ionic conductivity, a wide electrochemical stability window and good electrode compatibility are essential. Recently, Na-ion based complex metal hydrides have gained interest for this application, however, similar to Li-based complex hydrides their room temperature conductivity needs to be improved before they can be applied in all-solid-state batteries.

Despite the clear evidence for conductivity enhancement in LiBH_4 /oxide nanocomposites, studies on Na-based metal hydrides, such as NaBH_4 , $\text{NaCB}_{11}\text{H}_{12}$ and NaNH_2 , are scarce. To the best of our knowledge, the effect of nanocomposite formation on the Na^+ mobility in NaBH_4 has only been explored in two recent studies by Luo *et al.* and Dou *et al.*^{6,7} In the former study, it was shown that confinement of NaBH_4 in a mesoporous SiO_2 scaffold leads to a limited improvement in ionic conductivity of one order of magnitude.⁶ On the other hand, Dou *et al.* reported that a slightly larger conductivity increase to $5.8 \cdot 10^{-8} \text{ S cm}^{-1}$ at room temperature using MgAl-layered double hydroxides as the scaffold.⁷ The latter study demonstrates that the ionic conductivity of NaBH_4 -based nanocomposites differs greatly depending on the surface chemistry of the scaffold material, however, the conductivity enhancement remained rather modest. The same is true for $\text{NaCB}_{11}\text{H}_{12}/\text{SiO}_2$ nanocomposites, where a 30-fold conductivity improvement from $1 \cdot 10^{-5} \text{ S cm}^{-1}$ up to $3 \cdot 10^{-4} \text{ S cm}^{-1}$ is observed.⁸

Understanding the conductivity enhancement mechanism and the corresponding interplay between the metal hydride and the metal oxide is crucial to obtain nanocomposites with high Na-ion conductivity. So far, little is known about the exact interactions at metal hydride-oxide interface. In this work, we investigated the impact of nanocomposite formation on the Na-ion conductivity in metal hydrides in detail. In particular, we study how the ionic conductivity is affected by the properties of the oxide scaffold using nanocomposites based on NaBH_4 or NaNH_2 and metal oxides ($\gamma\text{-Al}_2\text{O}_3$ or SiO_2) as model systems. We found that the conductivity enhancement results from reactions leading to different interfacial compounds.

The interface reactions depend strongly on the interplay between the properties of the metal hydride and the oxide scaffold material. Based on this understanding, we achieved about three orders of magnitude increase in the ionic conductivities of the nanocomposites by using the appropriate metal oxide scaffold. While $\gamma\text{-Al}_2\text{O}_3$ induces the highest conductivity in the case of NaBH_4 , the highest conductivity for the NaNH_2 /oxide nanocomposites was obtained with SiO_2 . Using results from EIS, DRIFTS, and solid-state NMR measurements we determined that the difference in conductivity is due to the interaction strength between the hydrides and the oxide, which is influenced by the stability of the metal hydride and the surface chemistry of the oxide surface.

2.2 Experimental methods

Scaffold preparation

Mesoporous silica MCM-41 was synthesized following the procedure of Cheng *et al.*⁹ Hexadecyltrimethylammonium bromide (CTAB, Sigma Aldrich, $\geq 96.0\%$) and tetramethylammonium hydroxide solution (TMAOH, Sigma Aldrich, 25 wt% in H_2O) were mixed with 300 mL deionized water. As a silica source, Aerosil 380 (Evonik) was added to the mixture and the suspension was stirred for 2 hours at 30 °C. The mixture was aged at 30 °C for 24 hours without stirring in a closed polypropylene bottle. The composition of the mixture had a molar ratio of 1.00 SiO_2 : 0.19 TMAOH : 0.27 CTAB : 40 H_2O . The obtained gel mixture was transferred to a Teflon-line stainless steel autoclave and was left to react for 40 hours in a 140 °C pre-heated oven. The product was filtered and washed with deionized water to remove surfactants. Subsequently, the product was dried in static air at 120 °C for 8 hours and calcined under static air for 12 hours at 550 °C ($1.5\text{ }^\circ\text{C min}^{-1}$). Alumina ($\gamma\text{-Al}_2\text{O}_3$, Puralox SCCa-5/200, Sasol) was purchased and used without any further modifications. Alumina and as-synthesized MCM-41 were dried under nitrogen flow at 300 °C for 6 hours and subsequently stored in an Ar filled glovebox (H_2O , $\text{O}_2 < 1\text{ ppm}$).

Nanocomposite synthesis

Preparation of NaBH_4 and NaNH_2 /oxide nanocomposites has been performed via melt infiltration. NaBH_4 (Sigma-Aldrich, 99.99 %, trace metals basis) and NaNH_2 (Sigma-Aldrich, 98 %) were stored and handled in an Ar filled glovebox to avoid exposure to air (H_2O , $\text{O}_2 < 1\text{ ppm}$). The melt infiltration synthesis was started by hand mixing the Na-salt with the appropriate amount of oxide in an agate mortar for about 15 minutes. The amount of NaBH_4 or NaNH_2 is based on the volume needed to fill the pores of the oxide for a chosen percentage (the pore filling fraction). An overview of the composition of the investigated nanocomposites is provided in **Table 2.1**. In some cases, the pore filling percentage is more than 100 %, i.e., the volume of the metal hydride is larger than the total pore volume of the scaffold. This ensures a percolating network of fast Na^+ diffusion pathways on the outer surface of non-conducting oxide particles.

After extensive mixing, the physical mixtures (PMs) were placed in a quartz (NaNH_2) or alumina (NaBH_4) reactor within a stainless-steel autoclave. Prior to the synthesis, the autoclave is pressurized with either 8 bar of NH_3 or 5 bar of H_2 to prevent decomposition of NaNH_2 and NaBH_4 , respectively. Finally, melt infiltration was conducted for 30 minutes at either 225 °C (heating rate = $2.5\text{ }^\circ\text{C min}^{-1}$) for NaNH_2 and at 525 °C (heating rate = $3.5\text{ }^\circ\text{C min}^{-1}$) for NaBH_4 . Upon cooling, the molten sodium compounds solidify in the pores of the scaffold material to form nanoconfined NaNH_2 and NaBH_4 . After cooling to room temperature, the air-tight autoclaves were removed from the furnace and brought inside the glovebox. For the NaNH_2 /oxide nanocomposites, the NH_3 pressure was released before removing from the synthesis set-up, while the H_2 pressure used during the NaBH_4 melt infiltration was released in the glovebox. Subsequently, the nanocomposites were stored in an Ar filled glovebox and all further sample handling, characterization and measurements were performed under inert atmosphere either in the glovebox or using air-tight sample holders.

Table 2.1 – Composition of investigated nanocomposites

Nanocomposite	Pore filling fraction (%)	Weigh ratio metal hydride:oxide
NaNH ₂ /SiO ₂	15	0.24 : 1
	30	0.47 : 1
	70	1.09 : 1
	100	1.53 : 1
	130	2.30 : 1
NaNH ₂ /Al ₂ O ₃	15	0.10 : 1
	30	0.21 : 1
	70	0.46 : 1
	100	0.66 : 1
	130	0.83 : 1
NaBH ₄ /SiO ₂	130	1.80 : 1
NaBH ₄ /Al ₂ O ₃	15	0.08 : 1
	30	0.16 : 1
	50	0.26 : 1
	70	0.34 : 1
	90	0.47 : 1
	120	0.60 : 1
	130	~0.66:1
	150	0.78 : 1
	170	0.88 : 1

General characterization

The crystalline structure of the composites was measured with X-ray diffraction (XRD) on a Bruker-AXS D8 Advance powder X-ray diffractometer using Co ($K\alpha_{1,2}$) radiation ($\lambda = 1.79026 \text{ \AA}$) at 30 kV and 40 mA. Diffractograms were recorded at room temperature from 20 to 85° 2 θ with a 0.1° 2 θ step size and a step time of 1 - 3 s. Diffuse reflectance infrared Fourier transform spectroscopy (DRIFTS) measurements were performed in a Perkin-Elmer 2000 spectrometer equipped with a liquid nitrogen cooled MCT detector. Spectra were recorded from 4500 to 500 cm⁻¹ with 4 cm⁻¹ resolution, averaged over 16 scans, using anhydrous KBr as a background. Differential scanning calorimetry (DSC) measurements were conducted on NaBH₄ nanocomposites using a TA Instruments Discovery DSC. About 6.0 – 8.0 mg of sample was placed in a 40 mL Al sample pan, which was closed airtight. The samples were cooled to -90 °C and allowed to equilibrate for 5 minutes. Subsequently, the samples were heated to -50 °C (1 °C min⁻¹). The measurements were performed under N₂ flow (50 mL min⁻¹). The phase transition temperatures were obtained from the onset of the peaks of the total heat flow, and the corresponding enthalpies were calculated from the total heat flow. To probe the porosity of the samples, nitrogen physisorption measurements were performed on a Micromeritics Tristar 3000. Using the Brunauer, Emmett and Teller (BET) and Barrett, Joyner and Halenda (BJH) adsorption model theories, surface area and pore size distribution were obtained.^{10,11} The BET surface area (A_{BET}), total pore volume and average pore size of the scaffolds based on the adsorbed quantity close to nitrogen saturation pressure ($p = p_0$) are summarized in **Table 2.2**.

Table 2.2 – Nitrogen physisorption results of oxide scaffolds

Oxide scaffold	BET area (m ² g ⁻¹)	Pore volume (cm ³ g ⁻¹)	Average pore diameter (nm)
γ -Al ₂ O ₃	172	0.46	8.7
SiO ₂ (MCM-41)	1260	1.28	2.7

Conductivity measurements

The conductivities of the pristine metal hydrides and nanocomposites were measured with electrochemical impedance spectroscopy (EIS) using a Princeton Applied Research Parstat 2273 potentiostat placed in a custom made Büchi B-585 glass oven. Using a 13 mm pellet press, 150 - 250 mg was pressed between stainless-steel electrodes covered with sodium foil with a pressure of 150 MPa. Using this method, pellets with a thickness of 1.0-1.5 mm were obtained. The EIS measurements were performed by incrementally heating the samples from RT to 80 °C ($\Delta T = 10$ °C) and then incrementally cooling to RT ($\Delta T = 20$ °C). At each increment, the temperature was allowed to equilibrate for 45 min, after which an EIS measurement was acquired with a 20 mV root mean square (RMS) modulated alternating current (AC) potential in a frequency range from 1 MHz to 1 Hz. The obtained Nyquist plots were fitted to a least squares minimum with a circuit consisting of a resistor (R) in parallel with a constant phase element (CPE). Based on the resistance, the electrode area ($A = 1.33$ cm²) and thickness (t) of the pellet, the conductivity, σ , was calculated via $\sigma = t/AR$.

The electronic and Na-ion transport numbers were determined using DC voltage polarization measurements. The NaBH₄/Al₂O₃ and NaNH₂/SiO₂ nanocomposites were pressed into a pellet between two stainless steel cylinders ($\varnothing = 10$ mm) with a pressure of 190 MPa. For Na-ion transport measurements sodium foil was placed on either side of the pellet after pelletization, after which the measurement cell was closed hand-tight. After equilibration at 60 °C for at least 1 hour, a voltage of 0.5 V (electronic transport) or 0.01 V (Na-ion transport) was applied across the pellet and the resulting current was measured for 1 hour using a Parstat PMC-1000 potentiostat. An EIS measurement (20 mV RMS modulated AC potential, 1 MHz to 1 Hz) was performed before and after DC polarization.

Solid-state NMR

The interaction between the metal hydride and the oxide in NaBH₄/Al₂O₃, NaNH₂/Al₂O₃ and NaNH₂/SiO₂ was investigated with high-resolution solid-state nuclear magnetic resonance (ssNMR) measurements, performed on a 950 MHz Bruker NMR spectrometer equipped with a 1.3 mm triple channel (H/X/Y) CP-MAS probe at magic angle spinning (MAS) frequencies of 50 and 60 kHz. Due to frictional heating, the sample temperature was ~50 °C. ¹¹B spectra were obtained with a 30° single pulse using ¹H decoupling at a 16 kHz radio frequency field strength. The ²³Na and ²⁷Al NMR spectra were obtained under direct polarization conditions. For reference, the ¹¹B peak in pure NaBH₄ was set to -42.0 ppm, in line with literature, using CH₃CH₂OBF₃ as a reference ($\delta = 0$ ppm). The ²⁷Al data were referenced to a 1M solution of Al(NO₃)₃ as an external standard. The ²³Na spectra were referenced to a 1M solution of NaCl using NaBH₄ as an external standard. Sample preparation was performed in an Ar filled glovebox, transportation was done in air-tight holders, and the NMR measurements were performed under a dry nitrogen atmosphere.

2.3 Results and discussion

2.3.1 Structural differences between NaBH_4 - and NaNH_2 /oxide nanocomposites

The structural properties of the synthesized NaBH_4 /oxide and NaNH_2 /oxide nanocomposites with a pore filling fraction of 130 % have been investigated. As explained in the experimental section, in this case the volume of the metal hydride is larger than the total pore volume of the scaffold to ensure a connected network of Na^+ diffusion pathways on the outer surface of the oxide particles. First of all, the effectiveness of the melt infiltration synthesis, i.e. the incorporation of the metal hydrides in the pores of the mesoporous scaffolds, is discussed based on the chemical and structural changes revealed by DRIFTS, DSC, XRD and N_2 physisorption measurements.

In **Figure 2.1a** the DRIFTS absorbance spectra of the $\text{NaBH}_4/\text{Al}_2\text{O}_3$ and $\text{NaBH}_4/\text{SiO}_2$ nanocomposites, as well as pure NaBH_4 , $\gamma\text{-Al}_2\text{O}_3$ and SiO_2 are shown. In the spectra the characteristic vibrations of macrocrystalline NaBH_4 can be observed by bands between 2500 and 2000 cm^{-1} , corresponding to $[\text{BH}_4]^-$ stretching vibrations^{12,13}, and bands between 3200 and 3600 cm^{-1} .¹⁴ These characteristic bands are also present in the DRIFTS spectra of the $\text{NaBH}_4/\text{Al}_2\text{O}_3$ and $\text{NaBH}_4/\text{SiO}_2$ nanocomposites. In previous studies on nanoconfined LiBH_4 a broadening of these peaks was seen, which was attributed to an increase in the rotational freedom of $[\text{BH}_4]^-$ induced by nanocomposite formation.¹⁵ For the NaBH_4 nanocomposites, this effect is less evident, though slightly broader peaks are observed for the $\text{NaBH}_4/\text{Al}_2\text{O}_3$ nanocomposite.

The second region of interest corresponds to the hydroxyl stretching vibrations in $\gamma\text{-Al}_2\text{O}_3$ and SiO_2 appearing between 3850 cm^{-1} and 3000 cm^{-1} .¹⁶ For $\gamma\text{-Al}_2\text{O}_3$, several broad bands related to vibrations of linear and bridged hydroxyl groups are seen in the region between 3800–3000 cm^{-1} . In the SiO_2 spectrum, a sharp absorption peak is present at 3747 cm^{-1} , which is ascribed to isolated and geminal silanol groups, or “free” silanols. Additionally, a broad band that represents hydrogen bound (vicinal) silanol groups and physisorbed water is observed between 3700–3000 cm^{-1} . Notably, after melt infiltration the vibrations assigned to surface hydroxyl groups are no longer visible in the spectra of both

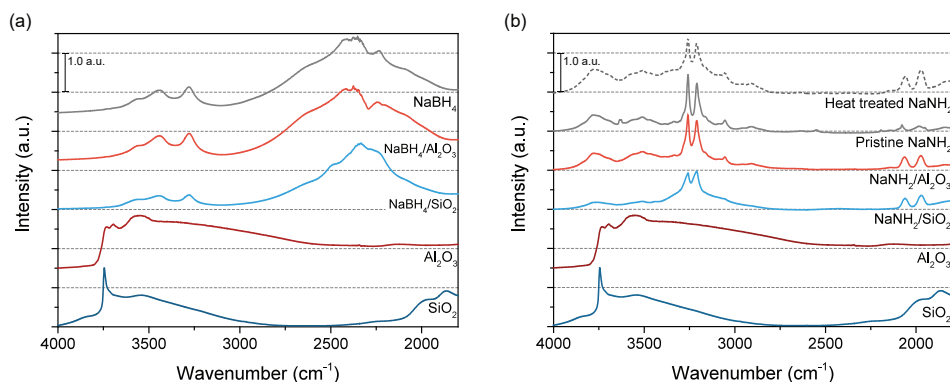


Figure 2.1 - DRIFTS spectra of (a) NaBH_4 /oxide and (b) NaNH_2 /oxide nanocomposites with 130% pore filling fraction displaying the regions related to hydroxyl stretching vibrations, as well as characteristic $[\text{BH}_4]^-$ and $[\text{NH}_2]^-$ vibrations. The spectrum of both pristine and heat treated NaNH_2 is shown with a straight and dotted line.

$\text{NaBH}_4/\text{Al}_2\text{O}_3$ and $\text{NaBH}_4/\text{SiO}_2$. Generally, this is associated with a reaction or interactions between the $-\text{[OH]}$ group and the confined electrolyte, thereby suppressing the hydroxyl vibration.^{15,17} This indicates that during melt infiltration NaBH_4 was (partially) incorporated in the scaffold pores and that an interaction or reaction occurs at the NaBH_4 – metal oxide interface.

In the same way as for $\text{NaBH}_4/\text{oxide}$ nanocomposites, DRIFTS analysis was used to study the structural properties of $\text{NaNH}_2/\text{Al}_2\text{O}_3$ and $\text{NaNH}_2/\text{SiO}_2$ nanocomposites. The DRIFTS spectra of the nanocomposites and pristine compounds are displayed in **Figure 2.1b**. In the spectra of both nanocomposites vibrations that are characteristic for NaNH_2 are observed between 3800 cm^{-1} and 2800 cm^{-1} .^{18,19} Especially the sharp vibrations at 3260 and 3210 cm^{-1} attributed to $[\text{NH}_2^-]$ stretching vibrations display differences compared to pristine NaNH_2 . Similar to LiBH_4 - and $\text{NaBH}_4/\text{oxide}$ nanocomposites, the peaks have become less intense and slightly broader after melt infiltration, in particular for the $\text{NaNH}_2/\text{SiO}_2$ nanocomposite. Moreover, in both nanocomposite spectra two bands are seen at 2060 and 1970 cm^{-1} that are less pronounced in pure NaNH_2 . To investigate the origin of these features, the DRIFTS spectrum of pure NaNH_2 subjected to the same heat treatment as the nanocomposites, i.e., 30 minutes at 225°C , was collected (**Figure 2.1b**). This spectrum displays the same features, confirming that the peaks are not the result of nanocomposite formation, but rather an irreversible structural change in NaNH_2 after heating to 225°C . Finally, in the spectra of the $\text{NaNH}_2/\text{oxide}$ nanocomposites the vibrations related to the metal oxide hydroxyl groups between $3700\text{--}3000\text{ cm}^{-1}$ are no longer present. Again, this can be assigned to interfacial interactions or reactions between the sodium compound and the surface hydroxyl groups.¹⁵ This shows that the used synthesis conditions result in incorporation of NaNH_2 in the oxide pores, as in the case of NaBH_4 .

The incorporation of NaBH_4 in the pores of the mesoporous scaffolds was studied in further detail with differential scanning calorimetry (DSC) and X-ray diffraction (XRD). The DSC curves of $\text{NaBH}_4/\text{SiO}_2$ and $\text{NaBH}_4/\text{Al}_2\text{O}_3$ nanocomposites as well as pure NaBH_4 are presented in **Figure 2.2a**. In the DSC curve of pure NaBH_4 the phase transition from tetragonal $\text{P4}_2/\text{nmc}$ (LT phase) to cubic $\text{F}_m\text{-}3\text{m}$ (HT phase) NaBH_4 is observed by an endothermic peak starting at -83°C .^{20,21} Using integration of the peak area, we verified

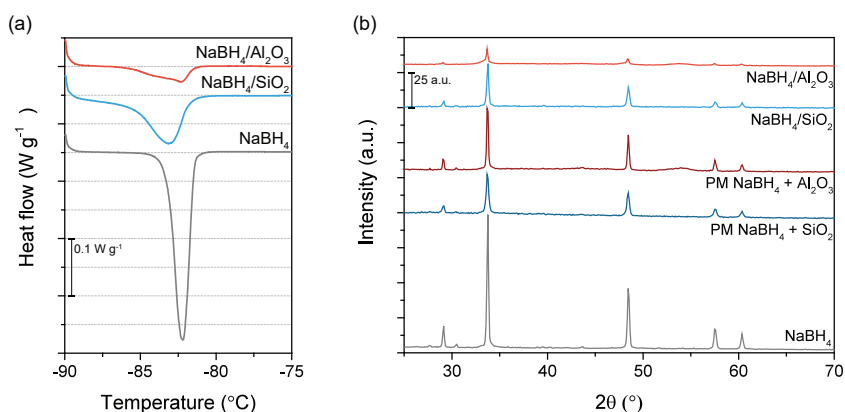


Figure 2.2 - (a) DSC graphs of macrocrystalline NaBH_4 and $\text{NaBH}_4/\text{oxide}$ nanocomposites with 130% pore filling fraction. (b) XRD diffraction patterns of $\text{NaBH}_4/\text{oxide}$ physical mixtures (PM) and corresponding nanocomposites. The diffraction pattern of NaBH_4 is shown for comparison.

that the enthalpy of this phase transition is 23.5 J g^{-1} (or 0.89 kJ mol^{-1}) in accordance with literature.²¹ Similarly, in the DSC curves of both NaBH_4 /oxide nanocomposites, a broad endothermic peak with an onset of $-85 \text{ }^\circ\text{C}$ is seen, which is attributed to the presence of macrocrystalline NaBH_4 . The phase transitions in nanoconfined materials typically occur at lower temperatures than the macrocrystalline material.²² In this case, no additional peaks are observed below $-85 \text{ }^\circ\text{C}$, which suggests that NaBH_4 nanoconfined in SiO_2 and $\gamma\text{-Al}_2\text{O}_3$ undergoes the phase transition at temperatures below the limit of the DSC apparatus ($-90 \text{ }^\circ\text{C}$).

Using the peak area of the macrocrystalline NaBH_4 peak and the enthalpy of the phase transition, it is possible to calculate the fractions of macrocrystalline (extraporous) and nanoconfined (intraporous) NaBH_4 in the nanocomposites.²² The results are summarized in **Table 2.3**. This approach shows that in the $\text{NaBH}_4/\text{Al}_2\text{O}_3$ nanocomposite the pores are completely filled with NaBH_4 . As a result, 79% of the total amount of NaBH_4 is confined inside the scaffold pores and 21% is present as extraporous NaBH_4 , as required to ensure sufficient Na^+ conduction over the non-conducting oxide particles. On the other hand, for the $\text{NaBH}_4/\text{SiO}_2$ nanocomposite it was found that 65% of NaBH_4 resides outside of the scaffold, which means only 35% of NaBH_4 has been incorporated in the SiO_2 pores. This corresponds to a pore filling of only 46%, significantly lower than intended. This demonstrates that melt infiltration has resulted in the complete infiltration of NaBH_4 in the pores of $\gamma\text{-Al}_2\text{O}_3$, whereas only partial incorporation occurs in the SiO_2 scaffold. These results are further corroborated by XRD analysis (**Figure 2.2b**), which shows a large decrease in the long-range crystallinity of NaBH_4 when it is melt infiltrated in $\gamma\text{-Al}_2\text{O}_3$, whereas long-range crystallinity is mostly preserved for $\text{NaBH}_4/\text{SiO}_2$. Nanoconfined materials typically lack long-range crystallinity, due to the nanosized crystallites that form in the small scaffold pores, which means that long-range crystallinity in metal hydride nanocomposites is often associated with extraporous (non-confined) material.²²

Table 2.3 - Differential scanning calorimetry results of NaBH_4 /oxide nanocomposites

Nanocomposite	$\text{NaBH}_4/\text{Al}_2\text{O}_3$	$\text{NaBH}_4/\text{SiO}_2$
Enthalpy (J g^{-1} nanocomposite)	1.92	9.82
Extraporous NaBH_4 (g g^{-1} nanocomposite)	0.08	0.42
Ratio extra/intraporous NaBH_4	0.21 : 0.79	0.65 : 0.35
Volume metal hydride / scaffold pore volume	1.03	0.46

The distinct difference in NaBH_4 infiltration in the different scaffolds can be explained by the physical principles governing melt infiltration. In general, pores of a certain scaffold can be filled spontaneously by a liquid (or molten solid) when capillary forces draw the liquid or molten phase inside the scaffold pores. This phenomenon occurs when the liquid readily spreads over, or ‘wets’, the surface of the solid. Whether a liquid wets a surface depends on the surface energy of the solid γ_{sv} , the surface tension of the liquid γ_{lv} , and the solid-liquid interface energy γ_{sl} . Based on Young’s equation (equation 2.1) it can be determined if a system “wetting” or “non-wetting”.

$$\cos \theta = \frac{\gamma_{sv} - \gamma_{sl}}{\gamma_{lv}} \quad (2.1)$$

A contact angle $\theta < 90^\circ$ corresponds to wetting, while a system is non-wetting if $\theta > 90^\circ$.²² By comparing the surface energies of SiO_2 and $\gamma\text{-Al}_2\text{O}_3$, it becomes clear that the surface energy for SiO_2 (0.26 Jm^{-2}) is significantly lower than that of $\gamma\text{-Al}_2\text{O}_3$ (1.52 Jm^{-2}).^{23,24} Therefore, it is more difficult for NaBH_4 to infiltrate the pores of SiO_2 and consequently only partial NaBH_4 incorporation is observed for $\text{NaBH}_4/\text{SiO}_2$, while complete infiltration is achieved for the $\text{NaBH}_4/\text{Al}_2\text{O}_3$ nanocomposite. This issue has not been encountered for $\text{LiBH}_4/\text{oxide}$ nanocomposites, because LiBH_4 has a lower surface tension γ_{lv} (0.12 Nm^{-1}) compared to NaBH_4 ($0.24 - 1.09 \text{ Nm}^{-1}$)²² and therefore easily infiltrates the pores of both SiO_2 and $\gamma\text{-Al}_2\text{O}_3$.

Due to the decomposition of NaNH_2 upon melting (in the absence of ammonia back pressure) and the absence of low temperature structural phase transitions, it was not possible to study the incorporation of NaNH_2 in mesoporous metal oxides with DSC measurements, as this would require an ammonia overpressure during the measurements. However, evidence for the infiltration of NaNH_2 into the oxide pores is provided by XRD analysis and N_2 physisorption. The XRD diffraction patterns of the $\text{NaNH}_2/\text{SiO}_2$ and $\text{NaNH}_2/\text{Al}_2\text{O}_3$ nanocomposites are shown in **Figure 2.3a**. For comparison, the XRD patterns of pure NaNH_2 and physical mixtures of NaNH_2 and the metal oxides are included. The sharp crystalline peaks that are observed in the diffraction patterns of the pure compound and the physical mixtures (PM), are not present for the nanocomposites. The XRD diffraction peaks for NaNH_2 are less intense in both $\text{NaNH}_2/\text{SiO}_2$ and $\text{NaNH}_2/\text{Al}_2\text{O}_3$. This absence of long-range crystallinity is attributed to successful incorporation of NaNH_2 in the oxide pores, since confined NaNH_2 forms nanosized crystallites in the oxide pores which cannot be probed by XRD.^{22,25} Moreover, the successful incorporation of NaNH_2 into the mesoporous oxides is further confirmed with N_2 physisorption. The physisorption curves of $\text{NaNH}_2/\text{SiO}_2$ and $\text{NaNH}_2/\text{Al}_2\text{O}_3$ nanocomposites with different pore filling fractions are shown in **Figure 2.3b**. Here, a gradual loss in pore volume is observed with increasing amount of NaNH_2 , consistent with infiltration of the metal hydride in the scaffold pores.^{25,26} Hence, it is clear that NaNH_2 is readily incorporated in both mesoporous oxide scaffolds, in line with the DRIFTS and XRD results.

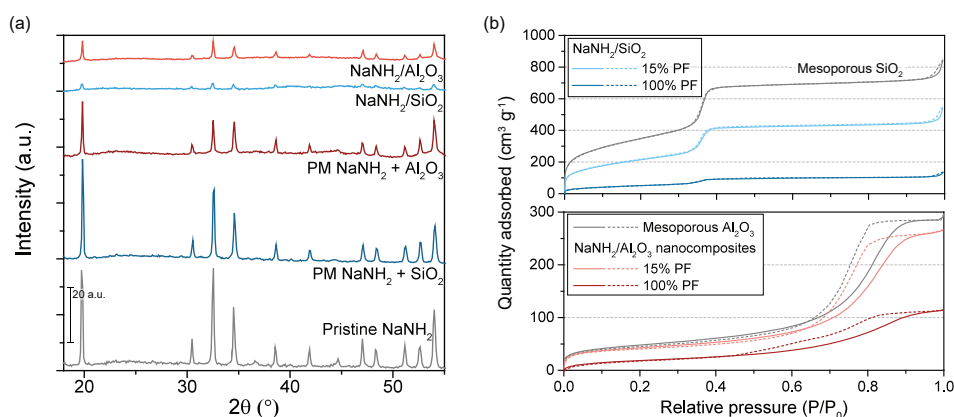


Figure 2.3 - (a) XRD diffraction patterns of $\text{NaNH}_2/\text{oxide}$ physical mixtures (PM) and corresponding nanocomposites. The diffraction pattern of NaNH_2 is shown for comparison. (b) N_2 physisorption isotherms of $\text{NaNH}_2/\text{SiO}_2$ and $\text{NaNH}_2/\text{Al}_2\text{O}_3$ nanocomposites with pore filling fractions of 15 and 100%, as well as the pristine oxides. The solid lines correspond to adsorption curves and the dashed lines correspond to desorption curves.

2.3.2 Conductivity in NaBH₄- and NaNH₂/oxide nanocomposites

To investigate the effect of the nanocomposite formation on the ionic conductivity, the impedance of the NaBH₄- and NaNH₂/oxide nanocomposites was determined by EIS. The temperature-dependent conductivities as derived from the complex impedance analysis are displayed in **Figure 2.4a** for NaNH₂/oxide nanocomposites and **Figure 2.4b** for NaBH₄/oxide nanocomposites. The corresponding electronic and Na-ion transport measurements are depicted in **Figures 2.4c** to **2.4f**. An overview of the conductivities at 80 °C is provided in **Table 2.4**. The conductivity did not change during heating and cooling, which indicates that the changes to the material during cycling are negligibly small.

The data depicted in **Figure 2.4** demonstrates that over the entire temperature range from room temperature to 80 °C all nanocomposites display an enhancement of the conductivity compared to pristine sodium compounds. The electronic and Na-ion transport measurements confirm that for both the NaNH₂- and NaBH₄/oxide nanocomposites, the conductivity determined from EIS corresponds directly to Na-ion transport, as the electronic transport is negligible and the Na-ion transport number is almost unity. Notably, for the NaNH₂/oxide nanocomposites (**Figure 2.4a**), the NaNH₂/SiO₂ sample possesses the highest conductivity. Contrarily, in case of NaBH₄ nanocomposite formation with SiO₂ only results in a slight increase, while the conductivity of NaBH₄/Al₂O₃ improved by almost 3 orders of magnitude compared to pristine NaBH₄ (**Figure 2.4b**). To compare, for LiBH₄ an increase over 3 orders of magnitude upon confinement in a similar SiO₂ scaffold (MCM-41) is typically observed.²⁷ Hence, while it is evident that nanocomposite formation leads to conductivity improvement for sodium-based complex hydrides analogous to lithium borohydride, the exact extent of the enhancement clearly differs from the lithium-based counterparts.

The temperature-dependence of the ionic conductivity (σ) indicates Arrhenius type behavior in the applied temperature range. This Arrhenius behavior is described by the following expression,

$$\sigma(T) = \frac{\sigma_0}{T} e^{-E_A/k_B T} \quad (2.2)$$

where k_B is the Boltzmann constant, σ_0 is a pre-exponential factor and E_A is the activation energy.²⁸ Accordingly, the activation energy for long-range ion transport in the nanocomposites could be derived by linearly fitting the data shown in **Figure 2.4**. A summary of the calculated activation energies is reported in **Table 2.4**.

The activation energies for charge transport in the NaNH₂/oxide nanocomposites (0.73 and 0.85 eV for NaNH₂/SiO₂ and NaNH₂/Al₂O₃, respectively) is considerably lower than the value obtained for pristine NaNH₂ (1.4 eV). The lowest activation energy is obtained for the most conductive NaNH₂/oxide nanocomposite, NaNH₂/SiO₂. Likewise, the activation energies of the NaBH₄/oxide nanocomposites display the same trend, i.e., a decreased E_A after nanocomposite formation. The calculated activation energies for NaBH₄/SiO₂ and NaBH₄/Al₂O₃ are 0.51 and 0.48 eV, smaller than the activation energy of 0.67 eV calculated for pristine NaBH₄. Thus, in agreement with the enhancement in conductivity, the activation energy for ion transport has decreased upon nanocomposite

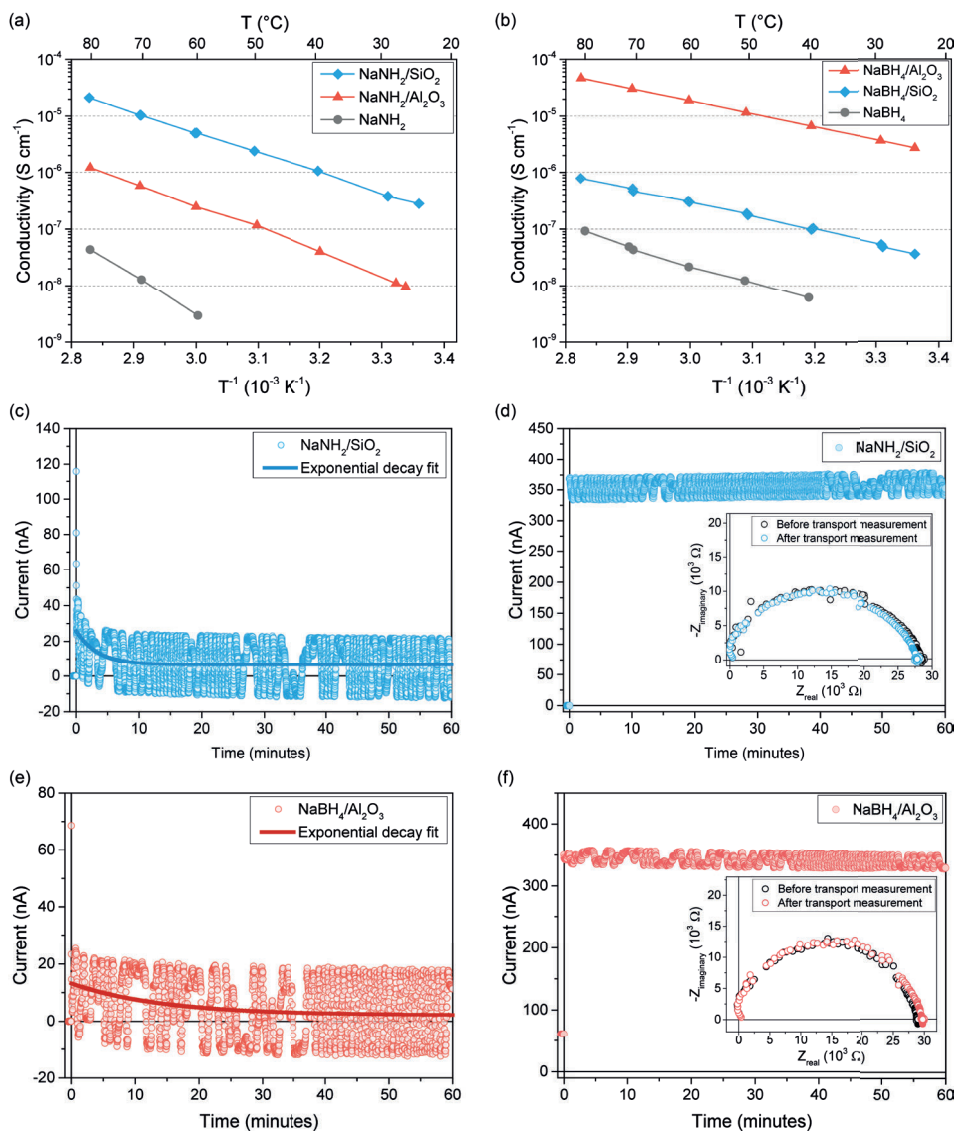


Figure 2.4 - Arrhenius plots of conductivity versus reciprocal temperature of (a) $NaBH_4$ /oxide and (b) $NaNH_2$ /oxide nanocomposites with 130% of the scaffold pores filled based on SiO_2 (blue) and $\gamma-Al_2O_3$ (red), as well as pure $NaBH_4$ or $NaNH_2$. The first temperature-dependent heating cycle is shown. (c-f) Electronic and Na-ion transport measurements on $NaNH_2/SiO_2$ (c,d) and $NaBH_4/Al_2O_3$ (e,f) symmetric cells. The electronic measurements (c,e) were performed on symmetric cells with blocking electrodes (SS) and Na-ion measurements (d,f) have been performed on symmetric cells with non-blocking electrodes (Na).

formation, similar to the behavior that has previously been established for $LiBH_4$ nanocomposites.²⁹ When comparing the conductivities and activation energies of the $NaNH_2$ /oxide nanocomposites and the $NaBH_4$ /oxide nanocomposites, it is observed that the largest conductivity improvement is achieved with a different scaffold, SiO_2 in the case of $NaNH_2$ and $\gamma-Al_2O_3$ in the case of $NaBH_4$. The origin of this behavior will be discussed in detail later.

Table 2.4 - Nanocomposite conductivity at 80 °C, activation energy (E_A) and $\ln(\sigma T)$ obtained from a linear plot of $\ln(\sigma T)$ and $10^{-3} T^{-1}$ of the second temperature dependent EIS cycle reported in Figure 2.4. The standard deviation is based on the 95% confidence interval of the linear fit.

Metal hydride/(oxide)	σ at 80 °C (S cm ⁻¹)	$\ln \sigma_0$	E_A (eV)
Pristine NaNH ₂	$4.35 \cdot 10^{-8}$	34 ± 17	1.4 ± 0.5
NaNH ₂ /SiO ₂	$2.12 \cdot 10^{-5}$	19.1 ± 0.6	0.73 ± 0.02
NaNH ₂ /Al ₂ O ₃	$1.22 \cdot 10^{-5}$	20 ± 1	0.85 ± 0.04
Pristine NaBH ₄	$9.23 \cdot 10^{-8}$	12 ± 3	0.67 ± 0.07
NaBH ₄ /SiO ₂	$7.85 \cdot 10^{-7}$	8.6 ± 0.5	0.51 ± 0.01
NaBH ₄ /Al ₂ O ₃	$4.66 \cdot 10^{-5}$	11.7 ± 0.1	0.48 ± 0.01

Before discussing the differences between the NaNH₂- and NaBH₄-nanocomposites, the effect of the metal hydride-to-metal oxide weight ratio (or pore filling) in the nanocomposite on the conductivity will be considered. Here we specifically analyzed the composition dependence for the NaBH₄/Al₂O₃ nanocomposite, as this system demonstrated the highest conductivity. The explored composition ranges from a NaBH₄ : Al₂O₃ weight ratio of 0.26:1 to a ratio of 0.88:1, which corresponds to pore filling fractions of 50 to 170 % (see **Table 2.1**). The Arrhenius plots for the conductivities of these NaBH₄/Al₂O₃ samples are displayed in **Figure 2.5a**. The dependence of the activation energy and conductivity (at 40 °C) on the pore filling is shown in **Figure 2.5b**. The highest σ value at 40 °C is reached for a pore filling fraction of 120 – 130% confirming the trend that has been previously reported. The conductivity increases with the increasing amount of NaBH₄ up to a pore filling fraction of 130 %, while the conductivity decreases after exceeding this value.

This can be explained by the presence of non-conducting phases in the NaBH₄/Al₂O₃ nanocomposites. A pore filling fraction that is lower than 120 % would result in an excess of insulating γ -Al₂O₃ that interrupts the Na-ion diffusion pathways, thereby decreasing conductivity. On the other hand, if the pore filling fraction (volume of NaBH₄ compared to γ -Al₂O₃ pore volume) exceeds 130%, long-range Li-ion transport is hindered by the presence of the poorly conducting macrocrystalline NaBH₄. It is worth noting that the calculated E_A values confirm this behavior as well. In fact, the E_A decreases up to 0.46 eV for a pore filling fraction of 130 %, verifying that this is the optimal composition for these

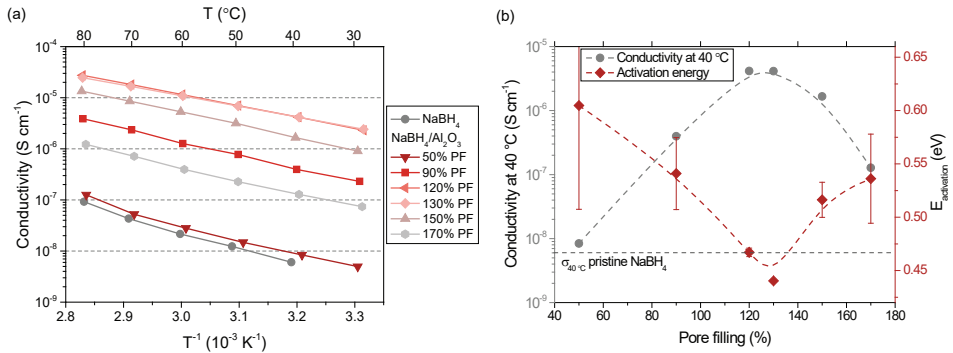


Figure 2.5 - (a) Arrhenius plots of conductivity versus reciprocal temperature of NaBH₄/Al₂O₃ nanocomposites with varying pore filling. (b) Conductivity at 50 °C (grey circles) and activation energy (red diamonds) as a function of pore filling (%). Dashed lines are added to guide the eye.

metal hydride nanocomposites. When the amount of NaBH_4 is increased or decreased, the activation energy increased, indicating less favorable Na-ion conduction pathways. It is also important to note that the conductivity of $\text{NaBH}_4/\text{Al}_2\text{O}_3$ with a pore filling fraction of 50% does not show complete Arrhenius behavior, as the conductivity does not follow a completely straight line. This suggests that in this case different diffusion mechanisms with different temperature dependences contribute to the conductivity.

The observed trend is in line with the one reported by Gulino *et al.*, which revealed a maximum of the Li-ion conductivity for the system $\text{LiBH}_4\text{-SiO}_2$ system for a complete pore volume filling (i.e. 100 %).²⁹ The slight difference in the composition for the maximum σ value can be explained considering the two different routes used to synthesize the nanocomposites, i.e., ball milling for Gulino *et al.* and melt infiltration in this work which typically requires a larger pore filling.^{17,30} For the first time, we have described how the structural parameter pore filling affects the conductivity in sodium composite electrolytes synthesized via melt infiltration. It is important to consider that this optimum in pore filling will not apply to nanocomposites in which the metal hydride does not completely infiltrate the scaffold pores, such as the $\text{NaBH}_4/\text{SiO}_2$ nanocomposite, as in this case more extraporous (macrocrystalline) metal hydride hinders long-range ionic transport.

2.3.3 Probing the metal hydride-oxide interface

The improved conductivity observed for the $\text{NaNH}_2/\text{oxide}$ and $\text{NaBH}_4/\text{oxide}$ nanocomposites could originate from the creation of a highly conductive interface layer at the metal hydride – oxide interface, as has been reported for $\text{LiBH}_4/\text{oxide}$ nanocomposites. For LiBH_4 , it has been demonstrated that the enhancement in conductivity upon nanocomposite formation with a mesoporous oxide originates from interactions between surface groups of the oxide and the metal hydride. This interface layer is characterized by high ion dynamics for both BH_4^- and Li^+ but has not yet been defined with a clear structure.^{15,30–32} De Kort *et al.* recently identified similar interface-induced ionic conductivity in $\text{LiBH}_4\text{-LiNH}_2/\text{oxide}$ nanocomposites.¹⁷ The physical and chemical properties of the oxide materials are critical for the interface reaction, and thereby the ionic conductivity of the nanocomposite materials, although the exact roles of the scaffold and the nature of the interface are not yet fully understood.

In section 2.2.2, it was demonstrated that for NaBH_4^- and $\text{NaNH}_2/\text{oxide}$ nanocomposites, the surface groups of the oxide scaffolds disappeared after melt infiltration due to the presence of the sodium metal hydrides (**Figure 2.1**). This suggests that also in the present case, interface interactions could have resulted in the formation of a highly conductive interface layer. Moreover, a remarkable difference in the ionic conductivity of $\text{NaNH}_2/\text{SiO}_2$ compared to $\text{NaNH}_2/\text{Al}_2\text{O}_3$, and $\text{NaBH}_4/\text{SiO}_2$ compared to $\text{NaBH}_4/\text{Al}_2\text{O}_3$, has been observed (**Figure 2.4**). The highest conductivity for $\text{NaNH}_2/\text{oxide}$ nanocomposites is obtained with the SiO_2 scaffold, while the $\text{NaBH}_4/\text{Al}_2\text{O}_3$ nanocomposite is more conductive than $\text{NaBH}_4/\text{SiO}_2$. Evidently, the interaction of the two sodium compounds with SiO_2 and $\gamma\text{-Al}_2\text{O}_3$ is different. This strongly suggests that the interface reaction does not only depend on the properties of the oxide scaffold, but also on the nature of the metal hydride.

To understand how the nanocomposite conductivity depends on the interactions between the metal hydride and the oxide scaffold, we have investigated the nature of the interface layer in the $\text{NaBH}_4/\text{Al}_2\text{O}_3$, $\text{NaNH}_2/\text{Al}_2\text{O}_3$ and $\text{NaNH}_2/\text{SiO}_2$ nanocomposites.

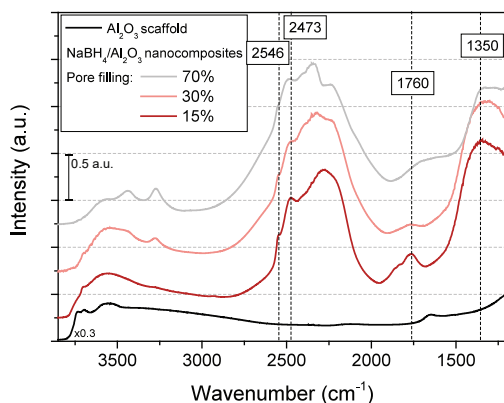


Figure 2.6 - DRIFTS spectra of $\text{NaBH}_4/\text{oxide}$ nanocomposites with pore filling fraction ranging from 15% to 130% displaying the regions related to hydroxyl stretching vibrations, as well as characteristic $[\text{BH}_4]^-$ vibrations. The spectrum of $\gamma\text{-Al}_2\text{O}_3$ is provided for comparison.

The interface interactions in the $\text{NaBH}_4/\text{SiO}_2$ nanocomposite are not studied, since the metal hydride does not completely infiltrate the mesoporous oxide due to poor wetting of NaBH_4 on the SiO_2 surface as illustrated by DSC (**Table 2.3**). While it is likely that the NaBH_4 interacts with the SiO_2 surface in this case as well (though rather weakly), the overall conductivity is governed by the larger amount of macrocrystalline NaBH_4 outside of the scaffold pores. Consequently, it is not possible to fairly compare the results of this sample to the other nanocomposites.

The metal hydride/oxide interface of the most conductive nanocomposite, $\text{NaBH}_4/\text{Al}_2\text{O}_3$, has been studied with DRIFTS and solid-state NMR (ssNMR). To this end, nanocomposites with low pore filling fractions were prepared to specifically probe the contribution of the $\text{NaBH}_4\text{-Al}_2\text{O}_3$ interface species, as the contribution of bulk-like NaBH_4 far away from the interface is minimized at these low metal hydride compositions. In **Figure 2.6** the DRIFTS spectra of $\text{NaBH}_4/\text{Al}_2\text{O}_3$ with different pore filling fractions are shown. With decreasing pore filling, the vibrations at 3438 cm^{-1} , 3275 cm^{-1} and between 2500 and 2000 cm^{-1} corresponding to NaBH_4 becomes less intense. At the same time, new peaks that are not associated with the $\gamma\text{-Al}_2\text{O}_3$ scaffold appear at 2547 cm^{-1} , 2473 cm^{-1} , 1760 cm^{-1} and around 1350 cm^{-1} , indicated by the dotted lines in **Figure 2.6**. The peaks around 2500 cm^{-1} are ascribed to B-H stretching vibrations in $\text{Na}_2\text{B}_{12}\text{H}_{12}$.³³ This indicates that near the scaffold surface NaBH_4 partially decomposes to form $\text{Na}_2\text{B}_{12}\text{H}_{12}$, as has already been demonstrated by Ngene *et al.* for NaBH_4/C nanocomposites.³⁴ Additionally, the vibrations at 1760 cm^{-1} and 1350 cm^{-1} are ascribed to asymmetric stretching vibrations of B-O bonds in trigonal BO_3 -units.³⁵ These results strongly suggest that the surface hydroxyl groups on $\gamma\text{-Al}_2\text{O}_3$ react with NaBH_4 to form B-O bonds as well as $\text{Na}_2\text{B}_{12}\text{H}_{12}$, thereby forming a tertiary interfacial phase with enhanced Na-ion mobility.

High-resolution ssNMR measurements were performed on the $\text{NaBH}_4/\text{Al}_2\text{O}_3$ nanocomposites to further study the interfacial species. In **Figure 2.7a** the ^{11}B spectra for pristine NaBH_4 , $\text{NaBH}_4/\text{Al}_2\text{O}_3$ nanocomposites with different pore filling and an empty sample holder (rotor) are shown. In **Figure 2.7b** an enlargement of the graph is provided so that the smaller peaks can be distinguished more easily. In the spectrum for pristine NaBH_4 , a single peak is observed at a chemical shift of -42.0 ppm , ascribed to bulk-like

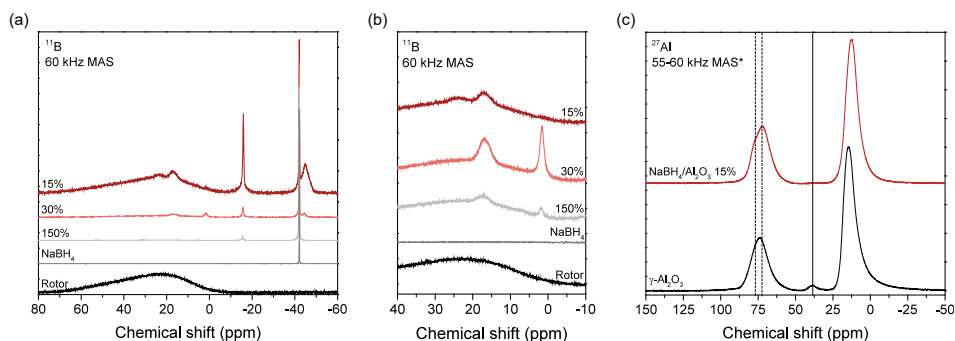


Figure 2.7 - (a,b) ^{11}B ssNMR spectra of pure NaBH_4 , $\text{NaBH}_4/\text{Al}_2\text{O}_3$ nanocomposites and an empty NMR rotor. The nanocomposite spectra are normalized to the peak at -42 ppm. The spectrum of the empty rotor is normalized to the same value as the 15% pore filling composite. (c) ^{27}Al ssNMR spectra of $\gamma\text{-Al}_2\text{O}_3$ and the $\text{NaBH}_4/\text{Al}_2\text{O}_3$ nanocomposite with 15% pore filling fraction. The spectra are normalized to the peak at 15 ppm.

$[\text{BH}_4]$ species.³⁶ Compared to the pure NaBH_4 spectrum, the nanocomposite spectra contain several additional peaks. First of all, at a slightly more negative chemical shift of -44.8 ppm a broad peak is seen, which becomes more pronounced with lower pore filling fractions. This peak can be assigned to the presence of more shielded NaBH_4 nanoclusters, as has been previously reported for nanoconfined LiBH_4 .³⁶ Secondly, in all nanocomposites a peak is present at a chemical shift of -15.6 ppm, which corresponds to the presence of $\text{Na}_2\text{B}_{12}\text{H}_{12}$ in the samples.^{36,37} Finally, in most of the $\text{NaBH}_4/\text{Al}_2\text{O}_3$ nanocomposite spectra, two peaks are seen at positive chemical shifts of 1.3 ppm and 17.4 ppm, while the spectrum of the nanocomposite with a pore filling fraction of 15% contains a third peak at 24.4 ppm. Each of these peaks corresponds to a specific B-O species, respectively, tetragonal $\text{BO}_{4/2}^-$, trigonal $\text{BO}_{3/2}$ and three-coordinated $\text{BO}_{2/2}\text{O}^-$ sites.³⁸

The interaction of the $[\text{BH}_4]^-$ anions with the oxide surface was investigated further with ^{27}Al ssNMR measurements. The ^{27}Al spectra of $\text{NaBH}_4/\text{Al}_2\text{O}_3$ with a low pore filling fraction (15%) and pristine $\gamma\text{-Al}_2\text{O}_3$ are displayed in **Figure 2.7c**. The spectra demonstrate that the unsaturated penta-coordinated Al sites on the oxide surface become saturated upon incorporation of NaBH_4 in the scaffold pores, which can be attributed to coordination of the $[\text{BH}_4]^-$ anion to the $[\text{AlO}_5]$ on the oxide surface.^{39,40} Thus, in line with the DRIFTS results, the ssNMR analysis confirms that incorporation of NaBH_4 in the $\gamma\text{-Al}_2\text{O}_3$ scaffold results in the formation of NaBH_4 nanoclusters, $\text{Na}_2\text{B}_{12}\text{H}_{12}$ and B-O species due to interaction with the oxide surface. The presence of B-O species and interaction with the oxide has previously been associated with the formation of a (conductive) interfacial layer in LiBH_4 , $\text{LiBH}_4\text{-LiI}$, and $\text{LiF}/\text{Al}_2\text{O}_3$ nanocomposites.^{32,39,41}

In an analogous way, the interface interactions at the metal hydride-metal oxide interface in $\text{NaNH}_2/\text{Al}_2\text{O}_3$ and $\text{NaNH}_2/\text{SiO}_2$ nanocomposites were studied with ssNMR and DRIFTS. Since boron is not present in these samples and ^{14}N and ^{15}N NMR did not give sufficient signal, the interfacial species were studied using ^{23}Na NMR and, for $\text{NaNH}_2/\text{Al}_2\text{O}_3$, ^{27}Al NMR. In **Figure 2.8a** the ^{27}Al NMR spectra of $\text{NaNH}_2/\text{Al}_2\text{O}_3$ nanocomposites with pore filling fractions of 100% and 15% are shown, as well as pristine $\gamma\text{-Al}_2\text{O}_3$ for comparison. The pure $\gamma\text{-Al}_2\text{O}_3$ spectrum contains intense signals at 15 ppm and 74 ppm, which reflect the presence of respectively six- and four-fold coordinated Al species.^{39,40} A

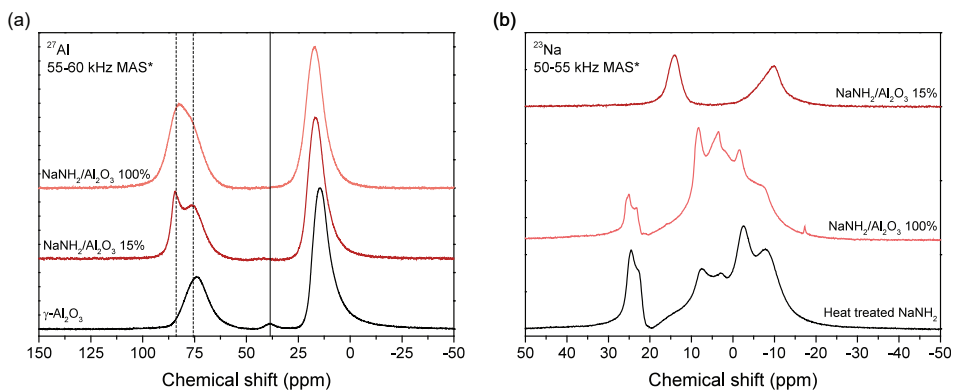


Figure 2.8 - (a) ^{27}Al ssNMR spectra of $\gamma\text{-Al}_2\text{O}_3$ and the $\text{NaNH}_2/\text{Al}_2\text{O}_3$ nanocomposite with 15% pore filling fraction. The spectra are normalized to the peak at 15 ppm. (b) ^{23}Na ssNMR spectra of heat treated NaNH_2 and $\text{NaNH}_2/\text{Al}_2\text{O}_3$ nanocomposites with 15% and 100% pore filling.

less intense signal is seen at 39 ppm, which represents unsaturated penta-coordinated Al ions near the surface of the oxide.^{39,40} It is known that these penta-coordinated sites can serve as anchoring points for foreign anions such as F^- from LiF or BH_4^- from LiBH_4 .^{39,41} As a consequence, the penta-coordinated sites become saturated and the signal around 39 ppm disappears.

This phenomenon clearly occurs for the studied $\text{NaNH}_2/\text{Al}_2\text{O}_3$ nanocomposites as well. In the ssNMR spectra of both nanocomposites pronounced signals related to four-fold and six-fold coordinated Al species are present, while no signal related to penta-coordinated Al is observed. Hence, it seems likely that the NH_2^- anion interacts with the $[\text{AlO}_5]$ surface group, possibly forming a $[\text{AlO}_5(\text{NH}_2)]$ -like species. In other conductor/insulator nanocomposites, such as $\text{LiF}/\text{Al}_2\text{O}_3$ the $[\text{AlO}_5\text{X}]$ sites formed in this way significantly influence the overall ionic transport as Li^+ vacancies are created that can be utilized by other Li^+ ions to perform hopping processes in the interface region. Similarly, it is expected that the conduction in the $\text{NaNH}_2/\text{oxide}$ nanocomposites depends on a surface-controlled diffusion mechanism.

The NMR signal related to four-fold-coordinated species consists of two peaks (at 84 ppm and 75 ppm), which can be clearly distinguished in the $\text{NaNH}_2/\text{Al}_2\text{O}_3$ nanocomposite with a pore filling fraction of 15%. This indicates that in addition to the four-fold-coordinated Al species in pristine $\gamma\text{-Al}_2\text{O}_3$, a second four-fold-coordinated species is formed in the nanocomposites due to interaction or reaction of the metal hydride with the $\gamma\text{-Al}_2\text{O}_3$ surface. It is interesting to note that similar peaks are also present in the ^{27}Al NMR spectra of the $\text{NaBH}_4/\text{Al}_2\text{O}_3$ nanocomposites (**Figure 2.7c**). While the higher δ_{iso} of this $[\text{AlO}_4]$ species demonstrates that this compound has a higher Al – O bond order and shorter bonds⁴⁰, ^{27}Al NMR does not provide further information on the possible nature of the interfacial compound(s) that might have formed.

Therefore, the chemical nature of the $\text{NaNH}_2/\text{Al}_2\text{O}_3$ interface was investigated further with ^{23}Na NMR and DRIFTS analysis shown in **Figure 2.8b** and **2.9**. The ^{23}Na NMR spectra (**Figure 2.8b**) of heat-treated NaNH_2 and $\text{NaNH}_2/\text{Al}_2\text{O}_3$ with a pore filling fraction of 100% both exhibit a big quadrupolar feature with several peaks between 30

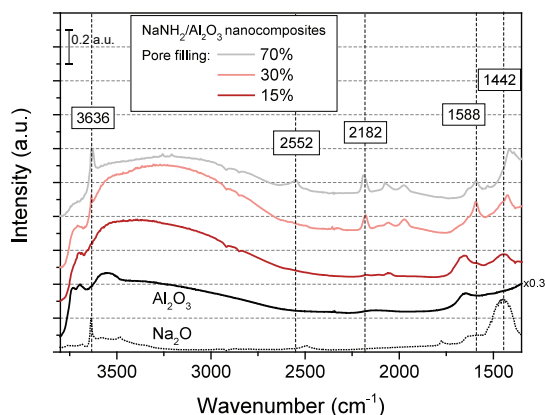


Figure 2.9 - DRIFTS spectra of $\text{NaNH}_2/\text{oxide}$ nanocomposites with pore filling fraction ranging from 15% to 70%. The spectrum of $\gamma\text{-Al}_2\text{O}_3$ and Na_2O are provided for comparison.

ppm and -20 ppm. In contrast, the spectrum of the $\text{NaNH}_2/\text{Al}_2\text{O}_3$ nanocomposite with a pore filling fraction of 15% only displays two signals at 14 ppm and -10 ppm. Evidently, two different Na species seem to have formed on the surface of the $\gamma\text{-Al}_2\text{O}_3$ scaffold. From these measurements it is not immediately clear to which Na-species these signals correlate. Possible compounds include Na_2O (-10 ppm)⁴², NaN_3 (-11 ppm)⁴², NaH (18 ppm)⁴³, NaNO_3 (-8.5 ppm)⁴⁴ and Na^+ ions coordinated to octahedral Al^{3+} (-8 and -14 ppm)^{45,46}. However, further investigation is required to confirm the assignment of both peaks.

In the DRIFTS spectra (**Figure 2.9**) of the $\text{NaNH}_2/\text{Al}_2\text{O}_3$ nanocomposites five peaks are observed, at 3636 cm^{-1} , 2552 cm^{-1} , 2182 cm^{-1} , 1588 cm^{-1} and 1424 cm^{-1} , that are not observed for pristine NaNH_2 , heat-treated NaNH_2 , or the $\text{NaNH}_2/\text{Al}_2\text{O}_3$ nanocomposites with a pore filling fraction of 130% (**Figure 2.1b**). Interestingly, the DRIFTS spectrum of pristine Na_2O displays a sharp peak at exactly 3636 cm^{-1} as well, coupled with a broad peak around 1450 cm^{-1} . In line with the ^{23}Na NMR results, this indicates that Na_2O might have formed at the $\text{NaNH}_2/\text{Al}_2\text{O}_3$ interface. While the assignment of the peaks at 2552 cm^{-1} , 2182 cm^{-1} and 1588 cm^{-1} to specific compounds is less evident, in most cases they point towards the formation of N-O species. For example, the peak at 2180 cm^{-1} is often assigned to N-O vibrations in NO^+ . Likewise, the peak at 1588 cm^{-1} could be ascribed to N-O vibrations related to NO_2^- and NO_3^- .^{47,48} Thus, both ssNMR and DRIFTS analysis demonstrate that NaNH_2 interacts with the surface groups of $\gamma\text{-Al}_2\text{O}_3$, akin to $\text{NaBH}_4/\text{Al}_2\text{O}_3$, thereby possibly forming Na_2O and N-O-containing interfacial compounds.

The $\text{NaNH}_2/\text{Al}_2\text{O}_3$ nanocomposite is less conductive than the nanocomposite based on SiO_2 . Consequently, it is interesting to see whether in $\text{NaNH}_2/\text{SiO}_2$ different and possibly more conductive interfacial compounds have formed. In **Figure 2.10**, the DRIFTS spectra and ^{23}Na NMR spectra of $\text{NaNH}_2/\text{SiO}_2$ nanocomposites with a pore filling fraction of 100%, 30% and 15% are shown. First of all, in the DRIFTS spectra of the $\text{NaNH}_2/\text{SiO}_2$ nanocomposites (**Figure 2.10a**) five new peaks are observed at 3636 cm^{-1} , 3506 cm^{-1} , 3438 cm^{-1} , 2182 cm^{-1} and 1424 cm^{-1} . Interestingly, none of them correspond to pristine NaNH_2 , heat-treated NaNH_2 or the $\text{NaNH}_2/\text{SiO}_2$ nanocomposite with a pore filling fraction of 130% (**Figure 2.1b**). Three of these peaks (3636 cm^{-1} , 2182 cm^{-1} and 1418 cm^{-1}) were also

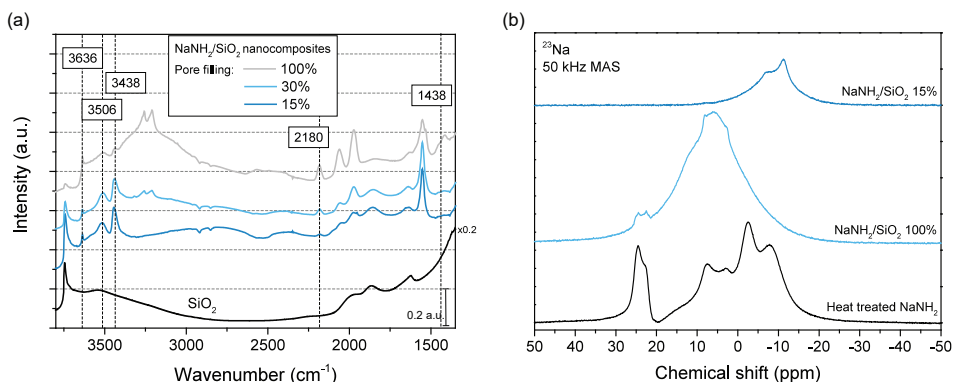


Figure 2.10 - (a) DRIFTS spectra of NaNH₂/SiO₂ nanocomposites with pore filling ranging from 15% to 100%. (b) ²³Na ssNMR spectra of heat treated NaNH₂ and NaNH₂/SiO₂ nanocomposites with 15% and 100% pore filling.

observed in the NaNH₂/Al₂O₃ nanocomposites with low pore filling fraction (**Figure 2.9**) and can correspondingly be assigned to the presence of Na₂O and possibly NO-containing compounds.

In contrast, the two remaining peaks at 3506 cm⁻¹ and 3438 cm⁻¹ are only seen in the NaNH₂/SiO₂ nanocomposites. Generally, peaks in the region between 3600 cm⁻¹ and 3300 cm⁻¹ can be assigned to O-H^{48–50} and N-H vibrations^{18,19,51}. Here, these peaks might be present, because the vibrational energy of the surface hydroxyl groups or the N-H groups in [NH₂]⁻ has changed due to interaction between the oxide surface and the metal hydride. Different from the NaNH₂/Al₂O₃ nanocomposite, it seems that the [NH₂]⁻ anions interact weakly with the SiO₂ surface and consequently the anions stay intact, and it is less likely that NO-containing compounds form at the interface. This is in line with the different activation energies found for ion conduction in the NaNH₂/oxide nanocomposites (**Table 2.4**), which indicates that the ion conduction mechanism differs between the nanocomposites, suggesting the formation of different interfacial compounds.

These results are further corroborated by the ²³Na NMR measurements shown in **Figure 2.10b**. Similar to the results on NaNH₂/Al₂O₃, the ²³Na NMR spectra of NaNH₂/SiO₂ with a pore filling fraction of 100% and 15% are distinctly different. While the former exhibits a broad quadrupolar feature with several peaks between 30 ppm and -10 ppm, the latter contains only two signals at -7.5 ppm and -11 ppm. The signal at -11 ppm could be related to the presence of Na₂O, akin to the signal at -10 ppm found for NaNH₂/Al₂O₃. The signal at -7.5 ppm has not been observed for NaNH₂/Al₂O₃ and could therefore be attributed to the unidentified interface compound revealed by DRIFTS. The chemical shift of this signal is comparable to that of published values for Na⁺ ions in silica matrixes, such as Na₂Si₂O₅ and NaAlSi₃O₈.^{52–54} It is important to realize that the interface compounds are typically defected and non-stoichiometric, which means that the local ²³Na environment will vary, resulting in a different chemical shift. As a result, it is not possible to determine the exact structure of the hydride/oxide interface. Nevertheless, this analysis shows that in the NaNH₂/SiO₂ and NaNH₂/Al₂O₃ nanocomposites different interfacial compounds have formed. Additionally, similarities and differences with the NaBH₄-based counterparts are identified. In the next section, the similarities and differences between both metal

hydrides will be compared and the implications they have on the ionic conductivities of the corresponding nanocomposites will be discussed.

2.3.4 Interplay between metal hydride reactivity and oxide surface chemistry

With the DRIFTS and ssNMR results discussed in the previous section, it was possible to show that a tertiary phase is formed at the metal hydride-metal oxide interface in the studied nanocomposites, i.e., $\text{NaBH}_4/\text{Al}_2\text{O}_3$, $\text{NaNH}_2/\text{Al}_2\text{O}_3$ and $\text{NaNH}_2/\text{SiO}_2$. In both Al_2O_3 -containing nanocomposites, penta-coordinated Al-surface species become saturated upon incorporation of the metal hydride. When NaBH_4 is incorporated, $\text{Na}_2\text{B}_{12}\text{H}_{12}$ and B-O bonds are formed at the metal hydride-oxide interface. Likewise, upon infiltration of NaNH_2 in the $\gamma\text{-Al}_2\text{O}_3$ pores, an interfacial layer containing Na_2O and N-O-species seems to form. The saturation of Al-surface species combined with the formation of B-O and N-O bonds demonstrates that there is a strong interaction between both metal hydrides and the $\gamma\text{-Al}_2\text{O}_3$ surface. In contrast, it seems that in the $\text{NaNH}_2/\text{SiO}_2$ nanocomposites the interaction between the silica surface and the metal hydride is weak, since in this case the $[\text{NH}_2]^-$ anions at the interface remain (partially) intact.

The differences in the interface composition can be ascribed to the different chemical nature and surface chemistry of the oxide scaffolds. As explained in section 2.3.1, the surface energy for SiO_2 differs significantly from $\gamma\text{-Al}_2\text{O}_3$. Additionally, both the amount and nature of surface hydroxyl groups differ greatly between SiO_2 and $\gamma\text{-Al}_2\text{O}_3$. A high density of surface hydroxyl groups is observed for $\gamma\text{-Al}_2\text{O}_3$, which contains about 10 hydroxyl groups per nm^2 , while SiO_2 only contains 4 to 5.5 groups per nm^2 .⁵⁵ Moreover, in contrast to the weakly (Brønsted) acidic hydroxyl groups present on the SiO_2 surface, $\gamma\text{-Al}_2\text{O}_3$ contains strong surface groups with both (Lewis) acidic and basic character. With this in mind, it is evident that the $\gamma\text{-Al}_2\text{O}_3$ scaffold interacts more strongly with the metal hydrides than SiO_2 . However, this does not explain why a stronger interface interaction leads to higher conductivity for $\text{NaBH}_4/\text{Al}_2\text{O}_3$, but a lower conductivity for $\text{NaNH}_2/\text{Al}_2\text{O}_3$.

Previous studies on LiBH_4 - and $\text{LiBH}_4\text{-LiNH}_2$ /oxide nanocomposites have shown that a higher number of surface groups or stronger surface groups lead to a higher conductivity.^{15,17,32} This also seems to apply to NaBH_4 /oxide nanocomposites. For NaBH_4 , a strong interaction with the oxide, and therefore improved wettability, is both beneficial for the complete incorporation in the pores of the scaffold as well as for the formation of a conductive interface consisting of NaBH_4 , $\text{Na}_2\text{B}_{12}\text{H}_{12}$ and B-O bonds between the metal hydride and the oxide surface. This is in line with results on LiBH_4 /oxide nanocomposites reported by Choi *et al.*, where a more conductive interface layer is formed in $\text{LiBH}_4/\text{Al}_2\text{O}_3$ compared to $\text{LiBH}_4/\text{SiO}_2$.³²

For NaNH_2 a strong interaction seems to be disadvantageous for the formation of a conductive NaNH_2 /oxide nanocomposite. In this case, a strong interaction is not needed to incorporate NaNH_2 in the scaffold pores, since it easily wets both the SiO_2 and $\gamma\text{-Al}_2\text{O}_3$ surface and is thereby readily incorporated in both scaffolds. Furthermore, the formation of N-O species resulting from a strong interaction between NaNH_2 and the $\gamma\text{-Al}_2\text{O}_3$ surface does not seem to result in a conductive interface layer. Instead, the weaker interaction with the silica surface in which the amide anion remains partially intact yields a higher nanocomposite conductivity, likely resulting in a more conductive metal hydride-oxide interface layer with a lower activation energy for long-range ionic transport.

The differences in conductivity of these metal hydride-based nanocomposites can be explained by their stability/reactivity. Based on their melting points and decomposition temperature, it is clear that NaNH_2 is a less stable and more reactive compound than NaBH_4 and LiBH_4 .^{56,57} It, therefore, interacts more strongly with the mesoporous oxide scaffolds. Consequently, NaNH_2 /oxide nanocomposites do not benefit much from a strong interface reaction, while it is a requirement for NaBH_4 /oxide nanocomposites. On the other hand, LiBH_4 has an intermediate stability compared to NaNH_2 and NaBH_4 , so upon nanocomposite formation with $\gamma\text{-Al}_2\text{O}_3$ and SiO_2 a conducting interface layer forms in both cases resulting in comparable conductivities.^{29,32} These results highlight that, since the conductivity enhancement in these nanocomposites originates from the formation of a tertiary phase at the hydride-oxide interface, both the surface chemistry of the mesoporous oxide and the reactivity of the metal hydride should be considered. While the pore structure of the scaffold can affect the conductivity of nanocomposites, for the present case the chemical nature of the oxides seems to play a more important role in determining the ionic conductivity.

2.4 Conclusions

In this work, the effect of nanocomposite formation with oxide scaffolds on the ionic conductivity of sodium-based complex hydrides has been investigated. By optimizing the interface interactions between the metal hydrides (NaNH_2 and NaBH_4) and the metal oxides (SiO_2 and $\gamma\text{-Al}_2\text{O}_3$), the conductivity at 80 °C was increased by three orders of magnitude to $4.66 \cdot 10^{-5} \text{ S cm}^{-1}$ and $2.12 \cdot 10^{-5} \text{ S cm}^{-1}$, respectively for $\text{NaBH}_4/\text{Al}_2\text{O}_3$ and $\text{NaNH}_2/\text{SiO}_2$. This study reveals that the enhancement in nanocomposite conductivity does not originate from the formation of a space charge layer as is often proposed for composite electrolytes. Instead, the conductivity improvement is the result of the formation of a tertiary phase at the metal hydride-oxide interface, which strongly depends on the metal hydride and the mesoporous oxide scaffold that are used.

A detailed investigation of the interactions between the metal hydrides and oxide scaffolds has shown that both the surface chemistry of the oxide scaffolds and reactivity of the complex hydrides are critical for the ionic conductivity of sodium-based nanocomposite electrolytes. For example, in the case of NaBH_4 high conductivity is only obtained if an oxide with a high surface energy or strong surface groups is used. On the other hand, for NaNH_2 , which is more reactive, a strong interface interaction can be detrimental for the nanocomposite conductivity.

Overall, this study demonstrates that while nanocomposite formation is an easy and versatile approach to enhance the ionic conductivity of complex hydrides, both the chemical nature of the metal hydride as well as the metal oxide are crucial for the conductivity enhancement. Optimizing the interaction at the complex hydride/oxide interface is imperative for the design of novel highly conductive solid-state ion conductors.

2.5 References

1. Slater, M. D., Kim, D., Lee, E. & Johnson, C. S. Sodium-ion batteries. *Adv. Funct. Mater.* **23**, 947–958 (2013).
2. Pan, H., Hu, Y. S. & Chen, L. Room-temperature stationary sodium-ion batteries for large-scale electric energy storage. *Energy Environ. Sci.* **6**, 2338–2360 (2013).
3. Vaalma, C., Buchholz, D., Weil, M. & Passerini, S. A cost and resource analysis of sodium-ion batteries. *Nat. Rev. Mater.* **3**, (2018).
4. Janek, J. & Zeier, W. G. A solid future for battery development. *Nat. Energy* **1**, 1–4 (2016).
5. Lu, X., Xia, G., Lemmon, J. P. & Yang, Z. Advanced materials for sodium-beta alumina batteries: Status, challenges and perspectives. *J. Power Sources* **195**, 2431–2442 (2010).
6. Luo, X., Rawal, A. & Aguey-Zinsou, K. F. Investigating the factors affecting the ionic conduction in nanoconfined NaBH_4 . *Inorganics* **9**, 1–10 (2021).
7. Dou, Y., Hansen, H. A., Xu, S. M. & Blanchard, D. Layered double hydroxides as advanced tracks to promote ionic conductivity in metal borohydride. *Mater. Chem. Front.* **5**, 4989–4996 (2021).
8. Andersson, M. S. *et al.* Promoting Persistent Superionic Conductivity in Sodium Monocarba-closo-dodecaborate $\text{NaCB}_{11}\text{H}_{12}$ via Confinement within Nanoporous Silica. *J. Phys. Chem. C* **125**, 16689–16699 (2021).
9. Cheng, C. F., Park, D. H. & Klinowski, J. Optimal parameters for the synthesis of the mesoporous molecular sieve [Sij]-MCM-41. *J. Chem. Soc. - Faraday Trans.* **93**, 193–197 (1997).
10. Brunauer, S., Emmett, P. H. & Teller, E. Adsorption of Gases in Multimolecular Layers. *J. Am. Chem. Soc.* **60**, 309–319 (1938).
11. Barrett, E. P., Joyner, L. G. & Halenda, P. P. The Determination of Pore Volume and Area Distributions in Porous Substances. I. Computations from Nitrogen Isotherms. *J. Am. Chem. Soc.* **73**, 373–380 (1951).
12. Filinchuk, Y. & Hagemann, H. Structure and properties of $\text{NaBH}_4 \cdot 2\text{H}_2\text{O}$ and NaBH_4 . *Eur. J. Inorg. Chem.* **112**, 3127–3133 (2008).
13. Harvey, K. B. & McQuaker, N. R. Infrared and Raman Spectra of Potassium and Sodium Borohydride. *Can. J. Chem.* **49**, 3272–3281 (1971).
14. Zhang, Y. & Tian, Q. The reactions in LiBH_4 - NaNH_2 hydrogen storage system. *Int. J. Hydrogen Energy* **36**, 9733–9742 (2011).
15. Ngene, P. *et al.* The influence of silica surface groups on the Li-ion conductivity of $\text{LiBH}_4/\text{SiO}_2$ nanocomposites. *Phys. Chem. Chem. Phys.* **21**, 22456–22466 (2019).
16. Hadjiivanov, K. Identification and Characterization of Surface Hydroxyl Groups by Infrared Spectroscopy. *Advances in Catalysis* vol. 57 (Elsevier Inc., 2014).
17. De Kort, L. M., Harmel, J., De Jongh, P. E. & Ngene, P. The effect of nanoscaffold porosity and surface chemistry on the Li-ion conductivity of LiBH_4 - LiNH_2 /metal oxide nanocomposites. *J. Mater. Chem. A* **8**, 20687–20697 (2020).
18. Bohger, J. P. O., Eßmann, R. R. & Jacobs, H. Infrared and Raman studies on the internal modes of lithium amide. *J. Mol. Struct.* **348**, 325–328 (1995).
19. Nibler, J. W. & Pimentel, G. C. Infrared spectrum and vibrational potential function of amide ion. *Spectrochim. Acta* **21**, 887–882 (1965).
20. Abrahams, S. C. & Kalnajs, J. The lattice constants of the alkali borohydrides and the low-temperature phase of sodium borohydride. *J. Chem. Phys.* **22**, 434–436 (1954).
21. Olsen, J. E., Karen, P., Sørby, M. H. & Hauback, B. C. Effect of chloride substitution on the order-disorder transition in NaBH_4 and $\text{Na}_{11}\text{BD}_4$. *J. Alloys Compd.* **587**, 374–379 (2014).
22. De Jongh, P. E. & Eggenhuisen, T. M. Melt infiltration: An emerging technique for the preparation of novel functional nanostructured materials. *Adv. Mater.* **25**, 6672–6690 (2013).
23. Brunauer, S., Kanro, D. L. & Weise, C. H. the Surface Energies of Amorphous Silica. *Can. J.*

- Chem.* **31**, 1483–1496 (1956).
24. Guzmán-Castillo, M. L. *et al.* The surface energy of quasi-amorphous γ alumina calculated from the temperature of the $\gamma \rightarrow \alpha$ transition. *J. Non. Cryst. Solids* **329**, 53–56 (2003).
 25. Suwarno *et al.* Confinement Effects for Lithium Borohydride: Comparing Silica and Carbon Scaffolds. *J. Phys. Chem. C* **121**, 4197–4205 (2017).
 26. Ngene, P., Adelhelm, P., Beale, A. M., De Jong, K. P. & De Jongh, P. E. LiBH₄/SBA-15 nanocomposites prepared by melt infiltration under hydrogen pressure: Synthesis and hydrogen sorption properties. *J. Phys. Chem. C* **114**, 6163–6168 (2010).
 27. Blanchard, D. *et al.* Nanoconfined LiBH₄ as a fast lithium ion conductor. *Adv. Funct. Mater.* **25**, 184–192 (2015).
 28. Tilley, R. J. D. *Defects in Solids*. (John Wiley & Sons, Inc., 2008). doi:10.1002/9780470380758.
 29. Gulino, V., Barberis, L., Ngene, P., Baricco, M. & De Jongh, P. E. Enhancing Li-Ion Conductivity in LiBH₄-Based Solid Electrolytes by Adding Various Nanosized Oxides. *ACS Appl. Energy Mater.* **3**, 4941–4948 (2020).
 30. Lambregts, S. F. H. *et al.* Phase Behavior and Ion Dynamics of Nanoconfined LiBH₄ in Silica. *J. Phys. Chem. C* **123**, 25559–25569 (2019).
 31. Blanchard, D. *et al.* Nanoconfined LiBH₄ as a fast lithium ion conductor. *Adv. Funct. Mater.* **25**, 184–192 (2015).
 32. Choi, Y. S. *et al.* Enhanced Li Ion Conductivity in LiBH₄-Al₂O₃ Mixture via Interface Engineering. *J. Phys. Chem. C* **121**, 26209–26215 (2017).
 33. Jensen, S. R. H. *et al.* Hydrogenation properties of lithium and sodium hydride-closoborate, [B₁₀H₁₀]²⁻ and [B₁₂H₁₂]²⁻, composites. *Phys. Chem. Chem. Phys.* **20**, 16266–16275 (2018).
 34. Ngene, P., Van Den Berg, R., Verkuijlen, M. H. W., De Jong, K. P. & De Jongh, P. E. Reversibility of the hydrogen desorption from NaBH₄ by confinement in nanoporous carbon. *Energy Environ. Sci.* **4**, 4108–4115 (2011).
 35. Gautam, C., Yadav, A. K. & Singh, A. K. A Review on Infrared Spectroscopy of Borate Glasses with Effects of Different Additives. *ISRN Ceram.* **2012**, 1–17 (2012).
 36. Łodziana, Z., Błoński, P., Yan, Y., Rentsch, D. & Remhof, A. NMR Chemical Shifts of ¹¹B in Metal Borohydrides from First-Principle Calculations. *J. Phys. Chem. C* **118**, 6594–6603 (2014).
 37. Hwang, S. J. *et al.* NMR confirmation for formation of [B₁₂H₁₂]²⁻ complexes during hydrogen desorption from metal borohydrides. *J. Phys. Chem. C* **112**, 3164–3169 (2008).
 38. Züchner, L., Chan, J. C. C., Müller-Warmuth, W. & Eckert, H. Short-range order and site connectivities in sodium aluminoborate glasses: I. Quantification of local environments by high-resolution ¹¹B, ²³Na, and ²⁷Al solid-state NMR. *J. Phys. Chem. B* **102**, 4495–4506 (1998).
 39. Zettl, R. *et al.* Li-Ion Diffusion in Nanoconfined LiBH₄-LiI/Al₂O₃: From 2D Bulk Transport to 3D Long-Range Interfacial Dynamics. *ACS Appl. Mater. Interfaces* **12**, 38570–38583 (2020).
 40. Choi, M., Matsunaga, K., Oba, F. & Tanaka, I. Al NMR chemical shifts in oxide crystals: a first-principles study. *J. Phys. Chem. C* **113**, 3869–3873 (2009).
 41. Breuer, S., Pregartner, V., Lunghammer, S. & Wilkening, H. M. R. Dispersed Solid Conductors: Fast Interfacial Li-Ion Dynamics in Nanostructured LiF and LiF γ -Al₂O₃ Composites. *J. Phys. Chem. C* **123**, 5222–5230 (2019).
 42. Bota, R. M., Houthoofd, K., Grobet, P. J., Jacobs, P. A. & Leuven, K. U. Superbase catalysts from thermally decomposed sodium azide supported on mesoporous γ -alumina. *Catal. Today* **152**, 99–103 (2010).
 43. Shimoda, K., Zhang, Y., Ichikawa, T., Miyaoka, H. & Kojima, Y. Solid state NMR study on the thermal decomposition pathway of sodium amidoborane NaNH₂BH₃. *J. Mater. Chem.* **21**, 2609–2615 (2011).
 44. Shen, J., Tu, M., Hu, C. & Chen, Y. Formation of surface basicity through the decomposition of alkali metal nitrates on γ -Al₂O₃. *Langmuir* **14**, 2756–2759 (1998).

45. Deng, F., Du, Y., Ye, C. & Kong, Y. Adsorption of Na⁺ onto γ -alumina studied by solid-state ²³Na and ²⁷Al nuclear magnetic resonance spectroscopy. *Solid State Nucl. Magn. Reson.* **2**, 317–324 (1993).
46. Xin, S. *et al.* Heteronuclear correlation experiments of ²³Na–²⁷Al in rotating solids. *Solid State Nucl. Magn. Reson.* **84**, 103–110 (2017).
47. Hadjiivanov, K. I. Identification of neutral and charged N_xO_y surface species by IR spectroscopy. *Catal. Rev. - Sci. Eng.* **42**, 71–144 (2000).
48. Hadjiivanov, K., Bushev, V., Kantcheva, M. & Kissurski, D. Infrared Spectroscopy Study of the Species Arising during NO₂ Adsorption on TiO₂ (Anatase). *Langmuir* **10**, 464–471 (1994).
49. Boukaoud, A., Chiba, Y. & Sebbar, D. A periodic DFT study of IR spectra of amino acids: An approach toward a better understanding of the N-H and O-H stretching regions. *Vib. Spectrosc.* **116**, 103280 (2021).
50. Piumetti, M., Armandi, M., Garrone, E. & Bonelli, B. An IR spectroscopy assessment of the surface acidity of mesoporous VO_x-SiO₂ catalysts. *Microporous Mesoporous Mater.* **164**, 111–119 (2012).
51. Teunissen, E. H., Van Santen, R. A., Jansen, A. P. J. & Van Duijneveldt, F. B. Ammonium in zeolites: coordination and solvation effects. *J. Phys. Chem.* **97**, 203–210 (1993).
52. Jones, A. R., Winter, R., Greaves, G. N. & Smith, I. H. ²³Na, ²⁹Si, and ¹³C MAS NMR Investigation of Glass-Forming Reactions between Na₂CO₃ and SiO₂. *J. Phys. Chem. B* **109**, 23154–23161 (2005).
53. Xue, X. & Stebbins, J. ²³Na NMR chemical shifts and local Na coordination environments in silicate crystals, melts and glasses. *Phys. Chem. Miner.* **20**, 297–307 (1993).
54. Koller, H., Engelhardt, G., Kentgens, A. P. M. & Sauer, J. ²³Na NMR spectroscopy of solids: Interpretation of quadrupole interaction parameters and chemical shifts. *J. Phys. Chem.* **98**, 1544–1551 (1994).
55. Chorkendorff, I. & Niemantsverdriet, J. W. *Concepts of Modern Catalysis and Kinetics*. (John Wiley & Sons, 2003). doi:10.1002/3527602658.ch5.
56. Lin, H. J. *et al.* Understanding the Decomposition Mechanisms of LiNH₂, Mg(NH₂)₂, and NaNH₂: A Joint Experimental and Theoretical Study. *J. Phys. Chem. C* **123**, 18180–18186 (2019).
57. Martelli, P. *et al.* Stability and decomposition of NaBH₄. *J. Phys. Chem. C* **114**, 7173–7177 (2010).



3

Preparation of ion-substituted metal hydride/oxide nanocomposites

Besides nanocomposite formation, partial ionic substitution is one of the main strategies used to enhance the room temperature conductivity of metal hydrides. In this chapter, we discuss the properties of ion-substituted metal hydride/oxide nanocomposites, in which both strategies are combined to further optimize the ionic conductivity. The nanocomposites are prepared by infiltrating LiI-substituted LiBH_4 and LiNH_2 -substituted LiBH_4 in mesoporous oxides (SiO_2 and $\gamma\text{-Al}_2\text{O}_3$) via melt infiltration and solution impregnation. In line with the results on pristine metal hydrides, this leads to an enhancement of the room temperature conductivity to $1.3 \cdot 10^{-4} \text{ S cm}^{-1}$ and $0.8 \cdot 10^{-4} \text{ S cm}^{-1}$ for $\text{LiBH}_4\text{-LiI/SiO}_2$ and $\text{LiBH}_4\text{-LiNH}_2\text{/SiO}_2$, respectively. This is a significant improvement compared to ion-substituted LiBH_4 prior to nanocomposite formation as well as pristine LiBH_4 /oxide nanocomposites prepared without ion substitution. This work demonstrates that it is beneficial to combine nanocomposite formation with partial ionic substitution. Clearly, nanocomposite formation can be used for both pristine as well as ion-substituted ion conductors, showing that it is a widely applicable approach

This chapter is based on: de Kort, L. M., Zettl, R., Gombotz, M., Wilkening, H. M. R., De Jongh, P. E., & Ngene, P. (2020). Combined effects of anion substitution and nanoconfinement on the ionic conductivity of Li-based complex hydrides. *The Journal of Physical Chemistry C*, 124(5), 2806-2816.

3.1 Introduction

In the previous chapters, it was shown that nanocomposite formation can significantly improve the room temperature ionic conductivity of pristine metal hydrides, e.g., LiBH_4 , NaBH_4 , NaNH_2 . For these metal hydride/oxide nanocomposites, it has been shown that the high ionic conductivity originates from an interface layer of about 1 – 2 nm between the metal hydride and the metal oxide with very high ion mobility at room temperature.^{1–3} On the other hand, a percolating network of fast Li^+ diffusion pathways is needed for facile Li-ion transport over long distances. Therefore, the overall long-range ionic conductivity of the nanocomposite might be further improved if the highly conductive interface regions are connected via fast Li^+ diffusion pathways in an ion conductor that is more conductive than a single-phase metal hydride.

Such highly conductive metal hydrides can be obtained by partial ionic substitution, one of the main strategies used to enhance metal hydride conductivity besides nanocomposite formation. In this approach, the complex anion (e.g., BH_4^-) is partially substituted with other anions, such as I^- or NH_2^- . As a result, either a homogenous solid solution is formed, in which the conductive polymorph is stabilized at lower temperatures, or a double-anion compound forms with a different structure. For example, ionic substitution of BH_4^- in pristine LiBH_4 with I^- or Br^- leads to stabilization of the hexagonal LiBH_4 polymorph, while the introduction of NH_2^- leads to the formation of $\text{Li}_2(\text{BH}_4)(\text{NH}_2)$, a conductive phase with a relatively low melting point.^{4,5} Both LiI - and LiNH_2 -substituted LiBH_4 have room temperature conductivities that are much higher than that of pristine LiBH_4 . Therefore, the combination of partial ion substitution and nanocomposite formation, forming ion-substituted metal hydride/oxide nanocomposites, could lead to a well-connected network of fast Li^+ diffusion pathways, and consequently, improved long-range ionic transport.

To study whether this is indeed the case, LiI - and LiNH_2 -substituted LiBH_4 /oxide nanocomposites were prepared. In these nanocomposites, the combined effects of partial anion substitution with I^- or NH_2^- , and nanocomposite formation with metal oxides (SiO_2 and $\gamma\text{-Al}_2\text{O}_3$) were investigated. In both cases, the combined approach leads to higher room temperature Li-ion conductivities compared to LiBH_4 /oxide nanocomposites and the macrocrystalline ion-substituted LiBH_4 systems ($\text{LiBH}_4\text{-LiI}$ and $\text{LiBH}_4\text{-LiNH}_2$). Using detailed structural characterization and ^7Li NMR line shape measurements, the ionic transport mechanism in $\text{LiBH}_4\text{-LiI/Al}_2\text{O}_3$ was unraveled. Indeed, the long-range ionic transport benefits from the formation of both a highly conductive interface layer between the metal hydride and oxide as well as the presence of conductive ion-substituted LiBH_4 located further away from the oxide surface.

3.2 Experimental methods

Scaffold synthesis

MCM-41 was synthesized using the procedure described by Cheng *et al.*⁶ In short, hexadecyltrimethyl-ammonium bromide (Sigma Aldrich, $\geq 96.0\%$) and tetramethylammonium hydroxide solution (Sigma Aldrich, 25 wt% in H_2O) were mixed with deionized water. After adding the silica source (Aerosil 380), the white suspension was stirred for 2 h at 30°C and kept at this temperature for another 24 h unstirred in a closed polypropylene bottle. The composition of the mixture was $1.00 \text{ SiO}_2 : 0.19 (\text{TMA})\text{OH} : 0.27 (\text{CTA})\text{Br} : 40 \text{ H}_2\text{O}$. The product was heated to 140°C in stainless steel autoclaves and kept there for 48 h. After cooling to room temperature, the mixture was thoroughly washed, filtered, and dried at 120°C for approximately 12 h. After drying at 100°C for 1 hour, the sample was calcined at 550°C for 12 hours.

SBA-15 was prepared following the procedure developed by Zhao *et al.*⁷ Poly(ethyleneglycol)-block-poly(propyleneglycol)-block-poly(ethyleneglycol) (Sigma Aldrich, PEG-PPG-PEG, Pluronic, P-123), hydrochloric acid fuming 37 % (Merck, for analysis) and deionized water were stirred at 35°C . Tetraethyl orthosilicate (Sigma Aldrich, $\geq 99.0\%$ GC, TEOS) was added dropwise to the solution and the solution was then stirred for 24 h at 40°C resulting in a composition of $0.015 \text{ P123} : 5.2 \text{ HCl} : 129 \text{ H}_2\text{O} : 1 \text{ TEOS}$. This mixture was kept at 100°C in a closed 1 L polypropylene bottle for 48 h, followed by extensive washing and filtration. Subsequently the product was pre-dried (60°C , 24 h, air), dried (120°C , 8 h, air) and calcined ($1.2^\circ\text{C min}^{-1}$, 550°C , 6 h, air).

Nanocomposite synthesis

Alumina ($\gamma\text{-Al}_2\text{O}_3$) was purchased from Sasol (product brand Puralox SCCa-5/200), while lithium amide (95 % pure), lithium iodide (98 % pure) and lithium borohydride (95 % pure) were purchased from Sigma Aldrich. The metal oxide scaffolds (MCM-41, SBA-15 and $\gamma\text{-Al}_2\text{O}_3$) were first dried under vacuum at 220°C overnight and subsequently stored in an Ar purified glovebox (MBraunLabmaster, H_2O and $\text{O}_2 < 1 \text{ ppm}$). All further sample handling and transfer was carried out in the glovebox to avoid contamination with air or traces of moisture.

The $\text{LiBH}_4\text{-LiI/oxide}$ nanocomposites were prepared using two different methods. An overview of the composition of the investigated nanocomposites is provided in **Table 3.1**. In the first method, LiBH_4 and LiI were physically mixed in molar ratios of 10, 20, 30 and 40 mol% LiI with respect to LiBH_4 . Subsequently, the materials were mixed with the desired amount of the oxide and placed in a quartz reactor which was then inserted inside a stainless-steel high-pressure autoclave (Parr). The amounts were calculated to fill the oxide pores by 130 %, meaning that all scaffold pores are filled and voids between oxide particles and grains are also filled. Melt infiltration was carried out at 50 bar H_2 pressure and a temperature of 295°C for 30 min; the heating rate was approximately 3°C min^{-1} .¹ During this process, LiI- LiBH_4 forms a solid solution $((1-x)\text{LiBH}_4\text{-}x\text{LiI})$ with $x = 0.1, 0.2, 0.3, 0.4$ which melts and infiltrates the pores of the oxide. Upon cooling, the molten solid solution solidifies in the pores of the mesoporous oxide and the excess amount remains at the external surface of the oxide.

Table 3.1 – Composition of investigated nanocomposites

Nanocomposite	LiBH ₄ content (wt%)	Lil/LiNH ₂ content (wt%)	Oxide content (wt%)
LiBH ₄ -20%Lil	39.4	60.6	-
LiBH ₄ -Lil/Al ₂ O ₃	17.8	27.4	54.8
LiBH ₄ -Lil/SBA-15	25.3	38.8	35.9
LiBH ₄ -Lil/MCM-41	25.8	39.6	34.6
LiBH ₄ -Lil/MCM-41 (impregnation)	25.8	39.6	34.6
LiBH ₄ -50%LiNH ₂	48.8	51.2	-
LiBH ₄ -75%LiNH ₂	26.6	27.9	45.5

In the second approach, the samples were prepared by combining solution impregnation and melt infiltration. A solution of Lil and water was prepared, which was added dropwise to the metal oxide scaffold contained in a round bottom flask using a syringe and a septum. To avoid air/moisture contamination, this procedure was performed on a Schlenk line. The impregnated oxide was kept at room temperature for 3 hours, after which the solvent was removed. Subsequently, the mixture was dried at 250 °C overnight under a dynamic vacuum. To reach the desired amount of Lil in the pores, the procedure was repeated twice. The Lil/metal oxide nanocomposite was mixed with LiBH₄ to reach a molar ratio Lil:LiBH₄ of 20 : 80 and a volume of LiBH₄-Lil corresponding to 130 % of the total pore volume of the scaffold. The mixture was then inserted into a sample holder placed inside a stainless-steel high-pressure autoclave, pressurized to 50 bar H₂ and heated at 3 °C min⁻¹ to 295 °C. The dwell time was 30 min. The molten LiBH₄ infiltrates the oxide pores and react with the infiltrated Lil to form LiBH₄-Lil.

Reference samples of LiBH₄-Lil solid solutions and LiBH₄/oxide nanocomposites were prepared under the same autoclave conditions as outlined above. Solid solutions were synthesized by heating mixtures of LiBH₄ and Lil without adding the metal oxide scaffold; LiBH₄/oxide nanocomposites were obtained without adding Lil to the mixture. A third reference sample was bulk LiBH₄, which was grinded and melted under the same autoclave conditions, and recrystallized.

LiBH₄-LiNH₂/oxide nanocomposites were prepared using a two-step preparation method. Firstly, LiBH₄ and LiNH₂ were physically mixed in a 1 : 1 molar ratio of LiNH₂ to LiBH₄. Afterwards the physical mixture was placed in a stainless-steel reactor which was then inserted into a stainless-steel high-pressure autoclave. The solid-state reaction was carried out at 50 bar H₂ pressure and at 150 °C (heating rate 2.5 °C min⁻¹) for 30 minutes to form a double-anion compound with the composition 0.5LiBH₄-0.5LiNH₂. Subsequently, the sample was mixed with the desired amount of oxide to fill the pores by 130 %. Melt infiltration was carried out at 50 bar H₂ pressure at 120 °C (2.5 °C min⁻¹) for 30 min. Upon cooling, the molten phase recrystallized in the pores of the scaffold material to form LiBH₄-LiNH₂.

General characterization

X-ray diffraction (XRD) was performed with a Bruker-AXS D-8 Advance X-ray diffractometer with CoK $\alpha_{1,2}$ radiation (λ = 1.79026 Å). The samples were placed in an airtight sample

holder and diffractograms were recorded at room temperature from 10 ° to 100 ° 2 θ for alumina-based samples and of 20 to 80 ° 2 θ for the silica containing samples as well as the crystalline samples. Rietveld refinement was carried out using the software X'PertHighScore Plus. A Le-Bail fit was applied to analyze the pattern; literature patterns of hexagonal LiBH₄ taken from the Inorganic Crystal Structure Database served as reference. To refine the patterns, the lattice parameters of hexagonal LiBH₄ were used as starting values ($a = 4.28$ Å, $b = 4.28$ Å, $c = 6.98$ Å).

Diffuse reflectance infrared Fourier transform spectra (DRIFTS) were obtained by a Perkin-Elmer 2000 spectrometer and a MCT detector. 16 scans were accumulated with a resolution of 4 cm⁻¹ in the range of 500 to 4500 cm⁻¹. An airtight sample holder (KBr background) guaranteed no air contamination during the measurements. Data acquisition was realized by recording absorbance versus wavenumber. For the LiBH₄-LiI/(oxide) samples, the absorbance was firstly measured in K-M units, introduced by Kubelka and Munk, which includes a scattering component. To clearly distinguish the peaks between 4000 and 3000 cm⁻¹, the measured K-M units shown in this work are converted to the absorbance intensity.

To probe the porosity of the mesoporous oxides and nanocomposites, nitrogen physisorption measurements were performed on a Micromeritics Tristar 3000. Using the Brunauer, Emmett and Teller (BET) and Barrett, Joyner and Halenda (BJH) adsorption model theories, surface area and pore size distribution were obtained.^{8,9} The specific surface area (A_{BET}), total pore volume and average pore size of the scaffolds as determined from the adsorbed quantity close to nitrogen saturation pressure ($p = p_0$) are summarized in **Table 3.2**.

Table 3.2 – Nitrogen physisorption results of oxide scaffolds

Oxide scaffold	BET area (m ² g ⁻¹)	Pore volume (cm ³ g ⁻¹)	Average Pore diameter (nm)
γ -Al ₂ O ₃	186	0.49	8.7
MCM-41 (SiO ₂)	1071	1.11	2.7
SBA-15 (SiO ₂)	800	1.05	5.8

Conductivity measurement

Alternating current (AC) impedance spectroscopy measurements were performed using a Princeton Applied Research Parstat 2273. Lithium foil (Sigma Aldrich, 99.9 %, 0.38 mm) was placed on top of two 13 mm stainless steel dies. The electrolyte (100 to 300 mg) was pressed between the dies with a pressure of 150 MPa, resulting in a final electrolyte thickness of 1 to 2 mm. The pressed pellet was placed in a custom-made cell housed in a Büchi B-585 glass oven that was placed in an Ar-filled glove box. The impedance measurements were performed during multiple heating-cooling cycles from room temperature to either 50 °C or 130 °C (depending on the sample). The impedance scans were acquired every 5 °C or 10 °C, after the measurement cell was allowed to equilibrate at the desired temperature. At each increment, an EIS measurement was acquired with an AC signal of 20 mV over a frequency range from 1 MHz to 1 Hz.

Matlab and ZView software were used to fit the raw data by using Nyquist plots. A constant phase element (CPE) and a resistor connected in parallel were used as

appropriate equivalent circuit to parametrize the data. Capacitances, C , were calculated according to $C = R^{(1-n)/n} \cdot Q^{1/n}$. R is the resistance in Ω , i.e., it denotes the real part of the complex impedance; Q has the numerical value of the admittance at $\omega = 1 \text{ rad s}^{-1}$. n is a dimensionless variable characterizing the deviation of the CPE from the behavior of an ideal RC unit, which would yield $n = 1$.

NMR line shape measurement

To underpin the findings of the conductivity measurements, ^7Li (spin-3/2) nuclear magnetic resonance (NMR) line shape measurements were performed at a magnetic field of 7 T, corresponding to a Larmor frequency of 116 MHz, by employing a Bruker Advance III solid-state spectrometer. A standard broadband probe was used to acquire variable-temperature NMR spectra with a one pulse sequence under static, i.e., non-rotating conditions. The $\pi/2$ pulse length slightly depended on temperature and ranged from 2.1 to 2.3 μs . Such short pulse lengths ensured non-selective excitation of the whole spectra. Up to 16 scans were accumulated to form an average free induction decay, which, after Fourier transformation, yield the ^7Li NMR spectra. The temperature in the sample chamber was monitored by a Eurotherm controller. Temperature adjustment was achieved, with an accuracy of $\pm 2 \text{ K}$, with a heater that was constantly flushed with a stream of dry nitrogen gas.

3.3 Results and discussion

3.3.1 Structural characterization of $\text{Li}(\text{BH}_4)_{1-x}\text{I}_x$ and $\text{Li}(\text{BH}_4)_{1-x}\text{I}_x/\text{oxide}$ nanocomposites

The structural properties of the $\text{LiBH}_4\text{-LiI}$ solid solutions ($\text{Li}(\text{BH}_4)_{1-x}\text{I}_x$) containing 10 to 40 mol% LiI ($x = 0.1, 0.2, 0.3$ and 0.4) and the $\text{LiBH}_4\text{-LiI}$ nanocomposites based on $\gamma\text{-Al}_2\text{O}_3$, SBA-15 and MCM-41 will be evaluated. The compositions of the samples in wt% and structural details of the oxides are given in **Table 3.1**. In **Figure 3.1a** the X-ray diffraction patterns of the $\text{LiBH}_4\text{-LiI}$ solid solutions are shown. For comparison, the XRD pattern of LiI, orthorhombic LiBH_4 and hexagonal LiBH_4 are included. The XRD patterns of the $\text{LiBH}_4\text{-LiI}$ solid solutions clearly differ from those of LiI and orthorhombic LiBH_4 . Their diffraction patterns resemble the pattern of hexagonal LiBH_4 . The characteristic $h\text{-LiBH}_4$ reflections in the range from 27° to 32° 2θ are shifted towards lower 2θ values by approximately 1° 2θ . Thus, in line with previous reports on LiX -substituted LiBH_4 (with $X = \text{I}, \text{Cl},$ or Br)¹⁰, the diffraction patterns reveal that I^- is successfully incorporated in the LiBH_4 lattice, which causes a lattice expansion due to the larger size of I^- ($r_{\text{I}^-} = 2.20 \text{ \AA}$) compared to BH_4^- ($r_{\text{BH}_4^-} = 2.03 \text{ \AA}$).¹¹ Rietveld refinement of the diffraction data of the $\text{LiBH}_4\text{-20\% LiI}$ solid solution yielded a hcp unit cell with the following lattice parameters $a = 4.44 \text{ \AA}$, $b = 4.44 \text{ \AA}$, and $c = 7.19 \text{ \AA}$. Simultaneously with the lattice expansion, the density increased from 0.67 g/cm^3 for bulk LiBH_4 to 1.20 g/cm^3 for $\text{LiBH}_4\text{-20\% LiI}$. For samples with more than 20 mol% LiI, reflections of pure LiI are present in the diffraction pattern, indicating that the solubility limit for the $\text{LiBH}_4\text{-LiI}$ system is reached.

In **Figure 3.1b** the X-ray diffraction patterns of the $\text{LiBH}_4\text{-20\% LiI/oxide}$ nanocomposites prepared using co-melt infiltration of LiI and LiBH_4 as well as impregnation of LiI followed by LiBH_4 melt infiltration (impregnation approach) are shown. To compare, the diffraction pattern of $\text{LiBH}_4\text{-20\% LiI}$ is provided as well. The diffraction peaks of $\text{LiBH}_4\text{-LiI/MCM-41}$, $\text{LiBH}_4\text{-LiI/SBA-15}$ and $\text{LiBH}_4\text{-LiI/Al}_2\text{O}_3$ have broadened and decreased in intensity compared to the $\text{LiBH}_4\text{-LiI}$ solid solution. Peak broadening can be caused by size effects and lattice strain, while the decrease in intensity suggests a decrease in the long-range order. Both changes indicate infiltration of the $\text{LiBH}_4\text{-LiI}$ solid solution in the pores of the oxide scaffolds. Note that the composites shown here contain 30 vol% more $\text{LiBH}_4\text{-LiI}$

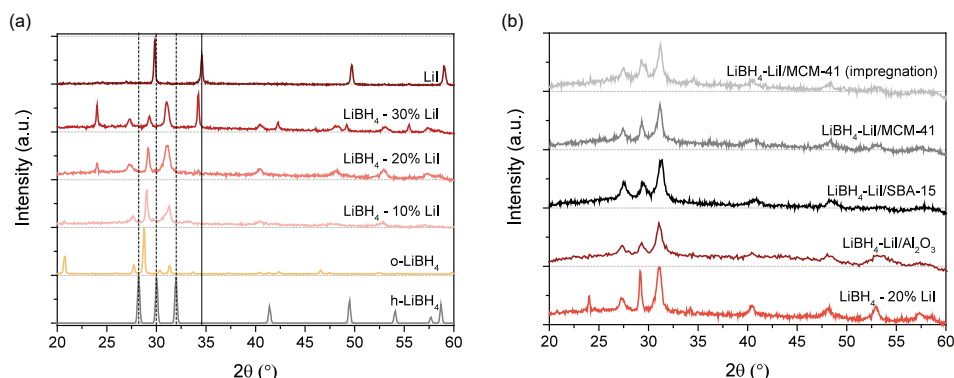


Figure 3.1 - XRD diffraction patterns of (a) $\text{LiBH}_4\text{-LiI}$ solid solutions with varying composition and (b) $\text{LiBH}_4\text{-LiI/oxide}$ nanocomposites based on different oxides. The patterns of LiI, $o\text{-LiBH}_4$, $h\text{-LiBH}_4$ are shown for comparison and characteristic reflections of LiI and $h\text{-LiBH}_4$ are indicated with straight and dashed lines, respectively.

than is required to fill all the pores of the scaffold. This is essential for interconnectivity between the LiBH_4 particles. For nanocomposites with a LiBH_4 -LiI volume smaller than 100 % of the total pore volume of the scaffold, no crystalline phase was observed.

Further evidence for successful incorporation of the solid solution into the oxide pores is provided by nitrogen physisorption measurements. The measurements showed that only a negligible amount of nitrogen was adsorbed by the nanocomposites. Hence, the pores of the oxide scaffolds seem to be filled with LiBH_4 -LiI solid solution, further corroborating that LiI-substituted LiBH_4 /oxide nanocomposites have been prepared. The similarity in the diffraction patterns of the LiBH_4 -LiI/MCM-41 nanocomposites prepared using the co-melt infiltration and the impregnation approach suggests that both methods can be used for the preparation of LiBH_4 -LiI/metal oxide nanocomposites. Finally, the use of different oxide scaffolds did not lead to major differences in the XRD patterns of the nanocomposites.

The chemical changes in the different samples were investigated with DRIFTS. In **Figure 3.2a** the spectrum of the LiBH_4 -LiI/ Al_2O_3 nanocomposite is compared to spectra of pristine LiBH_4 , LiBH_4 - 20% LiI and pristine $\gamma\text{-Al}_2\text{O}_3$. Pristine LiBH_4 shows characteristic bands (indicated with dashed lines) that correspond to $[\text{BH}_4]^-$ bending vibrations and $[\text{BH}_4]^-$ stretching vibrations between 1000 and 1500 cm^{-1} and between 2000 and 2800 cm^{-1} , respectively.^{12,13} The vibrations between 3200 and 3700 cm^{-1} are ascribed to $[\text{OH}]$ stretching vibrations from adsorbed moisture.¹⁴ The spectrum of the LiBH_4 -LiI solution mostly resembles that of LiBH_4 . The band characterizing the stretching vibration at 2379 cm^{-1} is slightly shifted toward a lower wavenumber. This shift might result from an increased unit cell by addition of I⁻, as previously observed for halide-substituted BH_4 .¹⁵ Also, a stronger electronic interaction between iodine and Li, because of the higher electronegativity of the halides compared to BH_4^- , can lead to such a change in vibrational energies.¹⁶

The spectrum of LiBH_4 -LiI/ Al_2O_3 has changed slightly compared to LiBH_4 -LiI. The characteristic $[\text{BH}_4]^-$ bands have broadened upon introduction of $\gamma\text{-Al}_2\text{O}_3$. A similar broadening effect is also observed for LiBH_4 / Al_2O_3 compared to pristine LiBH_4 . This generally suggests that the rotational freedom of the $[\text{BH}_4]^-$ anions in the nanocomposites has increased compared to the bulk compound due to structural changes induced by nanocomposite formation. This observation is in line with previous studies on LiBH_4 /

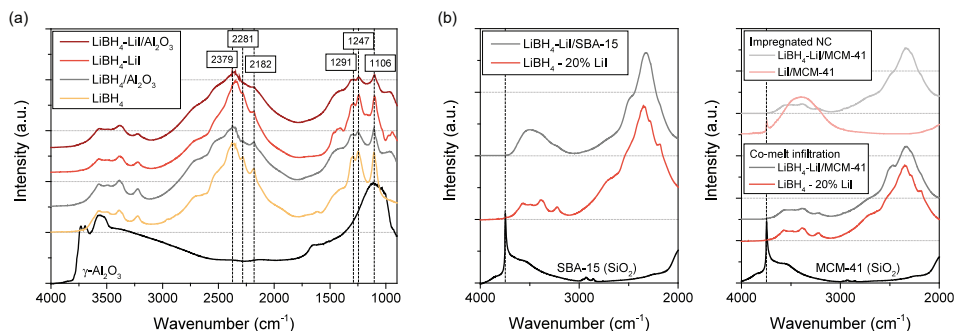


Figure 3.2 - DRIFTS spectra of (a) LiBH_4 -LiI/ Al_2O_3 nanocomposites and (b) LiBH_4 -LiI/ SiO_2 nanocomposites. The spectra of the oxides, pristine LiBH_4 and LiBH_4 / Al_2O_3 are provided for comparison. The characteristic vibrations of LiBH_4 and the characteristic silanol vibrations are shown with dashed lines.

oxide nanocomposites.^{17–20} Furthermore, the bands in the region from 3400 to 3800 cm^{-1} that correspond to hydroxyl surface groups of $\gamma\text{-Al}_2\text{O}_3$ ²¹ are not observed in the $\text{LiBH}_4\text{-LiI}/\text{Al}_2\text{O}_3$ nanocomposite. The same behavior is found for the characteristic vibrations of the silanol groups²² of both silica scaffolds (MCM-41 and SBA-15) in the $\text{LiBH}_4\text{-LiI}/\text{SBA-15}$ nanocomposite and in the $\text{LiBH}_4\text{-LiI}/\text{MCM-41}$ nanocomposites prepared via co-melt infiltration and via the impregnation approach (**Figure 3.2b**). The absence of the hydroxyl vibrations in metal hydride/oxide nanocomposites is typically attributed to interactions or reaction between the hydroxyl group and the infiltrated compound, which suppresses or eliminates the hydroxyl vibration. Hence, the DRIFTS spectra demonstrate that the infiltrated $\text{LiBH}_4\text{-LiI}$ interacts with the surface of the oxide scaffold.

It is important to realize that the interaction of LiBH_4 with the oxide surface is considered the origin of the high ionic conductivity of $\text{LiBH}_4/\text{oxide}$ nanocomposites. In the same way, a conductive interface layer could also have formed in the studied $\text{LiBH}_4\text{-LiI}/\text{oxide}$ nanocomposites, which might lead to an improved conductivity. Note that the vibration corresponding to the surface silanol groups is still present in the $\text{LiI}/\text{MCM-41}$ nanocomposite, in which LiI was impregnated in the scaffold, but LiBH_4 was not yet incorporated. This shows that after incorporation of LiI , but prior to LiBH_4 infiltration, there are still sufficient silanol groups available for LiBH_4 to interact with. Thus, it is not likely that the the formation of a $\text{LiBH}_4\text{-LiI}$ solid solution in the scaffold pores and its interaction with the oxide, is hindered by the presence of LiI .

3.3.2 Conductivity in $\text{Li}(\text{BH}_4)_{1-x}\text{I}_x$ and $\text{Li}(\text{BH}_4)_{1-x}\text{I}_x/\text{oxide}$ nanocomposites

The effects of different LiI concentrations on the conductivity of $\text{LiBH}_4\text{-LiI}$ solid solutions and the corresponding $\text{LiBH}_4\text{-LiI}/\text{MCM-41}$ nanocomposites were evaluated by recording complex impedance at different temperatures. The conductivities obtained at 25 °C are shown in **Figure 3.3a**. The conductivities of the solid solutions and nanocomposites discussed in this section were determined from Nyquist plots displaying single semicircles that could be fitted with an equivalent circuit consisting of a resistance and a constant phase element (CPE), similar to the Nyquist plots shown in **Figure 3.3b** for $\text{LiBH}_4 - 20\%$ LiI , $\text{LiBH}_4/\text{Al}_2\text{O}_3$ and $\text{LiBH}_4\text{-LiI}/\text{Al}_2\text{O}_3$. In **Figure 3.3a**, it is observed that the ionic conductivity of the pure solid solutions and the nanocomposites increased with an increasing amount of LiI from 0% to 20% LiI . At LiI contents higher than 20 mol%, the conductivity starts to decrease. This can be explained by the presence of crystalline (unreacted) LiI as observed by XRD (**Figure 3.1a**). Since the highest conductivity is observed for the $\text{LiBH}_4 - 20\%$ LiI solid solution, this sample was chosen for a more detailed study on the effect of nanocomposite formation on the ionic conductivity.

In **Figure 3.3b** the Nyquist plots recorded for $\text{LiBH}_4 - 20\%$ LiI , $\text{LiBH}_4/\text{Al}_2\text{O}_3$ and $\text{LiBH}_4\text{-LiI}/\text{Al}_2\text{O}_3$ at 25 °C are shown, as well as the fits obtained from equivalent circuit fitting. The capacitances C of these samples ranged from 147 to 210 pF. Values larger than 100 pF typically indicate electrical relaxation processes influenced by interfacial regions.²³ For nanocomposites, it is widely believed that ion transport mainly occurs along the heterogeneous solid-solid interphase between the insulating oxide and the

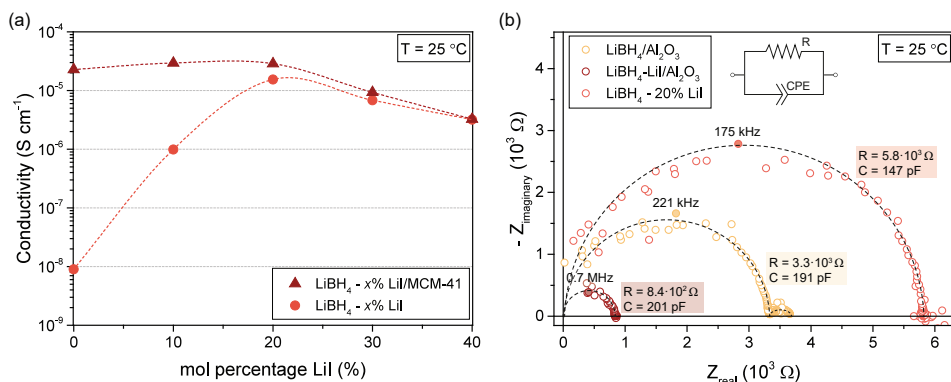


Figure 3.3 - (a) Conductivity of LiBH₄-LiI solid solutions (triangles) and the corresponding LiBH₄-LiI/MCM-41 nanocomposites (circles) as a function of LiI content (%). Dashed lines are added to guide the eye. (b) Nyquist plots of LiBH₄-LiI/Al₂O₃, LiBH₄/Al₂O₃ and LiBH₄ - 20% LiI. Resistances, capacitances, and characteristic frequencies are obtained from fitting the equivalent circuit. The second (high frequency) semicircle observed for LiBH₄/Al₂O₃ is not fitted and the dashed line is added only as guide to the eye. The data in (a) and (b) is obtained at room temperature after the second temperature-dependent cooling cycle.

ion conducting solid.²⁴⁻²⁶ The exponents n of the CPEs were close to 1 in all studied samples, meaning that the CPEs behaved almost like an ideal RC unit. This observation is in line with the interpretation that the semicircle seen in the complex plane plot is governed by a response strongly influenced by grain boundary effects.

For LiBH₄/Al₂O₃, two semicircles are observed after two heating cycles. The main semicircle with the higher electrical relaxation rate is attributed to LiBH₄ that interacts with the oxide surface. The second semicircle at lower frequencies was not present initially and formed during two heating cycles. The presence of the second semi-circle suggests that a second conducting phase is formed, which might be due to a reaction of the nanocomposite with the lithium electrodes, or a small resistance that occurred in the measurement set-up. The different conducting phases present in the samples will be evaluated in more detail later using ⁷Li NMR spectroscopy.

The temperature dependence of the conductivity of LiBH₄-LiI/Al₂O₃ and LiBH₄-LiI/SiO₂ (SBA-15) nanocomposites is displayed in **Figure 3.4** using Arrhenius plots. For comparison, the conductivity data referring to LiBH₄-LiI and LiBH₄/oxide nanocomposites are also shown. In **Table 3.3** the conductivity values and the activation energies (E_A) obtained by a linear fit of the Arrhenius plot ($\ln(\sigma T)$ versus $10^{-3} T^{-1}$) are summarized. The conductivity plots show that ionic transport at temperatures lower than 100 °C is faster in the LiBH₄-LiI/Al₂O₃ and LiBH₄-LiI/SiO₂ nanocomposites compared to LiBH₄- 20% LiI, and the LiBH₄/Al₂O₃ and LiBH₄/SiO₂ nanocomposites. For instance, at 25 °C the ionic conductivity of LiBH₄-LiI/Al₂O₃ ($1.3 \cdot 10^{-4}$ S cm⁻¹) was four times higher than that of LiBH₄/Al₂O₃ ($3.0 \cdot 10^{-5}$ S cm⁻¹) and eight times higher than that of LiBH₄-LiI ($1.5 \cdot 10^{-5}$ S cm⁻¹). In agreement with the trend in ionic conductivity, the activation energy for long-range ion transport decreased from 0.59 eV for LiBH₄-LiI and 0.52 eV for LiBH₄/oxide to 0.44 eV for LiBH₄-LiI/oxide. The same trends are observed for the nanocomposites based on SBA-15 (SiO₂).

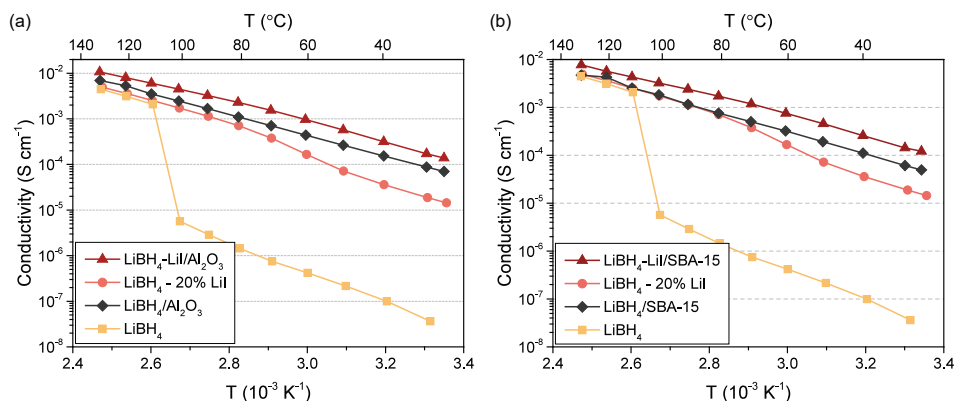


Figure 3.4 - Arrhenius plots of Li-ion conductivity versus reciprocal temperature of (a) LiBH₄-LiI/Al₂O₃ nanocomposites and (b) LiBH₄-LiI/SBA-15 nanocomposites. with 130% of the scaffold pores filled as well as pristine LiBH₄, LiBH₄ - 20% LiI and LiBH₄/oxide. The second temperature-dependent cooling cycle is shown.

Table 3.3 – Room temperature conductivities of LiBH₄-LiI/oxide nanocomposites and their activation energies (E_A) and pre-exponential factors $\ln(\sigma_0)$ obtained from a linear plot of $\ln(\sigma T)$ and $10^{-3} T^{-1}$ of complex impedance data. The standard deviation is based on the 95% confidence interval of the linear fit. Unless stated otherwise, the data is obtained from the second cooling cycle between 130 °C and 25 °C.

Metal hydride/(oxide)	$\sigma_{25^\circ\text{C}}$ ($10^{-4} \text{ S cm}^{-1}$)	$\ln \sigma_0$	E_A (eV)
LiBH ₄ -20%LiI	0.15	18 (± 2)	0.59 (± 0.05)
LiBH ₄ -LiI/Al ₂ O ₃	1.27	14.1 (± 0.9)	0.44 (± 0.02)
LiBH ₄ /Al ₂ O ₃	0.30	15.7 (± 0.3)	0.52 (± 0.01)
LiBH ₄ -LiI/SBA-15	1.28	13.5 (± 0.8)	0.43 (± 0.02)
LiBH ₄ /SBA-15	0.66	15.0 (± 0.3)	0.49 (± 0.01)
LiBH ₄ -LiI/MCM-41*	0.38	13.4 (± 0.5)	0.46 (± 0.01)
LiBH ₄ -LiI/MCM-41 (impregnation)	0.26	13.2 (± 0.4)	0.46 (± 0.01)

* E_A and $\ln(\sigma_0)$ are obtained from a linear fit between 100 °C and 25 °C.

The differences in conductivity of the nanocomposites prepared with different oxides (SBA-15, MCM-41 or γ -Al₂O₃) are most likely due to differences in the chemical nature (e.g., density and nature of surface groups) or physical properties (e.g., morphology, pore structure) of these materials. For instance, a comparison between the ionic conductivities of LiBH₄-LiI/SBA-15 and LiBH₄-LiI/MCM-41 ($1.3 \cdot 10^{-4} \text{ S cm}^{-1}$ versus $0.4 \cdot 10^{-4} \text{ S cm}^{-1}$) demonstrates that the physical properties of the oxide scaffold can play an important role, since these two silica materials mostly differ in their porosity and morphology.

Similarly, the importance of the surface chemistry of the scaffold is highlighted by the higher conductivity obtained for LiBH₄-LiI/Al₂O₃, despite the lower pore volume and smaller pore size compared to SBA-15 (**Table 3.2**). Mesoporous γ -Al₂O₃ has a higher density of surface groups, which are generally stronger acid and basic sites compared to the silanol groups present in SBA-15.^{21,27,28} This might be beneficial for the formation of a conductive interface layer between the metal hydride and the metal oxide. Elucidating

in detail the exact influence of these properties on ionic conductivity is, however, beyond the scope of the present work. Another interesting observation from **Table 3.3** is that the conductivities and activation energies of the $\text{LiBH}_4\text{-LiI/MCM-41}$ nanocomposites prepared via co-melt infiltration and via the impregnation approach are similar. Hence, both methods can be used to prepare metal hydride/oxide nanocomposites, though the exact synthesis conditions can influence the obtained conductivity.

3.3.3 Ionic transport mechanism in $\text{LiBH}_4\text{-LiI/Al}_2\text{O}_3$

To gain more insight on the conduction enhancement mechanism, the ion transport mechanism of the $\gamma\text{-Al}_2\text{O}_3$ -based nanocomposites was studied in more detail using ^7Li NMR. The NMR line shape spectra of these samples recorded at room temperature (22 °C), 30 °C and 90 °C are shown in **Figure 3.5**. The line spectra reveal that Li^+ acts as mobile charge carrier.²⁹ For the $\text{LiBH}_4\text{-20% LiI}$ solid solution (**Figure 3.5a**) the line at room temperature is composed of two contributions, a broad feature and a narrow line. The narrow line on top of the broader signal reflects the mobile Li spins whose jump rates exceed the line widths of this line in the rigid lattice. Deconvolution of the line spectrum shows that the fraction of these mobile Li ions is approximately 13%. Narrow NMR lines are caused by sufficiently fast Li^+ exchange processes able to average local dipole-dipole interactions that lead to line broadening at low temperatures.

In the case of $\text{LiBH}_4\text{-LiI}$, the line shape did not change much when going from room temperature to 30 °C. However, a significant change is seen at 90 °C, where a fully narrowed central line appeared that is on top of a quadrupole powder pattern. At elevated temperatures, quadrupole intensities become visible as a sharp powder pattern as dipole-dipole interactions are effectively averaged out due to rapid Li^+ exchange. This distinct

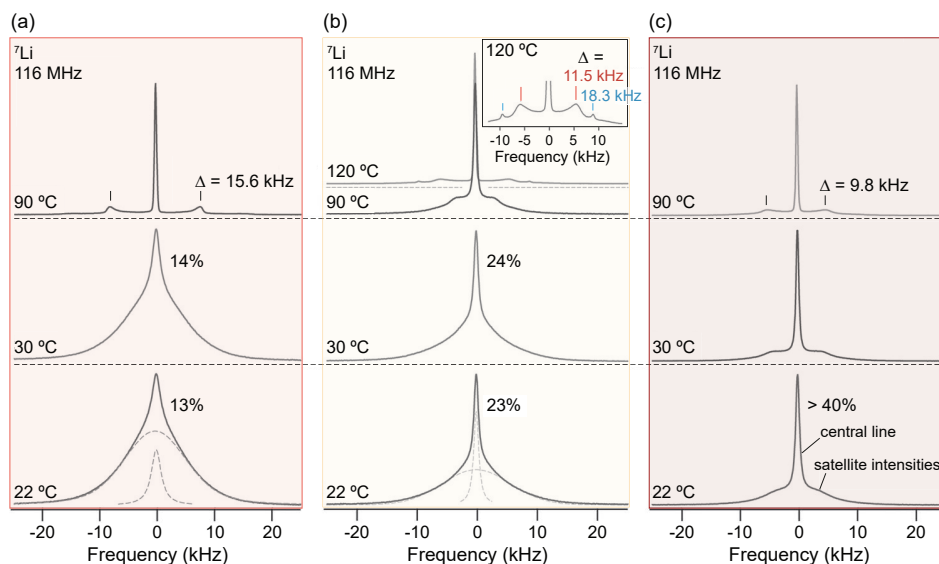


Figure 3.5 - ^7Li NMR line spectra of (a) $\text{LiBH}_4\text{-LiI}$, (b) $\text{LiBH}_4/\text{Al}_2\text{O}_3$ and (c) $\text{LiBH}_4\text{-LiI/Al}_2\text{O}_3$. The spectra were recorded at a Larmor frequency of 116 MHz and at the indicated temperatures. The dashed lines show the deconvolution of the line spectra with appropriate Gaussian and Lorentzian functions to estimate the fraction of mobile Li ions in these compounds.

pattern, showing sharp 90° singularities separated by $\Delta = 15.6$ kHz, is characteristic for hexagonal LiBH_4 (-LiI). A similar situation is seen for the $\text{LiBH}_4/\text{Al}_2\text{O}_3$ nanocomposite (**Figure 3.5b**). However, in this case the number fraction of rapid Li^+ ions is higher at 22 °C and 30 °C (24 %) compared to that seen for LiBH_4 -LiI. This difference is in line with the slightly higher conductivity seen for $\text{LiBH}_4/\text{Al}_2\text{O}_3$.

It is worth noting, the motion narrowed spectra recorded at 90 °C and at 120 °C were governed by electric quadrupole intensities being different to that of macrocrystalline LiBH_4 and macrocrystalline LiBH_4 -LiI. The spectra of pristine LiBH_4 and pristine LiBH_4 -LiI reveal patterns produced by a symmetric electric field gradient (EFG) the ions were subjected to. They agree with those of similar systems studied earlier.³⁰ In contrast to the pristine samples, the NMR line of the $\text{LiBH}_4/\text{Al}_2\text{O}_3$ nanocomposite recorded at 90 °C shows a non-symmetric EFG. Its shape points to structural disorder and strain the Li spins sense. Δ reduces from 15.6 kHz to 11.5 kHz. Careful inspection of the powder pattern shows that another set of singularities is present (see inset of **Figure 3.5b**), which is characterized by $\Delta = 18.3$ kHz. Assuming axial symmetry for this pattern, a quadrupole coupling constant δ_q of ca. 36.6 kHz was obtained which was identical with that of bulk LiBH_4 ($\delta_q = 37$ kHz).³¹ The two quadrupole patterns represents the Li ions near the insulator surface ($\Delta = 11.5$ kHz) and the ions farther away, that is, located in the bulk regions ($\Delta = 18.3$ kHz). NMR revealed that these two species are exposed to different electric interactions.

For the line spectrum of the LiBH_4 -LiI/ Al_2O_3 nanocomposite obtained at 90 °C (**Figure 3.5c**) a quadrupole powder pattern was observed as well, which is characterized by a lower Δ (9.8 kHz) than expected for bulk LiBH_4 (-LiI). However, a pronounced pattern attributable to Li ions in bulk LiBH_4 -LiI, as seen for $\text{LiBH}_4/\text{Al}_2\text{O}_3$ was missing. Instead, already at temperatures as low as 30 °C, an almost fully narrowed ^7Li NMR line was observed which points to very fast ion dynamics in this nanocomposite.²⁹ We conclude that the majority of ions in this nanocomposite takes part in rapid Li^+ exchange, which perfectly agrees with the conductivity trend seen in **Figure 3.4a**. Interestingly, different from $\text{LiBH}_4/\text{Al}_2\text{O}_3$, a single EFG pattern is observed for LiBH_4 -LiI/ Al_2O_3 , which points to an ensemble of Li^+ ions experiencing the same electric field gradient. This behavior has been described in detail in two recent studies by Zettl *et al.*^{32,33} In these papers, it is explained that while the Li spins participate in heterogeneous ion dynamics, the ions near the oxide surface and those farther away belong to an electrically homogeneous ensemble.

It is important to realize that the samples discussed here were prepared under the same conditions. The remarkable increase in ionic conduction for LiBH_4 -LiI/ Al_2O_3 seen by impedance spectroscopy and ^7Li NMR can, therefore, not be attributed to variations in the sample preparation. Instead, it is most likely caused by combined effects of partial ionic substitution with LiI via stabilization of the conductive hexagonal phase and nanocomposite formation through the formation of a conductive interface layer between the metal hydride and the metal oxide.

3.3.4 Structure and conductivity of $\text{Li}(\text{BH}_4)_{1-x}(\text{NH}_2)_x$ and $\text{Li}(\text{BH}_4)_{1-x}(\text{NH}_2)_x/\text{oxide}$ nanocomposites

To demonstrate the general applicability of the conductivity enhancement strategy outlined above, this approach was extended to $\text{Li}(\text{BH}_4)_{1-x}(\text{NH}_2)_x/\text{oxide}$ nanocomposites (with $x = 0.5$). In **Figure 3.6a** the X-ray diffraction patterns of LiNH_2 -substituted LiBH_4

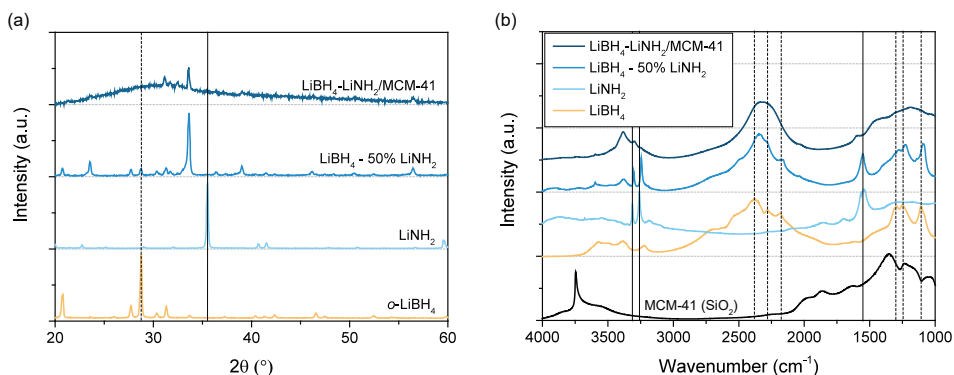


Figure 3.6 - (a) XRD diffraction patterns and (b) DRIFTS spectra of $\text{LiBH}_4\text{-LiNH}_2$ and the corresponding $\text{LiBH}_4\text{-LiNH}_2\text{/oxide}$ nanocomposite with 130% pore filling fraction. The diffraction patterns of pristine LiBH_4 and LiNH_2 are provided, as well as the DRIFTS spectra of LiBH_4 , LiNH_2 and MCM-41 (SiO_2). Relevant peaks are indicated with straight (LiNH_2) and dashed (LiBH_4) lines.

and the corresponding nanocomposite is shown. The diffraction patterns of LiNH_2 and LiBH_4 are included for comparison. The diffraction patterns reveal the formation of two new compounds viz. $\text{Li}_2(\text{BH}_4)(\text{NH}_2)$ and $\text{Li}_4(\text{BH}_4)(\text{NH}_2)_3$.^{4,34,35} In this case, new double-anion crystalline phases are formed, unlike the $\text{LiBH}_4\text{-LiX}$ systems where the high temperature phase of LiBH_4 was stabilized through the replacement of $[\text{BH}_4]^-$ by halides. On the other hand, upon nanocomposite formation the peaks of the $\text{LiBH}_4\text{-LiNH}_2\text{/MCM-41}$ diffraction pattern become less intense, similar to the $\text{LiBH}_4\text{-LiI/oxide}$ nanocomposites. Again, the loss in crystallinity corresponds to a reduction in long-range order. Thus, these results indicate that $\text{LiBH}_4\text{-LiNH}_2$ was successfully incorporated in the pores of the MCM-41 scaffold, as was previously observed for $\text{LiBH}_4\text{-LiI/oxide}$ nanocomposites.

The changes of $\text{LiBH}_4\text{-LiNH}_2$ upon nanocomposite formation with MCM-41 are studied in further detail with DRIFTS. The obtained DRIFTS spectra are shown in **Figure 3.6b**. Again the characteristic vibrations related to LiBH_4 (straight lines) and LiNH_2 ³⁶ (dashed lines) shifted toward lower wavenumbers and became significantly broader upon nanocomposite formation. In addition, the bands related to the surface silanol groups (3700 cm^{-1}) were absent. These changes demonstrate that upon infiltration of $\text{LiBH}_4\text{-LiNH}_2$ in the pores of the SiO_2 scaffold, the metal hydride interacts with the hydroxyl groups on the oxide surface and both the $[\text{BH}_4]^-$ and $[\text{NH}_2]^-$ anions experience more rotational freedom. Thus, similar to $\text{LiBH}_4\text{/oxide}$ and $\text{LiBH}_4\text{-LiI/oxide}$ nanocomposite, it was possible to prepare a $\text{LiBH}_4\text{-LiNH}_2\text{/SiO}_2$ nanocomposite leading to profound changes in the structure of $\text{LiBH}_4\text{-LiNH}_2$.

In **Figure 3.7** the conductivities of $\text{LiBH}_4\text{-LiNH}_2$ and $\text{LiBH}_4\text{-LiNH}_2\text{/MCM-41}$ are compared to the conductivities of pristine LiBH_4 and $\text{LiBH}_4\text{/MCM-41}$. The conductivity values at room temperature and the activation energies (E_a) obtained by a linear fit of the Arrhenius plot ($\ln(\sigma T)$ versus 10^{-3} T^{-1}) are summarized in **Table 3.4**. It can be observed that the addition of LiNH_2 to LiBH_4 increases the room temperature conductivity by approximately 2 orders of magnitude compared to LiBH_4 . This increase is ascribed to the formation of $\text{Li}_2(\text{BH}_4)(\text{NH}_2)$.^{5,37} The sudden increase in conductivity of $\text{Li}_2(\text{BH}_4)(\text{NH}_2)$ at approximately 40°C is caused by melting of the double-anion compound leading to a highly conductive molten phase at temperatures higher than 40°C .^{4,5} The $\text{LiBH}_4\text{-LiNH}_2\text{/}$

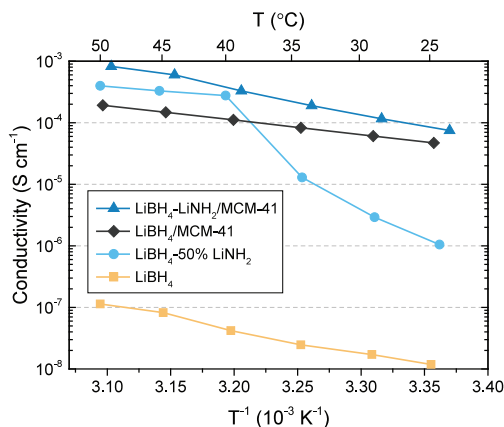


Figure 3.7 - Arrhenius plots of conductivity versus reciprocal temperature of $\text{LiBH}_4\text{-Li/MCM-41}$ nanocomposites with 130% of the scaffold pores filled as well as pristine LiBH_4 , $\text{LiBH}_4 - 50\% \text{LiNH}_2$ and $\text{LiBH}_4/\text{MCM-41}$. The first temperature-dependent heating cycle is shown.

MCM-41 nanocomposite exhibits an even higher conductivity at this temperature. Remarkably, this high conductivity was also preserved at ambient temperatures. The room temperature conductivity of $\text{LiBH}_4\text{-LiNH}_2/\text{MCM-41}$ improved 70-fold and 2-fold compared to $\text{LiBH}_4\text{-LiNH}_2$ and $\text{LiBH}_4/\text{MCM-41}$, respectively. Surprisingly, the activation energy for charge transport in $\text{LiBH}_4\text{-LiNH}_2/\text{MCM-41}$ (0.83 eV) is higher than those of $\text{LiBH}_4/\text{MCM-41}$ (0.49 eV) and the high temperature (molten) $\text{LiBH}_4\text{-LiNH}_2$ phase (0.3 eV). The higher conductivity is associated with a higher pre-exponential factor ($\ln \sigma_0 = 29$) observed for the $\text{LiBH}_4\text{-LiNH}_2/\text{oxide}$ nanocomposite, which corresponds to a higher concentration of mobile charge carriers, as will be explained in detail in **Chapter 4**. The remarkable increase in ionic conductivity is again attributed to the combined effect of anion substitution and nanocomposite formation. All in all, these results confirm that the combined approach is effective for both pristine as well as ion-substituted Li-ion conductors.

Table 3.4 – Room temperature conductivities of $\text{LiBH}_4\text{-LiNH}_2/\text{oxide}$ nanocomposites and their activation energies (E_A) and pre-exponential factors $\ln(\sigma_0)$ obtained from a linear plot of $\ln(\sigma T)$ and $10^{-3} T^{-1}$ of complex impedance data. The standard deviation is based on the 95% confidence interval of the linear fit. Unless stated otherwise, the data is obtained from the first temperature-dependent heating cycle between 25 °C and 50 °C.

Metal hydride/(oxide)	$\sigma_{25^\circ\text{C}}$ (S cm^{-1})	$\ln \sigma_0$	E_A (eV)
$\text{LiBH}_4\text{-50\%LiNH}_2^*$	$1.1 \cdot 10^{-6}$	$10 (\pm 8)$	$0.3 (\pm 0.2)$
$\text{LiBH}_4\text{-50\%LiNH}_2/\text{MCM-41}$	$7.5 \cdot 10^{-5}$	$29 (\pm 3)$	$0.83 (\pm 0.07)$
$\text{LiBH}_4/\text{MCM-41}$	$4.7 \cdot 10^{-5}$	$14.9 (\pm 0.2)$	$0.49 (\pm 0.01)$

* E_A and $\ln(\sigma_0)$ are obtained from a linear fit between 40 °C and 50 °C. Due to the limited temperature range and measurement points, the obtained activation energy is a rough estimation as evident from the large fitting error

3.4 Conclusions

Using complex hydrides as model systems, we developed an approach to prepare I⁻ and NH₂⁻-substituted LiBH₄/oxide nanocomposites based on SiO₂ and γ-Al₂O₃. In this way, two conductivity enhancement methods, i.e., partial ionic substitution and nanocomposite formation, are effectively combined to enhance the Li-ion conductivity of LiBH₄ at ambient conditions. The nanocomposites were prepared via co-melt infiltration of both substituent and LiBH₄ as well as via impregnation of the substituent followed by LiBH₄ melt infiltration.

The ionic conductivity of the LiBH₄-LiI/Al₂O₃ nanocomposite reached $1.3 \cdot 10^{-4}$ S cm⁻¹ at room temperature. The room temperature conductivities of pristine LiBH₄/Al₂O₃ and LiBH₄-LiI were one order of magnitude lower. In line with the trend in conductivity, the activation energies decrease from 0.52 eV and 0.59 eV for the LiBH₄/Al₂O₃ and LiBH₄-LiI, respectively, to 0.44 eV for LiBH₄-LiI/Al₂O₃. Detailed structural investigations and ⁷Li NMR line shape measurements show that the combined effects of interaction with the interface of the oxides and phase stabilization due to partial anion substitution (by the iodide anion), produces faster Li⁺ diffusion pathways in LiBH₄-LiI/oxide than in the case of LiBH₄/oxide and LiBH₄-LiI. Results on LiBH₄-LiNH₂/SiO₂ nanocomposites show that this concept is also applicable to other ion-substituted hydrides.

Although our study indicates that the increased conductivity in the ion-substituted metal hydride nanocomposites depends on the physical properties and chemical nature of the mesoporous oxides, the exact role of the mesoporous oxides remains unclear. Understanding the role of the oxide in the conductivity enhancement is essential to optimize the performance of metal hydride/oxide nanocomposites and will support the development of highly conductive nanocomposite-based electrolytes. Hence, this will be the topic of the next chapter.

3.5 References

1. Suwarno *et al.* Confinement Effects for Lithium Borohydride: Comparing Silica and Carbon Scaffolds. *J. Phys. Chem. C* **121**, 4197–4205 (2017).
2. Lefevr, J., Cervini, L., Griffin, J. M. & Blanchard, D. Lithium Conductivity and Ions Dynamics in $\text{LiBH}_4/\text{SiO}_2$ Solid Electrolytes Studied by Solid-State NMR and Quasi-Elastic Neutron Scattering and Applied in Lithium-Sulfur Batteries. *J. Phys. Chem. C* **122**, 15264–15275 (2018).
3. Gulino, V., Barberis, L., Ngene, P., Baricco, M. & De Jongh, P. E. Enhancing Li-Ion Conductivity in LiBH_4 -Based Solid Electrolytes by Adding Various Nanosized Oxides. *ACS Appl. Energy Mater.* **3**, 4941–4948 (2020).
4. Meisner, G. P., Scullin, M. L., Balogh, M. P., Pinkerton, F. E. & Meyer, M. S. Hydrogen release from mixtures of lithium borohydride and lithium amide: A phase diagram study. *J. Phys. Chem. B* **110**, 4186–4192 (2006).
5. Yan, Y. *et al.* A Lithium Amide-Borohydride Solid-State Electrolyte with Lithium-Ion Conductivities Comparable to Liquid Electrolytes. *Adv. Energy Mater.* **7**, 1–7 (2017).
6. Cheng, C. F., Park, D. H. & Klinowski, J. Optimal parameters for the synthesis of the mesoporous molecular sieve [Si]-MCM-41. *J. Chem. Soc. - Faraday Trans.* **93**, 193–197 (1997).
7. Zhao, D. *et al.* Triblock copolymer syntheses of mesoporous silica with periodic 50 to 300 angstrom pores. *Science (80-.)*. **279**, 548–552 (1998).
8. Brunauer, S., Emmett, P. H. & Teller, E. Adsorption of Gases in Multimolecular Layers. *J. Am. Chem. Soc.* **60**, 309–319 (1938).
9. Barrett, E. P., Joyner, L. G. & Halenda, P. P. The Determination of Pore Volume and Area Distributions in Porous Substances. I. Computations from Nitrogen Isotherms. *J. Am. Chem. Soc.* **73**, 373–380 (1951).
10. Matsuo, M. & Orimo, S. I. Lithium fast-ionic conduction in complex hydrides: Review and prospects. *Adv. Energy Mater.* **1**, 161–172 (2011).
11. Miyazaki, R. *et al.* Room temperature lithium fast-ion conduction and phase relationship of LiI stabilized LiBH_4 . *Solid State Ionics* **192**, 143–147 (2011).
12. Harvey, K. B. & McQuaker, N. R. Infrared and Raman Spectra of Potassium and Sodium Borohydride. *Can. J. Chem.* **49**, 3272–3281 (1971).
13. D'Anna, V., Spyratou, A., Sharma, M. & Hagemann, H. FT-IR spectra of inorganic borohydrides. *Spectrochim. Acta - Part A Mol. Biomol. Spectrosc.* **128**, 902–906 (2014).
14. Filinchuk, Y. & Hagemann, H. Structure and properties of $\text{NaBH}_4 \cdot 2\text{H}_2\text{O}$ and NaBH_4 . *Eur. J. Inorg. Chem.* **112**, 3127–3133 (2008).
15. D'Anna, V., Lawson Daku, L. M. & Hagemann, H. Quantitative Spectra-Structure Relations for Borohydrides. *J. Phys. Chem. C* **119**, 21868–21874 (2015).
16. Coates, J. Interpretation of Infrared Spectra, A Practical Approach. in *Encyclopedia of Analytical Chemistry* vol. 77 196–199 (John Wiley & Sons, Ltd, 2006).
17. Ngene, P. *et al.* The influence of silica surface groups on the Li-ion conductivity of $\text{LiBH}_4/\text{SiO}_2$ nanocomposites. *Phys. Chem. Chem. Phys.* **21**, 22456–22466 (2019).
18. Sun, T. *et al.* Confined LiBH_4 : Enabling fast hydrogen release at $\sim 100^\circ\text{C}$. *Int. J. Hydrogen Energy* **37**, 18920–18926 (2012).
19. Plerdsranoy, P. & Utke, R. Confined LiBH_4 - LiAlH_4 in nanopores of activated carbon nanofibers. *Int. J. Hydrogen Energy* **40**, 7083–7092 (2015).
20. Javadian, P., Sheppard, D. A., Buckley, C. E. & Jensen, T. R. Hydrogen storage properties of nanoconfined LiBH_4 - NaBH_4 . *Int. J. Hydrogen Energy* **40**, 14916–14924 (2015).
21. Liu, X. & Truitt, R. E. DRFT-IR studies of the surface of γ -Alumina. *J. Am. Chem. Soc.* **119**, 9856–9860 (1997).
22. Morrow, B. A. & McFarlan, A. J. Surface vibrational modes of silanol groups on silica. *J. Phys.*

- Chem.* **96**, 1395–1400 (1992).
23. Irvine, J. T. S., Sinclair, D. C. & West, A. R. Electroceramics: Characterization by Impedance Spectroscopy. *Adv. Mater.* **2**, 132–138 (1990).
 24. Epp, V. & Wilkening, M. Motion of Li^+ in nanoengineered LiBH_4 and $\text{LiBH}_4\text{:Al}_2\text{O}_3$ comparison with the microcrystalline form. *ChemPhysChem* **14**, 3706–3713 (2013).
 25. Choi, Y. S., Lee, Y. S., Oh, K. H. & Cho, Y. W. Interface-enhanced Li ion conduction in a $\text{LiBH}_4\text{-SiO}_2$ solid electrolyte. *Phys. Chem. Chem. Phys.* **18**, 22540–22547 (2016).
 26. Choi, Y. S. *et al.* Enhanced Li Ion Conductivity in $\text{LiBH}_4\text{-Al}_2\text{O}_3$ Mixture via Interface Engineering. *J. Phys. Chem. C* **121**, 26209–26215 (2017).
 27. Baca, M. *et al.* Characterization of mesoporous alumina prepared by surface aluminization of SBA-15. *Microporous Mesoporous Mater.* **110**, 232–241 (2008).
 28. Chorkendorff, I. & Niemantsverdriet, J. W. *Concepts of Modern Catalysis and Kinetics*. (John Wiley & Sons, 2003). doi:10.1002/3527602658.ch5.
 29. Verkuijlen, M. H. W. *et al.* Nanoconfined LiBH_4 and enhanced mobility of Li^+ and BH_4^- studied by solid-state NMR. *J. Phys. Chem. C* **116**, 22169–22178 (2012).
 30. Blanchard, D. *et al.* Nanoconfined LiBH_4 as a fast lithium ion conductor. *Adv. Funct. Mater.* **25**, 184–192 (2015).
 31. Epp, V. & Wilkening, M. Fast Li diffusion in crystalline LiBH_4 due to reduced dimensionality: Frequency-dependent NMR spectroscopy. *Phys. Rev. B - Condens. Matter Mater. Phys.* **82**, 4–7 (2010).
 32. Zettl, R. *et al.* Li-Ion Diffusion in Nanoconfined $\text{LiBH}_4\text{-LiI/Al}_2\text{O}_3$: From 2D Bulk Transport to 3D Long-Range Interfacial Dynamics. *ACS Appl. Mater. Interfaces* **12**, 38570–38583 (2020).
 33. Zettl, R. *et al.* Conductor-Insulator Interfaces in Solid Electrolytes: A Design Strategy to Enhance Li-Ion Dynamics in Nanoconfined $\text{LiBH}_4\text{/Al}_2\text{O}_3$. *J. Phys. Chem. C* **125**, 15052–15060 (2021).
 34. Noritake, T. *et al.* Crystal structure analysis of novel complex hydrides formed by the combination of LiBH_4 and LiNH_2 . *Appl. Phys. A Mater. Sci. Process.* **83**, 277–279 (2006).
 35. Yan, Y. *et al.* Ammonia-assisted fast Li-ion conductivity in a new hemiammine lithium borohydride, $\text{LiBH}_4\cdot 1/2\text{NH}_3$. *Chem. Commun.* **56**, 3971–3974 (2020).
 36. Bohger, J. P. O., Eßmann, R. R. & Jacobs, H. Infrared and Raman studies on the internal modes of lithium amide. *J. Mol. Struct.* **348**, 325–328 (1995).
 37. Matsuo, M. *et al.* Complex hydrides with $(\text{BH}_4)^-$ and $(\text{NH}_2)^-$ anions as new lithium fast-ion conductors. *J. Am. Chem. Soc.* **131**, 16389–16391 (2009).



4

The effect of nanoscaffold porosity and surface chemistry on the Li-ion conductivity of $\text{LiBH}_4\text{-LiNH}_2/\text{oxide}$ nanocomposites

In Chapter 3, it was demonstrated that partial ionic substitution of BH_4^- with NH_2^- followed by nanocomposite formation with a mesoporous oxide substantially increased the conductivity. However, the impact of the oxide properties on the conductivity enhancement was not clear. Here, we show that the conductivity of $\text{LiBH}_4\text{-LiNH}_2/\text{metal oxide}$ nanocomposites is strongly influenced by the chemical and physical nature of the scaffold material. By tuning both the surface chemistry, as well as the pore structure, the conductivity can be varied by three orders of magnitude at room temperature. Unexpectedly, even though a significant influence of the scaffold surface chemistry is observed, the nanocomposite conductivity is mainly dictated by the scaffold pore volume. This is in contrast to $\text{LiBH}_4/\text{oxide}$ nanocomposites, where the conductivity is mostly governed by the chemical nature of the mesoporous scaffold. For $\text{LiBH}_4\text{-LiNH}_2/\text{oxide}$ nanocomposites, the conductivity improvement is therefore attributed to stabilization of a highly conductive phase inside the scaffold pores, rather than the formation of a conductive interfacial layer at the oxide/hydride interface as observed for pristine LiBH_4 .

This chapter is based on: de Kort, L. M., Harmel, J., De Jongh, P. E., & Ngene, P. (2020). The effect of nanoscaffold porosity and surface chemistry on the Li-ion conductivity of $\text{LiBH}_4\text{-LiNH}_2/\text{metal oxide}$ nanocomposites. *Journal of Materials Chemistry A*, 8(39), 20687-20697.

4.1 Introduction

As described in **Chapter 3**, partial ionic substitution and nanocomposite formation were successfully combined to improve the Li-ion conductivity of LiBH_4 . Via the synthesis of anion-substituted complex hydride nanocomposites, such as $\text{LiBH}_4\text{-LiI}/\text{oxide}$ and $\text{LiBH}_4\text{-LiNH}_2/\text{oxide}$, ionic conductivities of 0.1 mS cm^{-1} could be achieved.^{1–3} However, the exact role of mesoporous oxide remained unclear.

For nanocomposites with pure metal hydrides, e.g., $\text{LiBH}_4/\text{SiO}_2$, it is known that the conductivity enhancement originates from the formation of a highly conductive interface layer between the metal hydride and the oxide scaffold. Consequently, the ionic conductivity is greatly affected by the surface properties of the scaffold, such as the nature and density of the surface groups.^{4–7} For anion-substituted metal hydrides, on the other hand, the influence of the scaffold properties on the ion mobility in the nanocomposites has not yet been investigated.

In this work, we aim to bridge this knowledge gap by studying the effect of the chemical nature and physical properties (surface area, pore size and pore volume) of different porous high surface area materials on the conductivity of $\text{LiBH}_4\text{-LiNH}_2/\text{metal oxide}$ nanocomposites. To this end, we prepared $\text{LiBH}_4\text{-LiNH}_2/\text{oxide}$ nanocomposites using SiO_2 scaffolds with varying pore structure and surface properties, as well as mesoporous $\gamma\text{-Al}_2\text{O}_3$, and studied the influence of the scaffold properties on the ionic conductivity.

4.2 Experimental methods

Scaffold synthesis

Mesoporous silica (MCM-41 and SBA-15) and aluminated silica (Al-SBA-15) were synthesized following the procedures described by Cheng *et al.*⁸, Lee *et al.*⁹ and Baca *et al.*¹⁰ For the preparation of MCM-41, 40.9 g hexadecyltrimethylammonium bromide (CTAB, > 96.0%, Aldrich) and 28.8 g tetramethylammonium hydroxide (TMAOH, 25 wt% in H₂O, Aldrich) was dissolved in 297.7 g deionized water. While stirring at 30 °C, 25.0 g SiO₂ (AEROSIL 380, Evonik) was added and allowed to react for 120 minutes. After 120 minutes, stirring was stopped and the mixture was aged at 30 °C for 24 hours. The obtained mixture was transferred to a Teflon-lined stainless-steel autoclave and placed in an oven preheated at 140 °C to react further for 40 hours. After synthesis, the product was filtrated and washed with deionized water to remove all surfactants. Finally, the product was dried at 120 °C in static air for 8 hours and calcined at 550 °C (heating rate 1.5 °C min⁻¹) for 12 hours.

SBA-15 was synthesized by dissolving 23.4 g Pluronic P123 (EO₂₀PO₇₀EO₂₀, average Mw = 5800, Aldrich) in 606.8 g of deionized water and 146.4 g hydrochloric acid in a cylindrical polypropylene bottle (1 L, h = 19.7 cm, Ø = 10.5 cm). To achieve thermal equilibrium, the mixture was stirred vigorously for at least three hours at 55 °C. Then, 50.0 g of tetraethyl orthosilicate (TEOS, > 99%) was added at once, after which the mixture was stirred for two minutes at 600 rpm. After 2 minutes, the stirring bar was removed, and the reaction bottle was closed. The mixture was kept at 55 °C for 24 hours. Following, the SBA-15 was allowed to condensate further for 24 hours at 45, 60, 75, 90, 100 or 120 °C. With this final condensation step the pore structure can be controlled. The as-prepared SBA-15 was filtered and washed with deionized water using a Büchner funnel until no HCl was left in the solution. The material was dried at 60 °C for 3 days and calcined in static air at 550 °C (heating rate 1 °C min⁻¹) for 6 hours.

Aluminated SBA-15 (Al-SBA-15) with a Si/Al ratio of 20 : 1 and 10 : 1 were prepared by adding a solution of aluminium isopropoxide in anhydrous cyclohexane to SBA-15 dried at 450 °C for 2 hours. This was left to react overnight at room temperature while stirring. The obtained suspension was washed with the corresponding anhydrous solvent before calcination at 500 °C for 4 hours. Depending on the amount of aluminium isopropoxide used, Al-SBA-15 with a Si/Al ratio of 20 : 1 or 10 : 1 were prepared, further referred to as Al(20)- and Al(10)-SBA-15.

Nanocomposite synthesis

Nanocomposites were prepared via a two-step synthesis consisting of the preparation of LiBH₄-LiNH₂ phase mixtures followed by melt infiltration of the as-prepared phase mixture. All storage and handling of the chemicals and prepared samples was done in an argon-filled glovebox (H₂O & O₂ < 0.1 ppm).

Several LiBH₄-LiNH₂ phase mixture were prepared by physically mixing LiBH₄ (≥ 95%, Sigma-Aldrich) and 5, 15, 25, 30, 40, 50, 67 and 75 molar percentage of LiNH₂ (95%, Sigma-Aldrich). The physical mixture was transferred to a stainless-steel reactor which was placed in a stainless-steel high-pressure autoclave (Parr, 250 mL). The mixture was allowed to react at 150 °C (heating rate 2.5 °C min⁻¹) under 50 bar H₂ pressure for 30 minutes. After

the reaction, the formed phase mixtures were ground to fine powders.

Preparation of the LiBH₄-LiNH₂/metal oxide nanocomposites and LiBH₄/metal oxide nanocomposites was achieved via melt infiltration following the procedure of Ngene *et al.*¹¹ In general, the LiBH₄-LiNH₂ phase mixture (or pristine LiBH₄) was mixed with the appropriate amount of the chosen scaffold in order to fill the scaffold pores by (typically) 130 volume percent. In this way, the LiBH₄ content is 30 vol% larger than the total pore volume of the scaffold material. This ensures a percolating network of fast Li⁺ diffusion pathways over the non-conducting oxide particles. In other words, Li⁺ transport occurs through the metal hydride phase, not through the oxide. The corresponding molar and mass fractions of the composites are provided in **Table 4.1**. The mixture was transferred to a stainless-steel reactor, which was placed in a stainless-steel high-pressure autoclave (Parr, 250 mL). The autoclave was pressurized with 50 bar H₂ and melt infiltration was carried out for 30 minutes at 120 °C (heating rate 2.5 °C min⁻¹) for LiBH₄-LiNH₂ and at 285 °C for LiBH₄. Upon cooling, the molten LiBH₄-LiNH₂ mixture solidifies in the pores of the scaffold material to form a LiBH₄-LiNH₂/oxide or LiBH₄/oxide nanocomposite.

Table 4.1 – Composition of solid solutions and nanocomposites in wt% and mol%

Pellets	Weight percentage			Molar percentage		
	LiBH ₄	LiNH ₂	-	LiBH ₄	LiNH ₂	-
Solid solutions						
LiBH ₄ -5%LiNH ₂	94%	6%		95%	5%	
LiBH ₄ -15%LiNH ₂	84%	16%		85%	15%	
LiBH ₄ -30%LiNH ₂	68%	32%		70%	30%	
LiBH ₄ -40%LiNH ₂	59%	41%		60%	40%	
LiBH ₄ -50%LiNH ₂	49%	51%		50%	50%	
LiBH ₄ -67%LiNH ₂	32%	68%		33%	67%	
LiBH ₄ -75%LiNH ₂	24%	76%		25%	75%	
Nanoconfined solid solutions	LiBH₄	LiNH₂	Oxide	LiBH₄	LiNH₂	Oxide
LiBH ₄ -30%LiNH ₂ /MCM-41	36%	17%	47%	52%	23%	25%
LiBH ₄ -40%LiNH ₂ /MCM-41	32%	22%	46%	46%	30%	24%
LiBH ₄ -50%LiNH ₂ /MCM-41	27%	28%	45%	38%	38%	24%
LiBH ₄ -50%LiNH ₂ /SBA-15_45C	18%	19%	62%	31%	31%	38%
LiBH ₄ -50%LiNH ₂ /SBA-15_60C	18%	19%	64%	30%	30%	39%
LiBH ₄ -50%LiNH ₂ /SBA-15_75C	22%	23%	55%	35%	34%	31%
LiBH ₄ -50%LiNH ₂ /SBA-15_90C	21%	23%	56%	34%	34%	32%
LiBH ₄ -50%LiNH ₂ /SBA-15_100C	26%	28%	46%	38%	38%	24%
LiBH ₄ -50%LiNH ₂ /SBA-15_120C	26%	27%	47%	38%	37%	25%
LiBH ₄ -50%LiNH ₂ /SBA-15_Si/Al_no_grafting	26%	27%	47%	37%	37%	25%
LiBH ₄ -50%LiNH ₂ /SBA-15_Si/Al_20	25%	26%	49%	37%	37%	26%
LiBH ₄ -50%LiNH ₂ /SBA-15_Si/Al_10	25%	26%	49%	37%	37%	25%
LiBH ₄ -50%LiNH ₂ /Al ₂ O ₃	17%	18%	65%	31%	31%	39%

General characterization

X-ray diffraction (XRD) was performed with a Bruker-AXS D8 Advance X-ray diffractometer with Co $K\alpha_{1,2}$ radiation ($\lambda = 1.78897 \text{ \AA}$). The samples were placed in an airtight sample holder. Diffractograms were recorded at room temperature from 20 to $80^\circ 2\theta$. Diffuse reflectance infrared Fourier transform spectroscopy (DRIFTS) measurements were performed on a Perkin-Elmer 2000 spectrometer equipped with a MCT detector. The sample was placed in an airtight sample holder with KBr windows. Spectra were acquired from 900 cm^{-1} to 4500 cm^{-1} with a resolution of 4 cm^{-1} . Differential scanning calorimetry (DSC) was conducted using a Mettler Toledo HP DSC 1-STAR. About 10 mg of sample was placed in a $40 \mu\text{L}$ Al sample pan. The measurement was performed under 2 bar Ar pressure and an Ar flow of 10 mL min^{-1} . The samples were cycled between 30°C and 300°C with a heating rate of $5^\circ \text{C min}^{-1}$ and a cooling rate of $10^\circ \text{C min}^{-1}$. Nitrogen physisorption measurements were carried out at -196°C on a Micromeritics TriStar II Plus Surface Area and Porosity analyser. No drying procedure was performed prior to the measurements, as all measured samples were stored under controlled atmosphere in an argon-filled glovebox. Analysis of the adsorption and desorption curves was performed following Brunauer, Emmett and Teller (BET) theory and Barrett, Joyner and Halenda (BJH) theory to determine surface area and pore size distribution, respectively.^{12,13}

4

Conductivity measurements

Electrochemical impedance spectroscopy measurements were performed using a Princeton Applied Research Parstat 2273 connected to a custom-made measurement cell in a Büchi B-585 glass oven placed in an argon-filled glovebox to avoid air and moisture exposure. Symmetrical pellets were prepared by firstly placing lithium foils on top of two stainless steel cylinders ($\varnothing = 13 \text{ mm}$). Using a standard pellet press, about $80 - 200 \text{ mg}$ sample was pressed between these cylinders with a pressure of 150 MPa . The same pressure was applied for all measurements to minimize differences in void fraction between pellets, which was generally below 20% . The prepared pellet was placed in the measurement cell.

In a typical conductivity measurement, the pellet is incrementally heated to 50°C ($\Delta T = 5^\circ \text{C}$) and incrementally cooled to room temperature ($\Delta T = 10^\circ \text{C}$). At each increment, the temperature was allowed to equilibrate for 35 min , after which an EIS measurement was performed using a 20 mV RMS modulated AC potential with frequencies from 1 MHz to 1 Hz . The Nyquist plots obtained from the data were fitted using an equivalent circuit consisting of a resistance and a constant phase element. The intersection of the fitted semicircle with the Z_{real} axis was assumed to represent the electrolyte resistance R . Following $\sigma = t/(AR)$, the conductivity σ of the solid electrolytes could be calculated using the electrolyte thickness t and geometric surface area A of the electrodes.

4.3 Results and discussion

4.3.1 Partial ionic substitution of BH_4^- with NH_2^-

First, the structural properties of $\text{LiBH}_4\text{-LiNH}_2$ mixtures containing 15 to 67 mol% LiNH_2 are discussed. The composition of all compounds in wt% and molar% is given in the experimental section (**Table 4.1**). In **Figure 4.1** the XRD diffraction patterns of $\text{LiBH}_4\text{-LiNH}_2$ containing 15, 40 and 67% LiNH_2 are presented. For comparison, the XRD patterns of LiBH_4 and LiNH_2 are included. The diffraction patterns of the mixtures clearly display features that do not correspond to the starting materials. New reflections are observed, which correspond to the presence of several $\text{LiBH}_4\text{-LiNH}_2$ phases, such as $\text{Li}_2(\text{BH}_4)(\text{NH}_2)$, $\text{Li}_3(\text{BH}_4)(\text{NH}_2)_2$ and $\text{Li}_4(\text{BH}_4)(\text{NH}_2)_3$. This is in accordance with previously reported results.^{14–18} Meisner *et al.* identified four different $\text{LiBH}_4\text{-LiNH}_2$ phases with different lattice symmetry and varying melting points of $\sim 45^\circ\text{C}$ (γ -phase), $75\text{--}90^\circ\text{C}$ (β -phase), $150\text{--}190^\circ\text{C}$ (α -phase) and $\sim 50^\circ\text{C}$ (δ -phase).¹⁷ In our case, the presence of multiple phases in most $\text{LiBH}_4\text{-LiNH}_2$ mixtures is clearly observed as well. The formation of $\text{LiBH}_4\text{-LiNH}_2$ phases as demonstrated by XRD is further corroborated with differential scanning calorimetry (DSC) and diffuse reflectance infrared Fourier transform spectroscopy (DRIFTS) as shown in **Figure 4.2a** and **Figure 4.2b**, respectively.

With differential scanning calorimetry, different $\text{LiBH}_4\text{-LiNH}_2$ phases can be distinguished by their specific phase transition (melting) temperature. In **Figure 4.2a** the DSC curves of $\text{LiBH}_4\text{-LiNH}_2$ phase mixtures containing 15 to 67 mol% LiNH_2 are shown. The DSC results reveal that up to three different $\text{LiBH}_4\text{-LiNH}_2$ phases are formed in the prepared $\text{LiBH}_4\text{-LiNH}_2$ mixtures. For compositions with 30 mol% LiNH_2 or less, the presence of unreacted LiBH_4 is reflected by an endothermic peak around 110°C due to the phase transition from orthorhombic to hexagonal LiBH_4 . Melting of the γ - and β -phase in the $\text{LiBH}_4\text{-LiNH}_2$ mixtures is revealed by endothermic peaks at 45°C and $90\text{--}110^\circ\text{C}$, respectively. Notably, for compositions containing 40 mol% LiNH_2 or more, the presence of LiBH_4 is no longer observed, while a third peak attributed to melting of the α -phase is identified between 120°C and 220°C . With increasing amount of LiNH_2 the area of this peak increases, indicating that the amount of the α -phase increases. The peak also shifts

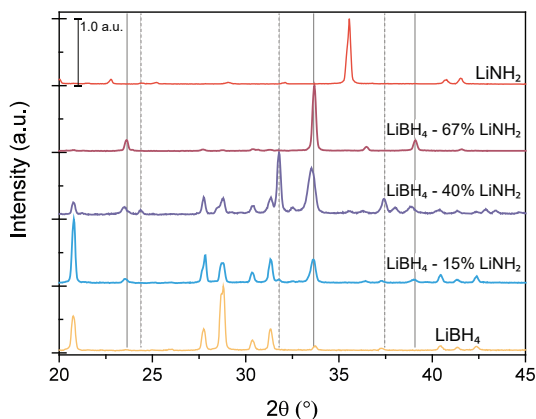


Figure 4.1 - XRD diffractograms of $\text{LiBH}_4\text{-LiNH}_2$ mixtures containing between 15 and 67% LiNH_2 . For comparison, XRD patterns of pristine LiBH_4 and LiNH_2 are included. The dashed and straight lines indicate reflections related to $\text{Li}_2(\text{BH}_4)(\text{NH}_2)$ and $\text{Li}_4(\text{BH}_4)(\text{NH}_2)_3$, respectively.

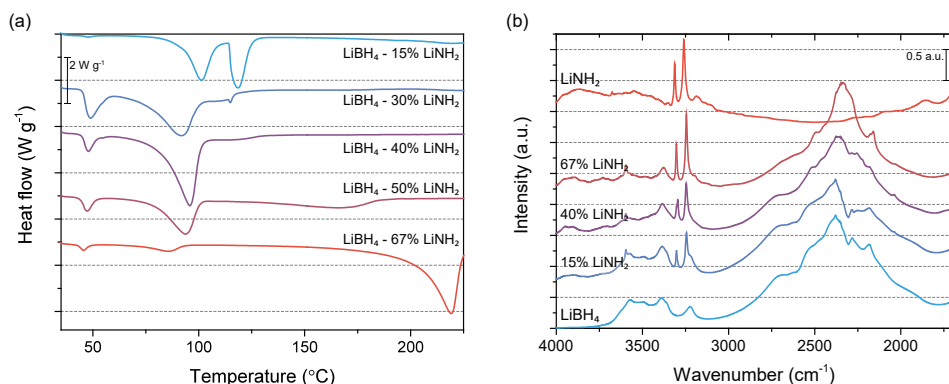


Figure 4.2 - (a) DSC graphs and (b) DRIFTS spectra of LiBH₄-LiNH₂ mixtures containing between 15 and 67% LiNH₂. For comparison, DRIFTS spectra of pristine LiBH₄ and LiNH₂ are included.

to higher temperatures, which can be ascribed to the formation of a more stable LiBH₄-LiNH₂ compound with increasing LiNH₂ content. The DRIFTS spectra shown in **Figure 4.2b** confirm that the borohydride and amide anions remain intact, as their characteristic bands are still clearly visible. To summarize, in line with the results described by Meisner *et al.* XRD, DSC and DRIFTS reveal the formation of new LiBH₄-LiNH₂ phases.¹⁷ Note here that the composition and thereby the melting temperature of the prepared LiBH₄-LiNH₂ mixture depends on the molar fraction of LiNH₂. The melting point of the LiBH₄-LiNH₂ mixture plays a key role in the preparation of the LiBH₄-LiNH₂/oxide nanocomposites through melt infiltration as will be discussed in the following section.

The effect of partial ionic substitution with LiNH₂ on the conductivity of LiBH₄ was analysed by recording the complex impedance of the LiBH₄-LiNH₂ mixtures over a range of temperatures. Previous studies have mainly focussed on the conductivity of LiBH₄-LiNH₂ with a high LiNH₂ content, i.e. 50, 67 and 75 mol% LiNH₂.^{14,15} In this study, the conductivity is determined for LiBH₄-LiNH₂ mixtures containing 5 to 75 mol% LiNH₂. The conductivity data as derived from the complex impedance analysis are displayed in **Figure 4.3a**. Overall, an improvement in conductivity compared to pure LiBH₄ is seen for all LiBH₄-LiNH₂ mixtures. Generally, a sharp increase in conductivity with temperature is observed between 25 °C and 40 °C as was previously observed by Yan *et al.* for Li₃(BH₄)(NH₂)₂.¹⁵ The increased conductivity is related to melting of the LiBH₄-LiNH₂ γ-phase, as revealed by DSC in **Figure 4.2a**. At temperatures above 40 °C the conductivity generally shows a negligible temperature dependence, suggesting a superionic conducting phase.

To demonstrate the difference in conductivity between the different phase mixtures in this region, the conductivity at 50 °C for each LiBH₄-LiNH₂ composition is shown in **Figure 4.3b**. In particular, the LiBH₄-LiNH₂ mixtures containing 30 to 50 mol% LiNH₂ exhibit high conductivities, reaching about $4 \cdot 10^{-4}$ S cm⁻¹ at 50 °C. Notably, in LiBH₄-LiNH₂ with a lower LiNH₂ content (less than 30 %) unreacted LiBH₄ is present, while materials with a higher LiNH₂ content (above 50%) predominantly contain the LiBH₄-LiNH₂ α-phase (**Figure 4.2a**). It is apparent that the presence of unreacted LiBH₄- or α-phase reduces the overall conductivity, in contrast to the LiBH₄-LiNH₂ γ- and β-phase that are beneficial for a higher conductivity. Consequently, an optimum in conductivity is achieved for LiBH₄-LiNH₂ containing 30 to 50 mol% LiNH₂, lower than the LiNH₂ content in the materials that were previously studied.

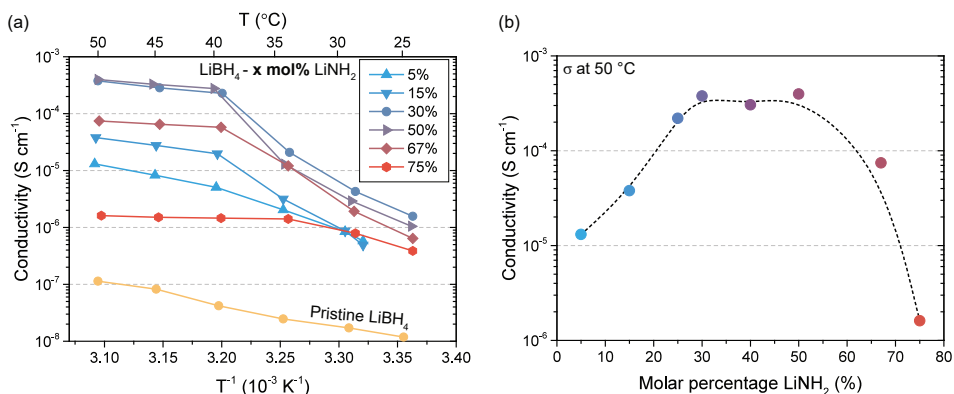


Figure 4.3 - (a) Arrhenius plots visualizing conductivity versus reciprocal temperature of $\text{LiBH}_4\text{-LiNH}_2$ mixtures with 5 and 75 mol% LiNH_2 as well as pristine LiBH_4 . (b) Conductivity dependence on LiNH_2 content in the $\text{LiBH}_4\text{-LiNH}_2$ mixtures. The dashed line is added to guide the eye and has no physical meaning.

4.3.2 Nanocomposite formation of $\text{LiBH}_4\text{-LiNH}_2$ with mesoporous SiO_2

The effect of nanocomposite formation with mesoporous MCM-41 (SiO_2) on the structure and conductivity of $\text{LiBH}_4\text{-LiNH}_2$ is discussed specifically for the mixtures containing 30 to 50 mol% LiNH_2 , as these compositions exhibit the highest conductivities. To start, we discuss the structural changes and effectiveness of the synthesis method, i.e., incorporation of the metal hydride in the pores of the mesoporous oxide, as observed by DRIFTS. In **Figure 4.4** the DRIFTS absorbance spectra of the prepared nanocomposites as well as MCM-41 are visualized. The spectra of the corresponding $\text{LiBH}_4\text{-LiNH}_2$ phase mixtures are provided in **Figure 4.2b**. In the DRIFTS spectra three regions of interest are identified. First, macrocrystalline LiBH_4 typically displays three characteristic bands between 2000 and 2800 cm^{-1} , corresponding to the $[\text{BH}_4]^-$ stretching vibrations.¹⁹ The nanocomposite spectra contain a broad band in this region. The broadening effect was observed in previous studies on nanoconfined LiBH_4 , and was attributed to increased rotational freedom of the $[\text{BH}_4]^-$ anion due to the structural changes induced by nanoconfinement.¹¹

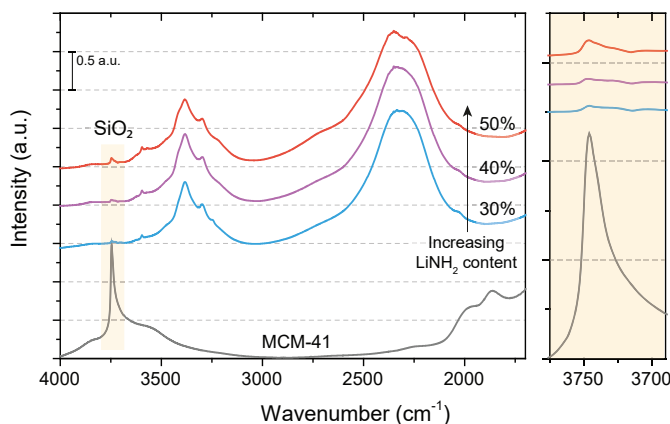


Figure 4.4 - DRIFTS spectra of $\text{LiBH}_4\text{-LiNH}_2/\text{SiO}_2$ nanocomposites. An enlargement is given of the region associated with hydroxyl stretching (3800–3700 cm^{-1}).

Secondly, two sharp bands related to [N-H] stretching vibrations of LiNH_2 are typically present at 3260 and 3310 cm^{-1} .²⁰ In the nanocomposites spectra, these sharp peaks are no longer observed. Instead, a broad peak at a slightly higher wavenumber (3000 - 3500 cm^{-1}) is seen. Similar to the observations on $[\text{BH}_4^-]$, the broadening effect indicates an increased rotational freedom of the $[\text{NH}_2^-]$ anion caused by structural changes upon nanocomposite formation. Likewise, the peak shift towards a higher wave number can be attributed to a change in the Li-N-H bonding due to interactions with the surface groups of the oxide scaffold, as reported for $\text{LiBH}_4/\text{Al}_2\text{O}_3$ and $\text{LiBH}_4/\text{SiO}_2$ nanocomposites.

The last region of interest is ascribed to the hydroxyl stretching vibration of the SiO_2 silanol groups appearing around 3746 cm^{-1} .²¹ Compared to the pristine MCM-41 scaffold, this vibration almost completely disappears in the $\text{LiBH}_4\text{-LiNH}_2/\text{SiO}_2$ nanocomposites with 30 to 50 mol% LiNH_2 . In previous studies it has been found that the silanol vibrations disappear when the pores of the scaffold are filled with an electrolyte salt, as the hydroxyl vibrations are suppressed by interactions or reaction between the silanol groups and the confined electrolyte.^{7,11} This is clearly also the case for nanoconfined $\text{LiBH}_4\text{-LiNH}_2$, implying that for the used compositions, the melt infiltration process results in the successful incorporation of $\text{LiBH}_4\text{-LiNH}_2$ in the oxide pores.

Further evidence for the incorporation of $\text{LiBH}_4\text{-LiNH}_2$ into the oxide pores is provided by XRD (**Figure 4.5a**) and N_2 physisorption (**Figure 4.5b**). The XRD diffraction pattern for the nanoconfined $\text{LiBH}_4\text{-50% LiNH}_2$ shows a complete loss of crystallinity, as expected for nanoconfined materials²², while with N_2 physisorption a loss in pore volume with increasing amount of $\text{LiBH}_4\text{-LiNH}_2$ is observed, consistent with successful infiltration of the metal hydride in the pores of the mesoporous oxide.^{11,22} Note that due to the compressibility of LiBH_4 it shrinks with increasing pressure, and subsequently expands with decreasing pressure. In a typical physisorption measurement, it is assumed that the volume of the sample does not change. Since this is not the case here, a negative slope is observed in the physisorption isotherms.²³

The conductivity of the nanocomposites is shown in **Figure 4.6**. In general, ionic transport at temperatures below 40 °C increased by one to two orders of

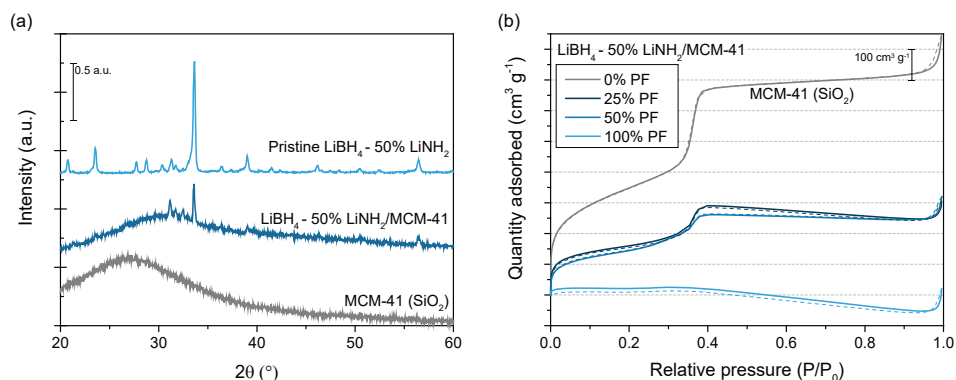


Figure 4.5 - (a) XRD diffractograms of LiBH_4 - 50 mol% LiNH_2 and LiBH_4 - 50 mol% $\text{LiNH}_2/\text{MCM-41}$. The XRD diffractogram of MCM-41 is shown for comparison. (b) N_2 physisorption isotherms of LiBH_4 - 50 mol% $\text{LiNH}_2/\text{MCM-41}$ nanocomposites with pore filling of 25, 50 and 100%.

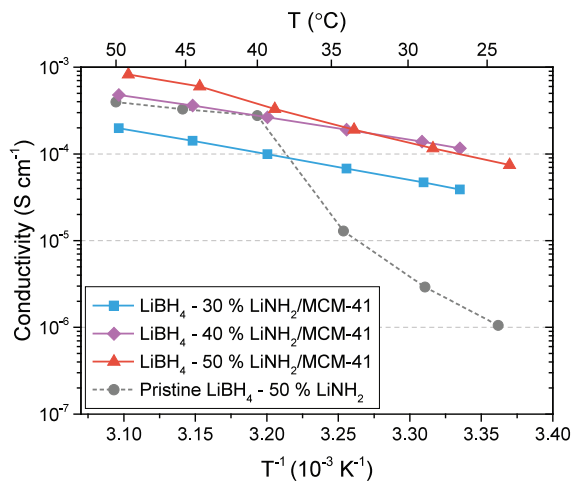


Figure 4.6 - Arrhenius plots visualizing conductivity versus reciprocal temperature of $\text{LiBH}_4\text{-LiNH}_2$ nanocomposites with different $\text{LiBH}_4\text{-LiNH}_2$ compositions.

magnitude compared to the corresponding $\text{LiBH}_4\text{-LiNH}_2$ phase mixtures. Notably, the highest conductivity of $1 \cdot 10^{-4} \text{ S cm}^{-1}$ at 30°C is achieved for $\text{LiBH}_4\text{-40\% LiNH}_2/\text{MCM-41}$, close to ionic conductivities observed for state of the art solid electrolytes, such as thiophosphates.^{24,25} As discussed in **Chapter 3**, the conductivity is 40 times higher than the initial (non-confined) $\text{LiBH}_4\text{-LiNH}_2$, 5 times higher than $\text{LiBH}_4/\text{MCM-41}$ and over 4 orders of magnitude higher than LiBH_4 and $\text{LiNH}_2/\text{MCM-41}$. Furthermore, over the recorded temperature range, no phase change-induced conductivity increase is identified, in contrast to non-confined $\text{LiBH}_4\text{-LiNH}_2$ that revealed a structural phase change leading to a highly conductive phase above 40°C . This suggests that the observed conductivity enhancement might originate from another phenomenon, such as stabilization of the high conductivity $\text{LiBH}_4\text{-LiNH}_2$ phase at lower temperatures through nanoconfinement in the oxide pores, in addition to the formation of a conductive interface layer as is the case for $\text{LiBH}_4/\text{oxide}$ nanocomposites.

The activation energy for long-range ion transport in the nanocomposites was derived from the slope in the Arrhenius plots. A summary of the activation energies is shown in **Table 4.2**. For the $\text{LiBH}_4\text{-LiNH}_2/\text{MCM-41}$ nanocomposites the activation energies vary from $0.54 (\pm 0.02) \text{ eV}$ to $0.83 (\pm 0.03) \text{ eV}$. Note that the activation energy of the high temperature (HT) $\text{LiBH}_4\text{-LiNH}_2$ phase (above 40°C) is lower, consistent with a molten phase in which the Li^+ -ions can move easily. This molten phase could be related to melting of $\text{LiBH}_4\text{-LiNH}_2$ γ -phase or the liquid phase $\text{LiBH}_4(\text{NH}_3)_{0.5}$ as described in a recent work by Yan *et al.*¹⁸ The variation in the activation energy for the different nanocomposites is due to the differences in composition of the $\text{LiBH}_4\text{-LiNH}_2$ nanocomposite. As explained in the previous section, in each $\text{LiBH}_4\text{-LiNH}_2$ mixture different phases are present, which has a consequence for the Li-ion dynamics within the materials. The higher activation energy of $\text{LiBH}_4\text{-30\% LiNH}_2/\text{MCM-41}$ and $\text{LiBH}_4\text{-50\% LiNH}_2/\text{MCM-41}$ compared to $\text{LiBH}_4\text{-40\% LiNH}_2/\text{MCM-41}$ can be explained by the presence of either unreacted LiBH_4 or α -phase $\text{LiBH}_4\text{-LiNH}_2$ in the respective $\text{LiBH}_4\text{-LiNH}_2$ phase mixtures.

Table 4.2 – Activation energies (E_a) and pre-exponential factors $\ln(\sigma_0)$ of $\text{LiBH}_4\text{-LiNH}_2/\text{oxide}$ nanocomposites obtained from a linear plot of $\ln(\sigma T)$ and $10^{-3} T^{-1}$ of complex impedance data. The standard deviation is based on the 95% confidence interval of the linear fit. Unless stated otherwise, the data is obtained from the first temperature-dependent heating cycle between 25 °C and 50 °C.

Sample	E_a (eV)	Pre-factor $\ln(\sigma_0)$
$\text{LiBH}_4\text{-50\%LiNH}_2$	0.3 (\pm 0.2)	10 (\pm 8)
$\text{LiBH}_4\text{-30\%LiNH}_2/\text{MCM-41}$	0.61 (\pm 0.01)	19.3 (\pm 0.4)
$\text{LiBH}_4\text{-40\%LiNH}_2/\text{MCM-41}$	0.54 (\pm 0.02)	17.5 (\pm 0.6)
$\text{LiBH}_4\text{-50\%LiNH}_2/\text{MCM-41}$	0.83 (\pm 0.03)	28 (\pm 2)

* E_a and $\ln(\sigma_0)$ of high temperature (HT) phase determined from between 40 °C to 50 °C. Due to the limited temperature range and measurement points, the obtained activation energy is a rough estimation as evident from the large fitting error.

4.3.3 Effects of the scaffold properties on nanocomposite conductivity

It is clear that the conductivities of the $\text{LiBH}_4\text{-LiNH}_2$ phase mixtures are significantly enhanced by nanocomposite formation with mesoporous silica (MCM-41). For pure LiBH_4 , the enhancement in conductivity upon nanoconfinement in a mesoporous oxide has been attributed to the interactions between surface groups of the oxide and the confined metal hydride, which leads to the formation of a space-charge region or highly defected layer at the $\text{LiBH}_4/\text{oxide}$ interface.^{7,26,27} In this case, the chemical nature of the scaffold, especially the surface chemistry, is crucial for the interface effects, and thereby the conductivity of the $\text{LiBH}_4/\text{oxide}$ nanocomposite. Alternatively, it is also known that nanoconfinement in small pores can lead to a reduction in phase transition temperature, which can profoundly influence the properties of nanoconfined complex hydrides. This effect depends strongly on the pore structure of the mesoporous oxides, as described by the Gibbs-Thomson equation which shows an inverse relationship between the phase transition temperature of a confined material and the size of the confining pore.^{28,29} It is, therefore, expected that the chemical and physical properties of the scaffold are important in determining the effect of nanocomposite formation, and thereby the conductivity of the metal hydride nanocomposites.

The impact of the chemical nature of the scaffold surface as well as the porosity on the nanocomposite conductivity is studied by preparing nanocomposites using SBA-15 (SiO_2) scaffolds with varying surface chemistry and porosity. Similar to MCM-41, SBA-15 is a hexagonally shaped mesoporous silica. The reason for using SBA-15 in this study is that unlike MCM-41, the pore diameter and pore volume of SBA-15 can be readily tuned by changing the condensation temperature (T_c), while particle size, and thereby pore length, as well as surface area are not (significantly) affected.^{9,30,31} Moreover, using surface grafting techniques, such as surface alumination, the surface chemistry of SBA-15 can be altered. Hence, SBA-15 is a good model system to study the impact of both the physical and chemical properties of scaffolds on the conductivity of the nanocomposites.

Surface chemistry effects: In the previous section, it was observed that the surface groups of the scaffold interact with the $\text{LiBH}_4\text{-LiNH}_2$ mixtures confined in the oxide pores (**Figure 4.4**), suggesting that interface interactions could impact nanocomposite conductivity. This was investigated in more detail by preparing nanocomposites of $\text{LiBH}_4\text{-LiNH}_2$ using SBA-15 (SiO_2) scaffolds with varying surface chemistry.

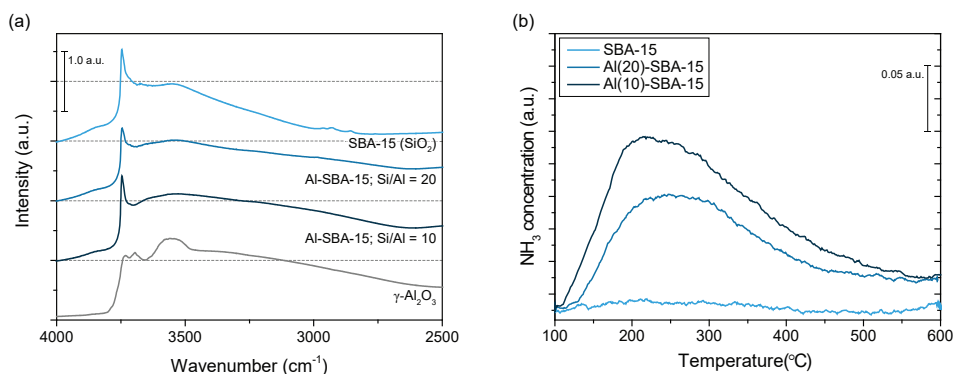


Figure 4.7 - (a) DRIFTS spectra of SBA-15, aluminated SBA-15 and $\gamma\text{-Al}_2\text{O}_3$, displaying the region related to hydroxyl stretching vibrations. (b) NH_3 -TPD of pristine SBA-15 and aluminated SBA-15.

For an accurate analysis of the role of interfacial interactions, the influence of other scaffold properties, such as morphology and porosity, should be minimal. For this purpose, aluminated (Al)-SBA-15, with Si/Al = 20 and 10, was prepared through surface alumination of pristine SBA-15. Upon alumination, the amount and chemical nature of surface hydroxyl groups is modified, which can be (qualitatively) observed in the DRIFTS spectra of the oxides provided in **Figure 4.7a**. Here, the difference in vibrational energy of the surface hydroxyl groups on SBA-15, Al-SBA-15 and $\gamma\text{-Al}_2\text{O}_3$ is visualized. In general, the hydroxyl groups of aluminated SBA-15 and $\gamma\text{-Al}_2\text{O}_3$ exhibit a larger variety in vibrational energy compared to unmodified SBA-15. This is related to the difference in the chemical nature of the surface hydroxyl groups on the oxides. Typically, SiO_2 (SBA-15) contains only weak Brønsted acidic silanol groups, while $\gamma\text{-Al}_2\text{O}_3$, and consequently Al-SBA-15, contain stronger Brønsted acidic and Brønsted basic sites as well as Lewis acid sites.^{10,32}

Using NH_3 -TPD, the number of acid sites present in pristine SBA-15 and aluminated SBA-15 that are sufficiently strong to interact with NH_3 was determined. In **Figure 4.7b**, the NH_3 -TPD measurements of SBA-15, Al(20)-SBA-15 and Al(10)-SBA-15 are depicted. It was found that the amount of acid sites increases from $18.5 \mu\text{mol g}^{-1}$ in the pristine scaffold to $204.1 \mu\text{mol g}^{-1}$ in Al(20)-SBA-15 and $295.5 \mu\text{mol g}^{-1}$ in Al(10)-SBA-15. To compare, $\gamma\text{-Al}_2\text{O}_3$ contains $624.0 \mu\text{mol g}^{-1}$ acid sites. Therefore, both DRIFTS and NH_3 -TPD analysis confirm that the surface of SBA-15 was successfully modified through alumination. Moreover, the porosity of the scaffolds was analysed with N_2 physisorption. The obtained information on porosity of the scaffolds is summarized in **Table 4.3**. Compared to the unmodified SBA-15, surface alumination results in a minor decrease in pore volume from 0.99 to $0.92 \text{ cm}^3 \text{ g}^{-1}$ for the aluminated scaffolds. Altogether, the prepared aluminated SBA-15 scaffolds are a useful model system with varying surface chemistry and without significant differences in pore size, pore volume or surface area.

Table 4.3 – Porosity of aluminated SBA-15 and $\gamma\text{-Al}_2\text{O}_3$ determined with N_2 physisorption

Scaffold		Pore volume ($\text{cm}^3 \text{ g}^{-1}$)	BET area ($\text{m}^2 \text{ g}^{-1}$)	Pore diameter (nm)
SBA-15	Pristine	0.99	726.3	6.6
Al-SBA-15	Si/Al = 20	0.92	657.2	6.7
Al-SBA-15	Si/Al = 10	0.92	643.4	6.6
$\gamma\text{-Al}_2\text{O}_3$	Pristine	0.48	188.3	9.3

The aluminated SBA-15 scaffolds were used to prepare nanoconfined $\text{LiBH}_4\text{-LiNH}_2$. In **Figure 4.8** the conductivities of the $\text{LiBH}_4\text{-LiNH}_2$ /metal oxide nanocomposites prepared with SBA-15, Al(20)-SBA-15, Al(10)-SBA-15 are shown. The room temperature conductivity of the prepared nanocomposites was larger than for non-confined $\text{LiBH}_4\text{-LiNH}_2$. Interestingly, the nanocomposite conductivity increased slightly from $2.0 \cdot 10^{-4} \text{ S cm}^{-1}$ to $3.6 \cdot 10^{-4} \text{ S cm}^{-1}$ with increasing surface alumination. It is not likely that this difference is related to the minor variations in scaffold porosity. This observation therefore suggests that the difference in conductivity results from the change in the surface chemistry arising from alumination.

Further insight into the effect of surface alumination is provided by analysis of the activation energy for ionic transport. For $\text{LiBH}_4\text{-LiNH}_2/\text{SBA-15}$ nanocomposites an activation energy of $0.70 (\pm 0.04) \text{ eV}$ is found, which is similar to the values observed for the MCM-41-based nanocomposites (**Table 4.2**). Surprisingly, the activation energy increases significantly in nanocomposites prepared with aluminated SBA-15 to $0.89 (\pm 0.07) \text{ eV}$ (Si/Al = 20) and $0.9 (\pm 0.1) \text{ eV}$ (Si/Al = 10). Here, a change in activation energy might be caused by the difference in surface chemistry through alumination, which influences the interactions between the scaffold surface and the metal hydride. This is another strong indication that the surface chemistry influences ion mobility in the nanocomposites.

The increase in conductivity with increasing surface alumination could be caused by two surface chemistry properties. Firstly, previous studies on LiBH_4 /oxide nanocomposites demonstrated that the ionic conductivity is strongly influenced by the density of the surface hydroxyl groups. Specifically, a higher density of surface hydroxyl groups is associated with a larger conductivity enhancement.^{4,7} Since alumina generally contains about 10 hydroxyl groups per nm^2 , while silica only contains 4 to 5.5 groups per nm^2 ³², it is expected that aluminated SBA-15 contains more surface hydroxyl groups than unmodified SBA-15, which could explain an increase in conductivity. Additionally, as illustrated with $\text{NH}_3\text{-TPD}$, the chemical nature of surface hydroxyl groups in pristine SBA-15 and aluminated SBA-15 varies significantly. While SiO_2 (SBA-15) contains weakly acidic hydroxyl groups, aluminated SBA-15 contain surface groups with stronger acidic character, and possibly basic sites similar to $\gamma\text{-Al}_2\text{O}_3$. The difference in chemical nature of

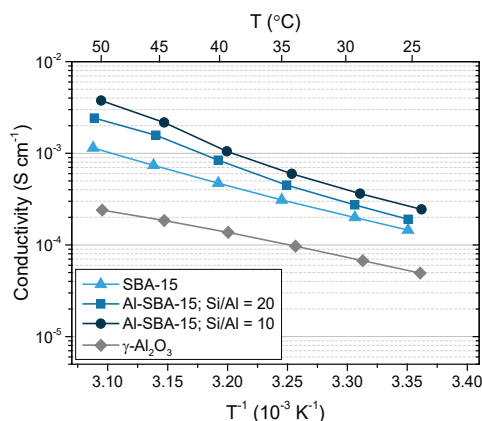


Figure 4.8 - Arrhenius plots of conductivity versus reciprocal temperature of $\text{LiBH}_4\text{-LiNH}_2$ nanoconfined in $\gamma\text{-Al}_2\text{O}_3$, SBA-15 and aluminated SBA-15.

the surface groups will likely alter the nature and strength of the interfacial interactions with nanoconfined $\text{LiBH}_4\text{-LiNH}_2$. With this in mind, it becomes clear that the surface chemistry of the scaffold can heavily impact the conductivity of $\text{LiBH}_4\text{-LiNH}_2/\text{metal oxide}$ nanocomposites.

Surprisingly, the conductivity of the nanocomposite prepared with pure alumina ($\text{LiBH}_4\text{-LiNH}_2/\gamma\text{-Al}_2\text{O}_3$) was significantly lower than for the nanocomposites prepared with SBA-15 and Al-SBA-15. In fact, at room temperature the conductivity was almost 10 times lower than that of $\text{LiBH}_4\text{-LiNH}_2/\text{Al}(10)\text{-SBA-15}$ ($6.7 \cdot 10^{-5} \text{ S cm}^{-1}$), despite the fact that the amount of surface acid sites present in $\gamma\text{-Al}_2\text{O}_3$ is significantly higher ($624.0 \mu\text{mol g}^{-1}$ compared to $295.5 \mu\text{mol g}^{-1}$). It is important to realize that the physical properties, especially the porosity, of $\gamma\text{-Al}_2\text{O}_3$ and aluminated SBA-15 differ substantially (**Table 4.3**). For instance, the pore volume is $0.92 \text{ cm}^3 \text{ g}^{-1}$ for Al-SBA-15 and $0.48 \text{ cm}^3 \text{ g}^{-1}$ for $\gamma\text{-Al}_2\text{O}_3$, while Al-SBA-15 contains small uniform pores ($\phi = 6.6 \text{ nm}$) and $\gamma\text{-Al}_2\text{O}_3$ has a broad pore size distribution ($\phi = 6.3 - 11.1 \text{ nm}$). Hence, the difference in conductivity cannot be solely ascribed to the difference in surface chemistry. Instead, it seems that other factors, especially the physical properties (surface area, pore structure and pore volume) of the scaffold, might play a crucial role in the enhancement of nanocomposite conductivity as well.

Porosity effects: The impact of scaffold porosity was studied by preparing nanocomposites using SBA-15 (SiO_2) scaffolds with varying pore sizes, tuned by varying the condensation temperature between 45°C and 120°C .^{9,30,31} Note that this approach also leads to changes in the specific surface area and pore volume of the scaffold. A summary of the properties of the SBA-15 as derived from the N_2 physisorption measurements is provided in **Table 4.4** and the pore size distribution of the synthesized SBA-15 scaffolds is shown in **Figure 4.9**. The scaffold pore volume increased with increasing condensation temperature from $0.54 \text{ cm}^3 \text{ g}^{-1}$ for SBA-15 prepared at 45°C , up to 1.06 and $1.00 \text{ cm}^3 \text{ g}^{-1}$ for SBA-15 prepared at 100 and 120°C , respectively. Likewise, the pore diameter increased from 5.1 to 8.3 nm when increasing the condensation temperature from 45°C to 100°C . Increasing the condensation temperature further from 100°C to 120°C led to a similar pore volume, but a decrease in the pore size to 6.9 nm . The surface area varied between 609.9 and $855.8 \text{ m}^2 \text{ g}^{-1}$,

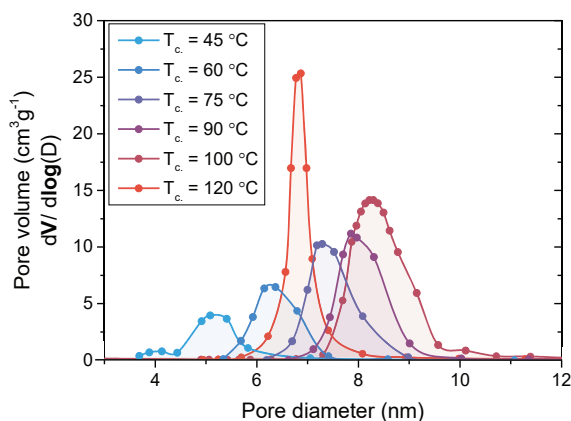


Figure 4.9 - Pore volume versus pore diameter as determined with BJH analysis of SBA-15 scaffolds synthesized with condensation temperatures varying from 45°C to 120°C .

however no obvious correlation between condensation temperature and surface area was observed. Thus, by varying condensation temperature, several mesoporous SBA-15 (SiO_2) scaffolds with large differences in pore structure were synthesized.

Table 4.4 – Porosity of SBA-15 scaffolds prepared at different condensation temperatures

$T_{\text{condensation}}$	Pore volume ($\text{cm}^3 \text{g}^{-1}$)	BET area ($\text{m}^2 \text{g}^{-1}$)	Pore diameter (nm)
45 °C	0.54	609.9	5.1
60 °C	0.51	610.5	63
75 °C	0.74	834.1	7.4
90 °C	0.71	720.9	7.9
100 °C	1.06	805.1	8.3
120 °C	1.00	628.7	6.9

The SBA-15 scaffolds were used to prepare LiBH_4 -50% LiNH_2 /oxide nanocomposites, as well as LiBH_4 /oxide nanocomposites for comparison. The conductivity of the resulting nanocomposites is displayed in **Figure 4.10**. It is evident that the conductivity of the LiBH_4 - LiNH_2 /SBA-15 nanocomposites differs significantly. At 30 °C the nanocomposites based on SBA-15 synthesized with $T_c = 60$ °C and $T_c = 120$ °C exhibit a difference of over three orders of magnitude in conductivity, from $3.6 \cdot 10^{-7} \text{ S cm}^{-1}$ to $5.1 \cdot 10^{-4} \text{ S cm}^{-1}$, respectively. In contrast, LiBH_4 /oxide nanocomposites prepared with these SBA-15 scaffolds display only a minor difference in conductivity, as the conductivity only differs by a factor of 4 when the nanocomposites are prepared with SBA-15 synthesized with $T_c = 90$ °C ($6.9 \cdot 10^{-6} \text{ S cm}^{-1}$) and $T_c = 120$ °C ($2.5 \cdot 10^{-5} \text{ S cm}^{-1}$).

It is important to realize that pellet porosity (void fraction) can be different for the different nanocomposites and thereby influence the conductivity. However, differences in void fractions are not expected to play a dominant role here, because LiBH_4 - LiNH_2 /oxide and LiBH_4 /oxide nanocomposites are both soft materials that likely exhibit a similar pellet porosity when compressed with the same force (as in this study). Furthermore, while a large difference in conductivity is observed for the LiBH_4 - LiNH_2 nanocomposites prepared with the different SBA-15 scaffolds, the activation energy for ion transport remains generally

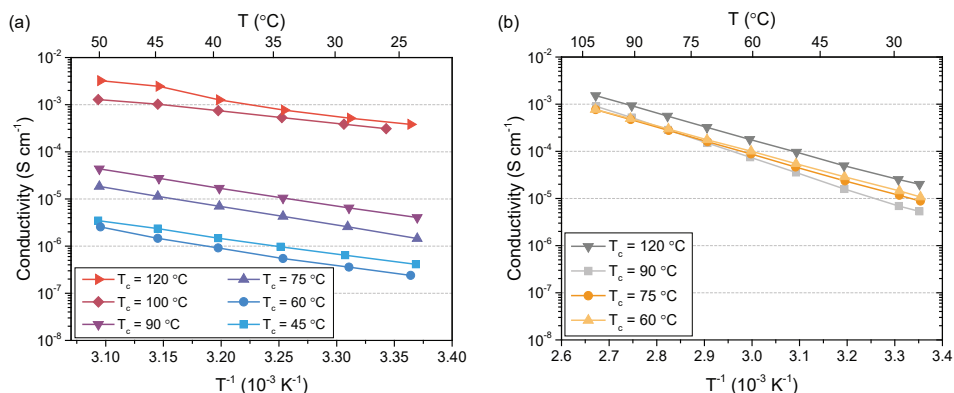


Figure 4.10 - Arrhenius plots showing conductivity versus reciprocal temperature of (a) LiBH_4 - LiNH_2 /metal oxide nanocomposites and (b) LiBH_4 /metal oxide nanocomposites prepared with the synthesized SBA-15 scaffolds.

the same. For example, an activation energy of $0.78 (\pm 0.08)$ eV and $0.75 (\pm 0.12)$ eV are found for nanocomposites prepared with the scaffolds synthesized at 60°C and 120°C , respectively. This indicates that the intrinsic conduction mechanism is similar in all $\text{LiBH}_4\text{-LiNH}_2/\text{SBA-15}$ nanocomposites, and that it is instead the density of charge carriers that influences the conductivity.

Even though it is obvious that scaffold porosity influences the nanocomposite conductivity, it is not easy to pinpoint which physical property, e.g., pore volume, surface area or pore diameter, dictates the overall conductivity. Variation in the SBA-15 condensation temperature affects each structural parameter, hence a detailed analysis is performed in which the conductivity is separately correlated to pore diameter, surface area and pore volume (**Figure 4.11**). Surprisingly, no clear trend was observed between the conductivity of the nanocomposites both the pore diameter and the surface area of the SBA-15. In fact, a clear correlation was only observed with the pore volume of the scaffold (**Figure 4.11c**). From a general linear fit ($y = a + bx$) on the log-linear scale, the relation $\log(\sigma) = -9.5 + 5.9 V_{\text{pore}}$ is derived, showing a clear dependence of the conductivity to the scaffold pore volume. The main dependence of the conductivity on pore volume is unexpected, as in the previous section it was shown that interface interactions contribute to an enhanced conductivity in anion-substituted metal hydride nanocomposites.

The strong correlation between conductivity and pore volume strongly suggests that the conductivity enhancement in $\text{LiBH}_4\text{-LiNH}_2/\text{metal oxide}$ nanocomposites is mostly a result of stabilization of a highly conductive HT phase at room temperature in the pores of the oxide scaffold. Note that this is distinctly different for $\text{LiBH}_4/\text{metal oxide}$ nanocomposites, in which the conductivity enhancement is ascribed to the formation of a conductive interface layer. This is also in accord with the temperature-dependence of the conductivity that indicates the absence of phase transitions over the temperature range between 25°C and 50°C . A large pore volume is indeed expected to be beneficial for conductivity enhancement by phase stabilization.

As explained in the experimental section, each nanocomposite contains an amount of $\text{LiBH}_4\text{-LiNH}_2$ that is equal to 130 % of the scaffold pore volume. Consequently, a higher pore volume results in a larger weight and volume fraction of the highly conductive phase (molten $\gamma\text{-LiBH}_4\text{-LiNH}_2$) compared to the weight fraction of insulating SiO_2 scaffold. For instance, the nanocomposite based on SBA-15 synthesized with $T_c = 60^\circ\text{C}$ contains 36.4 wt% $\text{LiBH}_4\text{-LiNH}_2$ and 63.6 wt% SiO_2 , while the nanocomposite based on SBA-15

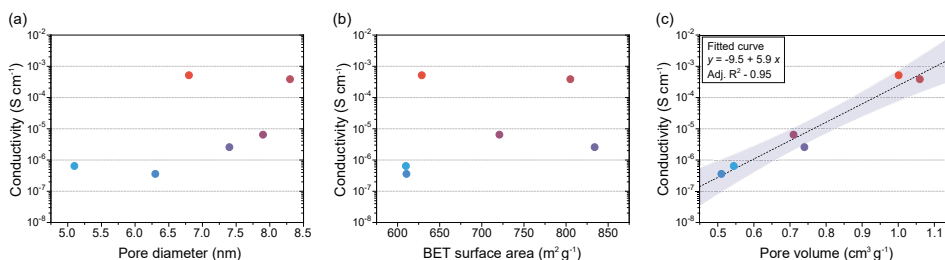


Figure 4.11 - Correlations between $\text{LiBH}_4\text{-LiNH}_2/\text{metal oxide}$ nanocomposite conductivity and (a) average pore diameter, (b) BET surface area and (c) pore volume of the used SBA-15 scaffold. A high correlation between conductivity and pore volume is found and shown with a linear fit and 95% confidence interval.

synthesized with $T_c = 120\text{ }^\circ\text{C}$ consists for 52.8 wt% of $\text{LiBH}_4\text{-LiNH}_2$ and 47.2 wt% of SiO_2 . The higher weight fraction of stabilized molten phase compared to the fraction of insulating SiO_2 leads to greater improvement in conductivity. As a result, a high scaffold pore volume is beneficial for the nanocomposite conductivity

This is in contrast to the case where the improved conductivity would be dictated by interface effects, as observed in nanoconfined LiBH_4 . In **Figure 4.10b**, it can be observed that the conductivity of $\text{LiBH}_4/\text{oxide}$ nanocomposites does not depend on the weight fraction of LiBH_4 , and correspondingly, the scaffold pore volume. The absence of this correlation is in line with previous studies indicating that not the stabilization of the HT hexagonal LiBH_4 phase, but rather a reaction or interaction at the interface with the oxide is responsible for the high conductivity of $\text{LiBH}_4/\text{oxide}$ nanocomposites. Hence, a high surface area and/or a high density of the reactive surface groups would give rise to an increase in scaffold-metal hydride interface interactions. The correlations between conductivity and pore diameter (**Figure 4.11a**) as well as BET surface area (**Figure 4.11b**) illustrate that this is not the case for the $\text{LiBH}_4\text{-LiNH}_2/\text{oxide}$ nanocomposites.

It is clear that within the range of the pore sizes (5.1 - 8.3 nm) studied here, the nanocomposites conductivity is mainly influenced by the scaffold pore volume, which determines the amount of the electrolyte that is nanoconfined per gram of mesoporous metal oxide. However, note that although no correlation exists between the conductivity and pore diameter, a pore diameter considerably larger than 8.3 nm will surely have a profound impact on the nanocomposite conductivity. According to the Gibbs-Thomson relation, the depression of the phase transition temperature of a confined material is inversely proportional to the pore size of the scaffold. Stabilization of the high temperature $\text{LiBH}_4\text{-LiNH}_2$ phase at room temperature will only occur in nanopores that are small enough to induce a sufficient decrease in the phase transition temperature. Therefore, we can conclude that when conductivity enhancement originates from conductive phase stabilization, scaffolds with high pore volume and small pores are beneficial, while for conductivity enhancement mainly driven by interface interactions, scaffolds with high surface area are essential.

4.4 Conclusions

The influence of scaffold properties on the conductivity of LiNH_2 -substituted $\text{LiBH}_4/\text{oxide}$ nanocomposites was systematically investigated using metal oxides with different surface chemistry and physical properties. The study reveals that the chemical nature of the scaffold influences the $\text{LiBH}_4\text{-LiNH}_2/\text{oxide}$ conductivity, as is expected. A conductivity improvement of a factor of two is achieved by changing the surface chemistry of SBA-15 through alumination. Surprisingly, the main factor contributing to an enhanced conductivity in $\text{LiBH}_4\text{-LiNH}_2/\text{metal oxide}$ nanocomposites, is the pore volume of the scaffold. A difference of three orders of magnitude in conductivity (reaching $5 \cdot 10^{-4} \text{ S cm}^{-1}$ at 30°C) is observed by varying the scaffold pore volume from 0.51 to $1.00 \text{ cm}^3 \text{ g}^{-1}$.

Our work demonstrates that the origin of the conductivity enhancement in anion-substituted complex hydride-based solid electrolytes is quite different from other nanoconfined complex hydrides, e.g., LiBH_4 . Specifically, the conductivity can be enhanced not only via the formation of a highly conductive interface layer, but also via the stabilization of a high temperature (highly conductive) phase at room temperature. Clearly, the conductivity of metal hydride-based nanocomposite ion conductors is closely linked to the properties of scaffold materials.

While the enhancement of electrolyte conductivity is the focus of this study, other electrolyte properties, such as electrochemical stability and interface stability with electrode materials, are also essential for application. This constitutes the next milestone for the $\text{LiBH}_4\text{-LiNH}_2/\text{oxide}$ nanocomposites. However, the successful application of similar materials, i.e., $\text{LiBH}_4\text{-LiI/SiO}_2$, $\text{LiBH}_4\text{-LiI/Al}_2\text{O}_3$ and non-confined $\text{Li(BH}_4\text{)}_{1-x}\text{(NH}_2\text{)}_x$, demonstrates that metal hydride-based electrolytes are promising candidates for all-solid-state batteries.

4.5 References

1. Zettl, R. *et al.* Combined Effects of Anion Substitution and Nanoconfinement on the Ionic Conductivity of Li-Based Complex Hydrides. *J. Phys. Chem. C* **124**, 2806–2816 (2020).
2. Zettl, R. *et al.* Li-Ion Diffusion in Nanoconfined $\text{LiBH}_4\text{-LiI/Al}_2\text{O}_3$: From 2D Bulk Transport to 3D Long-Range Interfacial Dynamics. *ACS Appl. Mater. Interfaces* **12**, 38570–38583 (2020).
3. Lu, F. *et al.* A High-Performance Li–B–H Electrolyte for All-Solid-State Li Batteries. *Adv. Funct. Mater.* **29**, 1–7 (2019).
4. Choi, Y. S. *et al.* Enhanced Li Ion Conductivity in $\text{LiBH}_4\text{-Al}_2\text{O}_3$ Mixture via Interface Engineering. *J. Phys. Chem. C* **121**, 26209–26215 (2017).
5. Lambregts, S. F. H. *et al.* Phase Behavior and Ion Dynamics of Nanoconfined LiBH_4 in Silica. *J. Phys. Chem. C* **123**, 25559–25569 (2019).
6. Choi, Y. S., Lee, Y. S., Oh, K. H. & Cho, Y. W. Interface-enhanced Li ion conduction in a $\text{LiBH}_4\text{-SiO}_2$ solid electrolyte. *Phys. Chem. Chem. Phys.* **18**, 22540–22547 (2016).
7. Ngene, P. *et al.* The influence of silica surface groups on the Li-ion conductivity of $\text{LiBH}_4\text{/SiO}_2$ nanocomposites. *Phys. Chem. Chem. Phys.* **21**, 22456–22466 (2019).
8. Cheng, C. F., Park, D. H. & Klinowski, J. Optimal parameters for the synthesis of the mesoporous molecular sieve [Si]-MCM-41. *J. Chem. Soc. - Faraday Trans.* **93**, 193–197 (1997).
9. Lee, H. I. *et al.* Morphology-selective synthesis of mesoporous SBA-15 particles over micrometer, submicrometer and nanometer scales. *J. Mater. Chem.* **20**, 8483–8487 (2010).
10. Baca, M. *et al.* Characterization of mesoporous alumina prepared by surface alumination of SBA-15. *Microporous Mesoporous Mater.* **110**, 232–241 (2008).
11. Ngene, P., Adelhelm, P., Beale, A. M., De Jong, K. P. & De Jongh, P. E. $\text{LiBH}_4\text{/SBA-15}$ nanocomposites prepared by melt infiltration under hydrogen pressure: Synthesis and hydrogen sorption properties. *J. Phys. Chem. C* **114**, 6163–6168 (2010).
12. Brunauer, S., Emmett, P. H. & Teller, E. Adsorption of Gases in Multimolecular Layers. *J. Am. Chem. Soc.* **60**, 309–319 (1938).
13. Barrett, E. P., Joyner, L. G. & Halenda, P. P. The Determination of Pore Volume and Area Distributions in Porous Substances. I. Computations from Nitrogen Isotherms. *J. Am. Chem. Soc.* **73**, 373–380 (1951).
14. Matsuo, M. *et al.* Complex hydrides with $(\text{BH}_4)^-$ and $(\text{NH}_2)^-$ anions as new lithium fast-ion conductors. *J. Am. Chem. Soc.* **131**, 16389–16391 (2009).
15. Yan, Y. *et al.* A Lithium Amide-Borohydride Solid-State Electrolyte with Lithium-Ion Conductivities Comparable to Liquid Electrolytes. *Adv. Energy Mater.* **7**, 1–7 (2017).
16. Noritake, T. *et al.* Crystal structure analysis of novel complex hydrides formed by the combination of LiBH_4 and LiNH_2 . *Appl. Phys. A Mater. Sci. Process.* **83**, 277–279 (2006).
17. Meisner, G. P., Scullin, M. L., Balogh, M. P., Pinkerton, F. E. & Meyer, M. S. Hydrogen release from mixtures of lithium borohydride and lithium amide: A phase diagram study. *J. Phys. Chem. B* **110**, 4186–4192 (2006).
18. Yan, Y. *et al.* Ammonia-assisted fast Li-ion conductivity in a new hemiammine lithium borohydride, $\text{LiBH}_4\cdot\frac{1}{2}\text{NH}_3$. *Chem. Commun.* **56**, 3971–3974 (2020).
19. D’Anna, V., Spyratou, A., Sharma, M. & Hagemann, H. FT-IR spectra of inorganic borohydrides. *Spectrochim. Acta - Part A Mol. Biomol. Spectrosc.* **128**, 902–906 (2014).
20. Bohger, J. P. O., Eßmann, R. R. & Jacobs, H. Infrared and Raman studies on the internal modes of lithium amide. *J. Mol. Struct.* **348**, 325–328 (1995).
21. Morrow, B. A. & McFarlan, A. J. Surface vibrational modes of silanol groups on silica. *J. Phys. Chem.* **96**, 1395–1400 (1992).
22. Suwarno *et al.* Confinement Effects for Lithium Borohydride: Comparing Silica and Carbon Scaffolds. *J. Phys. Chem. C* **121**, 4197–4205 (2017).

23. Jong, J. A. W. *et al.* Phenylglyoxaldehyde-Functionalized Polymeric Sorbents for Urea Removal from Aqueous Solutions. *ACS Appl. Polym. Mater.* **2**, 515–527 (2020).
24. Manthiram, A., Yu, X. & Wang, S. Lithium battery chemistries enabled by solid-state electrolytes. *Nat. Rev. Mater.* **2**, 1–16 (2017).
25. Takada, K. Progress in solid electrolytes toward realizing solid-state lithium batteries. *J. Power Sources* **394**, 74–85 (2018).
26. Verdal, N. *et al.* Dynamical perturbations of tetrahydroborate anions in LiBH_4 due to nanoconfinement in controlled-pore carbon scaffolds. *J. Phys. Chem. C* **117**, 17983–17995 (2013).
27. Maier, J. Ionic conduction in space charge regions. *Prog. Solid State Chem.* **23**, 171–263 (1995).
28. De Jongh, P. E. & Eggenhuisen, T. M. Nanoporous Materials and Confined Liquids. in *Nanoparticles: Workhorses of Nanoscience* (ed. de Mello Donegá, C.) 99–120 (Springer Berlin Heidelberg, 2014). doi:10.1007/978-3-662-44823-6_4.
29. Alba-Simionesco, C. *et al.* Effects of confinement on freezing and melting. *J. Phys. Condens. Matter* **18**, (2006).
30. Zhao, D., Sun, J., Li, Q. & Stucky, G. D. Morphological control of highly ordered mesoporous silica SBA-15. *Chem. Mater.* **12**, 275–279 (2000).
31. Zhao, D. *et al.* Triblock copolymer syntheses of mesoporous silica with periodic 50 to 300 angstrom pores. *Science* (80-.). **279**, 548–552 (1998).
32. Chorkendorff, I. & Niemantsverdriet, J. W. *Concepts of Modern Catalysis and Kinetics*. (John Wiley & Sons, 2003). doi:10.1002/3527602658.ch5.



5

X-ray Raman spectroscopy of conductive interfaces in LiBH_4 - and NaBH_4 /oxide nanocomposites

For most of the metal hydride/oxide nanocomposites that have been discussed so far, the interaction between the metal hydride and the metal oxide determines the nanocomposite conductivity. To further improve their conductivities, it is important to understand the nature of the interaction and to determine the composition of the interface. In this chapter, X-ray Raman scattering was employed to study the chemical environment of Li, Na, and B located at the metal hydride-metal oxide interface of LiBH_4 - and NaBH_4 /oxide nanocomposites. The results suggest that the interface layers in these nanocomposites consist mostly of trigonal compounds, e.g., LiBO_2 , H_3BO_3 or BH_3 . We observed that LiBH_4 /oxide nanocomposites that contain more trigonal boron, also exhibit higher conductivities. Additionally, small differences in the composition of the interface layers of the SiO_2 -based and $\gamma\text{-Al}_2\text{O}_3$ -based nanocomposites were revealed, which is attributed to differences in the interaction between the hydrides and the oxides. This study shows that X-ray Raman scattering can provide valuable new insights on the complex local structure of the metal hydride-oxide interface and is a promising technique for research on amorphous solid electrolytes and nanocomposites containing light elements.

This chapter is based on: de Kort, L. M., Longo, A., Gulino, V., Blanchard, D., Rodenburg, H.P., Lazemi, M., van der Eerden, A. M. J., de Groot, F. M. F. & Ngene, P. X-ray Raman Scattering Study of Conductive Interfaces in Complex Hydride Nanocomposite Electrolytes. *In preparation*.

5.1 Introduction

In previous chapters, it was shown that the formation of a highly conductive interface layer between the metal hydride and the mesoporous scaffold is critical for the success of the nanocomposite formation approach. To tune the interaction at the metal hydride – metal oxide interface and thereby the nanocomposite conductivity, it is essential that the nature of the interaction and the composition of the metal hydride-metal oxide interface is fully understood. Unfortunately, the investigation of metal hydrides and nanocomposite electrolytes is often complicated by their air- and moisture sensitivity, lack of long-range crystallinity, and low molecular weight. In addition, it is not possible to use techniques that require an in-vacuo set-up, such as soft X-ray techniques and electron microscopy, because most metal hydrides decompose under high vacuum.

So far, a few studies have attempted to specifically investigate the interactions between the metal hydride and the metal oxide using solid-state NMR, FT-IR, X-ray photoelectron spectroscopy (XPS) or Near Edge X-ray Absorption Fine Structures (NEXAFS).^{1–7} Although each of these studies confirmed that there is an interface reaction between the metal hydride and the oxide, the nature of the interaction is still being debated. To demonstrate, in the case of LiBH_4 /oxide nanocomposites, some NMR studies suggest that the $[\text{BH}_4]^-$ anion near the interface remains intact, while other NMR studies suggest the formation of B-O, SiO-BH_3 , Si-H, and Li-O bonds.^{1,2,6,7} For example, Dou *et al.* suggested the formation of SiO-BH_3 structure, while Lambregts *et al.* proposed a structure in which BH_4^- interacts with a Si site, as shown in **Figure 5.1a**.^{3,6} The presence of B-O bonds has also been observed with XPS, FT-IR and NEXAFS, but these results are obscured due to possible air exposure during the measurements, the small penetration depth of the techniques and the decomposition of LiBH_4 in high vacuum.^{1,3,4} Thus, no conclusive well-resolved information on the local interface structure has been obtained yet.

Fortunately, the encountered limitations might be circumvented by using a hard X-ray spectroscopic technique, called X-ray Raman scattering (XRS) spectroscopy, sometimes referred to as non-resonant inelastic X-ray scattering (NIXS).⁸ In this technique,

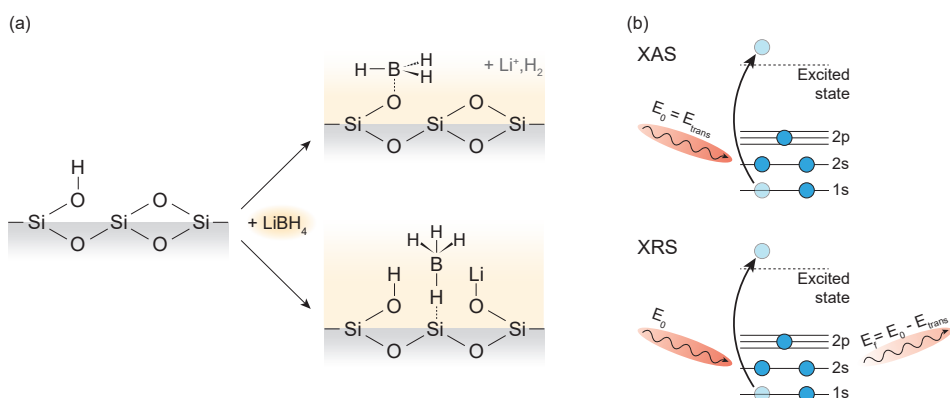


Figure 5.1 - (a) Two-dimensional representation of the LiBH_4 - SiO_2 interface structures proposed by Dou *et al.*³ and Lambregts *et al.*⁶ (b) A schematic representation of the X-ray Adsorption and X-ray Raman scattering process during which an incident photon (with E_0) interacts with an atom in the ground state. This results in the excitation of a core electron, and in case of XRS an inelastically scattered photon (with E_f).

a hard X-ray beam is used to excite electronic transitions at soft X-ray absorption edges. The energy loss between the incident and the scattered X-ray energy is measured and reveals information similar to soft X-ray absorption spectra (XAS). This is schematically shown in **Figure 5.1b**. Because XRS is an inelastic scattering technique, the scattering angle can be used to modify the dipole selection rule and enhance quadrupole excitations, similar to electron inelastic scattering (i.e., electron energy loss spectroscopy or EELS). In this way, the experimental advantages of hard X-ray techniques are retained, making XRS an ideal tool to obtain chemical information of light elements with bulk sensitivity, even for nanocrystalline and amorphous samples contained in complicated sample environments.^{9–13} In addition, it is possible to perform in-situ measurements^{9–11,14}, as well as 3D tomography studies^{15–17} by utilizing the imaging properties of XRS. Thus, XRS is a promising technique that could be applied to determine local structural environments in metal hydride/oxide nanocomposites for battery applications.

In this study, we explored the use of XRS as a technique to study interface effects in nanocomposite solid electrolytes. Using LiBH_4^- , and $\text{NaBH}_4/\text{oxide}$ nanocomposites as examples, we studied the chemical and structural transformations that occur in the local environments of Li, Na, and B upon nanocomposite formation. To this end, we prepared LiBH_4^- , and $\text{NaBH}_4/\text{oxide}$ nanocomposites with mesoporous SiO_2 and $\gamma\text{-Al}_2\text{O}_3$, which are the most widely used oxides for hydride/metal oxide nanocomposite electrolytes. Using nanocomposites with different metal hydride-metal oxide weight ratios, we are able to probe the interface layer that is responsible for the high conductivities in these nanocomposites. The local B, Li, and Na environments in this layer are immensely different compared to the pristine compounds. For example, near the interface between the metal hydride and SiO_2 , boron from $[\text{BH}_4^-]$ changes from a tetrahedral coordination to a trigonal configuration. In addition, changes in the Li and Na environment indicate that Li^+ and Na^+ (from the metal hydrides) are greatly affected by interaction with the oxide as well. All in all, this work provides new insight in the interface interaction in metal hydride/oxide nanocomposites and demonstrates that XRS is a promising technique to study light elements and amorphous materials.

5.2 Experimental methods

Samples and sample preparation

Several LiBH₄ and NaBH₄/metal oxide nanocomposites were prepared by melt infiltration following the procedures described in **Chapter 4** and **Chapter 2**. In short, LiBH₄ (purity > 98%, Sigma-Aldrich) was mixed with mesoporous alumina (γ -Al₂O₃), silica (SBA-15), and grafted silica (M-SBA-15, with M = Al, Zr) and subsequently infiltrated by heating to 285 °C under hydrogen pressure. NaBH₄ (99.99%, Sigma-Aldrich) was mixed with mesoporous alumina (γ -Al₂O₃) and silica (MCM-41), and subsequently infiltrated by heating to 525 °C under hydrogen pressure.

The amount of metal hydride confined in the oxide pores, i.e., the pore filling fraction, was varied from 15% to 130% to specifically probe the interface interaction. In other words, the volume of LiBH₄ corresponds to 0.15 to 1.3 times the pore volume of the oxide. By excluding the contribution of bulk metal hydride to the XRS signal, the interface interaction becomes more predominant at low concentrations of metal hydride in the nanocomposites. Reference compounds (e.g., Li₂B₁₂H₁₂, LiBO₂, and H₃BO₃) were purchased and used either without further treatment, or after an evacuation and drying procedure prior to storage under inert atmosphere. All storage and handling of the chemicals and prepared nanocomposites was done in an argon-filled glovebox (H₂O and O₂ < 0.1 ppm).

Grafted silica (M-SBA-15, with M = Al, Zr) was prepared by drying 1.2 g SBA-15 in static air for 2 hours at 250 °C. The grafting reaction was performed under N₂ atmosphere using a Schlenk line. The reaction mixture was prepared by dissolving the needed amount precursor salt, either Al(OC₃H₇)₃ or Zr(OC₃H₇)₄, to obtain a Si/M ratio of 10 in dry isopropanol. Subsequently, the dried silica scaffold was added, and the mixture was left to stir overnight. The resulting suspension was filtrated and washed with isopropanol. After a final drying (2 hours at 120 °C) and calcination procedure (4 hours at 500 °C, GHSV = 20 mL min⁻¹ g⁻¹ N₂/O₂ flow) the grafted silica was placed in an argon-filled glovebox.

General characterization

Diffuse reflectance infrared Fourier transform spectroscopy (DRIFTS) measurements were performed in a Perkin-Elmer 2000 spectrometer equipped with a liquid nitrogen cooled MCT detector. Spectra were recorded between 4500 and 500 cm⁻¹ with 4 cm⁻¹ resolution, averaging over 16 scans, and using anhydrous KBr as a background. The porosity of the mesoporous oxides was probed with nitrogen physisorption measurements performed on a Micromeritics Tristar 3000. Using the Brunauer, Emmett and Teller (BET) and Barrett, Joyner and Halenda (BJH) adsorption model theories, surface area and pore size distribution could be obtained.^{18,19} The specific surface area (A_{BET}) and total pore volume as determined from the adsorbed quantity close to nitrogen saturation pressure ($p = p_0$) are summarized in **Table 5.1**.

Table 5.1 – Nitrogen physisorption results of oxide scaffolds

Oxide scaffold	BET area (m ² g ⁻¹)	Pore volume (cm ³ g ⁻¹)	Average pore diameter (nm)
SiO ₂ (SBA-15)	722	0.68	6.4
Al-SiO ₂ (Al-SBA-15)	628	0.67	6.4
Zr-SiO ₂ (Zr-SBA-15)	640	0.64	6.2
SiO ₂ (MCM-41)	1071	1.11	2.7
γ-Al ₂ O ₃	172	0.46	8.7

The conductivities of the LiBH₄/(grafted) SiO₂ nanocomposites were determined by measuring electrochemical impedance spectroscopy (EIS) using a Princeton Applied Research Parstat 2273 potentiostat placed in a custom made Büchi B-585 glass oven. Pellets ($t = 0.5 - 1.0$ mm, $\phi = 13$ mm) were prepared by pressing ($P = 150$ MPa) about 80 – 150 mg between stainless-steel electrodes covered with lithium foil. The EIS measurements were performed by heating the samples from RT to 130 °C with increments of 10 °C. At each increment, an EIS measurement was acquired with a 20 mV RMS modulated alternating current potential in a frequency range from 1 MHz to 1 Hz. The complex impedance spectra were fitted to a least squares minimum with a circuit consisting of a resistor (R) in parallel with a constant phase element (CPE). Based on the obtained resistance value, the electrode area ($A = 1.33$ cm²) and thickness (t) of the pellet, the conductivity, σ , was calculated via $\sigma = t/AR$.

5 X-Ray Raman Scattering experiments

Lithium (Li) and boron (B) K-edge XRS spectra were collected at ESRF ID20. An air-tight, ex-situ XRS cell developed by our group (**Figure 5.2**) was placed in a pre-mounted cell holder in a transmission configuration, so that the cell was in the same position in every measurement. During the measurement the cell was kept under a vacuum environment. Sodium (Na) and boron (B) K-edge XRS spectra were collected at DESY Petra III P01. The

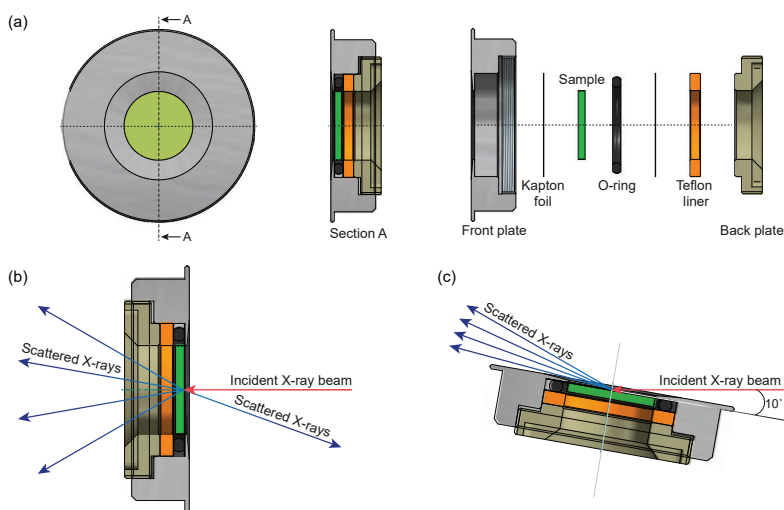


Figure 5.2 - (a) Schematic representation of the air-tight cell used for ex-situ XRS measurements used in the (b) transmission and (c) grazing incidence configurations.

XRS cell was mounted on a pre-constructed cell holder in a grazing incidence configuration with an incidence angle of 10°. Both at ESRF and at DESY, the samples were prepared in an argon filled glovebox by compressing 10 – 40 mg into a pellet (ϕ = 10 mm). Subsequently, the compressed pellet was placed in the XRS cell in between two Kapton foils (ESRF) or in between a Kapton foil and a Kapton/aluminium foil (DESY). The aluminium provides rigidity to the Kapton foil and prevents beam damage, thereby preventing contamination of the samples by air and moisture during measurement.

The XRS scans were performed using the inverse energy scan technique in which the scattered photons are analysed at a fixed energy and the energy transfer is controlled by tuning the incident photon energy. About 3- 10 scans were taken for a single measurement, depending on the quality of the signal from the measured edge. The incident photon energy was selected with a Si(311) monochromator. The XRS spectra were collected by scanning the incident beam energy relative to the fixed analyser energy of 9690 eV with a resolution of 7 eV. At ESRF, the XRS spectra were collected using Madipix detectors (2D photon-counting X-ray detectors with a 55 μ m spatial resolution) with an average q-vector of 4.1 to 4.9 \AA^{-1} (2θ = 50 - 60°). At DESY, the XRS spectra were collected using Madipix detectors with an average q-vector of 4.5 \AA^{-1} (2θ = 55°). The identification of the detector pixels that record scattering from the sample, or the regions of interest (ROIs), were defined manually. The scattering signals obtained from the selected ROIs were normalized to the f-sum rule²⁰ by background subtraction of parameterised Pearson VII functions guided by Hartree-Fock calculated core atomic profiles as described by Sahle *et al.* using the XRStools software package.²¹ The final spectra are plotted as normalized scattered intensity versus energy loss. The spectra of the nanocomposites were smoothened by adjacent averaging over 5 points.

Li- and B- XRS spectra of high purity LiBH₄ (99% purity) were measured to verify that the measurements cells are air-tight and that the samples are not exposed to air during sample preparation, transfer, and measurements. The spectrum of the high-purity sample did not show any peaks related to impurities or oxidized compounds, which confirms that our measurement cells are airtight and protect the samples from air exposure during sample preparation, transfer, and measurement. Oxidation or beam-induced sample damage during the XRS measurement was monitored by comparing the initial scans of the measurement to subsequent scans. In this case, a slight decrease in the intensities of the peaks is observed. This indicates that while the samples did not oxidize during the measurement, the sample is affected by prolonged beam exposure. These changes are attributed to the low stability of borohydrides in the beam. To prevent beam damage as much as possible, measurement times were minimized, and the beam was moved to different locations on the sample during long measurements.

5.3 Results and discussion

5.3.1 X-ray Raman Scattering analysis of $\text{LiBH}_4/\text{SiO}_2$ nanocomposites

Our analysis starts with $\text{LiBH}_4/\text{SiO}_2$ nanocomposites since this system is one of the most widely investigated metal hydride/oxide nanocomposites. Li- and B K-edge XRS spectra of pristine LiBH_4 and $\text{LiBH}_4/\text{SiO}_2$ nanocomposites with 130%, 50% and 15% pore filling have been measured. In the $\text{LiBH}_4/\text{SiO}_2$ nanocomposite with 130% pore filling, the LiBH_4 volume is 1.3 times the total pore volume of the scaffold, so that it completely fills the scaffold pores and additional LiBH_4 covers the outer surface of the oxide particles. The lower pore filling fractions roughly correspond to a 1 nm (PF = 50%) and 0.3 nm layer (PF = 15%) of LiBH_4 covering the SiO_2 pore walls, assuming that LiBH_4 completely wets the silica surface. The composition of the nanocomposites is shown schematically in **Figure 5.3a**. Since the interface layer in $\text{LiBH}_4/\text{oxide}$ nanocomposites is 1 – 2 nm^{22–24}, the nanocomposites with 50% and 15% pore filling fractions will likely provide more specific information on the $\text{LiBH}_4\text{-SiO}_2$ interface.

The changes in chemical structure of LiBH_4 upon nanocomposite formation in mesoporous SiO_2 are investigated by comparing pristine LiBH_4 to the $\text{LiBH}_4/\text{SiO}_2$ nanocomposites. In the Li K-edge spectra of pristine LiBH_4 (**Figure 5.3b**, black line), a clear absorption peak is observed at 59.9 eV. This feature corresponds to the transition of the 1s core electron to an unoccupied orbital (with p character), as has been reported for many lithium salts, including lithium halides and lithium borates.^{25–28} The B K-edge spectra (**Figure 5.3c**, black line) of pristine LiBH_4 shows three characteristic features. Firstly, an

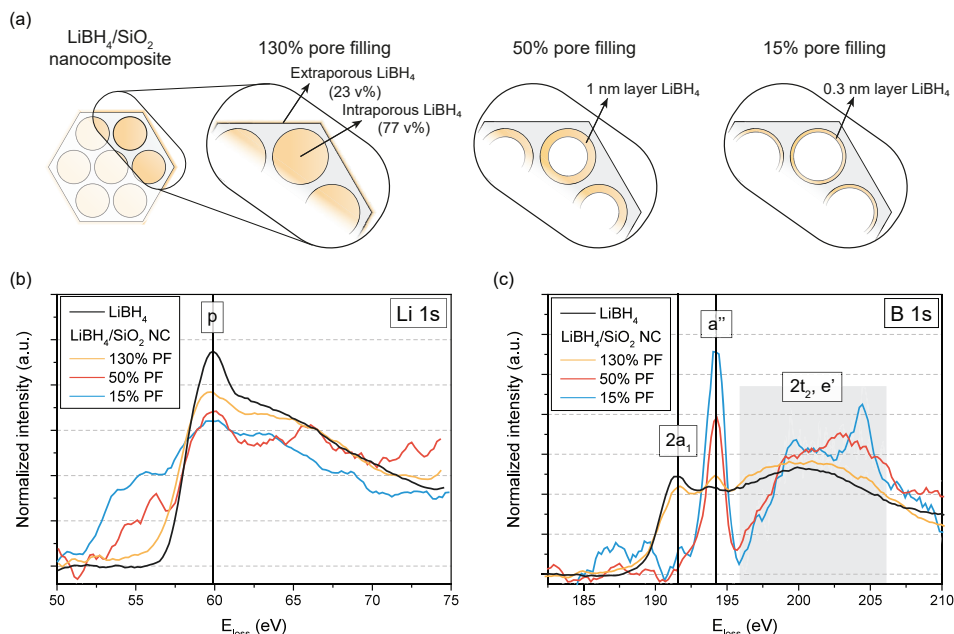


Figure 5.3 - (a) Schematic representations of the $\text{LiBH}_4/\text{SiO}_2$ nanocomposites with 130%, 50% and 15% pore filling fraction of LiBH_4 . (b) Li K-edge and (c) B K-edge XRS spectra of pristine LiBH_4 powder (95% purity) and $\text{LiBH}_4/\text{SiO}_2$ nanocomposites with pore filling fractions ranging of 130%, 50% and 15%. The spectra of the nanocomposites are smoothed using adjacent averaging over 5 points.

edge peak is observed at 191.5 eV. This peak is associated with the transition of a B 1s electron from the tetrahedral [BH₄]⁻ anion to an unoccupied boron antibonding 2a₁ orbital (**Figure 5.4a**).²⁹ Secondly, at 193.8 eV a small peak can be observed, which is attributed to the transition of B 1s electrons to unoccupied a'' orbitals in planar system^{29–33} (**Figure 5.4b**), such as BF₃, BH₃ or trigonal B-O from LiBO₂ or B₂O₃ impurities commonly found in commercially available LiBH₄. Finally, the broad band between 195 and 205 eV is related to the transition of a B 1s electron to an unoccupied 2t₂ orbital of tetrahedral boron.^{29–32} This broad band might also contain a contribution related to trigonal boron, as it also exhibits a transition to unoccupied orbitals (generally e') in this region.^{29–32} These results are in line with previous XRS data collected by Miedema *et al.*^{9,10}

Clear differences between the spectra of pristine LiBH₄ and the nanocomposites are observed. Firstly, in the Li K-edge spectrum (**Figure 5.3b**) of the LiBH₄/SiO₂ nanocomposites with 130% PF (yellow line), the peak at 59.9 eV has become less intense compared to pristine LiBH₄. Secondly, a broad feature is observed around 64 eV. With lower pore filling, the edge peak at 59.9 eV continuously decreases in intensity while a shoulder appears at 55.6 eV. Thirdly, the region between 62 eV and 75 eV starts to show several features. The reduced intensity of the peak at 59.9 eV combined with the formation of a shoulder demonstrates that the unoccupied orbitals in of Li⁺ become progressively filled and the bond between the anion and Li⁺ becomes more covalent, for example due to the presence of a less electronegative anion, or Li⁺ becoming more metallic.^{9,27,28} The features in the fingerprint region between 62 eV and 75 eV might be due to multiple scattering resonances or the presence of lithium compounds with stronger ionic bonds, such as Li₂O.^{27,34,35} Overall, it seems that near the SiO₂ surface, two different lithium compounds are present, one in which Li⁺ is weakly bonded to the anion, and one in which a strong Li-O bond is formed.

Similarly, in the B K-edge spectra (**Figure 5.3c**) clear changes are observed when comparing pristine LiBH₄ to the LiBH₄/SiO₂ nanocomposites. In the spectrum of the nanocomposite with 130% pore filling, the peak at 191.5 eV associated with the tetrahedral 2a₁ transition is less intense compared to the spectrum of pristine LiBH₄, while the feature attributed to trigonal boron is more intense and appears at a slightly more positive energy

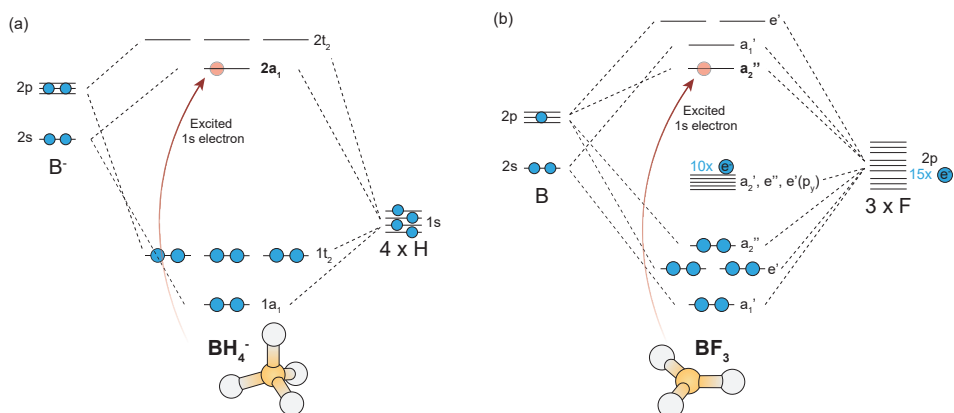


Figure 5.4 - Schematic representation of the molecular orbital diagrams of (a) BH₄⁻ and (b) BF₃ based on symmetry adapted linear combinations (SALCs). The corresponding molecular geometries, i.e., tetrahedral for BH₄⁻ and trigonal planar for BF₃, are provided as well.

(194.2 eV). In the B K-edge spectra of the nanocomposites with 50% and 15% PF, the characteristic $[\text{BH}_4]^-$ a_1 peak observed at 191.5 eV is not present anymore. Instead, the feature at 194.2 eV corresponding to trigonal B has become an intense, sharp peak. The change in the ratio between the tetrahedral and the trigonal boron peaks shows that the nanocomposites contain more trigonal boron than pristine LiBH_4 , especially in the nanocomposites with a smaller pore filling fraction. It seems that upon nanocomposite formation with mesoporous silica, an interface reaction occurs between LiBH_4 and the oxide that results in the formation of trigonal boron compounds from BH_4^- .

While this analysis provides general information about the chemical environment of lithium and boron in the nanocomposites, the exact interface composition remains unclear. Therefore, to obtain more detailed information, the spectra were fitted using a linear combination of relevant reference compounds. The experimental data of the $\text{LiBH}_4/\text{SiO}_2$ nanocomposites was fitted with the B K-edge spectra of pristine LiBH_4 , $\text{Li}_2\text{B}_{12}\text{H}_{12}$, LiBO_2 , and H_3BO_3 (**Figure 5.5a**) to distinguish between the tetrahedral and trigonal boron species present. It should be noted that the trigonal boron species in the nanocomposites could also be based on hydrogen (e.g., BH_3), especially as both LiBO_2 and H_3BO_3 are not ionically conductive. However, there are no suitable references for this configuration. The resulting linear combination fits are shown in **Figure 5.5** and the corresponding fitting parameters are given in **Table 5.2**. From a comparison of the linear combination fits to the measured data, it is clear that the model explains the data quite well (adjusted $R^2 > 0.83$), though the fits are not perfect. The origin of these discrepancies will be explained later.

Table 5.2 – Fitting parameters and molar fractions (in parentheses) from linear combination fits of the B K-edge. Dashes (-) indicate that this compound was neglected in the fit. For the estimation of the molar fractions, the stoichiometries of the references are considered, e.g., 12 B atoms in $\text{Li}_2\text{B}_{12}\text{H}_{12}$, on B atom in LiBH_4 .¹¹

References	$\text{LiBH}_4/\text{SiO}_2$ (130% PF)	$\text{LiBH}_4/\text{SiO}_2$ (50% PF)	$\text{LiBH}_4/\text{SiO}_2$ (15% PF)
LiBH_4	0.70 (82%)	-	-
$\text{Li}_2\text{B}_{12}\text{H}_{12}$	0.16 (1.6%)	-	-
LiBO_2	0.09 (11%)	0.69 (72%)	0.54 (56%)
H_3BO_3	0.05 (6%)	0.27 (28%)	0.42 (44%)

The linear combination fit of the $\text{LiBH}_4/\text{SiO}_2$ nanocomposite with 130% pore filling confirm that the nanocomposite consists largely of LiBH_4 . A small amount of $\text{Li}_2\text{B}_{12}\text{H}_{12}$, a well-known decomposition product of LiBH_4 , is observed as well. Furthermore, the trigonal feature at 194.2 eV can be fitted with a combination of the B-O species, mostly resembling LiBO_2 and partially resembling H_3BO_3 . Note that in the fit, the peak around 191.5 eV has a higher intensity compared to the experimental data. Hence, either the amount of LiBH_4 or $\text{Li}_2\text{B}_{12}\text{H}_{12}$ present in the nanocomposite is overestimated or the anions contain more negative charge (possibly due to the formation of Li^+ vacancies). In the nanocomposites with lower pore filling fractions, i.e., 50% and 15%, the contributions of LiBH_4 and $\text{Li}_2\text{B}_{12}\text{H}_{12}$ are not considered, since the characteristic peak around 191.5 eV is not present in these samples. Instead, the experimental data is fitted solely with the trigonal reference compounds. Based on the resulting linear combination fits of both nanocomposites, it seems that a mixture of trigonal boron phases is present at the $\text{LiBH}_4 - \text{SiO}_2$ interface.

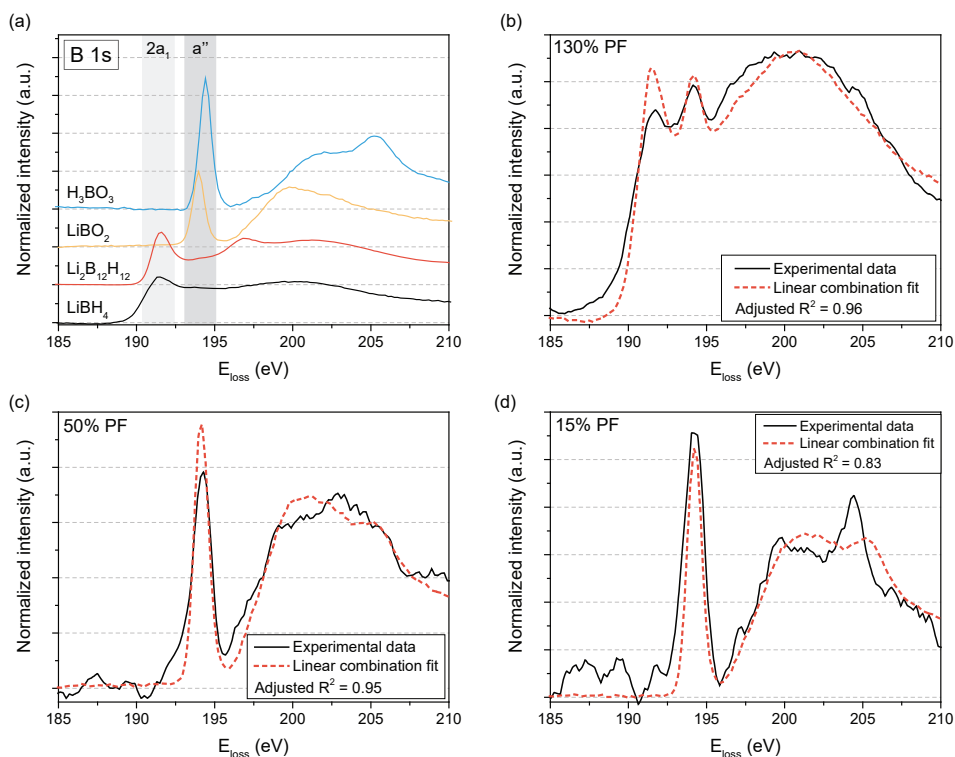


Figure 5.5 - (a) B K-edge XRS spectra of pristine LiBH_4 , $\text{Li}_2\text{B}_{12}\text{H}_{12}$, LiBO_2 , and H_3BO_3 . (b-d) Linear combination fit of the reference compounds to the B K-edge spectra of $\text{LiBH}_4/\text{SiO}_2$ with pore filling fraction of (b) 130%, (c) 50% and (d) 15%.

Interestingly, the ratio between LiBO_2 and H_3BO_3 character in the $\text{LiBH}_4/\text{SiO}_2$ nanocomposites changes when going from 50% PF to 15% PF. The fitting parameter of the LiBO_2 contribution becomes lower, while the fitting parameter of the H_3BO_3 contribution becomes larger. It seems that closer to the SiO_2 surface, the metal hydride-oxide interface layer contains compounds in which the energy associated with the trigonal a'' transition shifts to higher energies (as is the case for H_3BO_3 compared to LiBO_2). This illustrates that the structure within the interface layer differs depending on the proximity of the oxide or metal hydride, and possibly the proximity to different surface groups on the SiO_2 surface (e.g., surface siloxanes and isolated, geminal, vicinal silanols).

It is important to realize the interface layer is a highly defected and distorted phase. These defects and distortions can greatly affect the local chemical environment of the boron species. The B K-edge spectra show that the $\text{LiBH}_4 - \text{SiO}_2$ interface layer contains trigonal boron (such as LiBO_2 or BH_3), yet the exact chemical environment will be different from the purely crystalline phases that have been measured as reference compounds. The same is true for the chemical environment of Li^+ . While the Li K-edge spectra show features that can be attributed to the presence of Li_2O , it is more likely that these features are related to the formation of Li-O bonds. All in all, our observations are in line with the formation of a Si-H-BH_3 structure and Si-O-Li bond via the reduction of a siloxane bond as proposed by Lambregts *et al.*, though the formation of the Si-O-BH_3 structure discussed by Dou *et al.* cannot be excluded. In both cases it is possible to form

trigonal boron.^{3,6,7} We also observed the formation of a Li^+ -compound that has a weak interaction with the surrounding anions. This is in accordance with the reduced activation energies for ionic transport in $\text{LiBH}_4/\text{SiO}_2$ nanocomposites (0.4 – 0.5 eV) compared to pristine LiBH_4 (0.7 – 0.9 eV)^{22,23,36,37}, and could explain the enhanced ionic conductivity upon nanocomposite formation. To determine the exact chemical environment at the interface with more certainty, we are currently performing AIMD simulations combined with static DFT calculations to simulate XRS spectra.

5.3.2 Correlation to $\text{LiBH}_4/\text{SiO}_2$ conductivity

Based on the XRS results discussed in the previous section, it is clear that the interface between LiBH_4 and SiO_2 consists of trigonal boron compounds, Li-O compounds and Li^+ -compounds that interact weakly with the surrounding anions. To investigate the link between the formation of this interface layer and the ionic conductivity of the nanocomposites, we studied the conductivity and interface composition of $\text{LiBH}_4/\text{oxide}$ nanocomposites based on aluminium- and zirconium-grafted SiO_2 . The surface chemistry of the Al- and Zr-grafted SiO_2 scaffolds differs from pristine SiO_2 ^{38–41}, while their physical properties (e.g., surface area, pore volume, morphology) are the same. In this way, the strength of the interface interaction differs, which can change the properties of the $\text{LiBH}_4/\text{oxide}$ nanocomposites. This makes it possible to determine how the ionic conductivity is affected by the $\text{LiBH}_4\text{-SiO}_2$ interface composition.

In **Figure 5.6a**, the B K-edge XRS spectra of $\text{LiBH}_4/\text{M-SiO}_2$ nanocomposites (M = Al, Zr) with 130% pore filling are shown. Surprisingly, the peak at 191.5 eV decreases in intensity when going from SiO_2 to Al- SiO_2 to Zr- SiO_2 , while the peak at 194.0 eV increases. This indicates that the amount of tetrahedral boron species, i.e., BH_4^- , declines, while more trigonal boron compounds are present. The interface interaction between LiBH_4 and Zr- SiO_2 is stronger, and as a result more LiBH_4 is converted to trigonal interface species. In other words, the interface layer extends further from the interface.

To determine the impact of the different interaction strength, and thereby composition of the $\text{LiBH}_4\text{-oxide}$ interface, on the ionic conductivity, the complex impedance

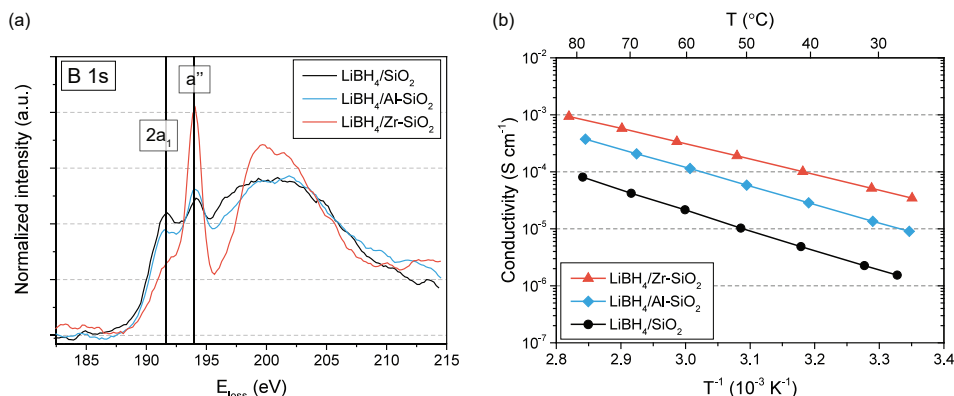


Figure 5.6 - (a) B K-edge XRS spectra of $\text{LiBH}_4/\text{SiO}_2$, $\text{LiBH}_4/\text{Al-SiO}_2$ and $\text{LiBH}_4/\text{Zr-SiO}_2$ nanocomposites with pore filling fraction of 130%. The spectra are smoothed using adjacent averaging over 5 points. (b) Arrhenius plots of conductivity versus reciprocal temperature of $\text{LiBH}_4/\text{SiO}_2$, $\text{LiBH}_4/\text{Al-SiO}_2$ and $\text{LiBH}_4/\text{Zr-SiO}_2$.

of the nanocomposites was recorded over a range of temperatures. The conductivity data derived from the complex impedance analysis are depicted in **Figure 5.6b**. At 30 °C, LiBH₄/SiO₂ exhibits a conductivity of $0.2 \cdot 10^{-5} \text{ S cm}^{-1}$. The nanocomposites based on grafted SiO₂ both exhibit higher conductivities of $1.4 \cdot 10^{-5} \text{ S cm}^{-1}$ and $5.1 \cdot 10^{-5} \text{ S cm}^{-1}$ for LiBH₄/Al-SiO₂ and LiBH₄/Zr-SiO₂, respectively. It seems that when the LiBH₄/oxide nanocomposite contains more trigonal B species, it exhibits a higher conductivity. It is possible that the formation of more trigonal boron, also corresponds to the formation of additional weakly coordinated Li-ions, thereby facilitating fast Li-ion transport.

5.3.3 Extension to NaBH₄/SiO₂ nanocomposites

In the same way as LiBH₄/SiO₂ nanocomposites, the effect of nanocomposite formation with mesoporous SiO₂ on the chemical structure of NaBH₄ was investigated by studying NaBH₄/SiO₂ nanocomposites with different pore filling (PF) fractions. In **Figure 5.7** the Na- and B K-edge XRS spectra of pristine NaBH₄ and NaBH₄/SiO₂ nanocomposites with 30%, 100 %, and 130% pore filling are shown. Firstly, the Na K-edge spectra of the NaBH₄/SiO₂ nanocomposites (**Figure 5.7a**) are compared to that of the pristine NaBH₄. In the spectrum of pristine NaBH₄, two peaks are observed at observed at 1076.2 eV and 1078.9 eV. These peaks likely correspond to the transition of a 1s electron to an unoccupied 3p state of Na⁺.^{42,43} The nanocomposites with 130% and 100% pore filling only differ slightly. In contrast, the Na K-edge spectrum of NaBH₄/SiO₂ with 30% PF contains an additional pre-edge peak at 1073.9 eV and a broad feature around 1082 eV. Similar changes were also observed in the Li K-edge spectra of LiBH₄/SiO₂, hence this points to both the formation of Na⁺ bonded to O, and Na⁺ that weakly interacts with its environment.

In the B K-edge spectra of the NaBH₄/SiO₂ nanocomposites (**Figure 5.7b**), clear differences with the spectrum of pristine NaBH₄ are observed. The peak at 191.7 eV, associated with the 2a₁ transition of tetrahedral B (in BH₄⁻) becomes less intense upon nanocomposite formation. At the same time, the spectra of the nanocomposites contain a feature at 194.1 eV, which is not observed in pristine NaBH₄. As explained in section 5.3.1 and **Figure 5.4**, the peak around 194 eV is attributed to the transition of B 1s electrons to unoccupied a'' orbitals of trigonal boron, such as BO₂⁻, H₃BO₃ and BH₃. In the NaBH₄/SiO₂ nanocomposite with 30% pore filling, the peak related to BH₄⁻ is smaller than the peak corresponding to trigonal boron. Thus, at the interface between NaBH₄ and SiO₂ a layer consisting of trigonal boron, Na-O and weakly coordinated Na⁺ seems to form, similar to the interface layer between LiBH₄ and SiO₂.

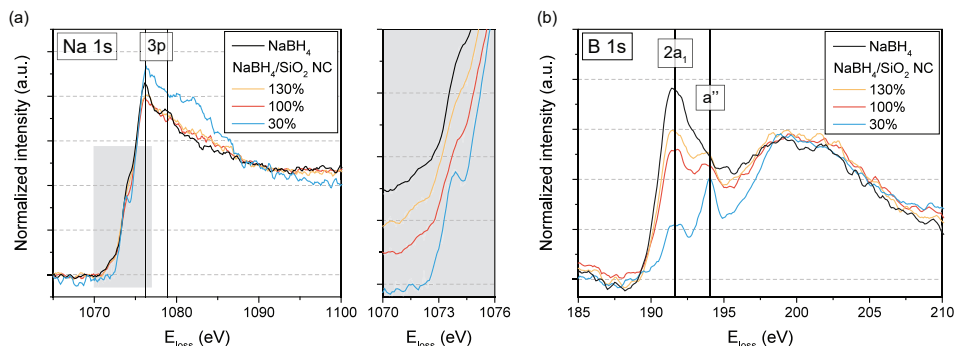


Figure 5.7 - (a) Na K-edge and (b) B K-edge XRS spectra of pristine NaBH₄ powder (99.99% purity) and NaBH₄/SiO₂ nanocomposites with pore filling fractions ranging of 130%, 100% and 30%. The spectra of the nanocomposites are smoothened using adjacent averaging over 5 points.

5.3.4 Comparison to γ - Al_2O_3 -based nanocomposites

In section 5.3.2, it was discussed that the composition of the nanocomposite is greatly affected by the chemical nature of the oxide. Therefore, it is interesting to study the effect of nanocomposite formation with mesoporous γ - Al_2O_3 on the chemical structure of LiBH_4 and NaBH_4 with X-ray Raman Scattering. The Li- and B K-edge XRS spectra of the $\text{LiBH}_4/\text{Al}_2\text{O}_3$ nanocomposites and the Na- and B K-edge XRS spectra of the $\text{NaBH}_4/\text{Al}_2\text{O}_3$ nanocomposites are shown in **Figure 5.8**. The spectra of pristine LiBH_4 and NaBH_4 are included for comparison. In **Figures 5.8a** and **5.8c**, it can be observed that the changes in the Li- and Na K-edge spectra of $\text{LiBH}_4/\text{Al}_2\text{O}_3$ and $\text{NaBH}_4/\text{Al}_2\text{O}_3$ are similar to those observed for $\text{LiBH}_4/\text{SiO}_2$ and $\text{NaBH}_4/\text{SiO}_2$. The intensity of the edge peak decreases, while the peaks broaden and a pre-edge shoulder appears, which points to a weakened ionic bond between Li^+ or Na^+ and BH_4^- , and at the same time that part of the Li^+ and Na^+ ions form Li-O and Na-O bonds near the γ - Al_2O_3 surface. Since the Li- and Na-ions exhibit similar chemical environments in the SiO_2 - and Al_2O_3 -based nanocomposites, the activation energy for ionic transport should also be comparable. Choi *et al.* reported recently that $\text{LiBH}_4/\text{SiO}_2$ and $\text{LiBH}_4/\text{Al}_2\text{O}_3$ nanocomposites prepared in the same manner indeed have similar activation energies of 0.43 eV and 0.44 eV, respectively.⁴ This is in line with the present study.

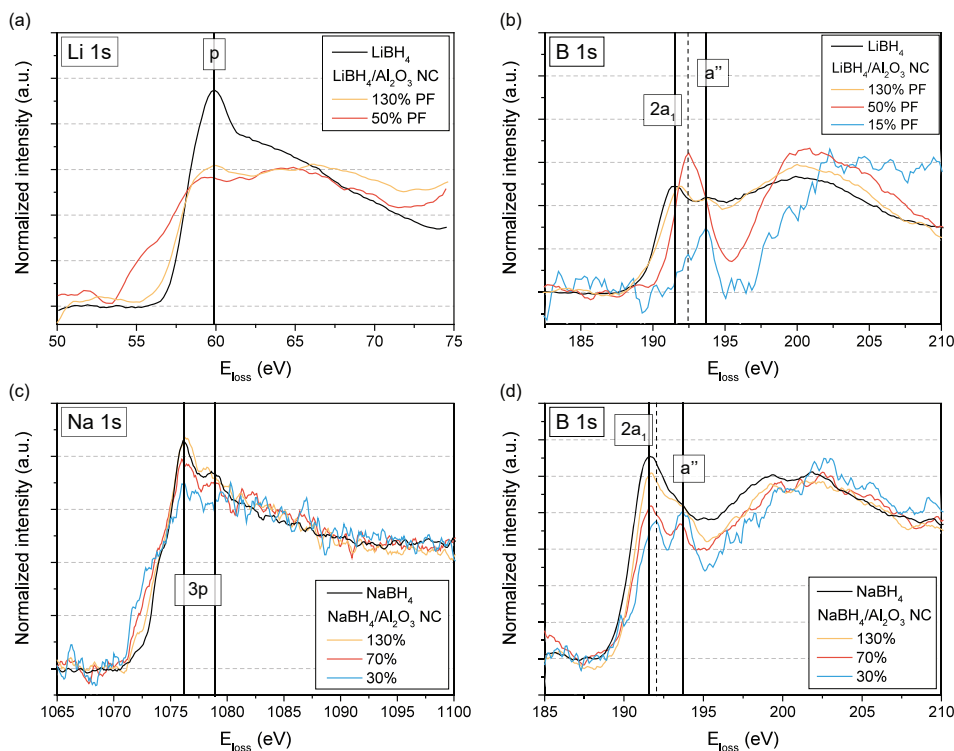


Figure 5.8 - (a) Li K-edge and (b) B K-edge XRS spectra of pristine LiBH_4 powder (95% purity) and $\text{LiBH}_4/\text{Al}_2\text{O}_3$ nanocomposites with pore filling fractions ranging of 130%, 50% and 15%. (c) Na K-edge and (d) B K-edge XRS spectra of pristine NaBH_4 powder (99.99% purity) and $\text{NaBH}_4/\text{Al}_2\text{O}_3$ nanocomposites with pore filling fractions ranging of 130%, 70% and 30%. The spectra of the nanocomposites are smoothed using adjacent averaging over 5 points.

The B K-edge spectra of the $\text{LiBH}_4/\text{Al}_2\text{O}_3$ (**Figure 5.8b**) and $\text{NaBH}_4/\text{Al}_2\text{O}_3$ (**Figure 5.8d**) nanocomposites show similarities and differences compared to the spectra of $\text{LiBH}_4/\text{SiO}_2$ (**Figure 5.3**) and $\text{NaBH}_4/\text{SiO}_2$ (**Figure 5.7**). Analogous to the SiO_2 -based nanocomposites, all $\gamma\text{-Al}_2\text{O}_3$ -based nanocomposites contain a peak around 194 eV indicative of interfacial trigonal boron compounds. Additionally, the peak at 191.5 eV that corresponds to BH_4^- becomes smaller with lower pore filling fractions. Both changes show that at the metal hydride-metal oxide interface LiBH_4 and NaBH_4 become partially oxidized and form trigonal boron species near the mesoporous oxide. Differently, the a'' peak that indicates the presence of interfacial trigonal compounds is shifted to slightly lower energies (193.7 eV) for the $\text{LiBH}_4/\text{Al}_2\text{O}_3$ and $\text{NaBH}_4/\text{Al}_2\text{O}_3$ nanocomposites, whereas it was observed around 194.1 eV in their SiO_2 -based counterparts. Furthermore, in both $\text{LiBH}_4/\text{Al}_2\text{O}_3$ and $\text{NaBH}_4/\text{Al}_2\text{O}_3$ an unidentified peak is observed around 192.0 – 192.5 eV that was not present in the spectra of $\text{LiBH}_4/\text{SiO}_2$ and $\text{NaBH}_4/\text{SiO}_2$.

These differences are likely caused by differences in the chemical nature or surface chemistry of alumina compared to silica. For example, the surface of silica generally contains about 4 to 5.5 hydroxyl groups per nm^2 , which are weak Brønsted acidic sites. The surface of $\gamma\text{-Al}_2\text{O}_3$ contains between 10 and 15 hydroxyl groups per nm^2 , both Brønsted bases and Brønsted acids. Furthermore, uncoordinated Al-sites can provide Lewis acid sites.⁴⁴ It is likely that Li^+ and BH_4^- interact differently with the $\gamma\text{-Al}_2\text{O}_3$ surface compared to the SiO_2 surface. For example, if BH_4^- interacts with an uncoordinated Al-site instead of an acidic hydroxyl group, the tetrahedral boron configuration might remain intact rather than forming a trigonal boron compound. As a result, the energy of the $1s$ to $2a_1$ transition would only shift to slightly higher energies.

To assign these subtle differences in the chemical environment of boron to specific compounds in the metal hydride-oxide interfacial layer, the experimental data needs to be supported by *ab initio* simulations. For this purpose, we are working on combining molecular dynamic studies with simulations and we are confident that this will allow us to gain more detailed understanding of the different interfacial species that are formed. Regardless, we have demonstrated for the first time that the interface layer in metal hydride/alumina nanocomposites has a distinctly different composition compared to metal hydride/silica nanocomposites, even though in both cases highly conductive nanocomposites can be obtained.

5.4 Conclusions

The chemical changes that occur in the local environment of Li, Na and B at the metal hydride-oxide interface of LiBH_4 - and NaBH_4 /oxide nanocomposites were investigated with X-ray Raman scattering. Linear combination fitting with relevant reference compounds confirms that the interface between LiBH_4 and SiO_2 consists mostly of trigonal boron compounds, for example BH_3 or LiBO_2 . Moreover, in this interface layer, part of the Li^+ ions form Li-O bonds with the oxide surface, while Li^+ ions with a weakened interaction to the surrounding anions remain present as well. By studying nanocomposites based on surface-modified SiO_2 scaffolds (i.e., Al-SiO_2 and Zr-SiO_2), the XRS data combined with electrochemical impedance spectroscopy revealed that LiBH_4 /oxide nanocomposites with a higher trigonal boron content, also exhibit higher conductivities.

The interface layer that forms between NaBH_4 and SiO_2 is composed of similar interfacial species, indicating that the interface interaction is similar in this case. In contrast, the composition of the $\text{LiBH}_4\text{-Al}_2\text{O}_3$ and $\text{NaBH}_4\text{-Al}_2\text{O}_3$ interface is distinctly different from the SiO_2 -based nanocomposites. Though the exact structure of the metal hydride- Al_2O_3 interface could not be determined, this is likely related to the difference in chemical nature of $\gamma\text{-Al}_2\text{O}_3$ compared to SiO_2 . This work has provided several new insights in the composition of the metal hydride - oxide interface. This demonstrates that X-ray Raman Scattering can give valuable information on light and amorphous materials that is not easily obtained by other techniques.

5.5 References

1. Zhao, W. *et al.* Li-Ion Conductivity Enhancement of LiBH₄·xNH₃ with in Situ Formed Li²O Nanoparticles. *ACS Appl. Mater. Interfaces* **13**, 31635–31641 (2021).
2. Luo, X., Rawal, A. & Aguey-Zinsou, K. F. Investigating the factors affecting the ionic conduction in nanoconfined NaBH₄. *Inorganics* **9**, 1–10 (2021).
3. Dou, Y., Hansen, H. A., Xu, S. M. & Blanchard, D. Layered double hydroxides as advanced tracks to promote ionic conductivity in metal borohydride. *Mater. Chem. Front.* **5**, 4989–4996 (2021).
4. Choi, Y. S. *et al.* Enhanced Li Ion Conductivity in LiBH₄-Al₂O₃ Mixture via Interface Engineering. *J. Phys. Chem. C* **121**, 26209–26215 (2017).
5. Liu, Z. *et al.* Lithium migration pathways at the composite interface of LiBH₄ and two-dimensional MoS₂ enabling superior ionic conductivity at room temperature. *Phys. Chem. Chem. Phys.* **22**, 4096–4105 (2020).
6. Lambregts, S. F. H., van Eck, E. R. H., Ngene, P. & Kentgens, A. P. M. The Nature of Interface Interactions Leading to High Ionic Conductivity in LiBH₄/SiO₂ Nanocomposites. *ACS Appl. Energy Mater.* (2022) doi:10.1021/acsaem.2c00527.
7. Hwang, S. J. *et al.* Probing molecular dynamics of metal borohydrides on the surface of mesoporous scaffolds by multinuclear high resolution solid state NMR. *J. Alloys Compd.* **645**, S316–S319 (2015).
8. Miedema, P. S. Raman Spectroscopy with X-Rays. in *Raman Spectroscopy and Applications* (InTech, 2017). doi:10.5772/65427.
9. Miedema, P. S. *et al.* In situ X-ray Raman spectroscopy of LiBH₄. *Phys. Chem. Chem. Phys.* **14**, 5581–5587 (2012).
10. Miedema, P. S. *et al.* In situ X-ray Raman spectroscopy study of the hydrogen sorption properties of lithium borohydride nanocomposites. *Phys. Chem. Chem. Phys.* **16**, 22651–22658 (2014).
11. Sahle, C. J. *et al.* In situ characterization of the decomposition behavior of Mg(BH₄)₂ by X-ray Raman scattering spectroscopy. *Phys. Chem. Chem. Phys.* **18**, 5397–5403 (2016).
12. Rajh, A. *et al.* Characterization of Electrochemical Processes in Metal–Organic Batteries by X-ray Raman Spectroscopy. *J. Phys. Chem. C* (2022) doi:10.1021/acs.jpcc.1c10622.
13. Fehse, M. *et al.* Bulk-Sensitive Soft X-ray Edge Probing for Elucidation of Charge Compensation in Battery Electrodes. *J. Phys. Chem. C* **123**, 24396–24403 (2019).
14. Nonaka, T., Kawaura, H., Makimura, Y., Nishimura, Y. F. & Dohmae, K. In situ X-ray Raman scattering spectroscopy of a graphite electrode for lithium-ion batteries. *J. Power Sources* **419**, 203–207 (2019).
15. Huotari, S., Pylkkänen, T., Verbeni, R., Monaco, G. & Hämäläinen, K. Direct tomography with chemical-bond contrast. *Nat. Mater.* **10**, 489–493 (2011).
16. Tack, P. *et al.* Identification of the Calcium, Aluminum, and Magnesium Distribution within Millimeter-Sized Extraterrestrial Materials Using Nonresonant X-ray Raman Spectroscopy in Preparation for the Hayabusa2 Sample Return Mission. *Anal. Chem.* **93**, 14651–14658 (2021).
17. Georgiou, R. *et al.* Carbon speciation in organic fossils using 2D to 3D x-ray Raman multispectral imaging. *Sci. Adv.* **5**, 1–10 (2019).
18. Brunauer, S., Emmett, P. H. & Teller, E. Adsorption of Gases in Multimolecular Layers. *J. Am. Chem. Soc.* **60**, 309–319 (1938).
19. Barrett, E. P., Joyner, L. G. & Halenda, P. P. The Determination of Pore Volume and Area Distributions in Porous Substances. I. Computations from Nitrogen Isotherms. *J. Am. Chem. Soc.* **73**, 373–380 (1951).
20. Johnson, D. L. Local field effects and the dielectric response matrix of insulators: A model. *Phys. Rev. B* **9**, 4475–4484 (1974).
21. Sahle, C. J. *et al.* Planning, performing and analyzing X-ray Raman scattering experiments. *J.*

- Synchrotron Radiat.* **22**, 400–409 (2015).
22. Gulino, V., Barberis, L., Ngene, P., Baricco, M. & De Jongh, P. E. Enhancing Li-Ion Conductivity in LiBH₄-Based Solid Electrolytes by Adding Various Nanosized Oxides. *ACS Appl. Energy Mater.* **3**, 4941–4948 (2020).
 23. Blanchard, D. *et al.* Nanoconfined LiBH₄ as a fast lithium ion conductor. *Adv. Funct. Mater.* **25**, 184–192 (2015).
 24. Suwarno *et al.* Confinement Effects for Lithium Borohydride: Comparing Silica and Carbon Scaffolds. *J. Phys. Chem. C* **121**, 4197–4205 (2017).
 25. Lee, S. K., Eng, P. J., Mao, H. K., Meng, Y. & Shu, J. Structure of alkali borate glasses at high pressure: B and Li K-edge inelastic X-ray scattering study. *Phys. Rev. Lett.* **98**, 1–4 (2007).
 26. Wang, D. & Zuin, L. Li K-edge X-ray absorption near edge structure spectra for a library of lithium compounds applied in lithium batteries. *J. Power Sources* **337**, 100–109 (2017).
 27. Tsuji, J. *et al.* Lithium K-edge XANES spectra for lithium compounds. *X-Ray Spectrom.* **31**, 319–326 (2002).
 28. Pascal, T. A. *et al.* Finite temperature effects on the X-ray absorption spectra of lithium compounds: First-principles interpretation of X-ray Raman measurements. *J. Chem. Phys.* **140**, (2014).
 29. Hallmeier, K. H., Szargan, R., Meisel, A., Hartmann, E. & Gluskin, E. S. Investigation of core-excited quantum yield spectra of high-symmetric boron compounds. *Spectrochim. Acta Part A Mol. Spectrosc.* **37**, 1049–1053 (1981).
 30. Fleet, M. E. & Liu, X. Boron K-edge XANES of boron oxides: Tetrahedral B-O distances and near-surface alteration. *Phys. Chem. Miner.* **28**, 421–427 (2001).
 31. Fleet, M. E. & Muthupari, S. Boron K-edge XANES of borate and borosilicate minerals. *Am. Mineral.* **85**, 1009–1021 (2000).
 32. Fleet, M. E. & Muthupari, S. Coordination of boron in alkali borosilicate glasses using XANES. *J. Non. Cryst. Solids* **255**, 233–241 (1999).
 33. Yumatov, V. D., Il'inchik, E. A., Mazalov, L. N., Volkov, O. V. & Volkov, V. V. X-ray and X-ray photoelectron spectroscopy studies of the electronic structure of borane derivatives. *J. Struct. Chem.* **42**, 281–295 (2001).
 34. Qiao, R., Chuang, Y. De, Yan, S. & Yang, W. Soft X-Ray Irradiation Effects of Li₂O₂, Li₂CO₃ and Li₂O Revealed by Absorption Spectroscopy. *PLoS One* **7**, 3–8 (2012).
 35. Yang, S. *et al.* Soft X-ray XANES studies of various phases related to LiFePO₄ based cathode materials. *Energy Environ. Sci.* **5**, 7007 (2012).
 36. Choi, Y. S., Lee, Y. S., Oh, K. H. & Cho, Y. W. Interface-enhanced Li ion conduction in a LiBH₄-SiO₂ solid electrolyte. *Phys. Chem. Chem. Phys.* **18**, 22540–22547 (2016).
 37. Matsuo, M., Nakamori, Y., Orimo, S. I., Maekawa, H. & Takamura, H. Lithium superionic conduction in lithium borohydride accompanied by structural transition. *Appl. Phys. Lett.* **91**, 2–5 (2007).
 38. De Kort, L. M., Harmel, J., De Jongh, P. E. & Ngene, P. The effect of nanoscaffold porosity and surface chemistry on the Li-ion conductivity of LiBH₄-LiNH₂/metal oxide nanocomposites. *J. Mater. Chem. A* **8**, 20687–20697 (2020).
 39. Baca, M. *et al.* Characterization of mesoporous alumina prepared by surface alumination of SBA-15. *Microporous Mesoporous Mater.* **110**, 232–241 (2008).
 40. Klimova, T., Peña, L., Lizama, L., Salcedo, C. & Gutiérrez, O. Y. Modification of activity and selectivity of NiMo/SBA-15 HDS catalysts by grafting of different metal oxides on the support surface. *Ind. Eng. Chem. Res.* **48**, 1126–1133 (2009).
 41. Ryoo, R., Jun, S., Kim, J. M. & Kim, M. J. Generalised route to the preparation of mesoporous metallosilicates via post-synthetic metal implantation. *Chem. Commun.* **41**, 2225–2226 (1997).
 42. Teodorescu, C. M., El Afif, A., Esteva, J. M. & Karnatak, R. C. Na 1s excitations in vapor and solid sodium halides. *Phys. Rev. B* **63**, 233106 (2001).

43. Neuville, D. R., Cormier, L., Flank, A.-M., Prado, R. J. & Lagarde, P. Na K-edge XANES spectra of minerals and glasses. *Eur. J. Mineral.* **16**, 809–816 (2004).
44. Chorkendorff, I. & Niemantsverdriet, J. W. *Concepts of Modern Catalysis and Kinetics*. (John Wiley & Sons, 2003). doi:10.1002/3527602658.ch5.



6

Exploratory study on Li- and Na-ion conduction in nitrate- and nitrite/oxide nanocomposites

In the previous chapters, it has been shown that nanocomposite formation significantly improves the conductivity of metal hydrides. However, besides metal hydrides, other classes of materials have been proposed as electrolytes for all-solid-state batteries. Nanocomposite formation might also be beneficial for the performance of these materials. Hence, as a proof-of-principle the effect of nanocomposite formation on the ionic conductivity of LiNO_3 , NaNO_2 and NaNO_3 was investigated. We show that this approach is indeed effective in enhancing the ionic conductivity of these non-hydride-based materials. Their conductivities are improved by over three orders of magnitude to $1.1 \cdot 10^{-5} \text{ S cm}^{-1}$, $1.1 \cdot 10^{-4} \text{ S cm}^{-1}$, and $1.4 \cdot 10^{-5} \text{ S cm}^{-1}$ at 80°C for $\text{LiNO}_3/\text{Nb}_2\text{O}_5$, $\text{NaNO}_2/\text{Al}_2\text{O}_3$ and $\text{NaNO}_3/\text{Al}_2\text{O}_3$, respectively. In general, the conductivity of these nanocomposites strongly depends on properties of the scaffold, as observed for metal hydride/oxide nanocomposites. In particular, we found that the conductivity of LiNO_3 /oxide nanocomposites increases with an increasing amount of acid sites present on the surface of the scaffold. This work demonstrates that nanocomposite formation is a versatile strategy that can be applied to a wide variety of ion conductors, both hydrides and oxides.

This chapter is based on: de Kort, L. M., van Ittersum, M. E. T., Peerlings, M. L. J., De Jongh, P. E. & Ngene, P., Enhanced Li- and Na-ion conductivity in LiNO_3 -, NaNO_2 - and NaNO_3 /oxide nanocomposites. *In preparation*.

6.1 Introduction

A wide variety of solid-state ion conductors are being investigated for implementation in all-solid-state batteries, as discussed in **Chapter 1**. In addition to metal hydrides, ion conductors based on polymers, sulfides and oxides have shown potential for application as solid electrolytes. Each class of materials has their own advantages and disadvantages. Similar to pristine complex hydrides, the properties of these ion conductors must be improved before they can be used for battery operation. Nanocomposite formation might be beneficial for the ion conductivity and electrochemical properties of these ion conductors. In fact, nanocomposite formation could even improve the mechanical properties and material cost of a solid electrolyte, in addition to an enhancement in conductivity. For example, composite solid electrolytes in which a polymer is combined with an inorganic solid are expected to simultaneously display improved ionic conductivity and mechanical strength, whilst maintaining the intrinsic flexibility and stability of the polymer.¹

Similar to metal hydride/oxide nanocomposites, it is likely that the chemical and physical properties of the oxide have an impact on the performance of the solid electrolyte. Unfortunately, studies on the influence of the mesoporous metal oxides on the ionic conductivity of non-hydride-based nanocomposites are scarce. In 2003, Anantha *et al.* reported on the enhanced conductivity in NaNO_3 /oxide nanocomposites based on CeO_2 , ZrO_2 , $\gamma\text{-Al}_2\text{O}_3$ and SiO_2 , which displays widely different conductivities depending on the oxide.^{2,3} The conductivity improvement was ascribed to the formation of an interfacial space charge layer.² To the best of our knowledge, no further investigation on the influence of metal oxides on the conductivity of MNO_3 nanocomposites, with $\text{M} = \text{Li}^+$ and Na^+ , has been performed to date.

In this exploratory study, we used LiNO_3 , NaNO_2 and NaNO_3 as a proof of principle to show that nanocomposite formation can be applied to widely different solid-state ion conductors, ranging from hydrides to oxides. Moreover, we have studied how the Li- and Na-ion conductivity in LiNO_3 , NaNO_2 and NaNO_3 depends on the chemical nature of the metal oxide. To this end, nanocomposites based on LiNO_3 , NaNO_2 and NaNO_3 were prepared with several mesoporous scaffolds, i.e., SiO_2 , $\gamma\text{-Al}_2\text{O}_3$, TiO_2 , and Nb_2O_5 . The results revealed that the ionic conductivity of the nanocomposites can be improved by over three orders of magnitude compared to the pristine compounds. Similar to hydride-based nanocomposites, the extent of the improvement depends on the mesoporous scaffold.

6.2 Experimental methods

Scaffold preparation

Mesoporous silica (SiO₂, SBA-15) was synthesized following the procedures described by Lee et al.⁴ To start, Pluronic P123 (EO₂₀PO₇₀EO₂₀, average Mw = 5800, Aldrich) was dissolved in a mixture of deionized water and hydrochloric acid (37% fuming, Emsure, analysis grade). The mixture was stirred vigorously for at least three hours at 55 °C in a cylindrical polypropylene bottle (1 L, h = 19.7 cm, Ø = 10.5 cm). About 50.0 g tetraethyl orthosilicate (TEOS, > 99%, Aldrich) was added to obtain a weight ratio of TEOS : Pluronic P123 : deionized water : HCl of 2:1:26:6. The mixture was stirred for two minutes at 600 rpm, after which the stirring bar was removed and the reaction bottle was closed. The mixture was kept at 55 °C for 24 hours. Following, the SBA-15 was allowed to condensate further at 90 °C for 24 hours. The as-prepared SBA-15 was filtered and washed with deionized water using a Büchner funnel until no HCl was left in the solution. The material was dried at 60 °C for 3 days and calcined in static air at 550 °C (heating rate 1 °C min⁻¹) for 6 hours. Alumina (γ-Al₂O₃, Puralex SCCa-5/200, Sasol), titanium oxide (TiO₂, Aeroxide P90, Evonik), and niobium(V) oxide hydrate (Nb₂O₅·nH₂O, AD/4465, CBMM) were purchased. All scaffolds were dried under vacuum at 120 – 200 °C overnight and transferred to an argon-filled glovebox before use.

Nanocomposite synthesis

Preparation of the LiNO₃, NaNO₂, and NaNO₃/metal oxide nanocomposites was achieved via melt infiltration based on the procedure of Ngene et al.⁵ LiNO₃, NaNO₂ and NaNO₃ were either purchased in non-hydrated form (LiNO₃) or dried at 150 °C under vacuum (NaNO₂ and NaNO₃) to obtain the non-hydrated form. The Li- or Na-compounds were mixed with the appropriate amount of the oxide scaffold in order to fill the scaffold pores by (typically) 130 volume percent. In this way, the nitrate/nitrite content is 30 vol% larger than the total pore volume of the scaffold material. This ensures a percolating network of fast ion diffusion pathways over the non-conducting oxide particles. The physical mixture was transferred to a glass reactor, which was placed in a stainless-steel high-pressure autoclave (Parr, 250 mL). The autoclave was pressurized with 30 bar Ar and melt infiltration was carried out for 30 minutes at either 275 °C (heating rate 2.5 °C min⁻¹) for LiNO₃ and at 300 °C (heating rate 3.2 °C min⁻¹) for NaNO₂ and NaNO₃. Upon cooling, the molten LiNO₃, NaNO₂ or NaNO₃ solidifies in the pores of the oxide to form a LiNO₃-, NaNO₃- or NaNO₂/oxide nanocomposite.

General characterization

X-ray diffraction (XRD) was performed with a Bruker-AXS D8 Advance X-ray diffractometer with Co Kα_{1,2} radiation (λ = 1.78897 Å). The samples were placed in an airtight sample holder. Diffractograms were recorded at room temperature from 20 to 80° 2θ. Diffuse reflectance infrared Fourier transform spectroscopy (DRIFTS) measurements were performed on a Perkin-Elmer 2000 spectrometer equipped with a MCT detector. The sample was placed in an airtight sample holder with KBr windows. Spectra were acquired from 900 cm⁻¹ to 4500 cm⁻¹ with a resolution of 4 cm⁻¹. Differential scanning calorimetry (DSC) was conducted using a Mettler Toledo HP DSC 1-STAR. About 10 mg of sample was placed in a 40 µL Al sample pan. The measurement was performed under 2 bar Ar pressure

and an Ar flow of 10 mL min⁻¹. The samples were cycled between 30 °C and 300 °C (LiNO₃) or 320 °C (NaNO₂, NaNO₃) with a heating rate of 5 °C min⁻¹. Three heating and cooling cycles were performed. Nitrogen physisorption measurements were carried out at -196 °C on a Micromeritics TriStar II Plus analyser. No drying procedure was performed prior to the measurements, as all measured samples were stored under controlled atmosphere in an argon-filled glovebox. Analysis of the adsorption and desorption curves was performed following Brunauer, Emmett and Teller (BET) theory and Barrett, Joyner and Halenda (BJH) theory to determine surface area and pore size distribution, respectively.^{6,7} The specific surface area (A_{BET}), total pore volume and average pore size of the scaffolds as determined by the adsorbed quantity close to nitrogen saturation pressure ($p = p_0$) are summarized in **Table 6.1**.

Table 6.1 – Nitrogen physisorption results of oxide scaffolds

Oxide scaffold	BET area (m ² g ⁻¹)	Pore volume (cm ³ g ⁻¹)	Average pore diameter (nm)
SBA -15 (SiO ₂)	787	1.14	6.7
γ -Al ₂ O ₃	172	0.45	8.7
TiO ₂	87	0.47	61 (broad range from 30 - 90)
Nb ₂ O ₅	143	0.12	3.9

Conductivity measurements

Electrochemical impedance spectroscopy measurements were performed using a Princeton Applied Research Parstat 2273 potentiostat connected to a custom-made measurement cell in a Büchi B-585 glass oven placed in an argon-filled glovebox to avoid air and moisture exposure. Symmetrical pellets were prepared by pressing 150 – 350 mg samples between two lithium or sodium covered stainless steel cylinders ($\varnothing = 13$ mm) with a pressure of 150 MPa. The prepared pellet was placed in the measurement cell. In a typical conductivity measurement, the pellet is incrementally heated to 130 °C ($\Delta T = 10$ °C) and incrementally cooled to room temperature ($\Delta T = 20$ °C). After temperature equilibration at each increment for 45 minutes, an EIS measurement was performed using a 20 mV RMS modulated AC potential with frequencies from 1 MHz to 1 Hz. The Nyquist plots obtained from the data were fitted using an equivalent circuit consisting of a resistance and a constant phase element connected in parallel. The intersection of the fitted semicircle with the Z_{real} axis was assumed to represent the electrolyte resistance R . Following $\sigma = t/(AR)$, the conductivity σ of the solid electrolytes could be calculated using the electrolyte thickness t and geometric surface area A of the electrodes.

The electronic conductivity has been measured using DC voltage polarization measurements.^{8,9} The NaNO₂/Al₂O₃ nanocomposite was pressed into a pellet between two stainless steel cylinders ($\varnothing = 10$ mm) with a pressure of 190 MPa. Using a Parstat PMC-1000 potentiostat, a voltage of 0.5 V was applied across the pellet and the resulting current was measured for 1 hour. The total conductivity was determined by performing an EIS measurement using a 10 mV RMS modulated AC potential with frequencies from 1 MHz to 1 Hz before and after the polarization measurement.

Surface chemistry analysis

The surface acidity of the scaffold was studied using pyridine and NH_3 as probe molecules. Adsorption and desorption of pyridine was followed with Fourier transform infrared (FT-IR) spectroscopy. The measurements were performed on a Perkin Elmer System 2000 with a DTGS detector. Spectra were recorded in transmission mode in the spectral range of $400 - 4000 \text{ cm}^{-1}$ with a resolution of 4 cm^{-1} . The sample ($\sim 10 \text{ mg}$) was pressed into a self-supporting wafer ($\varnothing = 7 \text{ mm}$) and placed in an air-tight measurement cell. At room temperature, pyridine vapour ($22\text{--}23 \text{ mbar}$) was dosed onto the sample for at least 30 minutes until saturation. Physisorbed pyridine was removed by evacuation for 30 minutes, after which the sample was heated to $150 \text{ }^\circ\text{C}$ ($2.5 \text{ }^\circ\text{C min}^{-1}$) followed by equilibration for 30 minutes. Subsequently, the sample was heated from $150 \text{ }^\circ\text{C}$ to $550 \text{ }^\circ\text{C}$ ($10 \text{ }^\circ\text{C min}^{-1}$), while recording spectra every $50 \text{ }^\circ\text{C}$ to follow the thermal pyridine desorption. The amounts of Brønsted and Lewis acid sites were determined by peak integration of the absorbance peaks at 1545 cm^{-1} (Brønsted) and 1455 cm^{-1} (Lewis).^{10–12} Assuming one pyridine molecule absorbs per acid site, Lambert Beer's law can be applied to determine the concentration C of Lewis and Brønsted sites¹¹:

$$C = \frac{A}{A_0 \rho} \quad (6.1)$$

Here, A is the integrated absorbance of the IR band corresponding to pyridine adsorbed on Brønsted (1545 cm^{-1}) or Lewis (1455 cm^{-1}) sites and A_0 represents the integral absorption coefficient of these bands, respectively, 1.67 and $2.22 \text{ cm } \mu\text{mol}^{-1}$. The effective cross-section ρ can be calculated using the mass and area of the sample wafer.

NH_3 -Temperature programmed desorption (TPD) measurements were performed on Micrometer Autochem II equipped with a thermal conductivity detector (TCD). About 80 to 100 mg of sample was placed in a glass tube. Subsequently, the sample was dried in-situ under a He flow ($50 \text{ cm}^3 \text{ STP min}^{-1}$) at $200 \text{ }^\circ\text{C}$ ($10 \text{ }^\circ\text{C min}^{-1}$) for 10 minutes. After drying, the sample was cooled down to $100 \text{ }^\circ\text{C}$. At this temperature, 15 ammonia pulses of $25 \text{ cm}^3 \text{ min}^{-1}$ were given to achieve saturation of the sample. Any physisorbed NH_3 was removed under flowing He ($50 \text{ cm}^3 \text{ min}^{-1}$) for 60 minutes. In a final step, thermal NH_3 desorption was carried out by heating the sample to $600 \text{ }^\circ\text{C}$ ($10 \text{ }^\circ\text{C min}^{-1}$, $50 \text{ cm}^3 \text{ min}^{-1}$ He flow). The amount of acid sites could be quantified after baseline subtraction and Gaussian peak fitting of the TCD concentrations versus time.^{13,14}

6.3 Results and Discussion

6.3.1 LiNO_3 -, NaNO_2 - and NaNO_3 /oxide nanocomposites based on SiO_2 and Al_2O_3

The impact of nanocomposite formation on the structural properties of LiNO_3 , NaNO_2 and NaNO_3 was first evaluated for nanocomposites based on mesoporous $\gamma\text{-Al}_2\text{O}_3$ and SiO_2 . The structural changes and effectiveness of the synthesis method, i.e., incorporation of LiNO_3 , NaNO_2 and NaNO_3 in the pores of the mesoporous scaffolds, as observed by DRIFTS and DSC will be discussed. In **Figure 6.1** the DRIFTS absorbance results of the $\text{LiNO}_3/\text{Al}_2\text{O}_3$ and $\text{LiNO}_3/\text{SiO}_2$ nanocomposites, as well as pure LiNO_3 , $\gamma\text{-Al}_2\text{O}_3$ and SiO_2 are shown. In the spectra, two regions of interest are identified. First, macrocrystalline LiNO_3 displays several characteristic bands between 3000 cm^{-1} and 1700 cm^{-1} . In the spectra of both $\text{LiNO}_3/\text{SiO}_2$ and $\text{LiNO}_3/\text{Al}_2\text{O}_3$ these bands are observed as well, which indicates that LiNO_3 did not decompose during the nanocomposite synthesis. Furthermore, all vibrations observed in the nanocomposite spectra can be ascribed to either LiNO_3 or the scaffolds. This shows that no new compounds were formed during melting and infiltration into the scaffold pores, confirming that LiNO_3 is stable during melt infiltration. The characteristic LiNO_3 bands are slightly less intense compared to pristine LiNO_3 . This is due to the presence of the mesoporous oxide, which dilutes the amount of LiNO_3 and reduces the intensity of the LiNO_3 vibrations.

The second region of interest is ascribed to the hydroxyl stretching vibrations in SiO_2 and $\gamma\text{-Al}_2\text{O}_3$ between 3850 cm^{-1} and 3000 cm^{-1} .¹⁵⁻¹⁷ For SiO_2 , a broad band between $3700\text{-}3000\text{ cm}^{-1}$ is observed, which represents hydrogen bound (vicinal) silanol groups and physisorbed water. Additionally, a sharp absorption peak around 3747 cm^{-1} is ascribed to "free" silanol groups, i.e. isolated and geminal silanol groups.¹⁶ For $\gamma\text{-Al}_2\text{O}_3$, several broad bands related to vibrations of linear and bridged hydroxyl groups, as well as physisorbed water, are observed in the region between $3800\text{-}3000\text{ cm}^{-1}$.¹⁵ After melt infiltration the vibrations corresponding to linear and bridged hydroxyl groups on $\gamma\text{-Al}_2\text{O}_3$ are no longer visible in the spectrum of the $\text{LiNO}_3/\text{Al}_2\text{O}_3$ nanocomposite. This contrasts with the spectrum of the $\text{LiNO}_3/\text{SiO}_2$ nanocomposite, where the silanol peak at 3747 cm^{-1} is still clearly present. In previous studies, it has been found that the hydroxyl vibrations disappear when

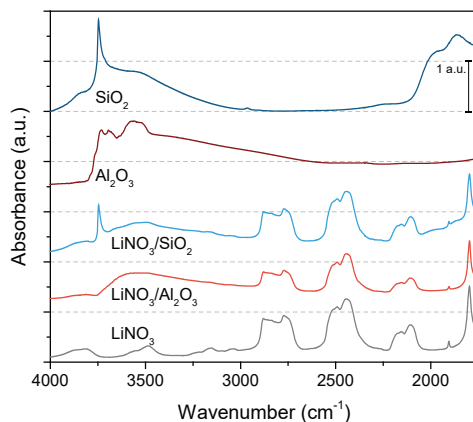


Figure 6.1 - DRIFTS spectra of LiNO_3 /oxide nanocomposites displaying the regions related to hydroxyl stretching vibrations, as well as characteristic LiNO_3 vibrations. The spectrum of LiNO_3 , SiO_2 and $\gamma\text{-Al}_2\text{O}_3$ are shown for comparison.

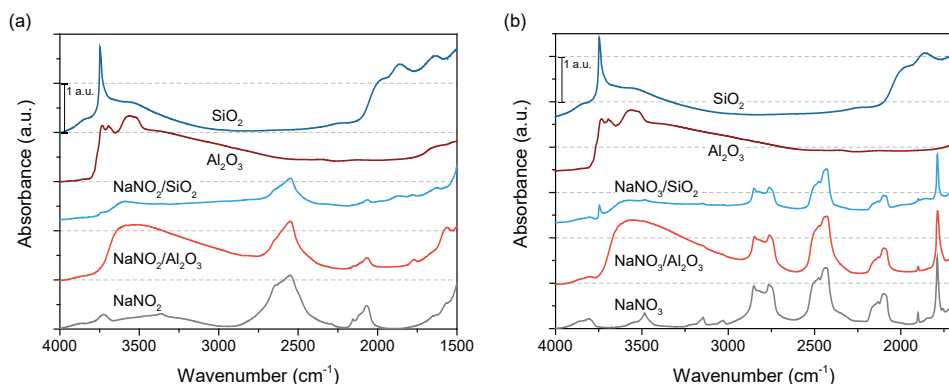


Figure 6.2 - DRIFTS spectra of (a) NaNO_2 /oxide and (b) NaNO_3 /oxide nanocomposites displaying the regions related to hydroxyl stretching vibrations, as well as characteristic NaNO_2 and NaNO_3 vibrations. The spectrum of pristine NaNO_2 , NaNO_3 , SiO_2 and $\gamma\text{-Al}_2\text{O}_3$ are shown for comparison.

the surface of the scaffold becomes covered with the infiltrated compound, because the hydroxyl vibrations are suppressed by interactions or reactions between the $[\text{OH}]$ groups and the infiltrate.^{18,19} Thus, the disappearance of the hydroxyl vibrations in the $\text{LiNO}_3/\text{Al}_2\text{O}_3$ spectrum indicates that (part of the) LiNO_3 has infiltrated the pores of $\gamma\text{-Al}_2\text{O}_3$ and interacts with the surface groups, while the presence of the silanol vibration for the $\text{LiNO}_3/\text{SiO}_2$ nanocomposites suggests that the pores of SiO_2 remain (largely) empty or that LiNO_3 does not interact with the surface groups.

In the same way, DRIFTS analysis is used to study the structural properties of NaNO_2 /oxide nanocomposites and NaNO_3 /oxide nanocomposites based on SiO_2 and $\gamma\text{-Al}_2\text{O}_3$. The DRIFTS spectra of the nanocomposites and the pure compounds are provided in **Figure 6.2**. In all nanocomposite spectra characteristic bands ascribed to either NaNO_2 or NaNO_3 ($3000 - 1700 \text{ cm}^{-1}$) are clearly present, confirming that both compounds are stable during nanocomposite formation, i.e., melt infiltration. Identical to the LiNO_3 /oxide nanocomposites, the vibrations that correspond to surface hydroxyl groups on $\gamma\text{-Al}_2\text{O}_3$ ($3700 - 3500 \text{ cm}^{-1}$) cannot be clearly distinguished in the $\text{NaNO}_2/\text{Al}_2\text{O}_3$ and $\text{NaNO}_3/\text{Al}_2\text{O}_3$ spectra. The peak that corresponds to the silanol vibration can still be observed in the spectra of $\text{NaNO}_2/\text{SiO}_2$ and $\text{NaNO}_3/\text{SiO}_2$, though it is less intense. Hence, both NaNO_2 and NaNO_3 seem to completely cover the surface of mesoporous $\gamma\text{-Al}_2\text{O}_3$, while this is not the case for the SiO_2 scaffold, similar to the LiNO_3 /oxide nanocomposites.

The incorporation of LiNO_3 , NaNO_2 and NaNO_3 in the pores of the mesoporous scaffolds is studied in further detail with differential scanning calorimetry (DSC). The DSC curves of $\text{LiNO}_3/\text{Al}_2\text{O}_3$ and $\text{LiNO}_3/\text{SiO}_2$ nanocomposites as well as pure LiNO_3 are presented in **Figure 6.3a**. In the DSC curve of LiNO_3 an endothermic peak starting at 251°C is observed, which is attributed to melting of macrocrystalline LiNO_3 .^{20,21} Using integration of the peak area, it was possible to verify that the enthalpy of the phase transition is -387 J g^{-1} , in accordance with literature.^{20,21} Likewise, in the DSC curves of both LiNO_3 /metal oxide nanocomposites an endothermic peak related to melting of macrocrystalline LiNO_3 was observed starting between 246 and 250°C . Furthermore, in addition to the peak that is related to macrocrystalline LiNO_3 , a second endothermic peak between 180°C and 235°C is clearly observed in the DSC curve of $\text{LiNO}_3/\text{Al}_2\text{O}_3$. This peak is ascribed to melting of

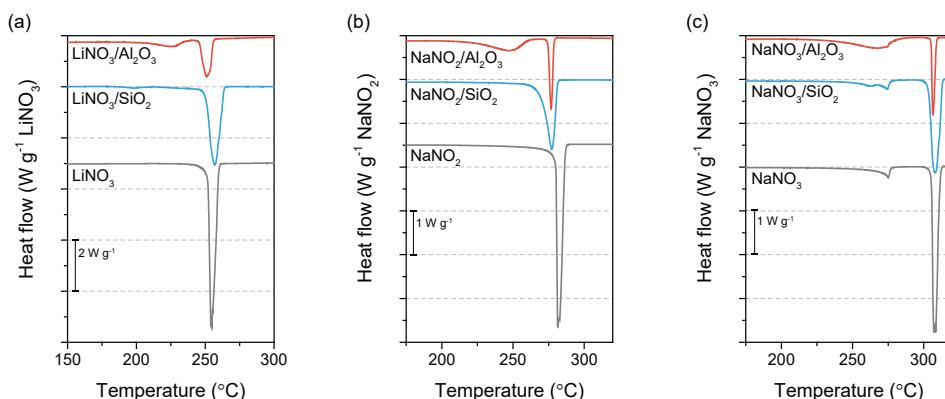


Figure 6.3 - DSC graphs of (a) LiNO_3 -, (b) NaNO_2 -, and (c) NaNO_3 /oxide nanocomposites based on SiO_2 and $\gamma\text{-Al}_2\text{O}_3$. To compare, the DSC graphs of LiNO_3 , NaNO_2 and NaNO_3 are included.

nanoconfined LiNO_3 , demonstrating that LiNO_3 infiltrated the pores of $\gamma\text{-Al}_2\text{O}_3$. Upon close examination of the DSC curve of $\text{LiNO}_3/\text{SiO}_2$, a small peak related to nanoconfined LiNO_3 is observed as well. This indicates that a small fraction of LiNO_3 has been incorporated in the pores of SiO_2 .

From the peak area and the melting enthalpy of the LiNO_3 , it is possible to calculate the fraction of extraporous (macrocrystalline) LiNO_3 . Combined with the total amount of LiNO_3 present in the nanocomposites, this can be used to estimate the amount of intraporous (nanoconfined) LiNO_3 and thereby the percentage of the scaffold pore volume that is filled.²² The results are summarized in **Table 6.2**. They confirm that 30% of the total amount of LiNO_3 is present as extraporous LiNO_3 , which means that 70% is confined inside the scaffold pores. As a result, LiNO_3 completely fills the pores of the $\gamma\text{-Al}_2\text{O}_3$ scaffold. This nicely corresponds to the intended nanocomposite composition in which the scaffold pores are filled with LiNO_3 , while extraporous LiNO_3 is present to ensure sufficient Li^+ conduction over the non-conducting oxide particles. On the other hand, for the $\text{LiNO}_3/\text{SiO}_2$ nanocomposite it was found that most of the LiNO_3 content ($\sim 75\%$) remained outside of the scaffold, while only 34% of the SiO_2 pore volume was filled with LiNO_3 . Thus, DRIFTS and DSC analysis demonstrate that melt infiltration synthesis has resulted in the complete infiltration of LiNO_3 in the pores of the $\gamma\text{-Al}_2\text{O}_3$ scaffold, while only partial incorporation is realized for the SiO_2 -based nanocomposite.

Table 6.2 - Differential Scanning Calorimetry results of LiNO_3 -, NaNO_2 - and NaNO_3 /oxide nanocomposites based on SiO_2 and $\gamma\text{-Al}_2\text{O}_3$

Infiltrate	LiNO_3		NaNO_2		NaNO_3	
Nanocomposite	$\text{LiNO}_3/\text{SiO}_2$	$\text{LiNO}_3/\text{Al}_2\text{O}_3$	$\text{NaNO}_2/\text{SiO}_2$	$\text{NaNO}_2/\text{Al}_2\text{O}_3$	$\text{NaNO}_3/\text{SiO}_2$	$\text{NaNO}_3/\text{Al}_2\text{O}_3$
Extra : Intra porous LiNO_3	75 : 25	30 : 70	78 : 22	19 : 81	88 : 22	26 : 74
Ratio infiltrate volume : pore volume	0.34	1.04	0.36	1.04	0.12	0.96

The results of the DSC measurements on the NaNO_2 - and NaNO_3 /oxide nanocomposites are shown in **Figure 6.3b** and **6.3c**. In the DSC curves of each nanocomposite an endothermic peak related to melting of either macrocrystalline NaNO_2 or NaNO_3 is observed at 275 and 305 °C, respectively.^{20,21,23} For NaNO_3 an additional peak is present at 275 °C related to a reversible lattice expansion.^{23,24} Based on the area of the melting peak, the fraction of intra- and extraporous NaNO_2 or NaNO_3 , and thereby the fraction of the pore volume that is filled, was determined. A summary of the nanocomposite compositions as derived from these measurements is provided in **Table 6.2**. Similar to $\text{LiNO}_3/\text{Al}_2\text{O}_3$ nanocomposite, after melt infiltration with NaNO_2 and NaNO_3 the pores of $\gamma\text{-Al}_2\text{O}_3$ are completely filled and a small fraction of NaNO_2 or NaNO_3 resides on the outer surface of the scaffold. In the $\text{NaNO}_2/\text{SiO}_2$ and $\text{NaNO}_3/\text{SiO}_2$ nanocomposites the scaffold pores are only filled for 36% and 12%, respectively. Consequently, a large fraction has not infiltrated the scaffold pores and is present as extraporous NaNO_2 or NaNO_3 . Overall, these results show that LiNO_3 , NaNO_2 and NaNO_3 are successfully infiltrated into mesoporous $\gamma\text{-Al}_2\text{O}_3$, while they are only partially incorporated into the SiO_2 scaffold.

Further evidence for the incorporation of LiNO_3 , NaNO_2 and NaNO_3 in the pores of mesoporous SiO_2 and $\gamma\text{-Al}_2\text{O}_3$ is provided by XRD and N_2 physisorption. The XRD diffraction patterns for the $\gamma\text{-Al}_2\text{O}_3$ -based nanocomposites show a loss of crystallinity, as expected for nanoconfined material. On the other hand, in the diffraction patterns of the SiO_2 -based nanocomposites, peaks related to the macrocrystalline LiNO_3 , NaNO_2 or NaNO_3 are clearly observed. Furthermore, using N_2 physisorption a gradual loss in pore volume is observed with when increasing the NaNO_2 or NaNO_3 content in NaNO_2 - and $\text{NaNO}_3/\text{Al}_2\text{O}_3$ nanocomposites. In contrast, for NaNO_2 - and $\text{NaNO}_3/\text{SiO}_2$ nanocomposites, the pore volume becomes negligible even with a low NaNO_2 or NaNO_3 content, indicating that the pores become blocked instead of partially filled. These observations are consistent with a complete infiltration in mesoporous $\gamma\text{-Al}_2\text{O}_3$ and partial incorporation in mesoporous SiO_2 . Note that similar results were obtained for the $\text{NaBH}_4/\text{SiO}_2$ and $\text{NaBH}_4/\text{Al}_2\text{O}_3$ nanocomposites discussed in **Chapter 2**, where the pores of the SiO_2 scaffold were only partially filled with NaBH_4 , resulting in a low ionic conductivity.

From the comparison of $\gamma\text{-Al}_2\text{O}_3$ and SiO_2 -based nanocomposites, it is clear

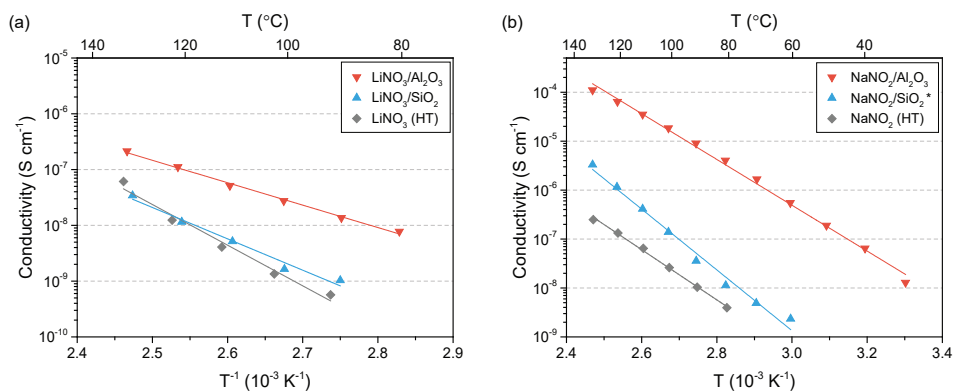


Figure 6.4 - Arrhenius plots of conductivity versus reciprocal temperature of (a) LiNO_3 /oxide and (b) NaNO_2 /oxide nanocomposites based on SiO_2 (blue) and $\gamma\text{-Al}_2\text{O}_3$ (red), as well as pristine LiNO_3 or NaNO_2 .

that incorporation of LiNO_3 , NaNO_2 and NaNO_3 depends on the properties of the mesoporous scaffold. The theory of melt infiltration synthesis provides an explanation for this behaviour.²² During melt infiltration, liquids are drawn in the pores of the chosen scaffold by capillary forces. Whether infiltration can occur or not, largely depends on the physicochemical properties of the infiltrate, the surface chemistry of the scaffold and the interfacial interaction between the infiltrate and the mesoporous material, i.e., wetting properties of the infiltrate on the scaffold surface. If the liquid infiltrate wets the solid, infiltration is spontaneous. If the liquid does not wet the surface of the solid, it does not infiltrate the scaffold.^{22,25} The surface energy for SiO_2 (0.26 J m^{-2}) is significantly lower than that of $\gamma\text{-Al}_2\text{O}_3$ (1.52 J m^{-2}).^{26,27} Young's equation (equation 2.1) shows that it is more difficult for an infiltrate to wet a SiO_2 surface than a $\gamma\text{-Al}_2\text{O}_3$ surface. Consequently, LiNO_3 , NaNO_2 and NaNO_3 are more readily incorporated in the $\gamma\text{-Al}_2\text{O}_3$ scaffold.

6.3.2 Nanocomposite conductivity of SiO_2 - and Al_2O_3 -based nanocomposites

The effect of nanocomposite formation with SiO_2 and $\gamma\text{-Al}_2\text{O}_3$ on the conductivity of LiNO_3 , NaNO_2 and NaNO_3 is analysed by recording the complex impedance of the prepared nanocomposites over a range of temperatures. The conductivities of the LiNO_3 - and NaNO_2 /oxide nanocomposites are displayed in **Figure 6.4**. Heat-treated (HT) LiNO_3 and NaNO_2 , which were treated under the same conditions as the melt infiltration synthesis, are included for comparison. Interestingly, in both cases the highest conductivity is obtained for the $\gamma\text{-Al}_2\text{O}_3$ -based nanocomposite, respectively, $1.7 \cdot 10^{-7} \text{ S cm}^{-1}$ and $1.1 \cdot 10^{-4} \text{ S cm}^{-1}$ at 130°C for $\text{LiNO}_3/\text{Al}_2\text{O}_3$ and $\text{NaNO}_2/\text{Al}_2\text{O}_3$. For $\text{LiNO}_3/\text{SiO}_2$ the conductivity did not improve compared to pristine LiNO_3 , while an improvement of one order of magnitude is observed for $\text{NaNO}_2/\text{SiO}_2$. The conductivities of the NaNO_3 /oxide nanocomposites are lower than their NaNO_2 -based counterparts, but the improvements compared to the heat treated NaNO_3 are similar, i.e., over three orders of magnitude for $\text{NaNO}_3/\text{Al}_2\text{O}_3$ and about 1 order of magnitude for $\text{NaNO}_3/\text{SiO}_2$. This is shown in **Figure 6.5** for the NaNO_2 - and NaNO_3 / Al_2O_3 nanocomposites. This indicates that a similar conductivity enhancement mechanism is at play.

The difference between SiO_2 and $\gamma\text{-Al}_2\text{O}_3$ can be explained by the incomplete infiltration of LiNO_3 , NaNO_2 and NaNO_3 in the SiO_2 pores. For example, in the previous

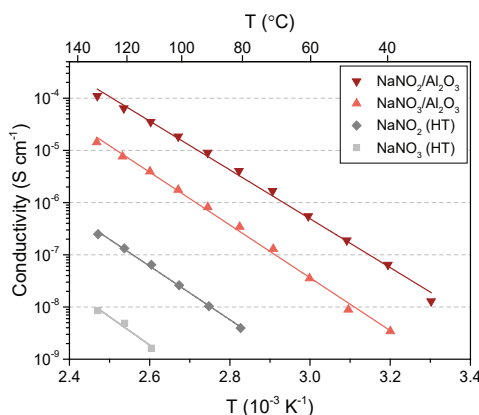


Figure 6.5 - Temperature-dependent Arrhenius conductivity plot of NaNO_2 , NaNO_3 , $\text{NaNO}_2/\text{Al}_2\text{O}_3$ and $\text{NaNO}_3/\text{Al}_2\text{O}_3$.

section it was shown that 75% of the LiNO_3 resides on the exterior of the SiO_2 particles, while only about 25% of the LiNO_3 has infiltrated the SiO_2 pores. Consequently, the long-range ionic transport is hindered by the presence of macrocrystalline LiNO_3 , or the lack of an interconnected Li^+ diffusion pathway through the nanoconfined LiNO_3 . The same behaviour has been observed in $\text{NaBH}_4/\text{SiO}_2$ nanocomposites (**Chapter 2**). On the other hand, despite the presence of macrocrystalline NaNO_2 and NaNO_3 , the conductivity of $\text{NaNO}_2/\text{SiO}_2$ and $\text{NaNO}_3/\text{SiO}_2$ has increased. Thus, it seems that the interaction of NaNO_2 and NaNO_3 with SiO_2 results in an increased number of mobile ions, whereas it does not in the case of LiNO_3 . This shows that the conductivity of the nanocomposites does not only depend on the chemical nature of the oxide, it is also determined by the interaction strength of the ion conductor, in line with the results discussed in **Chapter 2**.

Because the differences in conductivity between the SiO_2 - and $\gamma\text{-Al}_2\text{O}_3$ -based nanocomposites are likely related to the amount of pore infiltration, it is not possible to study how ionic conductivity in LiNO_3 , NaNO_2 and NaNO_3 is affected by surface chemistry of the mesoporous oxides. Therefore, we also prepared LiNO_3 -, NaNO_2 - and NaNO_3 /oxide nanocomposites based on TiO_2 and Nb_2O_5 . It is important to note that though both oxides are considered n-type semiconductors that can conduct electrons, high electronic conductivities are only observed at elevated temperatures ($> 700\text{ }^\circ\text{C}$), under reducing conditions or in non-stoichiometric oxides.^{28–32} The chemical nature and surface chemistry of these metal oxides differs greatly from SiO_2 and $\gamma\text{-Al}_2\text{O}_3$. This was confirmed with NH_3 -TPD and pyridine-IR. As explained in section 6.2, the interaction of these basic molecules (NH_3 and pyridine) with the oxides, provides information on the amount and strength of the acid sites present on the oxide surface. Additionally, since the characteristic vibrational modes of pyridine differ when it is coordinated to a Brønsted or Lewis acid site, it is possible to determine the amount of both sites with IR. The results are shown in **Figure 6.6** and **Table 6.3**. In short, SiO_2 contains very few Brønsted acid sites that only interact weakly with pyridine and NH_3 . In contrast, $\gamma\text{-Al}_2\text{O}_3$ and TiO_2 mainly contain Lewis acid sites with different strength. Finally, Nb_2O_5 contains strong Brønsted acid sites in addition to a significant amount of Lewis acid sites. Due to the presence of these widely different surface groups, it is possible to study how these surface groups affect the conductivity of the nanocomposites.

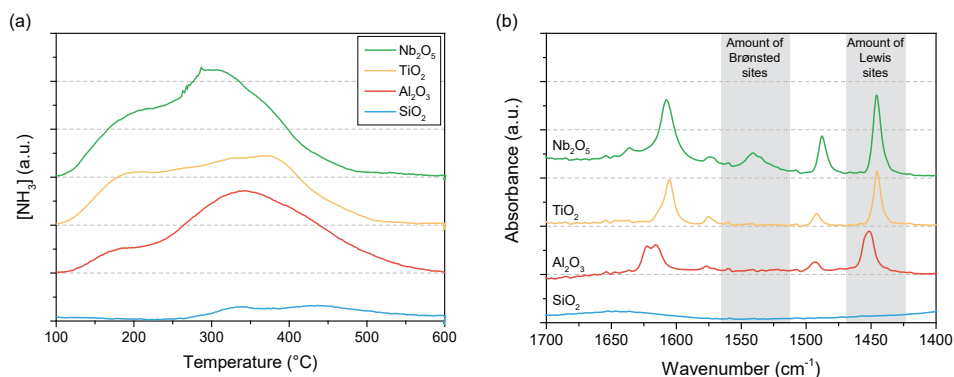


Figure 6.6 - (a) NH_3 -TPD measurements of the oxide scaffolds. The curves are normalized to the weight of the samples after baseline subtraction. (b) Pyridine FT-IR spectra of the oxide scaffolds after saturation with pyridine vapour, followed by evacuation at $150\text{ }^\circ\text{C}$ for 30 minutes. The spectra have been normalized to the weight of the samples.

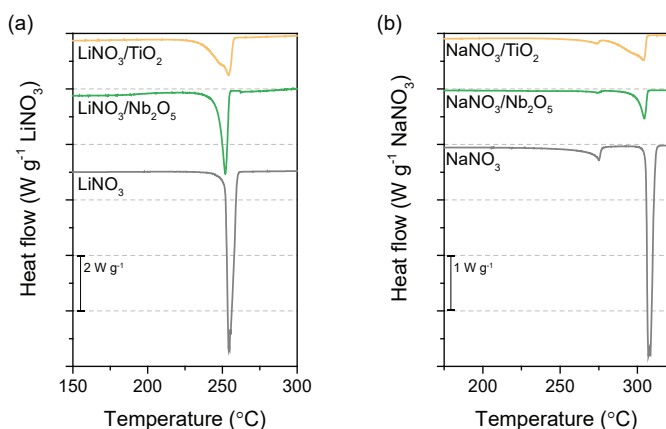
Table 6.3 – Quantitative results for the amounts of Brønsted and Lewis acid sites present on the oxide surfaces as determined with pyridine-IR

Oxide scaffold	Brønsted sites ($\mu\text{mol g}^{-1}$)	Lewis sites ($\mu\text{mol g}^{-1}$)	Total amount of acid sites ($\mu\text{mol g}^{-1}$)
SBA-15 (SiO_2)	-	-	-
$\gamma\text{-Al}_2\text{O}_3$	-	49	49
TiO_2	-	120	120
Nb_2O_5	55	108	163

6.3.3 LiNO_3 -, NaNO_2 - and NaNO_3 /oxide nanocomposites based on TiO_2 and Nb_2O_5

Similar to the SiO_2 - and $\gamma\text{-Al}_2\text{O}_3$ -based nanocomposites, the effectiveness of the synthesis method for the TiO_2 - and Nb_2O_5 -based nanocomposites as observed by DSC is discussed. In **Figure 6.7** the DSC curves of LiNO_3 /oxide and NaNO_3 /oxide nanocomposites based TiO_2 and Nb_2O_5 are shown. The curve of macrocrystalline LiNO_3 and NaNO_3 are provided for comparison. For each nanocomposite an endothermic peak related to melting of the macrocrystalline material is observed. A secondary melting peak related to nanoconfined material is not clearly observed for these nanocomposites. This can be because the pore volume of Nb_2O_5 is small ($0.12 \text{ cm}^3 \text{ g}^{-1}$), so that only a small amount LiNO_3 or NaNO_3 is present in the scaffold pores, which also implied that the melting enthalpy of the confined material is too low to be detected. Additionally, in the DSC curve of TiO_2 -based nanocomposites, the peak related to melting of macrocrystalline LiNO_3 and NaNO_3 is very broad and starts at a lower onset temperature. This behaviour can be explained by the large pores of TiO_2 , which has pores with an average pore size around 63 nm. Following the Gibbs-Thompson equation, large pores result in a relatively small melting point depression, which causes the peaks of macrocrystalline material and nanoconfined material to overlap.

The amount of intraporous and extraporous LiNO_3 , NaNO_3 , and NaNO_2 present in the nanocomposites is determined based on the peak area related to melting of macrocrystalline LiNO_3 , NaNO_2 , and NaNO_3 . The results are summarized in **Table 6.4**.

**Figure 6.7** - DSC graphs of (a) LiNO_3 -, and (b) NaNO_3 /oxide nanocomposites based on TiO_2 and Nb_2O_5 . The DSC graphs of LiNO_3 and NaNO_3 are included for comparison.

For the LiNO_3 - and NaNO_3 /oxide nanocomposites, melt infiltration occurs fairly easily. In the $\text{LiNO}_3/\text{TiO}_2$ and $\text{LiNO}_3/\text{Nb}_2\text{O}_5$ nanocomposites, the intraporous NaNO_3 volume is equivalent to 75% and 73% of the scaffold pore volume, respectively. In the case of NaNO_3 , the intraporous NaNO_3 volume in the Nb_2O_5 pores is equivalent to 94% of the pore volume, whereas in the case of the TiO_2 scaffold the intraporous NaNO_3 volume is about 45% of the scaffold pore volume. On the other hand, the pores of $\text{NaNO}_2/\text{TiO}_2$ are only filled for 32% and the DSC curve of $\text{NaNO}_2/\text{Nb}_2\text{O}_5$ did not show any peaks associated with NaNO_2 , neither macrocrystalline nor nanoconfined. In fact, further investigation on the $\text{NaNO}_2/\text{Nb}_2\text{O}_5$ nanocomposite with DRIFTS (**Figure 6.8**) indicates that NaNO_2 reacts during melt infiltration. Specifically, in the DRIFTS spectrum of $\text{NaNO}_2/\text{Nb}_2\text{O}_5$ peaks are observed around 2760, 2430 and 1790 cm^{-1} , which indicate the presence of NaNO_3 . Furthermore, the $\text{NaNO}_2/\text{Nb}_2\text{O}_5$ and $\text{NaNO}_3/\text{Nb}_2\text{O}_5$ spectra are surprisingly similar, confirming that NaNO_2 is not stable upon melt infiltration in Nb_2O_5 , but reacts to form NaNO_3 .

Table 6.4 - Differential Scanning Calorimetry results of LiNO_3 -, NaNO_2 - and NaNO_3 /oxide nanocomposites based on TiO_2 and Nb_2O_5

Infiltrate	LiNO_3		NaNO_3		NaNO_2	
Nanocomposite	$\text{LiNO}_3/\text{TiO}_2$	$\text{LiNO}_3/\text{Nb}_2\text{O}_5$	$\text{NaNO}_3/\text{SiO}_2$	$\text{NaNO}_3/\text{Nb}_2\text{O}_5$	$\text{NaNO}_2/\text{TiO}_2$	$\text{NaNO}_2/\text{Nb}_2\text{O}_5$
Extra : Intra porous LiNO_3	42 : 58	44 : 56	64 : 36	51 : 49	75 : 25	-
Ratio infiltrate volume : pore volume	0.75	0.73	0.45	0.94	0.32	-

Overall, the DSC analysis shows that melt infiltration works nicely for LiNO_3 , but it gives varying results for NaNO_3 and NaNO_2 . It will be interesting to study how this affects the conductivities of these nanocomposites. It is good to note that the amount of intraporous material in these nanocomposites might be underestimated. Both TiO_2 and Nb_2O_5 scaffold contain macropores, which are not sufficiently small to depress the melting point of confined material. Consequently, part of the material that is confined in the macropores contributes to the melting peak ascribed to macrocrystalline/extraporous

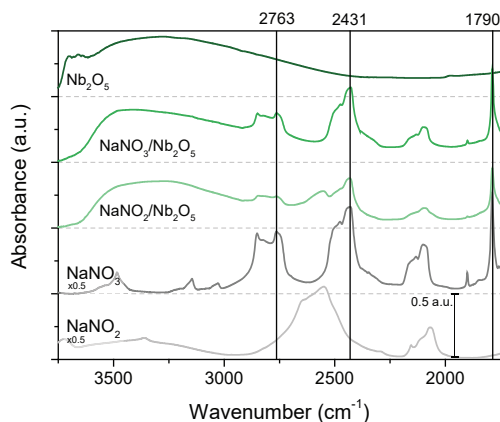


Figure 6.8 - DRIFTS spectra of $\text{NaNO}_2/\text{Nb}_2\text{O}_5$ and $\text{NaNO}_3/\text{Nb}_2\text{O}_5$ illustrating the similarities between the nanocomposites. The spectra of pristine NaNO_2 , NaNO_3 , Nb_2O_5 are shown for comparison.

LiNO₃. Secondly, due to the overlap between the peaks in the TiO₂-based nanocomposites, the amount of extraporous material was approximated with a Gaussian fit. These factors might have resulted in an underestimation of the fraction of the pore volume that is filled.

6.3.3 Conductivity in LiNO₃/oxide nanocomposites

The conductivities of all LiNO₃/oxide nanocomposites and heat-treated LiNO₃ are displayed in **Figure 6.9**. Overall, an improvement in conductivity of one to three orders of magnitude compared to LiNO₃ is seen for all nanocomposites, except LiNO₃/SiO₂. The extent of the enhancement varies substantially depending on the mesoporous oxide. To compare, at 130 °C the nanocomposites based on γ -Al₂O₃, TiO₂ and Nb₂O₅ exhibit conductivities of $1.7 \cdot 10^{-7}$ S cm⁻¹, $1.3 \cdot 10^{-6}$ S cm⁻¹ and $1.1 \cdot 10^{-5}$ S cm⁻¹, respectively. For all these nanocomposites, LiNO₃ readily fills the scaffold pores, which means that in this case the transport is not hindered by the presence of macrocrystalline LiNO₃. The differences in conductivity between the nanocomposites is, therefore, likely related to differences in the physical (e.g., morphology and pore structure) and chemical properties of the mesoporous oxides.

To study the conduction properties of the nanocomposites further, the activation energy for transport was derived from the conductivity data. A summary of the activation energies is shown in **Table 6.5**. The activation energy calculated for ionic transport in LiNO₃ is 1.5 eV, in line with the poor ionic conductivity of this compound. Upon nanocomposite formation, the activation energy decreased for all nanocomposites. The highest activation energy (1.2 eV) is observed for LiNO₃/SiO₂, which is also the nanocomposite with the lowest conductivity. The activation energies of the other nanocomposites, e.g., LiNO₃/Al₂O₃, LiNO₃/TiO₂, LiNO₃/Nb₂O₅ ranged between 0.82 eV and 0.97 eV, though no direct trend between activation energy and conductivity was observed. The most conductive nanocomposite, LiNO₃/Nb₂O₅, exhibits a low activation energy as well as high pre-exponential factor ($\ln \sigma_0$). The pre-exponential factor is a measure for the number of mobile charge carriers that contribute to the charge transport.^{33–35} Thus, it seems that conductive LiNO₃/oxide nanocomposites can be obtained with mesoporous oxides that lower the activation energy for transport, while also creating sufficient number of mobile carriers.

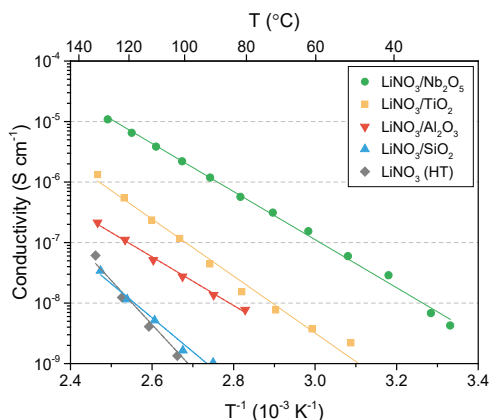


Figure 6.9 - Arrhenius plots of conductivity versus reciprocal temperature of heat treated LiNO₃ and LiNO₃/oxide nanocomposites based on SiO₂, γ -Al₂O₃, TiO₂ and Nb₂O₅. The first temperature-dependent heating cycle is shown.

Table 6.5 - Activation energy (E_A) and $\ln(\sigma T)$ obtained from a linear plot of $\ln(\sigma T)$ and $10^{-3} T^{-1}$ of the conductivity data reported in Figure 6.6. The standard deviation is based on the 95% confidence interval of the linear fit.

Metal hydride/(oxide)	$\ln \sigma_0$	E_A (eV)
Heat-treated LiNO_3	31 ± 6	1.5 ± 0.2
$\text{LiNO}_3/\text{SiO}_2$	22 ± 9	1.2 ± 0.3
$\text{LiNO}_3/\text{Al}_2\text{O}_3$	14 ± 2	0.83 ± 0.07
$\text{LiNO}_3/\text{TiO}_2$	20 ± 3	0.97 ± 0.08
$\text{LiNO}_3/\text{Nb}_2\text{O}_5$	18 ± 1	0.82 ± 0.03

Based on the conductivity data summarized in **Figure 6.9** and **Table 6.5**, it is not likely that the differences in conductivity originate from differences in the porosity of metal oxides, especially because the oxides with the lowest surface area and pore volume (TiO_2 and Nb_2O_5) gave the highest nanocomposite conductivities. To demonstrate, the most conductive nanocomposite ($\text{LiNO}_3/\text{Nb}_2\text{O}_5$) has a high weight fraction of the non-conducting oxide (74 wt%), and correspondingly a small amount of LiNO_3 (26 wt%), while $\text{LiNO}_3/\text{Al}_2\text{O}_3$ contains a larger fraction of LiNO_3 (58 wt%). Hence, the higher conductivity in these nanocomposites does not originate from the presence of a larger fraction of conducting material. This indicates that, like most metal hydride/oxide nanocomposites, the chemical nature of the mesoporous oxide determines the extent of the conductivity enhancement through the formation of a conductive interface layer between LiNO_3 and the mesoporous oxide.

To determine how surface chemistry affects the conductivity, the nanocomposite conductivity was correlated to the amount of Lewis and Brønsted acid sites, the total amount of acid sites and the average interaction strength as determined by pyridine-IR (**Table 6.3**). Surprisingly, the conductivity did not seem to depend on the strength of the acid sites, nor on the nature (Lewis or Brønsted) of the acid sites. Instead, a correlation between the conductivity of the LiNO_3 /oxide nanocomposites with the total number of acid sites present in the oxides was found, as is shown in **Figure 6.10**. From a general

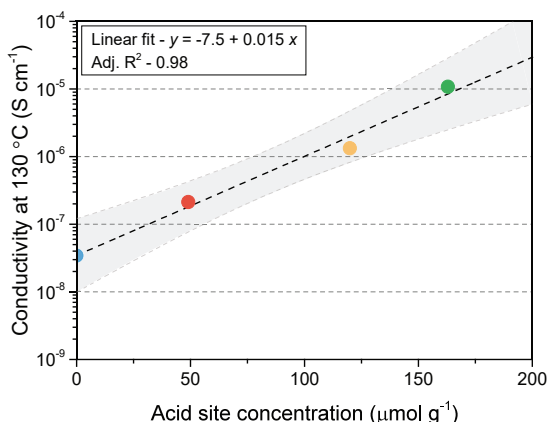


Figure 6.10 - Correlation between the conductivities of LiNO_3 /oxide nanocomposites and the amount of acid sites present on the oxides. The correlation is shown with a linear fit and the corresponding 95% confidence interval.

linear fit ($y = a + bx$) on the log-linear scale, the relation $\log(\sigma) = -7.5 + 0.015 C_{\text{acid sites}}$ is derived, showing a clear dependence. When increasing the amount of acid sites from 0 to $163 \mu\text{mol g}^{-1}$, the conductivity increases by almost three orders of magnitude from $3.4 \cdot 10^{-8} \text{ S cm}^{-1}$ to $1.1 \cdot 10^{-5} \text{ S cm}^{-1}$. This is a strong indication that the conductivity of nitrate/oxide nanocomposites largely depends on the chemical nature of the oxide. On the other hand, it is important to keep in mind that the conductivity might not directly depend on the surface acidity, as the basicity of the surface and the surface energy of the mesoporous scaffold are also related to these values. Additionally, the oxide scaffolds do not only differ in chemical nature, large differences are also observed in their physical properties. Therefore, to investigate whether a direct correlation between the amount of surface groups (or other chemical or physical properties) and the conductivity indeed exists, it is important to use a model system in which only one property is varied, while the others are kept constant, as described in **Chapter 4** for $\text{LiBH}_4\text{-LiNH}_2/\text{oxide}$ nanocomposites.

6.3.4 Conductivity in $\text{NaNO}_2\text{-}$ and $\text{NaNO}_3/\text{oxide}$ nanocomposites

Similar to the $\text{LiNO}_3/\text{oxide}$ nanocomposites, the conductivity of the $\text{NaNO}_2\text{-}$ and $\text{NaNO}_3/\text{metal oxide}$ nanocomposites was analysed. In **Figure 6.11a** the conductivities of the $\text{NaNO}_2/\text{oxide}$ nanocomposites are shown. Depending on the mesoporous scaffold, the conductivity improves by one to almost three orders of magnitude. In this case, the highest conductivity is observed for $\text{NaNO}_2/\text{Al}_2\text{O}_3$ ($1.1 \cdot 10^{-4} \text{ S cm}^{-1}$ at 130°C). Slightly lower conductivities of, respectively, $1.6 \cdot 10^{-5} \text{ S cm}^{-1}$ and $1.0 \cdot 10^{-5} \text{ S cm}^{-1}$ at 130°C were obtained for $\text{NaNO}_2/\text{Nb}_2\text{O}_5$ and $\text{NaNO}_2/\text{TiO}_2$. The lowest conductivity ($3.3 \cdot 10^{-6} \text{ S cm}^{-1}$ at 130°C) is obtained for the SiO_2 -based nanocomposite. The same trend ($\text{SiO}_2 > \text{TiO}_2 > \text{Nb}_2\text{O}_5 > \text{Al}_2\text{O}_3$) is observed for the $\text{NaNO}_3/\text{oxide}$ nanocomposites, though their conductivities are lower as shown for the $\gamma\text{-Al}_2\text{O}_3$ -based nanocomposites in **Figure 6.5**. In contrast, this trend differs from the $\text{LiNO}_3/\text{oxide}$ nanocomposites.

Unfortunately, it was not possible to derive a correlation between the conductivity of the $\text{NaNO}_2\text{-}$ and $\text{NaNO}_3/\text{oxide}$ nanocomposites and the scaffold properties. While the chemical nature of the scaffolds impacts the ionic conductivity differently compared to

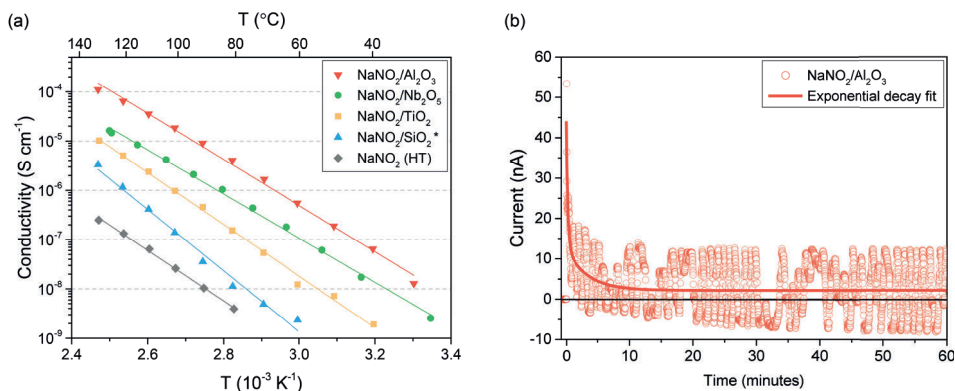


Figure 6.11 - (a) Arrhenius plots showing conductivity versus reciprocal temperature of $\text{NaNO}_2/\text{oxide}$ nanocomposites prepared with SiO_2 , $\gamma\text{-Al}_2\text{O}_3$, TiO_2 and Nb_2O_5 . (b) DC voltage polarization measurement on $\text{NaNO}_2/\text{Al}_2\text{O}_3$ showing the current as a function of time. An exponential decay curve is fitted to guide the eye. The steady-state current was based on the average current measured between 25 and 60 minutes.

LiNO₃/oxide nanocomposites, several other factors should be considered as well. First of all, from the DSC measurements, it is seen that NaNO₃ and NaNO₂ do not infiltrate the pores of the oxides as readily as LiNO₃. As a result, the scaffold pores are only partially filled and more macrocrystalline material remains present outside of the scaffold. Due to the low ionic conductivity of macrocrystalline NaNO₃ and NaNO₂, long-range ionic transport is hindered, leading to a lower nanocomposite conductivity. Additionally, it is not clear whether the partial oxidation of NaNO₂ in the NaNO₂/Nb₂O₅ nanocomposite positively or negatively affects the overall conductivity. Both differences can lead to a deviation from the correlation between surface acidity and conductivity that was clearly observed for LiNO₃.

It is good to consider that the NaNO₂ might become (partially) oxidized upon nanocomposite formation with strongly interacting oxides. As a result, the oxide might become partially reduced, which can induce electronic n-type conductivity. The conductivity measured with electrochemical impedance spectroscopy is the sum of both the ionic transport and electronic transport in the nanocomposite. To distinguish between electronic and ionic conductivity, the electronic conductivity of the most conductive nanocomposite (NaNO₂/Al₂O₃) was determined by DC voltage polarization. The results are shown in **Figure 6.11b**. It can be seen that the steady-state current after 40 minutes is about 2 nA, which shows that the electronic conductivity amounts to less than 0.1% of the total conductivity as determined from electrochemical impedance spectroscopy. Thus, it is expected that the conductivity in the most conductive NaNO₂/oxide nanocomposite is mostly due to ionic transport. If reducible scaffolds are used for nanocomposite formation, it remains important to consider that the prepared nanocomposite might exhibit electronic conductivity.

6.4 Conclusions

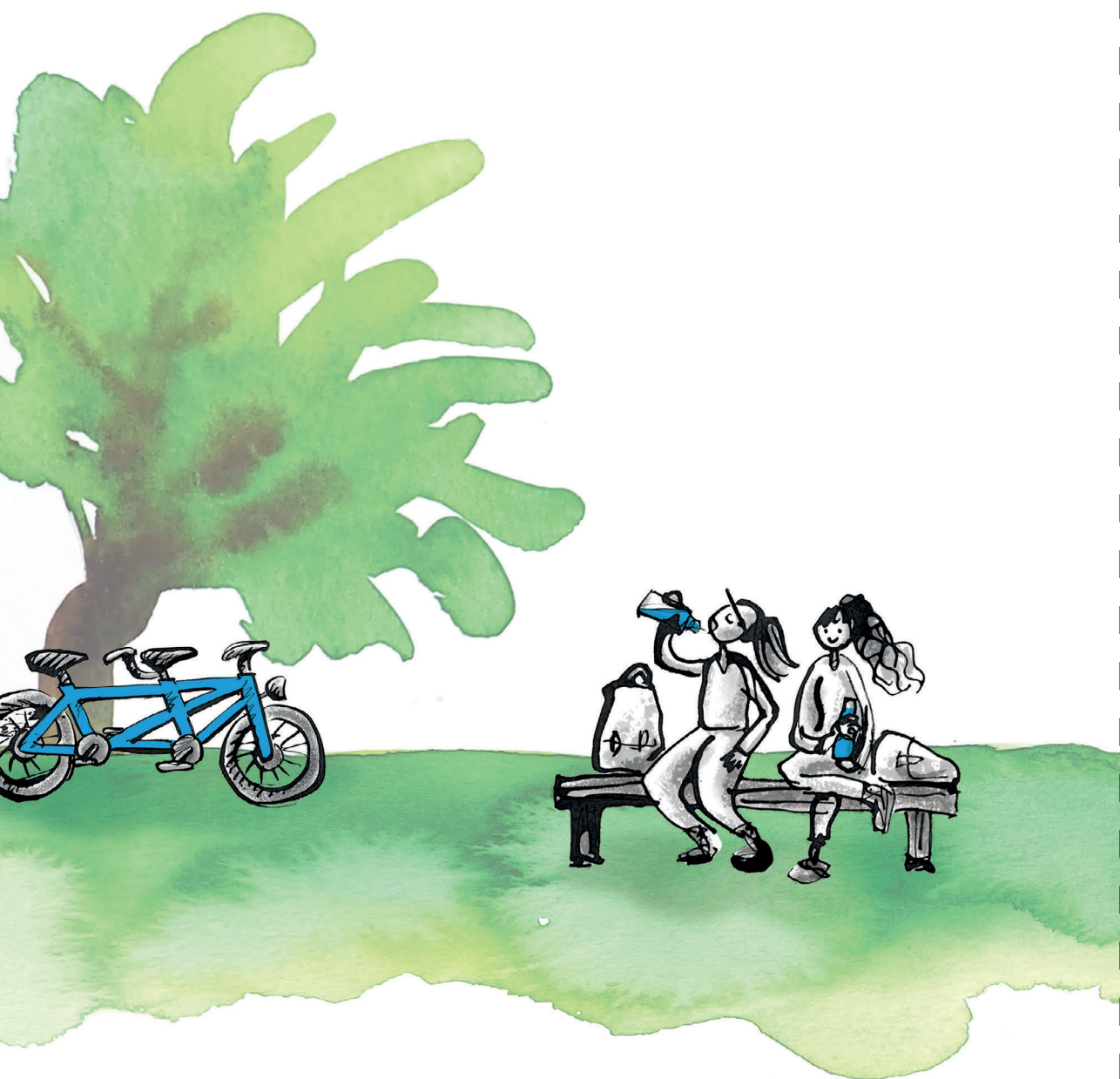
The effect of nanocomposite formation on the ionic conductivity of LiNO_3 , NaNO_2 and NaNO_3 was explored. Depending on the mesoporous scaffold that was used, e.g., SiO_2 , $\gamma\text{-Al}_2\text{O}_3$, TiO_2 , or Nb_2O_5 , the Li- and Na-ion conductivities were increased from one to three orders of magnitude. Notably, conductivities of $1.1 \cdot 10^{-5} \text{ S cm}^{-1}$, $1.1 \cdot 10^{-4} \text{ S cm}^{-1}$, and $1.4 \cdot 10^{-5} \text{ S cm}^{-1}$ at 80°C were obtained for $\text{LiNO}_3/\text{Nb}_2\text{O}_5$, $\text{NaNO}_2/\text{Al}_2\text{O}_3$ and $\text{NaNO}_3/\text{Al}_2\text{O}_3$, respectively. Similar to hydride-based nanocomposites, the conductivity of LiNO_3 -, NaNO_2 and NaNO_3 -based nanocomposites strongly depends on properties of the scaffold.

In particular, a correlation was found between the amount of acidic surface groups and the LiNO_3 /oxide conductivity. When increasing the concentration of acidic groups in the oxide from 0 to $163 \mu\text{mol g}^{-1}$, the conductivity increased from $3.4 \cdot 10^{-8} \text{ S cm}^{-1}$ to $1.1 \cdot 10^{-5} \text{ S cm}^{-1}$. Likewise, the conductivity of the NaNO_2 - and NaNO_3 -based nanocomposites heavily depends on the oxide scaffold that is used. In all cases, the conductivity of the nanocomposites is governed by the interplay between scaffold properties and the chemical nature of the lithium- or sodium compound. Overall, this proof-of-principle study shows that nanocomposite formation can be used to enhance performance of widely different solid-state ion conductors, ranging from hydrides to oxides.

6.5 References

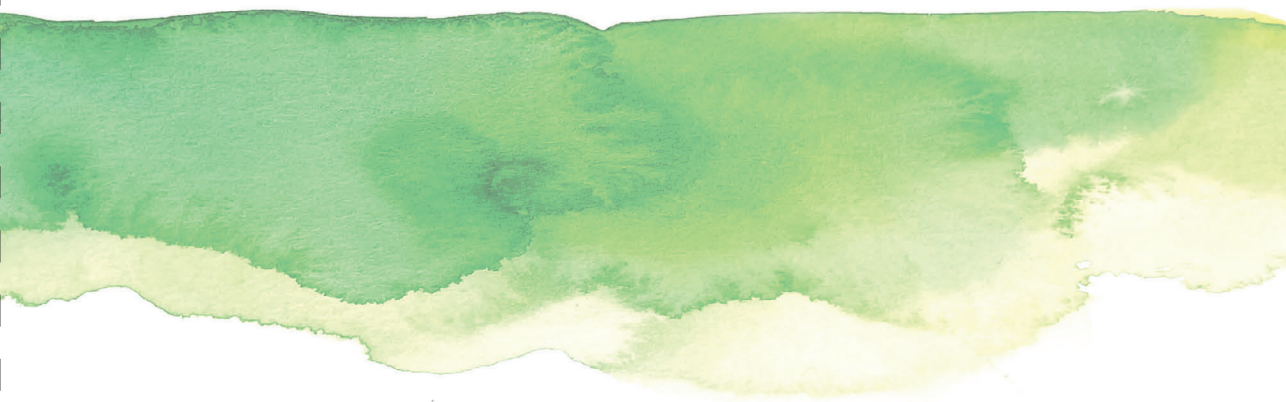
1. Ye, T., Li, L. & Zhang, Y. Recent Progress in Solid Electrolytes for Energy Storage Devices. *Adv. Funct. Mater.* **30**, 1–20 (2020).
2. Anantha, P. S. & Hariharan, K. Enhanced ionic conduction in NaNO_3 by dispersed oxide inclusions. *J. Phys. Chem. Solids* **64**, 1131–1137 (2003).
3. Anantha, P. S. & Hariharan, K. Ac conductivity analysis and dielectric relaxation behaviour of $\text{NaNO}_3\text{-Al}_2\text{O}_3$ composites. *Mater. Sci. Eng. B Solid-State Mater. Adv. Technol.* **121**, 12–19 (2005).
4. Lee, H. I. *et al.* Morphology-selective synthesis of mesoporous SBA-15 particles over micrometer, submicrometer and nanometer scales. *J. Mater. Chem.* **20**, 8483–8487 (2010).
5. Ngene, P., Adelhelm, P., Beale, A. M., De Jong, K. P. & De Jongh, P. E. $\text{LiBH}_4/\text{SBA-15}$ nanocomposites prepared by melt infiltration under hydrogen pressure: Synthesis and hydrogen sorption properties. *J. Phys. Chem. C* **114**, 6163–6168 (2010).
6. Brunauer, S., Emmett, P. H. & Teller, E. Adsorption of Gases in Multimolecular Layers. *J. Am. Chem. Soc.* **60**, 309–319 (1938).
7. Barrett, E. P., Joyner, L. G. & Halenda, P. P. The Determination of Pore Volume and Area Distributions in Porous Substances. I. Computations from Nitrogen Isotherms. *J. Am. Chem. Soc.* **73**, 373–380 (1951).
8. Matsuo, M., Takamura, H., Maekawa, H., Li, H. W. & Orimo, S. I. Stabilization of lithium superionic conduction phase and enhancement of conductivity of LiBH_4 by LiCl addition. *Appl. Phys. Lett.* **94**, 2–5 (2009).
9. Agrawal, R. C. DC polarisation: An experimental tool in the study of ionic conductors. *Indian J. Pure Appl. Phys.* **37**, 294–301 (1999).
10. Traver, A., Vimont, A., Sahibed-Dine, A., Daturi, M. & Lavalley, J. C. Use of pyridine CH(D) vibrations for the study of Lewis acidity of metal oxides. *Appl. Catal. A Gen.* **307**, 98–107 (2006).
11. Emeis, C. A. Determination of Integrated Molar Extinction Coefficients for Infrared Absorption Bands of Pyridine Adsorbed on Solid Acid Catalysts. *J. Catal.* **141**, 347–354 (1993).
12. Parry, E. P. An infrared study of pyridine adsorbed on acidic solids. Characterization of surface acidity. *J. Catal.* **2**, 371–379 (1963).
13. Niwa, M., Katada, N., Sawa, M. & Murakami, Y. Temperature-Programmed Desorption of Ammonia with Readsorption Based on the Derived Theoretical Equation. *J. Phys. Chem.* **99**, 8812–8816 (1995).
14. Datka, J. & Góra-Marek, K. IR studies of the formation of ammonia dimers in zeolites TON. *Catal. Today* **114**, 205–210 (2006).
15. Liu, X. & Truitt, R. E. DRFT-IR studies of the surface of γ -Alumina. *J. Am. Chem. Soc.* **119**, 9856–9860 (1997).
16. Morrow, B. A. & McFarlan, A. J. Surface vibrational modes of silanol groups on silica. *J. Phys. Chem.* **96**, 1395–1400 (1992).
17. Hadjiivanov, K. *Identification and Characterization of Surface Hydroxyl Groups by Infrared Spectroscopy. Advances in Catalysis* vol. 57 (Elsevier Inc., 2014).
18. Ngene, P. *et al.* The influence of silica surface groups on the Li-ion conductivity of $\text{LiBH}_4/\text{SiO}_2$ nanocomposites. *Phys. Chem. Chem. Phys.* **21**, 22456–22466 (2019).
19. De Kort, L. M., Harmel, J., De Jongh, P. E. & Ngene, P. The effect of nanoscaffold porosity and surface chemistry on the Li-ion conductivity of $\text{LiBH}_4\text{-LiNH}_2/\text{metal oxide}$ nanocomposites. *J. Mater. Chem. A* **8**, 20687–20697 (2020).
20. Cordaro, J. G., Kruijenga, A. M., Altmaier, R., Sampson, M. & Nissen, A. Thermodynamic properties of molten nitrate salts. *Granada (Spain): SolarPACES* **1**, 2011 (2011).
21. Takahashi, Y. & Sakamoto, R. Heat capacities and latent heats of LiNO_3 , NaNO_3 , and KNO_3 . *Int. J. Thermophys.* **9**, (1988).

22. De Jongh, P. E. & Eggenhuisen, T. M. Melt infiltration: An emerging technique for the preparation of novel functional nanostructured materials. *Adv. Mater.* **25**, 6672–6690 (2013).
23. Berg, R. W., Kerridge, D. H. & Larsen, P. H. $\text{NaNO}_2 + \text{NaNO}_3$ phase diagram: New data from DSC and raman spectroscopy. *J. Chem. Eng. Data* **51**, 34–39 (2006).
24. Johnson, E. R., Frances, A. & Wu, C. C. Phase transition in NaNO_3 . *J. Appl. Phys.* **47**, 1827–1828 (1976).
25. De Jongh, P. E. & Eggenhuisen, T. M. Nanoporous Materials and Confined Liquids. in *Nanoparticles: Workhorses of Nanoscience* (ed. de Mello Donegá, C.) 99–120 (Springer Berlin Heidelberg, 2014). doi:10.1007/978-3-662-44823-6_4.
26. Brunauer, S., Kantro, D. L. & Weise, C. H. the Surface Energies of Amorphous Silica. *Can. J. Chem.* **31**, 1483–1496 (1956).
27. Guzmán-Castillo, M. L. *et al.* The surface energy of quasi-amorphous γ alumina calculated from the temperature of the $\gamma \rightarrow \alpha$ transition. *J. Non. Cryst. Solids* **329**, 53–56 (2003).
28. Nico, C., Monteiro, T. & Graça, M. P. F. Niobium oxides and niobates physical properties: Review and prospects. *Prog. Mater. Sci.* **80**, 1–37 (2016).
29. Kofstad, P. Studies of electrical conductivity of Nb_2O_5 as a function of oxygen pressure at 600–1200°C. *J. Phys. Chem. Solids* **23**, 1571–1578 (1962).
30. Greener, E. H., Whitmore, D. H. & Fine, M. E. Electrical Conductivity of Near-Stoichiometric α - Nb_2O_5 . *J. Chem. Phys.* **34**, 1017–1023 (1961).
31. Nowotny, M. K., Bak, T. & Nowotny, J. Electrical properties and defect chemistry of TiO_2 single crystal. III. Equilibration kinetics and chemical diffusion. *J. Phys. Chem. B* **110**, 16292–16301 (2006).
32. Earle, M. D. The electrical conductivity of titanium dioxide. *Phys. Rev.* **61**, 56–62 (1942).
33. Manthiram, A., Yu, X. & Wang, S. Lithium battery chemistries enabled by solid-state electrolytes. *Nat. Rev. Mater.* **2**, 1–16 (2017).
34. Padma Kumar, P. & Yashonath, S. Ionic Conduction in the Solid State. *ChemInform* **37**, 135–154 (2006).
35. Famprikis, T., Canepa, P., Dawson, J. A., Islam, M. S. & Masquelier, C. Fundamentals of inorganic solid-state electrolytes for batteries. *Nat. Mater.* **18**, 1278–1291 (2019).



7

Summary and Future perspectives



7.1 Summary

This thesis discusses the development of novel electrolytes for all-solid-state batteries. These next generation batteries are expected to play a key role in the global transition from fossil fuel-based energy to a society that runs mostly on renewable energies as they enable high-capacity electricity storage with improved safety compared to conventional Li-ion batteries. Due to their light weight and the ability to form a good interface with most electrode materials, metal hydrides have been proposed as promising candidates for this application. Unfortunately, their room temperature ionic conductivity hinders their use in all-solid-state batteries. Hence, the main goal of my research has been to improve ionic transport in metal hydrides. To this end, we investigated how the interplay between the metal hydride and the metal oxide in metal hydride/oxide nanocomposites impacts their ionic conductivity. In other words, we searched for a dynamic duo.

The thesis starts with a general introduction on Li-ion batteries and metal hydrides, followed by a thorough review of the state-of-the-art of the research on metal hydride/oxide nanocomposites. So far, most research in this field has focussed on nanocomposites between LiBH_4 and metal oxides, in which the conductivity can be improved by four orders of magnitude depending on the oxide scaffold. This enhancement has been ascribed to the formation of a conductive layer of 1.0 to 2.0 nm at the interface between the metal hydride and the metal oxide. The Li-ion mobility in LiBH_4 /oxide nanocomposites heavily depends on the surface chemistry of the oxide scaffold. While the benefits of nanocomposite formation have clearly been shown for LiBH_4 , studies on other metal hydrides are scarce and their conductivity enhancements are generally less substantial. The interaction between the metal hydride and the metal oxide is not yet fully understood, which hinders the full exploitation of this approach to further improve the conductivity of nanocomposite electrolytes. Therefore, in this work we have aimed to bridge this knowledge gap.

The effect of nanocomposite formation on the Na-ion conductivity in complex metal hydrides was discussed in **Chapter 2**. NaBH_4 - and NaNH_2 /oxide nanocomposites based on SiO_2 and $\gamma\text{-Al}_2\text{O}_3$ were prepared via melt infiltration. We showed that depending on the oxide that was used, the conductivity of these nanocomposites was increased up to three orders of magnitude compared to the pristine metal hydrides. Similar to LiBH_4 /oxide nanocomposites, it was observed that the conductivity enhancement originates from the formation of a conductive interface layer between the metal hydride and the metal oxide. At the metal hydride-oxide interface, a highly conductive tertiary phase is formed, in contrast to a space charge layer as is generally assumed for most nanocomposite electrolytes.

The composition of the tertiary phase, and consequently the nanocomposite conductivity, strongly depends on the interplay between the metal hydride and the oxide scaffold. A detailed investigation based on EIS, DRIFTS and solid-state NMR measurements unveiled that both the surface chemistry of the oxide scaffold and the reactivity of the metal hydride are critical for the ionic conductivity. In the case of NaBH_4 , an oxide with a high surface energy or strong surface groups ensures wetting, and thereby complete incorporation of NaBH_4 in the pores of the scaffold and the formation of a conductive interface containing NaBH_4 nanoclusters, $\text{Na}_2\text{B}_{12}\text{H}_{12}$ and B-O species. Contrarily, a strongly interacting oxide is detrimental for the conductivity of NaNH_2 -based nanocomposites due to the lower stability of NaNH_2 . In $\text{NaNH}_2/\text{Al}_2\text{O}_3$ nanocomposites, a strong interface

interaction results in the formation of N-O species and a lower conductivity compared to $\text{NaNH}_2/\text{SiO}_2$, in which NaNH_2 remains partially intact. These results clearly show that for the preparation of metal hydride/oxide nanocomposites the surface chemistry of the oxide and the chemical nature of the metal hydride should be considered. This study further highlights the importance of the interface interactions in metal hydride/oxide nanocomposites.

The research described in the first two chapters showed that the formation of a conductive interface layer in metal hydride/oxide nanocomposites enhances their ionic conductivity. While the interface layer is largely responsible for the high ionic conductivity in these nanocomposites, long range ionic transport can only be achieved via an interconnected pathway through both the conductive interface layer and bulk metal hydride further away from the interface. In most metal hydride/oxide nanocomposites, the metal hydride further away from the oxide surface exhibits low ionic conductivity. To determine whether the ionic transport might be improved by using modified metal hydrides with high conductivities instead of pristine metal hydrides, the preparation of LiI- and LiNH_2 -substituted LiBH_4 /oxide nanocomposites was discussed in **Chapter 3**. In these nanocomposites, partial ionic substitution with LiI or LiNH_2 (leading to the formation of conductive $\text{Li}(\text{BH}_4)_{1-x}\text{I}_x$ and $\text{Li}(\text{BH}_4)_{1-x}(\text{NH}_2)_x$) is combined with nanocomposite formation with mesoporous SiO_2 or $\gamma\text{-Al}_2\text{O}_3$ to further optimize the ionic conductivity. Indeed, the combined approach resulted in a higher room temperature conductivity for both LiBH_4 -LiI/oxide and LiBH_4 - LiNH_2 /oxide nanocomposites compared to pristine LiBH_4 /oxide nanocomposites.

The ionic transport mechanism in the most conductive nanocomposite, LiBH_4 -LiI/ Al_2O_3 , was investigated using EIS and ^7Li NMR line shape measurements. The analysis demonstrates that LiBH_4 -LiI/ Al_2O_3 contains a larger fraction of highly mobile Li^+ ions compared to pristine LiBH_4 -LiI and $\text{LiBH}_4/\text{Al}_2\text{O}_3$. The long-range ionic transport is no longer hindered by the presence of bulk LiBH_4 with low conductivity far away from the metal hydride-oxide interface, resulting in a higher nanocomposite conductivity. Moreover, the difference in ionic conductivity of the nanocomposites prepared with different oxides demonstrate that both the physical properties and the surface chemistry of the oxide affect the overall conductivity. It is expected that the performance of metal hydride/oxide nanocomposites can be improved further by resolving the dependence on the mesoporous oxide properties.

In **Chapter 4**, the conductivity of the LiNH_2 -substituted LiBH_4 /oxide nanocomposites was considered in more detail, focussing on how the chemical nature and physical properties of the metal oxide influence the overall conductivity. To this end, LiBH_4 - LiNH_2 /oxide nanocomposites were prepared using SiO_2 scaffolds (SBA-15) with varying pore structure and surface chemistry, as well as mesoporous $\gamma\text{-Al}_2\text{O}_3$. By systematically tuning the scaffold properties, structure-conductivity relationships could be established, and the origin of the conductivity enhancement could be determined. This work demonstrates that, similar to LiBH_4 /oxide nanocomposites, the chemical nature of the oxide influences the LiBH_4 - LiNH_2 /oxide conductivity. By changing the surface chemistry of SBA-15 through alumination, the conductivity could be improved by a factor of two. Different from LiBH_4 /oxide nanocomposites, the main factor affecting the nanocomposite conductivity is the pore volume of the mesoporous oxide. Unexpectedly, the conductivity varied over three orders of magnitude by altering the pore volume from 0.51 to $1.00 \text{ cm}^3 \text{ g}^{-1}$.

The correlation between conductivity and pore volume demonstrates that the conductivity enhancement in LiNH_2 -substituted LiBH_4 /oxide nanocomposites has a different origin than most other metal hydride/oxide nanocomposites, e.g., LiBH_4 /oxide and LiBH_4 -LiI/oxide nanocomposites where such a correlation is not observed. In the case of LiBH_4 - LiNH_2 /oxide nanocomposites, the conductivity is attributed to stabilization of a highly conductive high temperature phase inside the pores of the scaffold instead of a conductive interface layer at the hydride/oxide interface. Thus, the origin of the conductivity enhancement in metal hydride/oxide nanocomposites can differ depending on the metal hydride, and as a result the chemical and physical properties of the oxide will have a different impact on the conductivity.

For a rational design of highly conductive nanocomposite electrolytes, it is imperative to understand the nature of the interface interactions. Unfortunately, characterization of the metal hydride-metal oxide interface is hindered by the air- and moisture sensitivity, light elements (with low Z) and nanocrystalline nature of the nanocomposites. Many techniques that can provide information on the local structure at the interface, such as XRD, NMR, XPS and NEXAFS difficult, cannot be used. Therefore, in **Chapter 5** X-ray Raman scattering is considered as a technique to study the chemical and structural changes that occur in local environment of Li, Na, and B located at the metal hydride-metal oxide interface of LiBH_4 - and NaBH_4 /oxide nanocomposites. The interface layers in the nanocomposites could be distinguished from the bulk regions by varying the metal hydride-metal oxide weight ratios and in this way, it was possible to study the interface layer. The structure and chemical composition at the interface were analysed using linear combination fitting with relevant reference compounds.

At the interface between LiBH_4 and SiO_2 , the local boron environment resembles a trigonal boron species, such as LiBO_2 or BH_3 . At the same time the Li K-edge spectra suggest that two different Li^+ -compounds are formed, one that interacts strongly with oxygen from the scaffold and one that has a weak interaction with the surrounding anions. By introducing surface modifications to the SiO_2 scaffold (i.e., Al- SiO_2 and Zr- SiO_2), it was possible to show that the interaction between LiBH_4 and the oxide surface changes. A stronger interaction results in the presence of more trigonal boron in the nanocomposite, which results in a higher conductivity. The presence of similar interface species was also observed for NaBH_4 /oxide nanocomposites, indicating that the interface layer based on trigonal boron compounds conducts both Li- and Na-ions. This work illustrates that X-ray Raman scattering is certainly a promising technique to determine local structural environments in metal hydride/oxide nanocomposites

As a proof of principle, the effect of nanocomposite formation on the ionic conductivity of non-hydride-based materials, specifically lithium nitrate, sodium nitrate and sodium nitrite, is considered in **Chapter 6**. In the same way as the metal hydride/oxide nanocomposites, LiNO_3 -, NaNO_3 -, and NaNO_2 /oxide nanocomposites based on different oxides (SiO_2 , Al_2O_3 , TiO_2 , and Nb_2O_5) were prepared via melt infiltration. Surprisingly, the conductivity of these nanocomposites was improved up to three orders of magnitude. In all three cases, the conductivity varied substantially depending on the oxide scaffold that was used. For the LiNO_3 /oxide nanocomposites, a strong correlation was found between the ionic conductivity and the number of acid sites present on the oxide scaffold. This exploratory study demonstrates that nanocomposite formation is not limited to metal

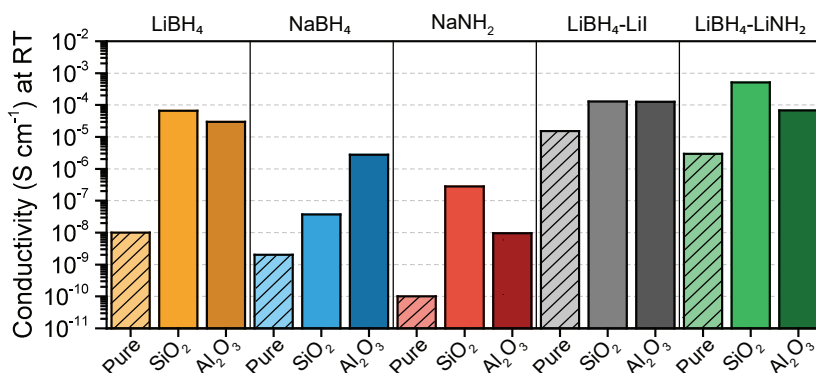


Figure 7.1 – Overview of the ionic conductivities of the metal hydride/oxide nanocomposites discussed in this thesis at room temperature ($T = 20 - 30\text{ }^{\circ}\text{C}$).

hydrides but can be applied to widely different solid-state ion conductors. Again, the chemical and physical properties of the oxides seem to have a large impact on the ionic transport and should be studied systematically.

The work described in this thesis has shown that the conductivity of monophasic (pristine), as well as ion-substituted metal hydrides can be greatly enhanced via nanocomposite formation with oxide scaffolds. An overview of the discussed metal hydride-based nanocomposites and the corresponding conductivities is provided in **Figure 7.1**. In the five different systems that were studied interesting similarities and surprising differences were observed. For each studied nanocomposite, the conductivity of the nanocomposite heavily depends on the properties of the mesoporous oxide, i.e., the chemical nature or physical properties. In most cases, the conductivity enhancement originates from the formation of a conductive layer at the hydride-oxide interface. This is not true for the LiBH₄-LiNH₂/oxide nanocomposite. Here, the conductivity enhancement upon nanocomposite formation arises mostly from stabilization of a conductive high temperature phase at ambient temperature, illustrating that nanocomposite formation offers more than one way to improve ionic transport in solid electrolytes.

7.2 Future perspectives

In addition to the work described in this thesis, several research questions remain interesting to investigate. Firstly, throughout this thesis we have mainly focused on the ionic conductivity of our nanocomposites. For the application of metal hydride/oxide nanocomposites in all-solid-state batteries, studies on their thermal and (electro) chemical stability, device integration and large-scale manufacturing are highly relevant as well. Moreover, changes in practical aspects, such as long-term battery performance, manufacturing costs and (gravimetric and volumetric) energy density, arising from nanocomposite formation should be investigated. For example, we recently observed that the addition of oxide nanoparticles to complex hydride electrolytes can substantially improve battery cycle life.¹ Additionally, several studies have reported capacity fading and unfavourable side reactions during cycling in metal hydride-based all-solid-state batteries.^{2–4} Presently, these phenomena are poorly understood, and better understanding of their origin will aid the future development of all-solid-state batteries based on complex hydride- and nanocomposite electrolytes.

The mechanisms at play during battery operation might be elucidated by performing in-situ and operando studies during charging and discharging. Specifically, such experiments could make it possible to observe the formation of dendrites, (stable) interface layers between the electrolyte and electrodes or cracks and contact losses within the battery, which are difficult to observe in ex-situ studies. In recent years, several techniques have successfully been used to study all-solid-state batteries during operation, including X-ray adsorption spectroscopy (XAS), resonant inelastic X-ray scattering (RIXS), neutron diffraction (ND), and electron microscopy (EM).^{5,6} For example, in a recent study by Zheng *et al.* the formation of a stable interphase between a Li_3PS_4 electrolyte with a Li_2RuO_3 cathode during cycling was followed using XAS⁷, while Golozar *et al.* were able to visualize the formation of Li dendrites and dead Li in a $\text{Li} - \text{LiFePO}_4$ battery based on a polymer electrolyte in-situ with scanning electron microscopy.⁸ Unfortunately, these techniques are not suitable to study the light elements (Li, Na, B, N, H) present in metal hydride-based all-solid-state batteries. For these batteries, it would be interesting to apply X-ray Raman scattering to study the chemical changes during operation, especially because it has sufficient spatial resolution to distinguish between battery components.

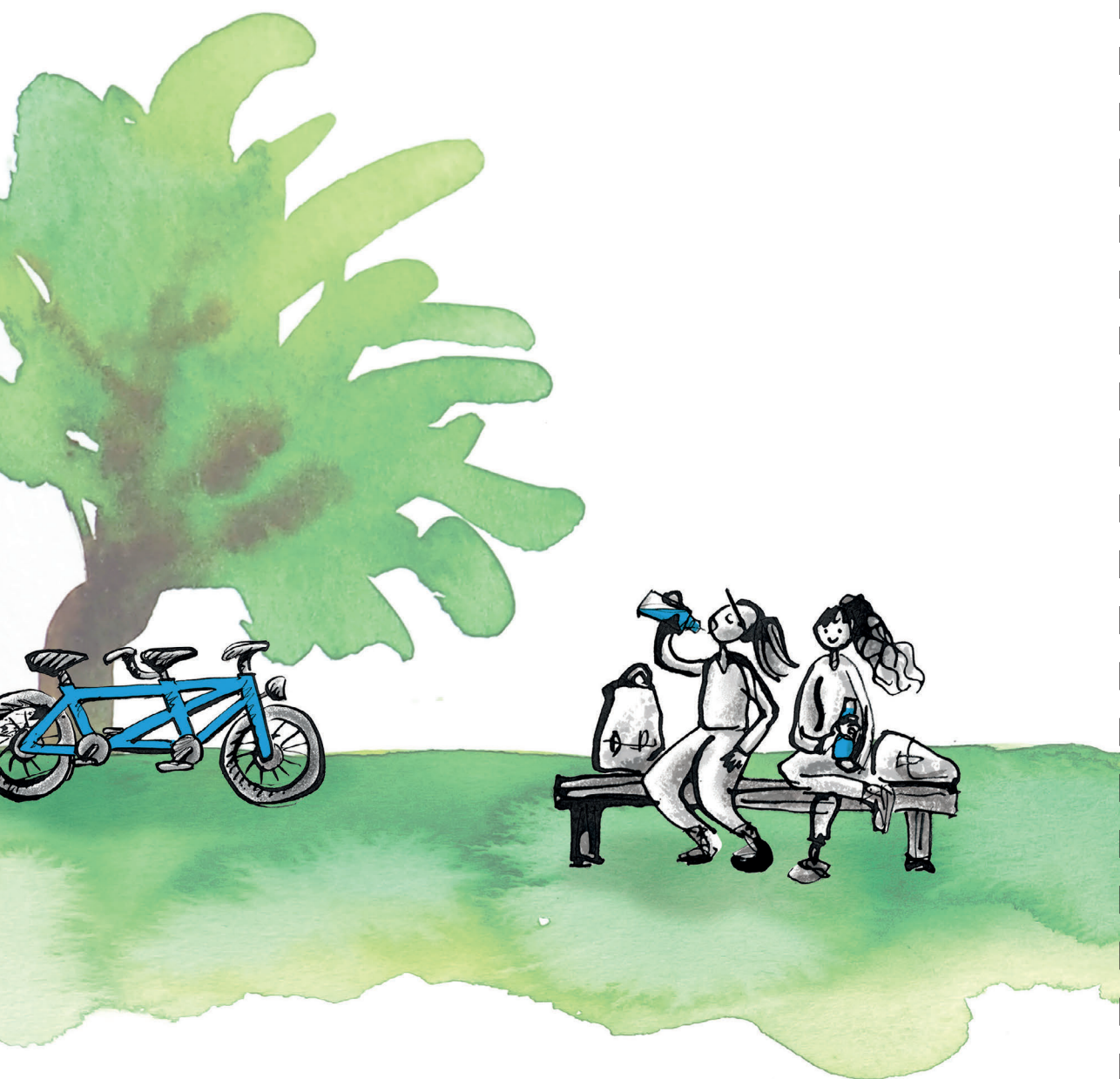
As discussed in **Chapter 1**, besides the metal hydrides discussed in this thesis, many other interesting solid-state ion conductors are being investigated as well. For example, metal hydride ion conductors based on *closo*-borate and *closo*-carborate cluster anions (e.g., $\text{LiCB}_{11}\text{H}_{12}$ and $\text{Na}_2(\text{B}_{12}\text{H}_{12})(\text{B}_{10}\text{H}_{10})$) exhibit exceptionally high conductivities at room temperature. Combined with their large electrochemical stability window and high thermal stability, *closo*-(car)borates are very promising candidates for application in all-solid-state batteries. Amongst the other material classes that are being investigated, polymer-based electrolytes, such as polyethylene oxide (PEO), also show great potential. Their key benefits compared to other electrolytes are their processability and mechanical compatibility with electrodes. Both *closo*-(car)borate- and polymer-based electrolytes could benefit from nanocomposite formation with an inorganic scaffold to further improve their performance. To demonstrate, it has been shown that the introduction of ceramic additives to polymer electrolytes leads to significant improvements in their room temperature conductivity.⁹ Different from metal hydride/oxide nanocomposite, this enhancement generally originates

from structural changes in the polymer chain rather than the formation of a conductive interface. To date, little is currently known about the (chemical) interactions between the polymer and metal oxide.^{10–12} Hence, it would be interesting to further explore how the conductivity and performance of polymer/oxide nanocomposite electrolytes depends on the physical and chemical properties of the oxide.

Finally, it is important to realize that renewable energy utilization, and thereby, renewable energy storage, will become increasingly important in the coming years. As a result, the development of suitable rechargeable batteries will be critical. While conventional Li-ion batteries are already an integral part of our society, especially for portable devices, all-solid-state batteries might soon become equally important. Whether these batteries will be based on a metal hydride-based ion conductor, such as $\text{LiCB}_{11}\text{H}_{12}$, or a nanocomposite electrolyte, such as a $\text{PEO}/\text{Al}_2\text{O}_3$ electrolyte, will depend on many factors (e.g., scalability, cost, capacity retention) in comparison to the other competitors, such as $\text{Li}_7\text{P}_3\text{S}_{11}$ and $\text{Li}_7\text{La}_3\text{Zr}_2\text{O}_{12}$. Nonetheless, both are promising candidates that might be widely applied in future energy storage devices. We hope that the insights gained in this thesis on hydride-based electrolytes, nanocomposite formation and X-ray Raman scattering will inspire insightful studies for the future design of novel solid-state ion conductors with excellent electrochemical performances for next generation batteries.

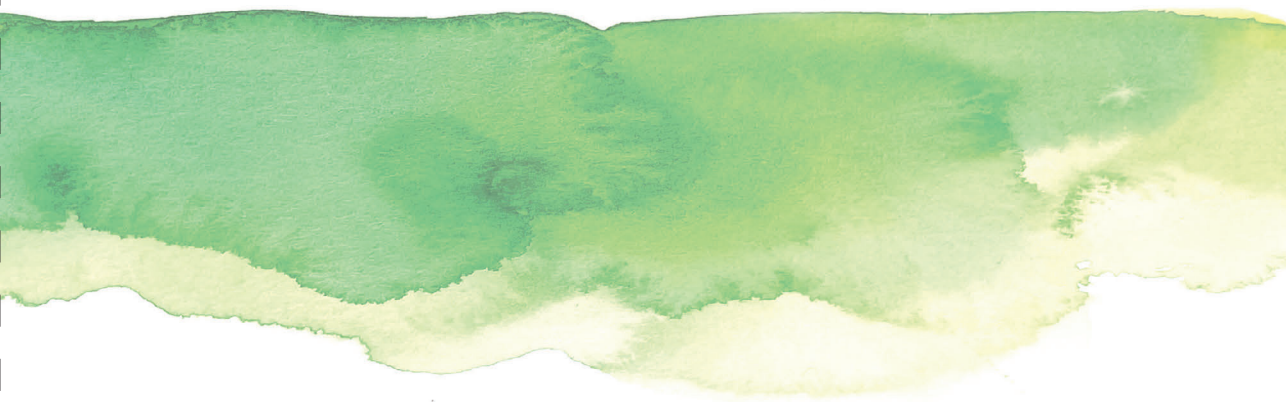
7.3 References

1. De Jongh, P. E., de Kort, L. M., Ngene, P., Baricco, M. & Gulino, V. Improving the cycle life of solid-state batteries by addition of oxide nanoparticles to a complex hydride solid electrolyte. *ChemComm*, Under review (2022).
2. Latroche, M. *et al.* Full-cell hydride-based solid-state Li batteries for energy storage. *Int. J. Hydrogen Energy* **44**, 7875–7887 (2019).
3. Duchêne, L., Remhof, A., Hagemann, H. & Battaglia, C. Status and prospects of hydroborate electrolytes for all-solid-state batteries. *Energy Storage Mater.* **25**, 782–794 (2020).
4. Gulino, V. *et al.* Room-Temperature Solid-State Lithium-Ion Battery Using a $\text{LiBH}_4\text{-MgO}$ Composite Electrolyte. *ACS Appl. Energy Mater.* **4**, 1228–1236 (2021).
5. Dixit, M. B., Park, J.-S., Kenesei, P., Almer, J. & Hatzell, K. B. Status and prospect of in situ and operando characterization of solid-state batteries. *Energy Environ. Sci.* **14**, 4672–4711 (2021).
6. Liu, D. *et al.* Review of Recent Development of In Situ/Operando Characterization Techniques for Lithium Battery Research. *Adv. Mater.* **31**, 1806620 (2019).
7. Zheng, Y. *et al.* Reversible lithium intercalation in a lithium-rich layered rocksalt Li_2RuO_3 cathode through a Li_3PO_4 solid electrolyte. *J. Power Sources* **300**, 413–418 (2015).
8. Golozar, M. *et al.* In situ observation of solid electrolyte interphase evolution in a lithium metal battery. *Commun. Chem.* **2**, 131 (2019).
9. Jiang, Y. *et al.* Development of the PEO based solid polymer electrolytes for all-solid state lithium ion batteries. *Polymers*. **10**, 1237 (2018).
10. Chen, X. & Vereecken, P. M. Solid and Solid-Like Composite Electrolyte for Lithium Ion Batteries: Engineering the Ion Conductivity at Interfaces. *Adv. Mater. Interfaces* **6**, 1–31 (2019).
11. Li, S. *et al.* Progress and Perspective of Ceramic/Polymer Composite Solid Electrolytes for Lithium Batteries. *Adv. Sci.* **7**, (2020).
12. Zou, Z. *et al.* Mobile Ions in Composite Solids. *Chem. Rev.* **120**, 4169–4221 (2020).



8

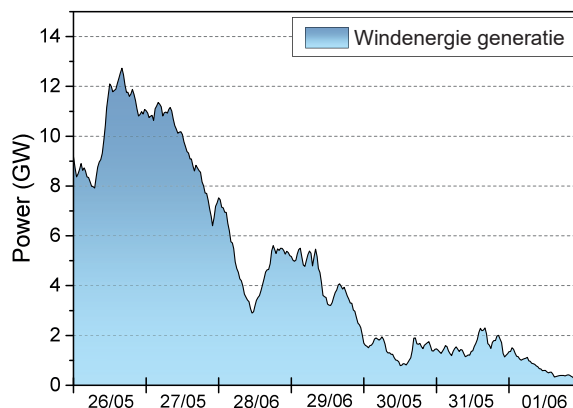
Nederlandse samenvatting



8.1 Energieopslag in batterijen

Het doel van dit proefschrift is het onderzoeken van het gebruik van metaalhydriden als vaste elektrolyten voor batterijen. Het is de verwachting dat batterijen zonder vloeistoffen een grote rol zullen spelen in het oplossen van het huidige klimaatprobleem. Een belangrijk onderdeel van de oplossing van het klimaatprobleem is grootschalige inzet van wind- en zonne-energie. Helaas fluctueert de elektriciteitsproductie van deze duurzame energiebronnen afhankelijk van hoe hard het waait of hoeveel de zon schijnt. Ter illustratie is in **Figuur 8.1** een voorbeeld van elektriciteitsopwekking door windenergie in de laatste week van mei 2022 te zien. In het begin van de week werd er veel windenergie opgewekt, terwijl het aan het eind van de week bijna windstil was en daardoor veel minder energie gegenereerd werd. Daarnaast wordt er alleen overdag (als de zon schijnt), zonne-energie opgewekt. Op dagen dat het minderig of zonnig is kan er veel duurzame elektriciteit worden opgewekt, waardoor er een overschot ontstaat dat niet efficiënt gebruikt kan worden. Op andere dagen is de energie die opgewekt wordt juist niet voldoende om aan de vraag te voldoen. Effectieve opslag zou ons in staat stellen om de fluctuerende elektriciteitsopbrengst van hernieuwbare bronnen te egaliseren, en op die manier wind- en zonne-energie zo efficiënt mogelijk te gebruiken.

Elektriciteit kan op verschillende manieren opgeslagen worden. Een manier die wereldwijd veel gebruikt wordt is hydro-elektrische energieopslag. Bij hydro-elektrische energieopslag wordt gebruik gemaakt van pompen die bij een elektriciteitsoverschot water van een laaggelegen gebied naar een hoger gelegen gebied pompen. Bij een tekort aan energie stroomt het water terug, waarbij met behulp van turbines elektriciteit wordt herwonnen. Een andere belangrijke opslagmethode is elektrochemische energieopslag in oplaadbare batterijen, waarbij elektrische energie omgezet wordt in chemische energie en vice versa. In het begin van de twintigste eeuw werden batterijen, zoals de zink-koolstofbatterij en de loodaccu, voor het eerst gebruikt voor elektriciteitsopslag. In 1991 werd de lithium-ion batterij door Sony op de markt gebracht, die inmiddels niet meer weg te denken is uit onze huidige maatschappij.



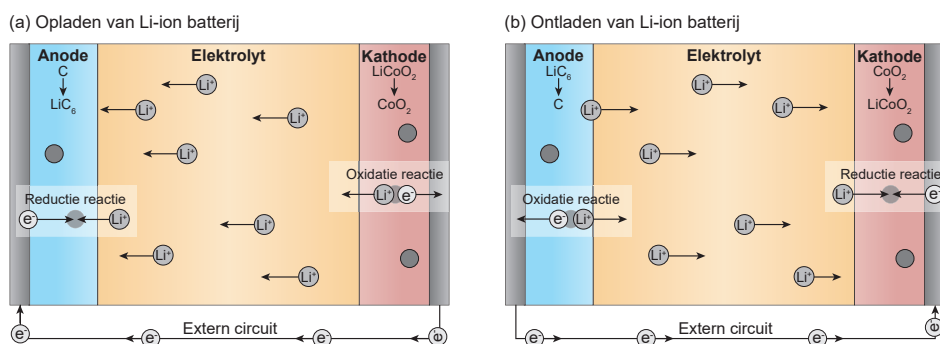
Figuur 8.1 – Voorbeeld van de wisselende elektriciteitsopwekking door windenergie in de laatste week van mei (26-05-'22 t/m 01-06-'22). Data van National Grid ESO Open Data.

8.1.2 Lithium-ion batterijen

Tegenwoordig zijn lithium-ion batterijen een van de meest gebruikte technologieën voor elektriciteitsopslag. Ze worden gebruikt in draagbare elektronica, zoals mobiele telefoons en laptops, in elektrisch gereedschap en in elektrische auto's. De lithium-ion batterij overtreft concurrerende technologieën vooral door zijn hoge energiedichtheid (opgeslagen hoeveelheid energie per gram) gecombineerd met een lange levensduur en kleine conversieverliezen tijdens laden en ontladen ($< 1\%$). Net als andere batterijen bestaat de lithium-ion batterij uit een negatieve pool ofwel anode en een positieve pool ofwel kathode. In de lithium-ion batterij zijn dit een grafiet-anode en een lithiumkobaltoxide-kathode. Tussen de anode en de kathode zit een elektrolyt, een materiaal dat lithiumionen geleidt, zodat deze van de ene naar de andere elektrode kunnen bewegen. De elektrolyt geleidt geen elektronen, waardoor deze gedwongen worden via een extern circuit te bewegen, in de vorm van elektrische stroom. Een schematische weergave van de lithium-ion batterij is weergegeven in **Figuur 8.2**.

Tijdens het opladen van de batterij, zorgt een externe spanning ervoor dat de lithiumionen (Li^+ -ionen) van de kathode door de elektrolyt naar de anode bewegen (**Figuur 8.2a**). Eenmaal bij de grafiet-anode (C) aangekomen reageren de lithiumionen met elektronen (e^-) die door het externe circuit hebben bewogen. Deze zogenoemde reductie reactie (van Li^+ , e^- en C naar LiC_6) kost energie, waardoor de elektrische energie "opgeslagen" wordt in de chemische verbinding tussen het grafiet en de lithium ionen. Dit proces vindt omgekeerd plaats tijdens het ontladen van de batterij (**Figuur 8.2b**). Tijdens het ontladen wordt de chemische verbinding tussen het grafiet en de lithium ionen verbroken door een oxidatie reactie (van LiC_6 naar Li^+ , e^- en C), waarbij lithiumionen en elektronen vrijkomen. Bij deze reactie komt elektrische energie vrij. De vrijgekomen lithiumionen bewegen via de elektrolyt van de grafiet-anode naar de kobaltoxide-kathode, terwijl elektronen door het externe circuit van de anode naar de kathode bewegen. Via de externe elektronenstroom kan stroom geleverd worden voor het opladen van bijvoorbeeld, een mobiele telefoon, camera of elektrische auto. Bij de kathode reageren de lithiumionen en de elektronen, waarbij lithiumkobaltoxide (LiCoO_2) gevormd wordt.

De elektrolyt is een belangrijk onderdeel van de lithium-ion batterij, omdat deze ervoor zorgt dat de lithiumionen tussen de elektroden kunnen bewegen zonder dat er



Figuur 8.2 – Schematische representatie van de lithium-ion batterij tijdens (a) opladen en (b) ontladen van de batterij.

kortsluiting ontstaat in de batterij. Voor een goede werking van de batterij is het van belang dat de elektrolyt gemakkelijk lithium ionen doorlaat. De mate van ionengeleiding, ofwel ionische geleidbaarheid, in een materiaal wordt uitgedrukt in Siemens per centimeter (S cm^{-1}). Voor het gebruik in een batterij heeft een elektrolyt een geleidbaarheid van tenminste $10^{-3} \text{ S cm}^{-1}$ nodig. De huidige lithium-ion batterijen bevatten een elektrolyt dat bestaat uit een organisch vloeistof met daarin opgelost lithiumzout. Deze oplossingen kunnen erg goed lithiumionen doorlaten, met een ionische geleidbaarheid ver boven de $10^{-3} \text{ S cm}^{-1}$. Een probleem van de lithium-ion batterij is de brandbaarheid, waardoor een telefoon kan ontploffen of een elektrische auto in brand kan vliegen. Daarnaast zijn organische vloeistoffen niet bestand tegen veel elektrodematerialen, met name materialen die de energiedichtheid van de batterij kunnen verhogen. Hierdoor wordt de hoeveelheid energie die kan worden opgeslagen in de lithium-ion batterij beperkt. De belangrijkste doelen in het huidige batterijenonderzoek zijn daarom het verhogen van de veiligheid en energiedichtheid van de lithium-ion batterij. Beide doelen kunnen behaald worden door de vloeistof te vervangen voor een vaste stof.

8.1.3 Vastestofbatterijen

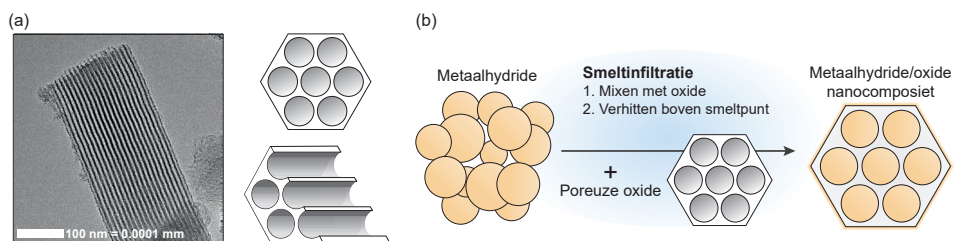
Een lithium-ion batterij op basis van een vaste stof elektrolyt wordt ook wel een vastestofbatterij ("solid-state battery") genoemd. Het is een van de belangrijkste kanshebbers voor duurzame elektriciteitsopslag in de toekomst. Vaste stoffen zijn veiliger dan organische vloeistoffen, omdat ze minder brandbaar en explosief zijn. Daarnaast kunnen ze in veel gevallen gebruikt worden in combinatie met elektroden met een hoge energiedichtheid. Een belangrijk nadeel van vaste stoffen is dat lithium ionen er over het algemeen moeilijker doorheen bewegen, ofwel de lithium-ionengeleiding is slechter dan die van een vloeibaar elektrolyt.

Op dit moment worden verschillende vaste stoffen onderzocht om te kijken welke de beste eigenschappen heeft om toegepast te worden, waaronder elektrolyten op basis van polymeren, zwavelverbindingen (sulfides), zuurstofverbindingen (oxides) of metaalhydriden (waterstofhoudende stoffen). Elk van deze materialen heeft specifieke voor- en nadelen. Zo hebben sulfides een uitstekende ionische geleidbaarheid, maar zijn ze chemisch niet bestand tegen verschillende elektrodematerialen. Oxide elektrolyten hebben daarentegen een hoge (elektro)chemische stabiliteit, maar zijn erg duur om op grote schaal te produceren. Het onderzoek heeft zich in de afgelopen jaren voornamelijk gericht op sulfide-, oxide- en polymeer-vaste stof elektrolyten, maar recentelijk zijn de metaalhydriden naar voren gekomen als interessant alternatief.

Vergeleken met andere vaste stoffen hebben metaalhydriden een aantal unieke eigenschappen die gunstig kunnen zijn voor vastestofbatterijen. Ze zijn erg licht en hebben een hoge elektrochemische stabiliteit, waardoor vastestofbatterijen op basis van metaalhydriden een laag gewicht hebben en veel energie op kunnen slaan. In dit proefschrift wordt de toepasbaarheid van metaalhydriden in batterijen onderzocht, waarbij we vooral kijken naar hun vermogen om ionen te geleiden.

8.2 Ion geleiding in metaalhydriden

Metaalhydriden zijn anorganische vaste stoffen die bestaan uit een ionrooster van kationen (positief geladen ionen), zoals Li^+ , Na^+ en Mg^{2+} , en anionen (negatief geladen ionen) met

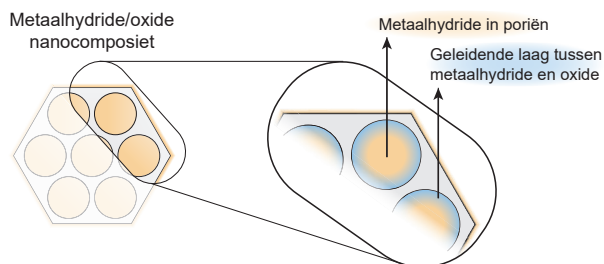


Figuur 8.3 – (a) Mesoporous silica gemeten met transmissie electronen microscopie (TEM) en een schematische weergave van de poriestructuur van deze metaaloxide. (b) Schematische weergave van de bereiding van metaalhydride/oxide nanocomposieten via smeltinfiltratie.

daarin een waterstofatoom, zoals BH_4^- , AlH_6^{3-} en $\text{B}_{12}\text{H}_{12}^{2-}$. Zoals besproken in de vorige paragraaf, hebben metaalhydriden een aantal eigenschappen waardoor ze interessant zijn als elektrolyten voor toepassing in vastestofbatterijen. Ze hebben echter één belangrijk nadeel. De meeste metaalhydriden hebben alleen een hoge ionische geleidbaarheid ($> 10^{-3} \text{ S cm}^{-1}$) bij temperaturen boven de 100°C . Dit komt doordat de structuur verandert bij hogere temperaturen. Bij kamertemperatuur kunnen de lithiumionen niet snel genoeg tussen de anode en de kathode bewegen. Het meeste onderzoek op het gebied van metaalhydriden richt zich daarom op de ionenmobiliteit in metaalhydriden en het ontwikkelen van strategieën die geleidbaarheid bij kamertemperatuur verbeteren. Daarmee draagt dit proefschrift bij aan de zoektocht naar veiligere en efficiëntere batterijen.

Er zijn verschillende methoden die gebruikt kunnen worden om de ion geleiding in een vaste stof te verbeteren, waaronder anionenvervanging en de vorming van nanocomposieten. Met name het effect van de laatste strategie wordt in dit proefschrift besproken. Bij deze methode wordt het metaalhydride gemengd met een poreus metaaloxide, zoals silica of aluminiumoxide, waarbij zich een metaalhydride/oxide nanocomposiet vormt. Een poreus metaaloxide is te vergelijken met een spons vol kleine poriën. Een voorbeeld van een poreus silica is weergegeven in **Figuur 8.3a**. Het gaat hier om een mesoporeus silica met geordende cilindrische poriën van 7 nm in diameter die parallel door het silica deeltje lopen. De metaalhydride/oxide nanocomposieten die worden besproken in dit proefschrift zijn gemaakt door middel van smeltinfiltratie. In deze synthese methode wordt een mengsel van het metaalhydride en het poreuze metaaloxide verwarmd tot een temperatuur boven het smeltpunt van het metaalhydride. Hierdoor wordt het metaalhydride vloeibaar en dringt deze binnen in de poriën van het poreuze metaaloxide. Dit is vergelijkbaar met een spons die water opneemt. In **Figuur 8.3b** wordt de bereiding van de materialen via smelt infiltratie schematisch weergegeven.

Tot op heden is het effect van nanocomposietvorming vooral onderzocht voor de lithium-ion geleiding in lithium boorhydride. Door lithium boorhydride via smeltinfiltratie te mengen met silica, aluminiumoxide of magnesiumoxide kan de ionische geleidbaarheid bij kamertemperatuur verhoogd worden van $10^{-8} \text{ S cm}^{-1}$ naar $10^{-4} \text{ S cm}^{-1}$, een verhoging van vier orden van grootte. Deze verbetering wordt toegeschreven aan de vorming van een geleidende laag tussen metaalhydride en metaaloxide, zoals schematisch weergegeven in **Figuur 8.4**. In deze geleidende laag bewegen de lithium ionen veel sneller dan in het metaalhydride en in het metaaloxide. Dit heeft als resultaat dat de geleidbaarheid van de lithium boorhydride/oxide nanocomposiet veel hoger is dan die van de individuele componenten. Hoewel bekend is dat dit goed werkt om de lithium-



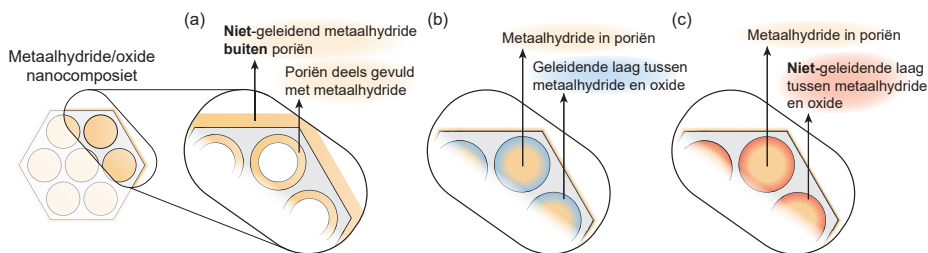
Figuur 8.4 – Schematische weergave van de geleidende laag die gevormd wordt op het grensvlak tussen de metaalhydride en metaaloxide in metaalhydride/oxide nanocomposieten.

ion geleidbaarheid van lithium boorhydride te verhogen, heeft deze strategie nog niet voor vergelijkbare verbeteringen in de ion geleiding gezorgd van andere metaalhydriden. Ook is er nog weinig bekend over de precieze interactie tussen het metaalhydride en het metaaloxide en over de wijze waarop deze de ion geleiding in metaalhydride/oxide nanocomposieten beïnvloedt. De verdere ontwikkeling van vaste stof elektrolyten op basis van metaalhydriden en nanocomposieten wordt hierdoor belemmerd. Het doel van dit proefschrift is daarom om te onderzoeken hoe die ion geleiding in verschillende metaalhydriden wordt beïnvloed door nanocomposietvorming en te ontdekken welke rol de fysieke en chemische eigenschappen van het poreuze metaaloxide hierin spelen.

8.3 Uitkomsten van dit proefschrift

Ik heb onderzocht hoe een metaalhydride en een metaaloxide samen een geleidende nanocomposiet vormen, kortom ik ben op zoek gegaan naar een dynamisch duo. Om te beginnen is het effect op de natrium-ion geleiding in natrium boorhydride en natrium amide onderzocht (**hoofdstuk 2**). Door middel van smelt infiltratie zijn nanocomposieten van natrium boorhydride- en natrium amide gemaakt. Net als in lithium boorhydride/oxide nanocomposieten, werd in deze materialen een verbetering in de ionengeleiding waargenomen als gevolg van een geleidende grenslaag tussen het metaalhydride en het metaaloxide. De samenstelling van de grenslaag, en daarmee de ion mobiliteit, hangt sterk af van de wisselwerking tussen het metaalhydride en het metaaloxide. Zowel de oppervlakchemie van het metaaloxide als de stabiliteit en reactiviteit van het metaalhydride spelen daarin een rol.

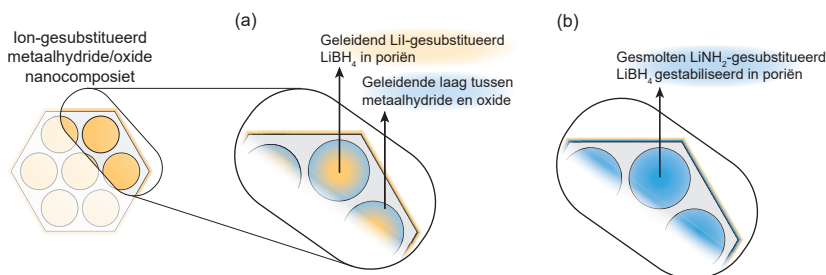
Bij gebruik van natrium boorhydride blijkt een sterke interactie tussen het metaalhydride en het metaaloxide essentieel. Als de interactie zwak is, dan infiltreert natrium boorhydride de poriën van het metaaloxide niet en blijft een deel van het metaalhydride buiten de poriën (**Figuur 8.5a**), waardoor de ionische geleidbaarheid van de nanocomposiet laag is. Wanneer de interactie sterk genoeg is, worden de poriën van het metaaloxide helemaal gevuld en ontstaat een goed geleidende laag tussen metaalhydride en metaaloxide (**Figuur 8.5b**). Dit resulteert in een natrium boorhydride/oxide nanocomposiet met een hoge natrium-ion geleidbaarheid. Een sterke interactie tussen het metaalhydride en het metaaloxide is juist nadelig voor de ion geleiding in natrium amide/oxide nanocomposieten. In dit geval wordt een laag tussen het metaalhydride en het metaaloxide gevormd met een lage natrium-ion mobiliteit (**Figuur 8.5c**). Alleen wanneer natrium amide en het metaaloxide weinig interactie hebben, ontstaat er een geleidende laag tussen beide componenten.



Figuur 8.5 – Grafische weergave van de resultaten die besproken worden in hoofdstuk 2. (a) In het geval van een zwakke interactie tussen natrium boorhydride en het metaaloxide, blijft natrium boorhydride deels buiten de poriën van het metaaloxide. (b) Wanneer de interactie sterk genoeg is, worden de poriën geheel gevuld en ontstaat er een geleidende laag tussen beide componenten. (c) In natrium amide/oxide nanocomposieten zorgt een sterke interactie juist voor een niet-geleidende laag op het grensvlak.

In de eerste twee hoofdstukken wordt vooral het belang van een geleidende grenslaag in metaalhydride/oxide nanocomposieten besproken. Voor ionisch transport over lange afstand is het daarnaast ook van belang dat een verbonden (geleidend) netwerk gevormd wordt tussen de geleidende grenslaag en het metaalhydride verder weg van het grensvlak. **Hoofdstuk 3** behandelt of het ionische transport over lange afstand verbeterd kan worden door aangepaste metaalhydriden met een goede ion geleiding te gebruiken in plaats van de originele metaalhydriden. Hiervoor zijn zowel jodide- als amide-gesubstitueerde lithium boorhydride/oxide nanocomposieten gemaakt. Hierdoor worden de voordelen van anionenvervanging door ofwel jodide ofwel amide gecombineerd met de voordelen van nanocomposietvorming. De combinatie levert een verdere verbetering op vergeleken met de individuele methoden. Een gedetailleerde analyse toont aan dat het aandeel mobiele lithium ionen groter is in jodide-gesubstitueerde lithium boorhydride/oxide nanocomposieten dan in jodide-gesubstitueerde lithium boorhydride en lithium boorhydride/oxide (**Figuur 8.6a**). Dit duidt erop dat het ionische transport over lange afstand minder wordt gehinderd door de aanwezigheid van niet-geleidend lithium boorhydride ver weg van het metaalhydride-oxide grensvlak. Bovendien werd duidelijk dat de ionische geleidbaarheid van de nanocomposieten afhangt van de fysieke en/of chemische eigenschappen van het gebruikte metaaloxide.

In **hoofdstuk 4** is de ion geleiding in amide-gesubstitueerde lithium boorhydride/oxide nanocomposieten uitgebreid besproken, met name hoe het metaaloxide de ion geleiding beïnvloedt. Door de fysieke en chemische eigenschappen van het metaaloxide systematisch aan te passen was het mogelijk om relaties tussen deze eigenschappen en de geleidbaarheid vast te stellen. Net als voor lithium boorhydride/oxide nanocomposieten, hebben de chemische eigenschappen van het metaaloxide invloed. Door de oppervlaktechemie van het metaaloxide te veranderen, kon de geleidbaarheid met een factor twee worden verhoogd. Echter, de belangrijkste factor die de ion geleiding in deze nanocomposieten beïnvloedt is het porievolume van het mesoporeuze metaaloxide. Door het porievolume van het metaaloxide te verdubbelen (van 0.5 naar $1.0 \text{ cm}^3 \text{ g}^{-1}$) kon de geleidbaarheid met drie orden van grootte verbeterd worden. Dit is anders dan in lithium boorhydride/oxide nanocomposieten, waar verschillen in de poriestructuur van het metaaloxide weinig invloed hebben op de geleidbaarheid.



Figuur 8.6 – Grafische weergave van de resultaten die besproken worden in hoofdstuk 4 en 5. (a) In jodide-gesubstitueerd lithium boorhydride/oxide nanocomposieten is zowel geleidend jodide-gesubstitueerd lithium boorhydride aanwezig, als een geleidende laag op het grensvlak. (b) In amide-gesubstitueerd lithium boorhydride/oxide nanocomposieten wordt gesmolten amide-gesubstitueerd lithium boorhydride bij kamertemperatuur gestabiliseerd in de poriën van het metaaloxide.

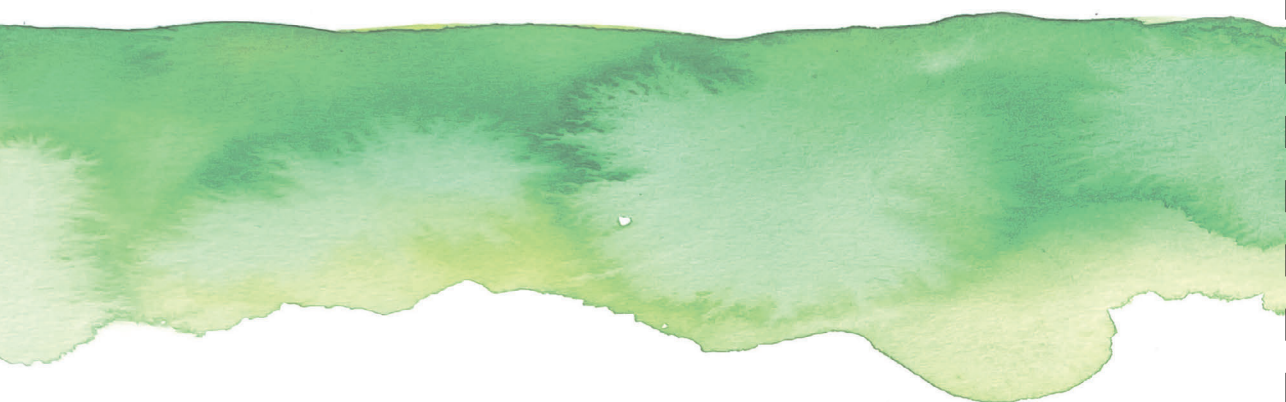
De samenhang tussen geleidbaarheid en porievolume toont aan dat de verbetering van de ion geleiding in amide-gesubstitueerde lithium boorhydride/oxide nanocomposieten een andere oorzaak heeft dan voor de meeste metaalhydride/oxide nanocomposieten. Meestal wordt de snelle ion geleiding veroorzaakt door de vorming van een geleidende grenslaag op het metaalhydride-oxide grensvlak. Echter, in dit geval wordt de verhoging in geleidbaarheid veroorzaakt door het nano-opsluiting (of nanoconfinement) effect, waarbij het smeltpunt van amide-gesubstitueerd lithium boorhydride verlaagd wordt door opsluiting in kleine poriën. Als amide-gesubstitueerd lithium boorhydride niet is opgesloten in poriën, dan smelt deze stof bij temperaturen boven de 40 °C. Door amide-gesubstitueerd lithium boorhydride op te sluiten in de poriën van het metaaloxide smelt het al bij kamertemperatuur, waardoor het gemakkelijk ionen geleidt (**Figuur 8.6b**). Deze resultaten laten zien dat de oorzaak van de verbetering van de ion geleiding in metaalhydride/oxide nanocomposieten kan verschillen en kan samenhangen met zowel de chemische eigenschappen als de fysieke eigenschappen van het metaaloxide.

Uit de voorgaande hoofdstukken blijkt dat (in de meeste gevallen) de interactie tussen het metaalhydride en metaaloxide een sleutelrol speelt in de vorming van een metaalhydride/oxide nanocomposiet met een hoge ionische geleidbaarheid. Helaas is het niet eenvoudig om de precieze structuur en compositie van de grenslaag te bepalen. Dit komt omdat de materialen gevoelig zijn voor lucht en vocht, en de meeste technieken zijn niet geschikt om lichte elementen (zoals lithium en boor) of amorfe structuren (zoals nanocomposieten) te bestuderen. Röntgenstraling Raman verstrooiing (X-ray Raman scattering ofwel XRS) is wel geschikt voor het bestuderen van lichte en amorfe materialen. Daarom hebben we, zoals beschreven in **hoofdstuk 5**, geprobeerd om met behulp van XRS de structuur van de grenslaag in lithium boorhydride- en natrium boorhydride/oxide nanocomposieten te bepalen. Met deze techniek konden we kleine verschillen bestuderen in de lokale omgeving van de lithium, natrium, boor en stikstof atomen die aanwezig zijn in de grenslaag tussen het metaalhydride en metaaloxide in deze nanocomposieten.

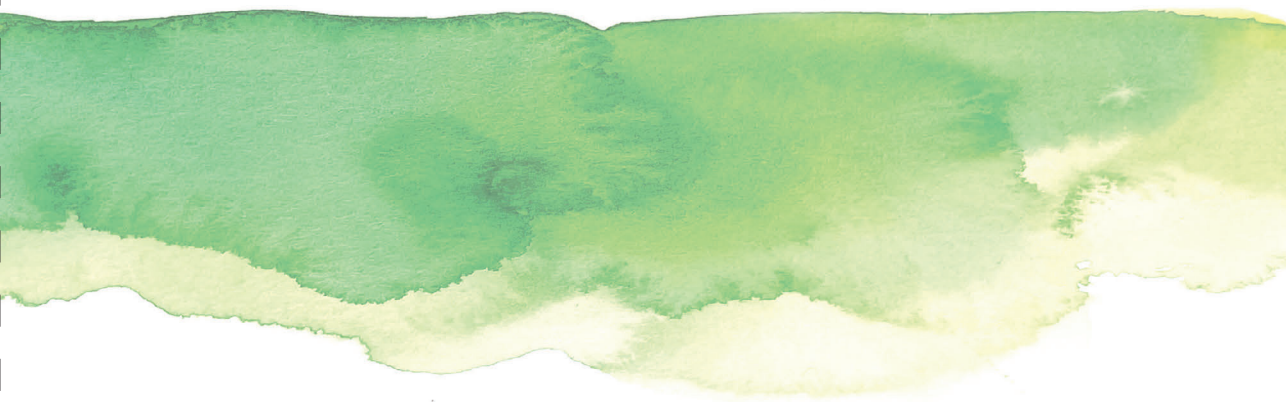
Uit de XRS-data werd duidelijk dat op het grensvlak tussen lithium boorhydride en silica, de structuur rondom boor verandert is. Deze wordt niet meer omringt door vier waterstofatomen, maar wordt bij het grensvlak omringt door drie atomen. Eenzelfde verbinding is aanwezig in het grensvlak tussen natrium boorhydride en silica, en natrium boorhydride en aluminiumoxide in natrium boorhydride/oxide nanocomposieten. Dit

toont aan dat zowel lithium ionen als natrium ionen makkelijk door deze grenslaag kunnen bewegen, waardoor de nanocomposieten een hoge ionische geleidbaarheid hebben. Deze studie laat zien dat XRS een veelbelovende techniek is om lokale structuren in metaalhydride/oxide nanocomposieten te bepalen. Om de structuur van de metaalhydride/oxide grenslaag op een betrouwbare manier vast te stellen is het daarbij wel van belang dat de experimentele resultaten van deze techniek vergeleken met berekende resultaten voor mogelijke grensvlakstructuren.

Om te onderzoeken of nanocomposietvorming ook toegepast kan worden op andere vaste stof elektrolyten, werd het effect van nanocomposietvorming op de lithium-ion geleiding in lithium nitraat en natrium-ion geleiding in natrium nitraat en natrium nitriet bestudeerd (**hoofdstuk 6**). In alle drie de gevallen kon de geleiding met drie orden van grootte verbeterd worden. Net als metaalhydride/oxide nanocomposieten, hangt de geleiding af van de reactiviteit van de elektrolyt en de oppervlaktechemie van het metaaloxide. Voor de lithium nitraat/oxide nanocomposieten, werd een correlatie gevonden tussen de ion geleiding en de hoeveelheid zure groepen op de oppervlakte van de oxides. Dit verkennende onderzoek laat zien dat nanocomposietvorming breed toepasbaar is en een positief effect kan hebben op de ion geleiding in verschillende vaste stof elektrolyten.



List of publications and presentations



Publications discussed in this thesis

L. M. de Kort, V. Gulino, P. E. de Jongh, & P. Ngene, (2021). Ionic conductivity in complex metal hydride-based nanocomposite materials: The impact of nanostructuring and nanocomposite formation. *Journal of Alloys and Compounds*, 163474. (Chapter 1)

L. M. de Kort, O. E. Brandt Corstius, V. Gulino, A. Gurinov, M. Baldus, & P. Ngene, (2023). Designing conductive sodium-based metal hydride nanocomposites: Interplay between hydride and oxide properties. *Advanced Functional Materials*, accepted. (Chapter 2)

L. M. de Kort, R. Zettl, M. Gombotz, H. M. R. Wilkening, P. E. de Jongh, & P. Ngene, (2020). Combined effects of anion substitution and nanoconfinement on the ionic conductivity of Li-based complex hydrides. *The Journal of Physical Chemistry C*, 124(5), 2806-2816. (Chapter 3)

L. M. de Kort, J. Harmel, P. E. de Jongh, and P. Ngene, (2020). The effect of nanoscaffold porosity and surface chemistry on the Li-ion conductivity of $\text{LiBH}_4\text{-LiNH}_2$ /metal oxide nanocomposites. *Journal of Materials Chemistry A*, 8(39), 20687-20697. (Chapter 4)

L. M. de Kort, A. Longo, A. Gulino, D. Blanchard, H. P. Rodenburg, M. Lazemi, A. M. J. van der Eerden, F. M. F. de Groot, and P. Ngene, X-ray Raman Scattering Study of Conductive Interfaces in Complex Hydride Nanocomposite Electrolytes. *In preparation*. (Chapter 5)

L. M. de Kort, M. E. T. van Ittersum, M. L. J. Peerlings, P. E. de Jongh, and P. Ngene, Enhanced Li- and Na-ion conductivity in LiNO_3 -, NaNO_2 - and NaNO_3 /oxide nanocomposites. *In preparation*. (Chapter 6)

Other publications by the author

M. S. Ram, L. M. de Kort, J. de Riet, R. Verbeek, T. Bel, G. Gelinck, and A. J. Kronemeijer, (2019). Submicrometer top-gate self-aligned a-IGZO TFTs by substrate conformal imprint lithography. *IEEE Transactions on Electron Devices*, 66(4), 1778-1782.

A. M. Hernández-Giménez, L. M. de Kort, G. T. Whiting, H. Hernando, B. Puértolas, J. Pérez-Ramírez, D. P. Serrano, P. C. A. Bruijninx, and B. M. Weckhuysen, (2021). Upscaling Effects on Alkali Metal-Grafted Ultrastable Y Zeolite Extrudates for Modeled Catalytic Deoxygenation of Bio-oils. *ChemCatChem*, 13(8), 1951-1965.

L. M. de Kort, V. Gulino, D. Blanchard, and P. Ngene, (2022). Effects of LiBF_4 addition on the lithium-ion conductivity of LiBH_4 . *Molecules*, 27(7), 2187.

F. Cuevas, M. B. Amdisen, M. Baricco, C. E. Buckley, Y. W. Cho, P. E. de Jongh, L. M. de Kort, ... and M. Latroche, (2022). Metallic and complex hydride-based electrochemical storage of energy. *Progress in Energy*, 4(3), 032001.

L. M. de Kort, P. Ngene, M. Baricco, P. E. de Jongh and V. Gulino, (2023). Improving the cycle life of solid-state batteries by addition of oxide nanoparticles to a complex hydride solid electrolyte. *The Journal of Physical Chemistry C*, submitted.

Oral presentations

NWO Materials4Sustainability Kick-off Meeting, Amsterdam, June 5th 2019, 'Enhanced Ionic Conductivity in LiBH₄-Based Solid State Conductors'

NWO CHAINS, Veldhoven, December 10th - 11th 2019, 'Metal hydride-based nanocomposites as electrolytes for all-solid-state batteries'

The Netherlands' Catalysis and Chemistry Conference (NCCC), Noordwijkerhout, March 2nd - 4th 2020, 'Metal hydride-based nanocomposites as electrolytes for all-solid-state batteries'

Physics@Veldhoven, Virtual, January 20th 2021, 'Ionic conductivity in metal hydride nanocomposites: The effect of nanoscaffold porosity and surface chemistry'

EUROMAT, Virtual, September 13th - 17th 2021, 'Ionic conductivity in metal hydride nanocomposites: The effect of nanoscaffold porosity and surface chemistry'

240th ECS Meeting, Virtual, October 10th - 14th 2021, 'Ionic conductivity in metal hydride nanocomposites: The effect of nanoscaffold porosity and surface chemistry'

The Netherlands' Catalysis and Chemistry Conference (NCCC), Noordwijkerhout, May 9th - 11th 2022, 'Enhanced ionic conductivity in metal hydride/oxide nanocomposites: The effect of nanoscaffold porosity and surface chemistry'

Hydrides as Energy Materials (HydEM), Louvain-la-Neuve, Belgium, May 18th - 20th 2022, 'Enhanced Li- and Na-ion Conductivities in Metal Hydride/Oxide Nanocomposites'

241th ECS Meeting, Vancouver, Canada, May 29th - June 2nd 2022, 'Nanoscaffold Porosity and Surface Chemistry Effects on Li-Ion Conductivity in Metal Hydride Nanocomposite Electrolytes'

23rd International Conference for Solid-State Ionics, Boston, USA, July 17th - 22nd 2022, 'Li-Ion Conductivity in Metal Hydride-Based Nanocomposite Electrolytes—The Effect of Nanoscaffold Porosity and Surface Chemistry'

Poster presentations

The Netherlands' Catalysis and Chemistry Conference (NCCC), Noordwijkerhout, March 4th - 6th 2019

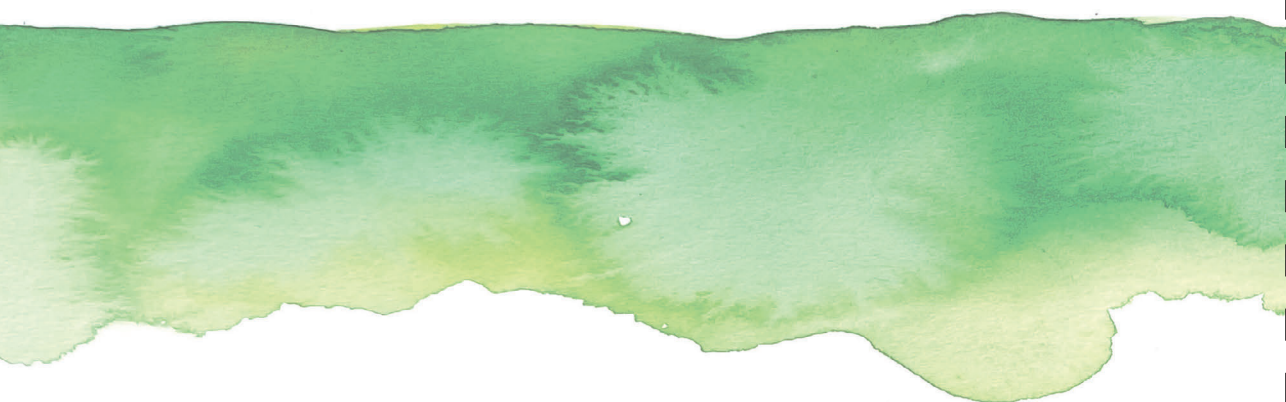
NWO Materials4Sustainability Kick-off Meeting, Amsterdam, June 5th 2019

1st ECCM Graduate School, Eerbeek, November 27th - 29th 2019

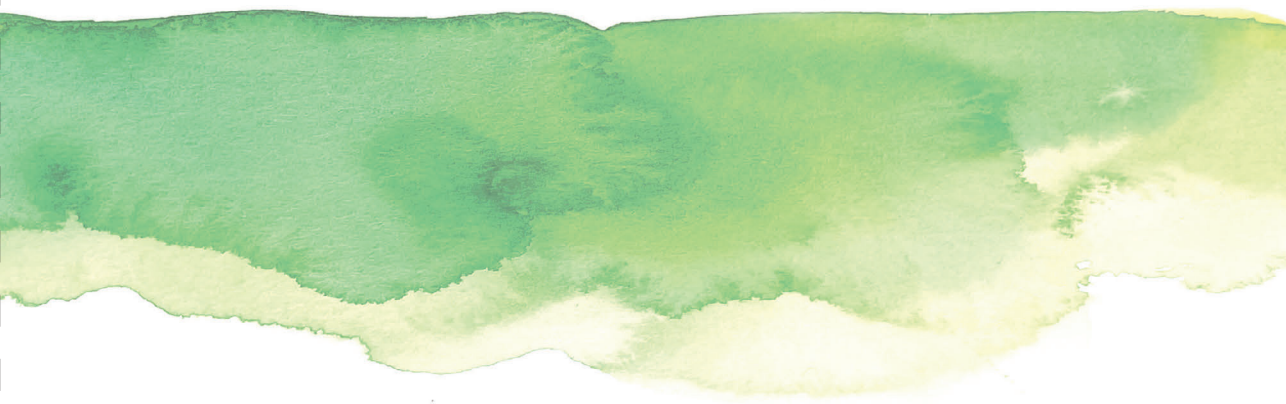
ECCM Research Day, Eindhoven, November 11th 2021

NWO CHAINS, Virtual, December 7th - 8th 2021

Physics@Veldhoven, Virtual, January 25th - 26th 2022



Acknowledgements | Dankwoord



Hoewel alleen mijn eigen naam op de voorkant van dit proefschrift staat, had deze niet geschreven kunnen worden zonder de hulp van verschillende mensen. Allereerst wil ik mijn promotor **Petra de Jongh** bedanken. Ik ben enorm dankbaar dat je me de kans hebt gegeven om dit onderzoek te mogen uitvoeren. Je enthousiasme over het onderwerp en je kritische blik op de wetenschappelijke resultaten brachten dit werk naar een hoger niveau en dat was erg waardevol. Ik vond het daarnaast bijzonder om samen met jou het vak "Electrochemie" te ontwikkelen, en daarbij te leren over jouw visie op het overbrengen van kennis.

Of course I would also like to thank my co-promoter **Peter Ngene**. I was very happy that, after only writing a short literature review under your supervision, you were confident that I would be a good candidate for this battery project. Your positive attitude and (many) ideas resulted in fruitful discussions, which were vital for the research we have done over the past years. You were a great supervisor and I enjoyed the time we spend together during several conferences and our beamtrip to DESY.

The scientific discussions I had with **Krijn de Jong, Frank de Groot, Nong Artrith, Marc Baldus, Alessandro Longo** and **Florian Meier** yielded valuable scientific insights and I would like to thank all of you for your useful advice.

Naast wetenschappelijke ondersteuning, had het werk uit dit proefschrift niet kunnen slagen zonder de technische ondersteuning van **Jan Willem, Dennie, Remco, en Ad**. Ook **Hans, Pascal, en Oscar** wil ik bedanken voor hun hulp en dat ze altijd klaar stonden voor vragen. Daarnaast was het ontzettend fijn dat ik met grote en kleine vragen terecht kon bij het secretariaat, waar **Ilonka en Sylvia** altijd klaar staan om te helpen.

Het begeleiden van studenten vond ik een van de leukste onderdelen van mijn PhD. Ik heb met erg veel plezier samengewerkt met **Oscar, Matt, Maaïke, Jeppe, Ties, en Lars**. Bedankt voor jullie inzet tijdens jullie tijd als battery teammembers. Het werk van Oscar vormt de basis voor hoofdstuk 3 en het werk van Matt en Maaïke is terug te vinden in hoofdstuk 6. Deze hoofdstukken waren er niet geweest zonder jullie enthousiasme, kennis en kritische blik. De literatuurstudies geschreven door **Jan, Jeroen, Nicolette, Daphne en Douwe** waren een waardevolle ondersteuning van mijn werk.

Four years ago, the battery team consisted of very few people (read: one). Luckily, it has grown substantially since then and I had the pleasure of working together with **Sander, Valerio** and **Henrik**. Sander, ondanks dat we maar een aantal weken samen hebben gewerkt, wil ik je bedanken voor je hulp in die korte periode. Jouw kennis en expertise zorgde ervoor dat ik een vliegende start kon maken met mijn project. Valerio, I am incredibly grateful that you joined our group after your short exchange. While your help and scientific input were essential for the papers we wrote together and for surviving the two beamtrips, I especially enjoyed our

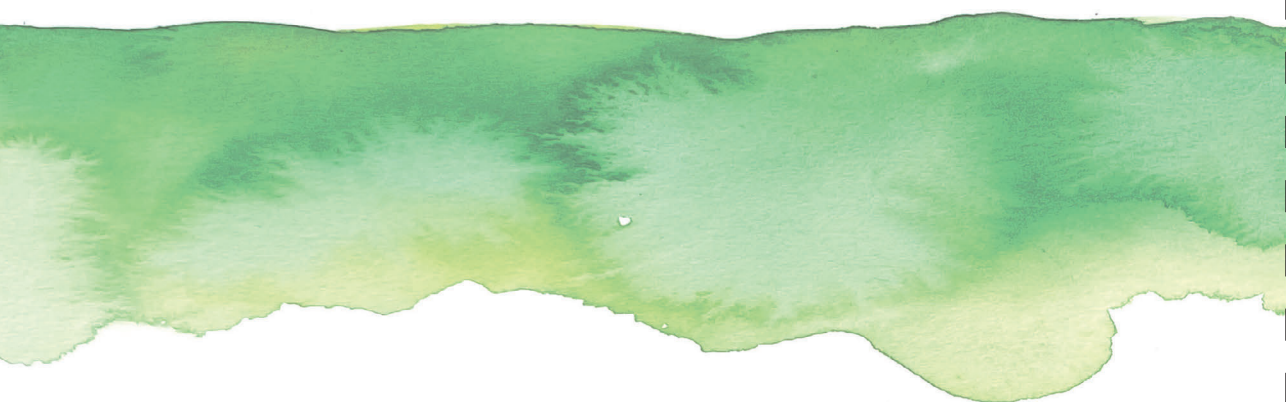
gossip-sessions over coffee! Henrik, hoewel onze onderzoeken nogal van elkaar verschilden, stond je altijd klaar om mee te denken over problemen. Bedankt voor je hulp tijdens (en na) de beamtrip naar DESY en de gezellige sfeer op het lab.

Besides the battery team, I am also thankful for all the help I got from several MCC and ICC group members. **Masoud**, thank you for joining our beamtrip at ESRF, even though it was very last-minute. **Yadi**, I enjoyed working together, thank you for all your effort. **Silvia, Joren, Giorgio, Laura B., Nikos and Suzan**, thank you for the N₂ physisorption measurements. **Kristiaan**, bedankt voor de mooie TEM en EDX metingen.

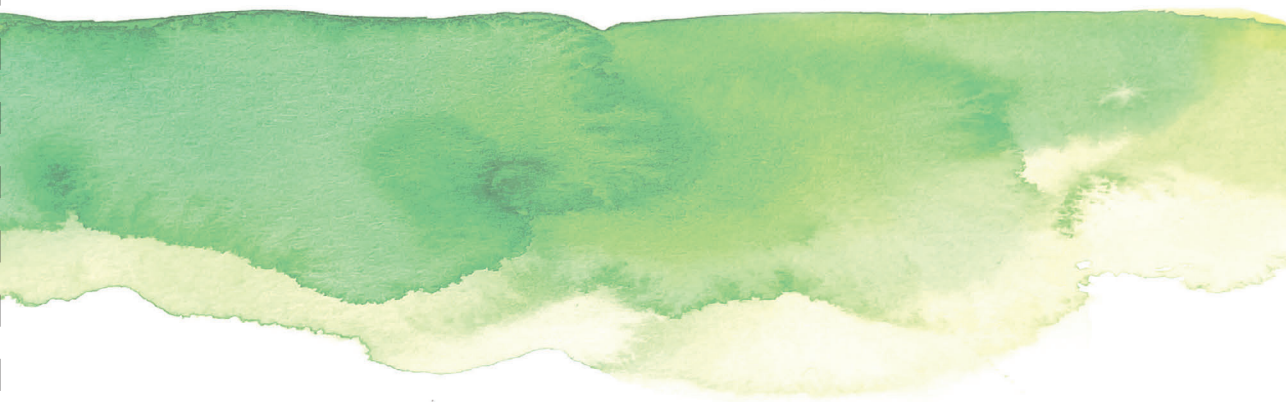
Besides the scientific help, there are many additional people I need to thank! Allereerst, mijn overburen **Frédérique, Luc en Suzan**, het was fijn dat jullie altijd tijd hadden voor een kletspraatje tussen de (soms frustrerende) experimenten door. Bedankt voor jullie gezelligheid en steun. **Frédérique**, ik was erg blij dat jij mijn directe overbuurvrouw werd en wil je naast de vele koffietjes op de groep ook bedanken voor alle mooie momenten daarbuiten. I would also like to thank my fellow teaching assistants, **Francesco, Marisol, Nynke, Oscar, and Savannah**. Working together with you made the teaching hours much more enjoyable. Ofcourse, I would also like to thank all of you and many more, including **Christa, Claudia, Erik, Johan, Jogchum, Jonas, Juliette, Giorgio, Henrik, Kristiaan, Lars, Laura B., Maaïke, Matt, Marta, Miguel, Petra K. and Valerio**, for the fun moments in the lab, at conferences and during coffee breaks and borrels. En last but not least, **Nienke**, bedankt voor alle goede gesprekken en mooie momenten de afgelopen 10 (!) jaar. Of het nu was onder het genot van een koffietje of biertje, tijdens een conferentie, spelletjesavond, writing retreat, of avontuurlijke fietstocht. Met alles kon ik bij jou terecht, en ik ben blij dat we na de bachelor en master ook het PhD avontuur samen konden doorlopen.

Ook buiten het David de Wied, zijn er verschillende mensen aan wie ik veel heb gehad. **Adrian, Daniel, Frédérique, Hilde, Isa, Jasper, Kim, Lies, Luara, Lucas, Nienke, Sander, Sophie, Thomas, Vanessa, Marije, mama en papa**, het was fijn om met jullie de mooie én uitdagende kanten die een promotieonderzoek met zich mee brengt te kunnen delen. De spelletjesmiddagen, etentjes, wijnproeverijen, feestjes, weekendjes weg, borrels, vakanties en - tijdens de corona lockdown-koffie wandelingen waren van grote waarde. **Marije**, als dynamische tweeling duo leerden we al jong hoe 1 + 1 meer kan zijn dan twee. Bedankt voor je eeuwige steun en uitdaging, en je waardevolle blik vanuit een andere hoek.

Mijn laatste bedankje is voor mijn thuiswerkcollega **Joost**. Toen we tijdens de eerste lockdown ineens tegen over elkaar aan de keukentafel zaten, was het even wennen. Eigenlijk vond ik het best leuk om samen in ons geïmproviseerde kantoor aan het werk te zijn. Bedankt dat je naar al mijn oefenpresentaties wilde luisteren en elke keer vol enthousiasme naar mijn nieuwste grafiek of figuur kwam kijken. Dankjewel voor alles de afgelopen jaren.



About the author



Laura Maria de Kort was born on the 23th of February 1994 in Almere (Flevoland, the Netherlands). In 2012, she finished her pre-university education (VWO) at the Oostvaarders College and moved to Utrecht to pursue a bachelor degree in chemistry at Utrecht University. During this three year degree, she performed her bachelor thesis research in the Condensed Matter and Interface group under the supervision of prof. dr. Daniël vanmaekelbergh.



After obtaining her BSc. degree in 2016, Laura continued her studies at Utrecht University with a master degree in 'Nanomaterials: Chemistry and Physics'. She performed her master thesis research in the group of prof. dr. ir. Bert Weckhuysen, during which she investigated the catalytic performance of zeolite extrudates. Afterward, Laura worked as a research intern at Holst Centre (Eindhoven, the Netherlands) for six months. During this time, she studied electrical doping effects in thin film transistors.

In 2018, Laura started her PhD research in the Materials Chemistry and Catalysis group under the supervision of prof. dr. Petra de Jongh and dr. Peter Ngene. During this research project, Laura studied the effect of nanocomposite formation on the ionic conductivity of metal hydride-based solid electrolytes. The results of this project are described in this thesis, have been published in internationally renowned journals and were presented during both national and international conferences. After finalizing her PhD research in November 2022, Laura continued her work on the development of novel battery technology as a research scientist at LionVolt (Eindhoven, the Netherlands).

